



**Reliability evaluation and optimization of multi-energy systems
considering energy storage devices effects under weather uncertainties**

A thesis submitted to the University of Manchester for the degree of
Master of Philosophy
in the Faculty of Science and Engineering

2022

Ziyan Liao
Department of Electrical and Electronic Engineering

Contents

Contents.....	2
List of figures.....	6
List of tables.....	11
List of publications.....	13
List of notations.....	14
Terms and abbreviations.....	19
Abstract.....	21
Declaration of originality.....	23
Copyright statement.....	24
Acknowledgements.....	25
Chapter 1.....	26
Introduction.....	26
1.1 The research background of multi-energy systems.....	26
1.2 Literature review.....	27
1.2.1 MES modeling.....	27
1.2.2 MES reliability assessment.....	28
1.2.3 MES reliability optimization.....	30
1.2.4 MES resilience analysis.....	31
1.3 Research gaps.....	32
1.4 Main contributions.....	32
1.5 Research aims and objectives.....	33
1.6 Thesis structure.....	34
Chapter 2.....	36
Overall modeling architecture of multi-energy system.....	36
2.1 Introduction.....	36

2.2 The structure of MES.....	36
2.3 Component models.....	37
2.3.1 Photovoltaic power generation system modeling.....	37
2.3.2 Wind power generation system modeling.....	48
2.3.3 Battery storage system modeling.....	53
2.3.4 Gas turbine modeling.....	56
2.3.5 Ground source heat pump modeling.....	59
2.3.6 CHP unit modeling.....	69
2.3.7 GB modeling.....	70
2.3.8 P2G device modeling.....	70
2.3.9 Energy storage devices modeling.....	70
2.3.10 V2G modeling.....	72
2.4 Energy networks modeling.....	79
2.4.1 Power system modeling.....	79
2.4.2 Heating system modeling.....	83
2.4.3 Gas network modeling.....	84
2.5 Summary.....	87
Chapter 3.....	88
Uncertainty modeling.....	88
3.1 Introduction.....	88
3.2 Stochastic modeling of renewable energy generation.....	88
3.2.1 Wind power generation.....	88
3.2.2 Solar power generation.....	89
3.3 Time-varying load forecasting.....	90
3.4 Time varying load and cost model.....	92
3.5 Summary.....	93
Chapter 4.....	94
Reliability evaluation of multi-energy system with storage devices.....	94
4.1 Introduction.....	94
4.2 Reliability indices for MES.....	94
4.2.1 Load-point reliability indices.....	94
4.2.2 System-level reliability indices.....	95
4.3 Monte Carlo simulation for reliability assessment.....	96
4.3.1 Sequential Monte Carlo simulation.....	97

4.4 Reliability evaluation of MES with storage devices under weather uncertainties..	98
4.5 Summary.....	101
Chapter 5.....	102
Reliability optimization of multi-energy system with storage devices.....	102
5.1 Introduction.....	102
5.2 Reliability optimization problem formulation.....	102
5.2.1 Reliability indicator.....	102
5.2.2 Economic indicator.....	103
5.2.3 Objective function.....	104
5.2.4 Constraints.....	105
5.2.5 Normalization of objective functions.....	106
5.2.6 Problem formulation.....	106
5.3 Multi-objective optimization algorithms.....	107
5.3.1 NSGA-II.....	107
5.3.2 SPEA2.....	110
5.3.3 MOPSO.....	111
5.4 Reliability optimization process.....	113
5.5 Summary.....	114
Chapter 6.....	115
Case studies for reliability evaluation and optimization in MES.....	115
6.1 Introduction.....	115
6.2 Simulation parameters.....	115
6.3 Case study 1 for reliability optimization under weather uncertainties.....	128
6.4 Case study 2 for reliability optimization under weather uncertainties.....	132
6.5 Sensitivity analysis.....	137
6.6 Summary.....	139
Chapter 7.....	141
Multi-energy system resilience to extreme weather.....	141
7.1 Introduction.....	141
7.2 Multi-energy system resilience definition.....	141
7.3 Resilience modeling of MESs under extreme weather.....	143
7.4 Multi-temporal and multi-regional resilience assessment of MESs using sequential	

MCS.....	144
7.5 Resilience enhancement analysis and adaptation strategies.....	146
7.6 Resilience study of MES 1.....	148
7.7 Summary.....	155
Chapter 8.....	156
Conclusions and future work.....	156
8.1 Achievements and contributions.....	156
8.2 Future expansions.....	157
References.....	159
Appendix A.....	170
A.1 MES reliability assessment code.....	170
A.2 NSGA-II optimization code [100].....	195
A.3 SPEA2 optimization code [101].....	201
A.4 MOPSO optimization code [102].....	207

Word count: 37022

List of figures

Figure 1.1: World primary energy consumption [1].....	26
Figure 2.1: The structure of MES.....	36
Figure 2.2: The equivalent circuit of photovoltaic cells [42].....	37
Figure 2.3: Mask block for PV module.....	39
Figure 2.4: Simulation model for PV module.....	40
Figure 2.5: Boost converter topology [43].....	40
Figure 2.6: Boost converter operating principle: (a) when switch S is conducting; (b) when switch S is disconnecting.....	41
Figure 2.7: MPPT control for PV module [45].....	42
Figure 2.8: The flow chart of perturb and observation method [45].....	42
Figure 2.9: Perturb and observation method MPPT control Simulink model.....	43
Figure 2.10: The inverter structure Simulink model of PV.....	44
Figure 2.11: The inverter control module for PV.....	45
Figure 2.12: The current regulator module.....	46
Figure 2.13: The current regulator module parameters for PV.....	46
Figure 2.14: The grid-connected simulation model of photovoltaic power generation system.....	47
Figure 2.15: PV active power generation.....	47
Figure 2.16: The structure of wind power generation system [49].....	48
Figure 2.17: The inverter structure of wind module.....	49
Figure 2.18: The controller module for wind.....	50
Figure 2.19: The DC voltage regulator module.....	50

Figure 2.20: The DC voltage regulator parameters.....	51
Figure 2.21: The current regulator parameters.....	51
Figure 2.22: The grid-connected simulation model of wind power generation system.....	52
Figure 2.23: Wind active power generation.....	53
Figure 2.24: Bidirectional interleaved buck-boost converter [52].....	53
Figure 2.25: Simulation model of DC/DC battery storage system.....	54
Figure 2.26: The inverter block for battery.....	54
Figure 2.27: The VF control block for battery.....	55
Figure 2.28: The grid-connected simulation model of DC/DC battery storage system.....	56
Figure 2.29: Schematic diagram of a typical HDGT and its major components [53].....	57
Figure 2.30: The Brayton cycle [53].....	57
Figure 2.31: Rowen's model for HDGT [53].....	58
Figure 2.32: Simulation model of Rowen's model for HDGT.....	59
Figure 2.33: Simulink model of the whole gas turbine system.....	59
Figure 2.34: Schematic diagram of GSHP [57].....	60
Figure 2.35: Heat exchanger simulation block.....	61
Figure 2.36: Evaporator simulation block.....	64
Figure 2.37: Condenser simulation block.....	67
Figure 2.38: Compressor simulation block.....	68
Figure 2.39: The simulation model of ground source heat pump.....	69
Figure 2.40: Configuration of V2G system [13].....	72
Figure 2.41: V2G AC/DC simulation block.....	73
Figure 2.42: The control model for AC/DC converter in V2G.....	74

Figure 2.43: The DC/DC block for V2G.....	74
Figure 2.44: The charging block for V2G.....	75
Figure 2.45: The discharging block for V2G.....	76
Figure 2.46: The diagram of PWM converter based on SVPWM control [64].....	77
Figure 2.47: Simulink model of a bidirectional electrical vehicle charging station.....	77
Figure 2.48: Probability density function for the available energy in 150 EVs (a) between 7 - 8 p.m.; (b) between 5-6 a.m. [27].....	78
Figure 2.49: Configuration of V2G system [27].....	79
Figure 2.50: IEEE 24 Bus system [69].....	80
Figure 2.51: The upper part simulation model of IEEE 24 Bus system.....	81
Figure 2.52: The lower part simulation model of IEEE 24 Bus system.....	82
Figure 2.53: The schematic diagram of RBTS Bus 5 system [16].....	82
Figure 2.54: The simulation model of RBTS Bus 5 system.....	83
Figure 2.55: The heating system of each load [63].....	84
Figure 2.56: The 13 node heat network simulation model.....	84
Figure 2.57: The gas pipeline simulation model.....	85
Figure 2.58: The 9 node gas network simulation model.....	86
Figure 2.59: The gas load block.....	86
Figure 2.60: The Simulink model of the MES.....	87
Figure 3.1: Variation curve of wind farm output power with wind speed [65].....	89
Figure 4.1: The two-state Markov model [4].....	97
Figure 4.2: The operating and failure time of a component [76].....	98
Figure 4.3: The MCS process with storage device under weather uncertainties.....	101

Figure 5.1: (a) Non-dominated sorting procedure; (b) Crowding distance calculation [79].	109
Figure 5.2: The reliability optimization flow chart.....	114
Figure 6.1: (a) Weibull distribution of wind speed; (b) Beta distribution of solar radiation.	116
Figure 6.2: BP neural network training performance for MES 1: (a) 24-node power load forecasting; (b) 13-node heat load forecasting; (c) 9-node gas load forecasting.....	117
Figure 6.3: BP neural network training performance for MES 2: (a) 39-node power load forecasting; (b) 32-node heat load forecasting; (c) 20-node gas load forecasting.....	118
Figure 6.4: Time-varying cost weight factors: (a) For residential, agriculture and large user customers; (b) For Govt/Inst and industrial customers; (c) For office and Commercial customers [40].....	119
Figure 6.5: The schematic diagram of the first multi-energy system.....	129
Figure 6.6: Convergence curve of: (a) SAIDI (h/Ca); (b) Cost (k\$).....	129
Figure 6.7: Pareto Front results of three multi-objective algorithms for MES 1.....	130
Figure 6.8: The schematic diagram of the second multi-energy system.....	133
Figure 6.9: Convergence curve of: (a) SAIDI (h/Ca); (b) Cost (k\$).....	133
Figure 6.10: Pareto Front results of three multi-objective algorithms for MES 2.....	134
Figure 7.1: The multiphase robust performance response curve of MESs [93].....	141
Figure 7.2: Overhead line fragile curve [93].....	143
Figure 7.3: Wind fragile curves of transmission lines (base and robust case studies) [91].	147
Figure 7.4: Weather regions of test MES.....	148
Figure 7.5: Probability density function of regional wind profiles with $w_{max} = 40$ m/s [91].	149
Figure 7.6: Hourly wind profiles with $w_{max} = 40$ m/s [91].....	149
Figure 7.7: Impact of increasing maximum wind speed on LOLF and EENS.....	150
Figure 7.8: Ranking results of: (a) EELC; (b) EHLC; (c) EGLC.....	151

Figure 7.9: The impact of resilience enhancement at different wind speeds: (a) $w_{max} = 40$ m/s; (b) $w_{max} = 50$ m/s; (c) $w_{max} = 60$ m/s.....154

List of tables

Table 6.1. Weibull distribution parameters.....	115
Table 6.2. Beta distribution parameters.....	115
Table 6.3: BP neural network parameters.....	116
Table 6.4: The failure rate and repair time of the components in MES [4].....	118
Table 6.5: Sector interruption cost (\$/kW) [40].....	119
Table 6.6: The installation cost coefficient and capacity for storage devices.....	120
Table 6.7: The capacity of PV, WT, and GT.....	120
Table 6.8: IEEE 24 bus system transmission line length and forced outage rate [69].....	120
Table 6.8 (continue): IEEE 24 bus system transmission line length and forced outage rate [69].....	121
Table 6.9: IEEE 24 bus system generator locations [69].....	121
Table 6.10: IEEE 24 bus system generating unit reliability data [69].....	121
Table 6.11: IEEE 24 bus system load and customer data [69].....	122
Table 6.12: 13-node heat network load and customer data [4].....	122
Table 6.13: 9-node gas network pipe length [71].....	123
Table 6.14: 9-node gas network load and customer data [71].....	123
Table 6.15: IEEE 39 bus system line data [84].....	123
Table 6.15 (continue): IEEE 39 bus system line data [84].....	124
Table 6.16: IEEE 39 bus system load and customer data [84].....	124
Table 6.16 (continue): IEEE 39 bus system load and customer data [84].....	125
Table 6.17: IEEE 39 bus system generator data [84].....	125

Table 6.18: 32-node heat network pipe length [85].....	125
Table 6.18 (continue): 32-node heat network pipe length [85].....	126
Table 6.19: 32-node heat network load and customer data [85].....	126
Table 6.20: 20-node Belgian natural gas system pipe length [86].....	127
Table 6.21: 20-node Belgian natural gas system load and customer data [86].....	127
Table 6.22: Multi-objective optimization algorithms parameters [88].....	128
Table 6.23: NSGA-II optimization result for MES 1.....	131
Table 6.24: MOPSO optimization result for MES 1.....	131
Table 6.25: SPEA2 optimization result for MES 1.....	131
Table 6.26: Comparison of execution times for MES 1.....	132
Table 6.27: Comparison of reliability indices before and after optimization for MES 1... 132	
Table 6.28: NSGA-II optimization result for MES 2.....	134
Table 6.28 (continue): NSGA-II optimization result for MES 2.....	135
Table 6.29: MOPSO optimization result for MES 2.....	135
Table 6.30: SPEA2 optimization result for MES 2.....	136
Table 6.31: Comparison of execution times for MES 2.....	136
Table 6.32: Comparison of reliability indices before and after optimization for MES 2... 136	
Table 6.33: Sensitivity analysis result of MES 1 to failure rate in scenario 1.....	138
Table 6.34: Sensitivity analysis result of MES 2 to failure rate in scenario 1.....	138
Table 6.35: Sensitive analysis result of MES 1 to repair time in scenario 2.....	138
Table 6.36: Sensitive analysis result of MES 2 to repair time in scenario 2.....	139

List of publications

Liao, Z., & Parisio, A. (2022). Reliability Optimization of Multi-Energy System Considering Energy Storage Devices Effects under Weather Uncertainties. *Energies*, 15(3), 696.

List of notations

k	Boltzmann's constant
q	Elementary charge
T	Absolute temperature
D	Conduction ratio
ρ	Air density
τ	Time variable
$\Delta G_{iL}^{b \cdot \Delta t}$	Gas load curtailment
$\Delta H_{iL}^{b \cdot \Delta t}$	Heat load curtailment
$\Delta P_{iL}^{b \cdot \Delta t}$	Power load curtailment
COP_{CHP}	Coefficient of the performance parameter of the CHP unit
LHV_{ng}	Heating value of natural gas
TVC^t	Time-varying cost
pc_{ij}	Per unit interruption cost
$v_{i,D}(t)$	Velocity of the particle i in the D-dimensional space in the t^{th} iteration
$x_{i,D}(t)$	Position of the particle i in the D-dimensional space in the t^{th} iteration
$c_{p,w}$	Specific heat capacity of water at constant pressure
$C_{investment}$	Investment cost
$C_{interrupt}$	Interruption cost
$C_{install}$	Installation cost coefficient
$N_{archive}$	Archive size
P_{grid}	Grid power supply

$C_{loss}^{i,t}$	Outage cost during failure time t at load i
P_{Load}^t	Time-varying load
G_{ref}	Light intensity
L_{aij}	Average load
N_{pop}	Population size
T_{ref}	Battery temperature
w_{max}	Maximum wind speed
η_{CHP}	CHP unit efficiency
G_{CHP}^t	Natural gas consumption
H_{CHP}^t	Heat power generation of CHP unit during time period t
P_{CHP}^t	Electric power generation of CHP unit during time period t
I_{PV}	PV current
I_{sc}	Short-circuit current
V_{PV}	PV voltage
V_{ci}	Cut-in wind speed
V_{co}	Cut-out wind speed
V_{oc}	Open-circuit voltage
C_{ij}	Per-unit interruption cost
η_{GB}	GB unit efficiency
$G_{gs}^{y,t}$	Gas volume of gas storage device y at hour t
G_{GB}^t	Natural gas consumption
H_{GB}^t	Heat output of the GB unit during time period t
T_{dn}^p	Load point p failure time

T_{up}^p	Operating time of load point p
a_{ij}^t	Operation state of overhead line ij at time t
I_{ph}	Light current
$H_{hs}^{i,t}$	Heat energy of heat storage device i at hour t
C_T	Aerodynamic torque coefficient
F_c	Condenser's heat transfer area
F_d	Soil heat transfer area
F_e	Heat transfer area of evaporator
G_c	Mass flow of chilled water
G_c	Cooling water flow in condenser
G_r	Refrigerant flow
I_m	Current at maximum power point
K_c	Condenser's heat transfer coefficient
K_d	Soil heat transfer coefficient
K_e	Heat transfer coefficient of evaporator
K_s	Soil thermal conductivity
L_y	Annual peak load
P_L	Load power
P_d	Ratio of daily load to weekly peak
P_m	Maximum power point
P_r	Wind turbine's rated power output
P_w	Ratio of weekly load to annual peak
Q_c	Heating capacity of condenser
Q_e	Cooling capacity of evaporator

R_p	Shunt resistance
R_s	Series resistance
U_p	Average outage time of load point p
V_d	Diode terminal voltage
V_m	Voltage at maximum power point
V_o	Average output voltage
V_r	Rated wind speed
W^t	Time-varying cost weight factor
f_p	Number of outages affecting load point p
m_c	Refrigerant quality in the condenser
m_e	Refrigerant quality of evaporator
r_p	Average repair time of load point p
t_b	Buried pipe temperature
t_g	Environmental soil temperature at the remote point
η_c	Compressor efficiency
η_e	Compressor power consumption
η_t	Turbine efficiency
h	Enthalpy
η_v	Compressor volumetric efficiency
λ_p	Average failure rate of load point p
$P_L(w)$	Line failure probability of wind speed w
$P_t^{discharging}$	Discharging power
$P_t^{charging}$	Charging power
$P_i^{subs}(w)$	Failure probability of substation i at wind speed w

P_h^t	Ratio of hourly load to daily peak
\overline{P}_L	Line failure probability in good weather
F_0	Fourier number
I_0	Diode reverse saturation current
η_{P2G}	P2G unit efficiency
G_{P2G}^t	Natural gas generation
P_{P2G}^t	Electric power consumption of P2G unit during time period t

Terms and abbreviations

ASAI	Average service availability index
CAIDI	Customer average interruption duration index
CCHP	Combined cooling, heat and power
CDF	Customer damage function
CHP	Combined heat and power
ECOST	Expected interruption cost
EELC	Expected electrical load curtailment
EENS	Expected energy not supplied
EGLC	Expected gas load curtailment
EHLC	Expected heat load curtailment
ES	Electricity storage
FMEA	Failure mode and effect analysis
GB	Gas boiler
GN	Gas network
GS	Gas storage
GSHP	Ground source heat pump
HDGT	Heavy duty gas turbine
HN	Heat network
HS	Heat storage
LOLF	Loss of load frequency
MCS	Monte Carlo simulation
MES	Multi-energy system
MOEA	Multi-objective evolutionary algorithm
MOPSO	Multiple objective particle swarm optimization

MPPT	Maximum power point tracking
NSGA-II	Non-dominated sorting genetic algorithm II
P2G	Power to gas
PG	Power grid
PMSG	Permanent magnet synchronous generator
RBTS	Roy Billinton test system
SAIDI	System average interruption duration index
SAIFI	System average interruption frequency index
SPEA2	Strength pareto evolution algorithm 2
SVPWM	Space vector pulse width modulation
TSS	Thermal storage strategies
TST	Total specified simulation period in years
TTF	Time to failure
TTR	Time to repair
TTS	Time to switch
TVCM	Time-varying cost model
V2G	Vehicle to grid

Abstract

Since traditional fossil energy sources such as coal and oil are non-renewable, increasing energy efficiency and expanding broad use of renewable energy sources have become an inevitable choice to solve energy shortages. The multi-energy system (MES) can realize the cascade utilization of energy through various forms of energy coupling such as electricity, gas, cold/heat, etc., and effectively improve the comprehensive utilization efficiency of energy. Moreover, through its coupling characteristics and complementary substitution, multi-energy system can make up for the obvious intermittence and random fluctuation of renewable energy, such as wind power and solar energy, and promote the development and usage of renewable energy. In addition, the energy storage system plays a critical role in the multi-energy system.

Due to its bidirectional charge-discharge feature, it can compensate for insufficient energy supply caused by system failure and store excess energy when the system is operating normally, which improves the flexibility of the multi-energy system. Therefore, this project presents an approach for evaluating and optimizing reliability under weather uncertainty considering various energy storage configuration strategies.

Firstly, the simulation model of the whole MES is created in Matlab/Simulink. Secondly, sequential Monte Carlo simulation is used to evaluate MES reliability. Then, a multi-objective reliability optimization is proposed aiming at minimizing system interruption duration and reliability cost. SAIDI (system average interruption index) reliability index is adopted as the reliability indicator to reflect MES reliability performance. The cost indicator includes both system interruption costs and investment costs. Different meta-heuristic optimization algorithms have been considered such as NSGA-II (non-dominated sorting genetic algorithm II), MOPSO (multiple objective particle swarm optimization), and SPEA2 (strength Pareto evolution algorithm 2) to compare the reliability optimization results and demonstrate the feasibility of the proposed methodology.

Case studies that are applied on two typical MES layouts of increasing complexity are also given afterward. Both case studies' results show that NSGA-II leads to the best optimal values and converges the fastest among the three algorithms. After optimization, the SAIDI declined by 90.78% in case study 1 and 86.92% in case study 2, respectively. Last but not

least, this project also investigates the resilient analysis of MES. The resilient modeling and evaluation of MES are given to investigate the effect of the resilience enhancement strategies on different wind speeds. The simulation results have concluded that the priority of resilience strengthening actions may vary depending on the wind speed profile. Improving line robustness gives significant improvements in resilience index at high wind speed, whereas redundancy case is most significant at extreme wind speeds.

Keywords: multi-energy system; weather uncertainty; energy storage configuration strategies; sequential Monte Carlo simulation; reliability optimization; meta-heuristic optimization algorithms; resilient analysis

Declaration of originality

I hereby confirm that no portion of the work referred to in the thesis has been submitted in support of an application for another degree or qualification of this or any other university or other institute of learning.

Copyright statement

- i. The author of this thesis (including any appendices and/or schedules to this thesis) owns certain copyright or related rights in it (the “Copyright”) and s/he has given The University of Manchester certain rights to use such Copyright, including for administrative purposes.
- ii. Copies of this thesis, either in full or in extracts and whether in hard or electronic copy, may be made only in accordance with the Copyright, Designs and Patents Act 1988 (as amended) and regulations issued under it or, where appropriate, in accordance with licensing agreements which the University has from time to time. This page must form part of any such copies made.
- iii. The ownership of certain Copyright, patents, designs, trademarks and other intellectual property (the “Intellectual Property”) and any reproductions of copyright works in the thesis, for example graphs and tables (“Reproductions”), which may be described in this thesis, may not be owned by the author and may be owned by third parties. Such Intellectual Property and Reproductions cannot and must not be made available for use without the prior written permission of the owner(s) of the relevant Intellectual Property and/or Reproductions.
- iv. Further information on the conditions under which disclosure, publication and commercialisation of this thesis, the Copyright and any Intellectual Property and/or Reproductions described in it may take place is available in the University IP Policy (see <http://documents.manchester.ac.uk/DocuInfo.aspx?DocID=24420>), in any relevant Thesis restriction declarations deposited in the University Library, The University Library’s regulations (see <http://www.library.manchester.ac.uk/about/regulations/>) and in The University’s policy on Presentation of Theses.

Acknowledgements

I would like to express the deepest appreciation to my supervisor **Dr Alessandra Parisio**, who gives me strong support and patient guidance for my MPhil project. I am grateful to her for everything she taught me this year. The meetings and conversations were vital in inspiring me to think out of the box, from multiple perspectives to form a comprehensive and objective critique. It is her valuable suggestions and encouragement that drive me to accomplish this project.

I would like to thank all the staff at the University of Manchester. It is their kind help and support that have made my study and life in the UK a wonderful time. Finally, I would like to express my gratitude to my parents. Without their tremendous understanding and encouragement over the past few years, it would be impossible for me to complete my study.

Chapter 1

Introduction

The multi-energy system refers to a new energy system concept formed by the coupling of multiple energy sources such as electricity, heat, and gas in energy production, transmission, and utilization, which breaks the traditional mode of single power supply and independent operation of the power grid. During the process of planning, design, construction and operation, multi-energy systems coordinate and optimize all types of energy supplies, making full use of renewable energy to improve system flexibility, economy, and reliability. This chapter mainly introduces the definition, characteristics, and research background of the multi-energy systems, as well as the current level of research in MES modeling, reliability evaluation, and optimization.

1.1 The research background of multi-energy systems

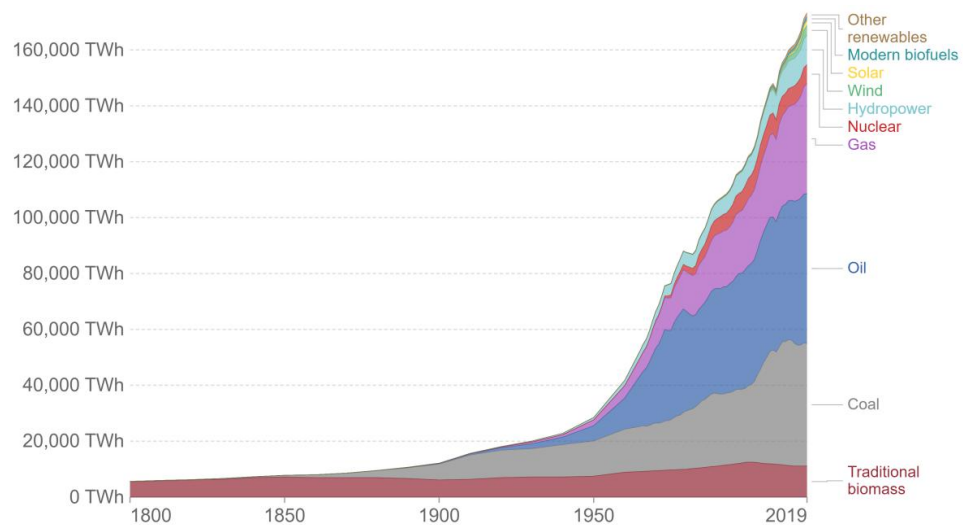


Figure 1.1: World primary energy consumption [1].

The rapid development of society depends on the massive demand for energy, Figure 1.1 depicts global primary energy consumption by source [1]. Fossil fuels will undoubtedly hold an important role in satisfying the world's rising energy demands. However, fossil energy reserves are limited and will eventually face the crisis of energy depletion. Therefore, in an attempt to address the energy crisis and alleviate the severe pollution brought by fossil energy to the environment, it is necessary to develop the combined

power-gas-heat multi-energy system to enhance the efficiency of energy usage.

The multi-energy system, which is based on the principle of cascading energy utilization to realize the centralized supply of various energy sources, emphasizes the coupling and coordination between various energy sources [2]. Due to the realization of energy cascade utilization and the decrease of energy consumption and overall system operation costs, the multi-energy system has the following significant advantages [3]: improve conversion efficiency and usage of primary energy sources through distributing multi-generation; increase MES flexibility, for instance, by allowing other forms of energy conversion devices (e.g. CHP) to participate in power system balancing.

Compared with the traditional power grid which only delivers electrical energy source to customers, the MES places a greater emphasis on the coordinating relationship between multiple energy sources, which can achieve a better operational state by complementing one another. Moreover, the current research on the optimal configuration of the MES only focuses on single coupling networks such as combined heat and power networks or electric-gas networks. The optimization operation of MES becomes more sophisticated due to the interaction between the power grid, heat network, and the natural gas network, therefore the current research is still in the early stages and requires further investigation.

1.2 Literature review

1.2.1 MES modeling

Simulation modeling studies based on the gas, heat, and electricity multi-energy systems usually include different coupling systems. The authors in [5] develop a CHP model including electrical and thermal storage systems in Simulink/MATLAB and the results show that the CHP system can run continuously with optimal efficiency through the additional energy storage systems. A co-generation facility (CHP system) as well as a thermal energy storage system is modeled in [6] and applied to a university campus to satisfy the heating requirement of the buildings. The authors in [7] construct a model of the CCHP system, as well simulations of the lithium bromide refrigerator, waste heat boiler, and micro gas turbine. The impacts of three thermal storage strategies (TSS) which include traditional, active, and novel TSS upon the efficiency of the CCHP system are modeled and evaluated in [8] by using MATLAB and TRNSYS software. The authors in [9] develop two modeling approaches for power to gas systems in Simulink/ MATLAB, the one is through a component level (in particular for the electrolyzer and the methanation

process), the other is through a system level. The authors in [10] present a mathematical model of gas and power systems, and appropriate numerical methods are adopted to analyze the impact of gas and power network dynamics. The authors of [11] provide optimal operation of combined power and gas systems through integrating interconnected energy hubs. Despite coupling system CHP and P2G, researchers also draw great attention to V2G (vehicle to grid) technology. A single-phase bidirectional electric car charger model that can function in all four quadrants of the P-Q plane is proposed in [12]. The authors in [13] propose the control and simulation of bidirectional electrical vehicle charging stations to the power grids using a three-level AC/DC converter and PI-Fuzzy controller. The CHP and electrical vehicle charging station integrated into a micro-grid are modeled and simulated in [14] on the MATLAB/Simulink platform.

Although the above references have laid a foundation for MES modeling, most of the scholars only focused on single coupling systems such as electricity-heat coupling systems or electricity-gas systems and rarely focused on the whole multi-energy systems which include all the three energy forms. This project has considered all three networks which are power grid, heat network, and gas network and their coupling components such as CHP, GB, P2G, and V2G and simulated the whole MES in Simulink/ MATLAB.

1.2.2 MES reliability assessment

The ability or possibility of a multi-energy system to complete energy supply within a set time and under specified working conditions is known as reliability [15]. The system's composition is becoming increasingly complicated with science and technology development, and the reliability problem of the system is increasingly prominent. Reliability evaluation can use qualitative or quantitative indicators such as ENS (energy not supplied) to indicate the system's risk of energy supply interruption, guiding the MES planning, operation, and other production activities. The MES is directly related to a variety of loads such as electricity, gas, cold, and heat, it is critical to assure the integrated energy system's reliability and to conduct reliability evaluation research.

Following Roy Billiton's introduction of the reliability evaluation study [16], a significant number of researchers have investigated the reliability of multi-energy systems. However, the most of study has concentrated on single coupling systems, for example, combined

power and heat systems or combined power and gas systems [17]. Monte Carlo simulation is adopted to evaluate the reliability of an integrated power-heat energy system including heat pumps in [18]. The authors in [19] examine the implications of a CCHP system (combined cooling, heating, and power system) on energy supply reliability, indicating that combining energy sources can dramatically improve entire system reliability. The authors in [20] proposed a reliability assessment approach for a combined power-gas network including power-gas conversion and established the corresponding energy flow model and load reduction optimization model.

A few research on power-gas-heat multi-energy systems has been undertaken based on the reliability evaluation of single coupling systems. The authors introduced a reliability evaluation methodology for integrated energy systems in [21], which uses the Monte Carlo simulation technique to produce system states and takes into account energy flow models in different energy networks when investigating the state analysis. The authors in [22] proposed the reliability assessment method of the integrated energy system on the basis of smart agent communication, while also considering the influence of system reconfiguration. The authors in [23] examine the reliability of a multi-carrier energy system with different levels of demand while also taking into account the uncertainty of different weather conditions. Although the aforementioned literature has conducted their research on the whole multi-energy system and uncertainty modeling also has been included in [23], the effect of energy storage systems on the whole MES has not been considered. A reliability assessment method for integrated energy systems taking into account the energy storage has been proposed in [24]. The influence of different capacity and operation strategies of energy storage equipment on the reliability of user-level integrated energy systems has also been analyzed. A time-varying reliability evaluation method has been provided in [25] to assess the district MES while also taking into account the energy storage optimal control. The FMEA (failure mode and effect analysis) method and Monte Carlo simulation are combined in [26] to investigate multi-energy micro-grids reliability whilst examining different operational strategies for energy storage devices.

Because of the impact of energy storage systems on the reliability of multi-energy systems, it is necessary to consider it in reliability evaluations in order to optimize the overall system's operation and reliability. The energy storage system can be used as a backup source when the MES fails to supply the energy to customers while also storing the surplus

energy when the MES operates normally. The V2G (vehicle to grid) system also plays a significant role in the bi-directional energy flow, and enhances the MES flexibility and reliability. The authors in [27] put forward the 24h available energy model of electric vehicles to study the effect of V2G on power distribution system reliability. From the above literature, it is apparent to see how different storage configuration schemes can have a huge impact effect on overall system reliability; as a result, it is vital to consider storage systems when evaluating and optimizing MES reliability.

Monte Carlo simulation method is a probabilistic based method, which obtains the estimated value of the result by sampling random variables with different distributions, and is often used for reliability assessment and uncertainty modeling [33]. It is particularly well suited to some problems that are difficult or impossible to address using analytical approaches due to a large number of random variables. Non-sequential Monte Carlo and sequential Monte Carlo are the two sorts of Monte Carlo simulations. In contrast to the non-sequential approach, the sequential Monte Carlo simulation models system states in chronological order.

1.2.3 MES reliability optimization

On the basis of reliability assessment, the way to enhance the reliability of the energy supply of MES is also worthy of further exploration. An optimal reliability planning for a composite electric power system through Monte Carlo simulation and particle swarm optimization has been provided in [28]. The authors in [29] focused on reliability optimization of regional MES, which also consider the high renewable penetration. The authors in [30] propose a multi-objective optimization of a grid-connected PV-wind hybrid system that considers reliability, economics, and environmental issues. In [31], the researchers optimize residential buildings for energy demand by applying reliability limitations without taking prices into account. In [32], the researchers investigate an optimal day-ahead dispatch and predictive control model for energy hubs, but without taking into account the optimal system design. The aforementioned studies have concentrated on either single energy system optimization or single objective optimization. The multiple energy vectors are not considered together in these assessment and optimization studies. Moreover, the uncertainty analysis was not involved in most multi-energy system research. Multi-energy systems' economic and reliability are still not co-

optimized at the same time, despite the fact that both are important factors to consider.

In general, deterministic methods (also known as analytical methods) and probability-based approaches are the two types of optimization algorithms. The analytical approaches in which the solution strategy is guided by well-defined principles and does not include any random elements. The probability-based approach, whose evolution is based on random decisions during the evolution. Moreover, meta-heuristic optimization algorithms have been widely used to solve various problems. NSGA-II, MOPSO, and SPEA2 appear to be the most frequently utilized Pareto-based MOEA (multi-objective evolutionary algorithm). The main principle of NSGA-II [35] is the fast non-dominated sorting, which can rank all the particles and preserve the elite solution. The principle of SPEA2 [36] is similar to that of NSGA2. It also adopts non-dominated sorting but adds clustering analysis to prune the non-inferior solution set. MOPSO [37] calculates the fitness values to obtain the optimal solution by constantly updating the particle's velocity and position. The principle and process are relatively simple compared to NSGA-II and SPEA2.

1.2.4 MES resilience analysis

With the increasing frequency of extreme weather due to climate change, the resilient operation of MES may be threatened by the extreme weather, resulting in prolonged disruption of energy supply to consumers. Therefore, MES must not only be reliable in the face of recognized and severe attacks, but it must also be resilient to extreme weather. Resilience is described as a system's ability to anticipate, prevent, endure, react to, adjust to, and recuperate from a disruption, taking into account the relevance of activities taken prior to, during, and after the occurrence of an adverse event [92]. Most of the previous studies focus on the power system resilience assessment. The authors in [38] investigate the methods of power system resilience assessment under natural disasters. Power system resilience metrics and evaluation methods are summarized in [39]. The authors in [91] provide fragile modeling for individual components such as transmission lines and substations, and proposed a probabilistic method to assess power system resilience. However, the aforementioned studies only consider the single energy network resilience assessment without considering the energy interactions between different energy networks.

1.3 Research gaps

Despite the fact that the research described above is valuable, there are still considerable gaps and issues to be addressed:

1. MES reliability is generally evaluated for single coupling systems and seldom for the whole MES that incorporates all three energy sources of power, heat, and natural gas;
2. the existing methods for MES reliability evaluation are oversimplified, which do not consider the weather uncertainty and time-varying load;
3. most aforementioned studies treat the problem as a single optimization problem with the sole purpose of increasing reliability or lowering costs, and there has yet to be a comprehensive study of optimal storage system design for multi-energy system reliability.

The sequential Monte Carlo simulation is adopted for reliability evaluation and optimization due to the complex structure and time-varying feature of MES in this project [34]. Therefore, the reliability optimization problem is defined as a multi-objective optimization problem with the goal of maximizing MES reliability while minimizing total costs. In this project, the optimization problem is highly complex and non-convex, with a large number of variables and strongly coupled subsystems. Moreover, the objective functions are calculated through MCS by random sampling from the random variables. The weather uncertainty modeling is also considered, which uses the Weibull distribution to model uncertain winds and the Beta distribution to model uncertain PV. Therefore, the meta-heuristic methods are a viable choice as these methods can guarantee to reach the global optimum through population-based search. Due to their different characteristics, the three algorithms are adopted in this project to demonstrate and compare the effectiveness of the generated outcomes.

1.4 Main contributions

In order to fill up these gaps, the following are the project's major contributions:

1. the whole MES model which includes the time-varying load and weather uncertainty modeling has been well established considering the power, heat, and gas three energy

forms;

2. a time-varying cost and load model based on the sector customer damage function (SCDF) [40] is used to calculate the EENS (expected energy not supplied) and the interruption cost in objective functions;
3. the optimization problem is formulated as a multi-objective optimization problem that has the reliability indicator SAIDI and economic indicator cost. The optimization results have been compared through three different meta-heuristic algorithms to demonstrate the effectiveness of the proposed method.
4. In addition to the reliability analysis of MES, this project also has a preliminary discussion of the resilient analysis. Sequential MCS is adopted again to evaluate MES resilience. The assessment of various resilience strengthening measures is also provided.

1.5 Research aims and objectives

This project aims to develop a methodology for reliability evaluation and optimization of MES considering different energy storage configuration schemes under weather uncertainties. Finally, this project also investigates the resilient analysis of MES. The following research objectives have been established in order to achieve these aims:

1. review and summarize existing methods for modeling, reliability assessment, and optimization of multi-energy systems.
2. develop the simulation model of MES in Simulink/ MATLAB including three energy systems (power system, heat energy system, and natural gas system) and the coupling components such as CHP and V2G.
3. develop the mathematical reliability model of MES with PV and wind renewable energies, taking into account their operation constraints and weather uncertainties.
4. apply the multi-objective optimization algorithms to the existing model to minimize the reliability index SAIDI and reliability cost and find the optimal energy storage configuration schemes.

5. demonstrate the effectiveness of the proposed methodology by comparing different MES layouts.
6. develop the fragile model and assess system resilience to investigate the effect of resilience enhancement strategies on different wind speeds.

1.6 Thesis structure

This project is divided into six chapters, each of which is summarized as follows:

Chapter 1 provides a general overview of the thesis, which starts with the definition, characteristics, and research background of multi-energy systems. Then, the existing approaches for simulation, reliability assessment, and optimization of multi-energy systems are reviewed and summarized, subsequently with the discussion of the project's aims and objectives. Finally, the main contributions of the thesis based on the existing gaps and open challenges are summarized and the thesis structure is presented.

Chapter 2 mainly introduces the modeling and simulation part of MES in MATLAB/Simulink, from MES sources to the coupling components such as CHP, GB, P2G, and V2G. The simulation model is built as a power-model, the power link has been used to connect different components in three energy networks.

Chapter 3 introduces uncertainty modeling which includes the stochastic modeling of renewable energy generation and the BP neural network for load forecasting. Considering the weather uncertainty in PV and wind model is quite essential to improve the overall MES reliability, stochastic modeling for PV and wind renewable energy is adopted in this project. Moreover, time-varying load forecasting by the error back propagation (BP) neural network is also considered to simulate a realistic operating MES.

Chapter 4 illustrates the reliability evaluation process of MES considering storage devices. Firstly, load-point and system-level reliability indices are introduced. Secondly, Monte Carlo simulation is adopted as the MES reliability assessment method. Finally, the use of sequential Monte Carlo simulation in multi-energy system reliability assessment with different energy storage devices considering time-varying cost models and weather uncertainties is elucidated.

Chapter 5 proposes the reliability optimization problem and its solving algorithms. The reliability optimization problem is presented as a multi-objective problem aiming at determining the optimal location number of the storage device in the power grid, heat network, and gas network at the lowest possible cost and highest reliability under weather uncertainty. Metaheuristics such as NSGA-II, MOPSO, and SPEA2 are adopted to address the optimization problem and compare the reliability optimization results.

Chapter 6 develops case studies implemented on two different MES layouts with increasing complexity to validate the proposed technique is effective. The specified reliability optimization problem is addressed by a comparison analysis applying commonly utilized multi-objective algorithms, such as NSGA-II, MOPSO, and SPEA2. The sensitive analysis is considered to reflect the degree and pattern of change in system reliability induced by minor changes in component parameters.

Chapter 7 investigates the resilient analysis of MES. The resilient modeling and evaluation of MES are given to investigate the effect of resilience enhancement strategies on different wind speeds.

Chapter 8 delivers the main contributions of the whole project. Future expansions are also suggested at the end of the chapter.

Chapter 2

Overall modeling architecture of multi-energy system

2.1 Introduction

This chapter introduces multi-energy system modeling and simulation, starting with an overview of the MES system then introducing components from MES sources such as PV and wind renewable energy sources, as well as the gas turbine to MES coupling components such as CHP, GB, P2G, and V2G. All the components built in this chapter are fully dynamic models, which can be helpful to understand each component principle in detail.

2.2 The structure of MES

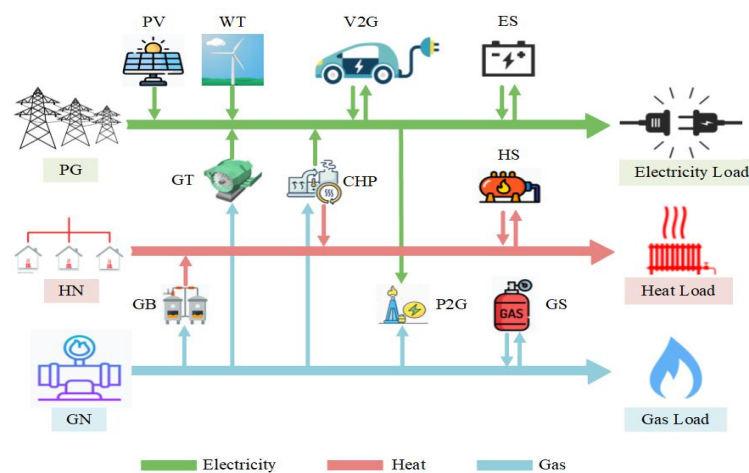


Figure 2.1: The structure of MES.

Figure 2.1 shows a schematic diagram of the MES structure. In this project, the MES mainly consists of three energy networks which are the power grid (PG), heat network (HN), and gas network (GN). Photovoltaic (PV) and wind turbine (WT) as the renewable generation units. The coupling components such as gas turbine (GT), gas boiler (GB), combined heat and power (CHP), and power to gas (P2G) are used as the links to connect different energy networks together. The energy storage system which comprises ES

(electricity storage), HS (heat storage), and GS (gas storage) can be utilized as the backup source to realize bi-directional charge and discharge. The vehicle to grid (V2G) unit performs the same as the energy storage system to help the power grid operate efficiently. This chapter would introduce all the MES component models.

2.3 Component models

2.3.1 Photovoltaic power generation system modeling

1. Mathematical model of photovoltaic cell

The photovoltaic cell is a PN junction, which is made based on the photovoltaic effect of semiconductor materials. The I-V characteristics of the photovoltaic cell are not constant but change with the change of received light intensity G (W/m^2) and surface temperature T ($^{\circ}C$). Photovoltaic cells have similar basic features to diodes, Figure 2.2 presents its equivalent circuit [42].

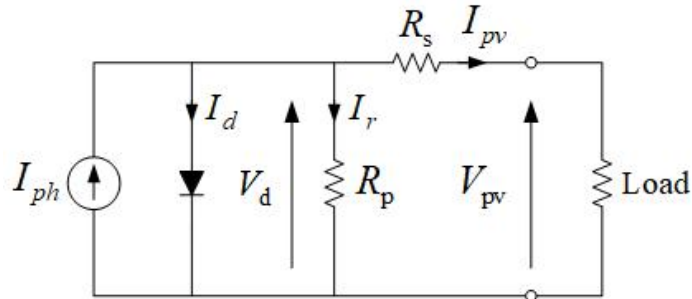


Figure 2.2: The equivalent circuit of photovoltaic cells [42].

The photovoltaic cell's area and light intensity are proportional to the current I_{ph} . Under the action of photogenerating electromotive force, a PN junction will cause a leakage current to flow in the opposite direction as the photogenerated current through the diode, which is called dark current I_d . The shunt resistance R_p is usually several thousand ohms. The series resistance R_s is small, usually between $10^{-3} \Omega$ and a few ohms. R_s and R_p are the internal resistance of photovoltaic cells [42].

According to Kirchhoff's law and the equivalent circuit of a photovoltaic cell as presented in Figure 2.2, the current equation of the photovoltaic cell power generation process is:

$$I_{PV} = I_{ph} - I_d - I_r = I_{ph} - I_0 \left(\exp \frac{qV_d}{AkT} - 1 \right) - \frac{V_{PV} + R_s I_{PV}}{R_p}, \quad (2.1)$$

where V_{PV} is the PV voltage, I_{PV} is the PV current, I_{ph} is the light current, I_0 is the diode reverse saturation current, R_s is the series resistance, R_p is the shunt resistance, q is the elementary charge which equals to $1.6 \times 10^{-19}C$, V_d is the equivalent diode terminal voltage, k is the Boltzmann's constant which equals to $1.38 \times 10^{-23}J/K$, T is the absolute temperature $300K$, A is the ideal factor of PV junction, which equals to 2.8.

Generally, the following test parameters of the photovoltaic model will be given by the manufacturer according to the standard conditions (light intensity $G_{ref} = 1000 W/m^2$, battery temperature $T_{ref} = 25^\circ C$):

V_{oc} , open-circuit voltage (V),

I_{sc} , short-circuit current (A),

I_m , current at maximum power point (A),

V_m , voltage at maximum power point (V).

Since shunt resistance R_p is very large, $\frac{V_{PV} + R_s I_{PV}}{R_p}$ is much smaller than the photovoltaic current, $\frac{V_{PV} + R_s I_{PV}}{R_p}$ can be ignored. R_s is far less than the diode forward guide resistance, so it is approximately $I_{sc} = I_{PV}$. It is defined that ① in the case of open circuit, $I=0$, $V = V_{oc}$; ② at the maximum power point P_m , $V = V_m$, $I = I_m$. Therefore, the characteristic relational expression of photovoltaic cells can be simplified as:

$$I = I_{sc} \left\{ 1 - C_1 \left[\exp \left(\frac{V}{C_2 V_{oc}} \right) - 1 \right] \right\}. \quad (2.2)$$

Under normal temperature conditions, $\exp \left(\frac{V}{C_2 V_{oc}} \right) \gg 1$, therefore "-1" in the above formula can be ignored, and C_1 can be solved as below:

$$C_1 = \left(1 - \frac{I_m}{I_{sc}} \right) \exp \left(\frac{-V_m}{C_2 V_{oc}} \right). \quad (2.3)$$

In the open circuit case, when $I = 0$, $V = V_{oc}$, and substitute the above equation into the simplified formula of volt-ampere characteristic:

$$0 = I_{sc} \left\{ 1 - \left(1 - \frac{I_m}{I_{sc}} \right) \exp \left(\frac{-V_m}{C_2 V_{oc}} \right) \left[\exp \left(\frac{1}{C_2} \right) - 1 \right] \right\}, \quad (2.4)$$

$\exp\left(\frac{1}{C_2}\right) \gg 1$, therefore "-1" in the above formula can be ignored, and C_2 can be solved:

$$C_2 = \left(\frac{V_m}{V_{oc}} \right) \left[\ln \left(1 - \frac{I_m}{I_{sc}} \right) \right]^{-1}. \quad (2.5)$$

Thus, C_1 and C_2 can be calculated according to the specifications I_{sc} , V_{oc} , I_m , and V_m .

Under the standard light intensity 1000 W/m^2 and temperature 25°C , we can package the PV model through the four given values provided by the manufacturer which are open-circuit voltage V_{oc} (65 V), short-circuit current I_{sc} (38.58 A), maximum power point current (33.94 A), maximum power point voltage (50.7 V) and obtain the PV cell current as the output port. The mask block for the PV parameters setting is given in Figure 2.3. The circuit diagram simulated in Matlab/Simulink according to Equations 2.1-2.5 is shown in Figure 2.4.

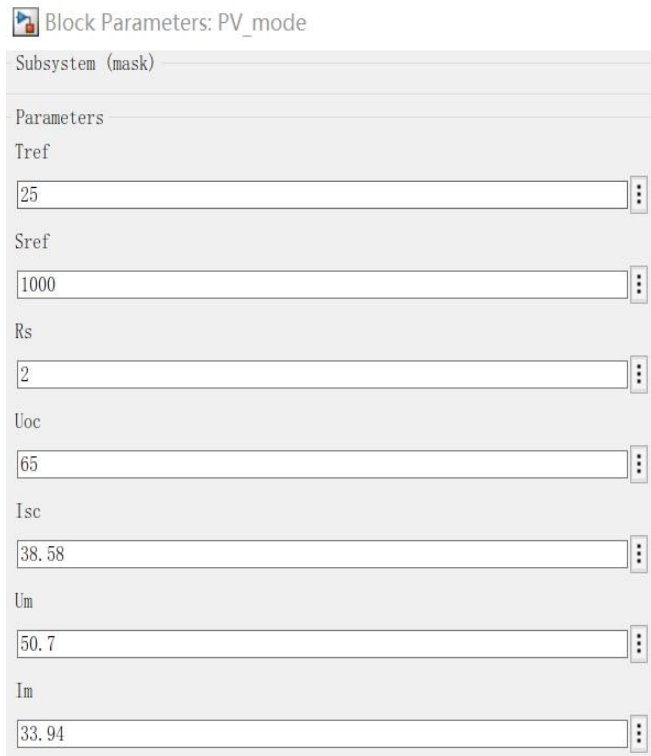


Figure 2.3: Mask block for PV module.

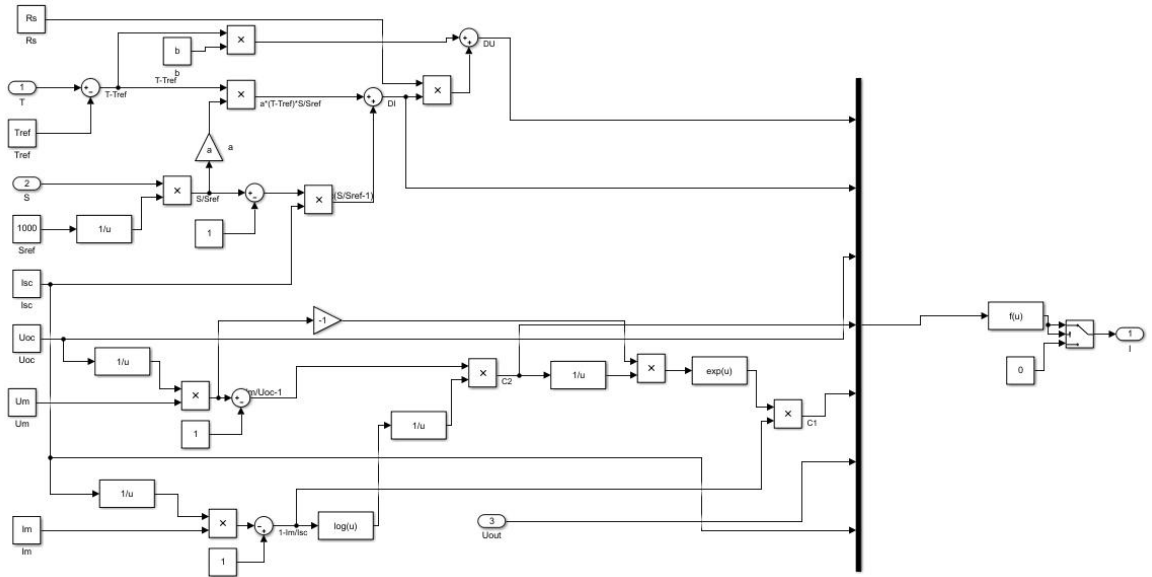


Figure 2.4: Simulation model for PV module.

2. Boost converter module

Because the external environment (light intensity, ambient temperature) changes constantly during photovoltaic power generation, the output power must be changed and the voltage must be controlled in real time. The commonly used method is to connect the solar cell to the load via a DC/DC converter. The actual control mechanism only requires changing the conduction rate of the switch in the DC/DC converter, allowing the actual voltage to be modified to control the solar cell and achieve maximum power point tracking control.

Boost converters can raise the voltage of a load by discharging it as an inductive current source. Figure 2.5 depicts the Boost converter's circuit topology [43].

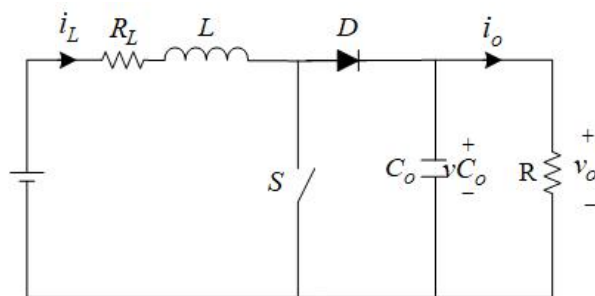


Figure 2.5: Boost converter topology [43].

The basic principle of the Boost converter circuit is as follows: when the switch S conducts, as presented in Figure 2.6 (a), capacitor C provides power to load R, while inductor L is charged to store electric energy; when the switch S is disconnected, as presented in Figure

2.6 (b), the load receives power from both the power supply and the inductor, and the voltage of the average load output is greater than that of the power supply.

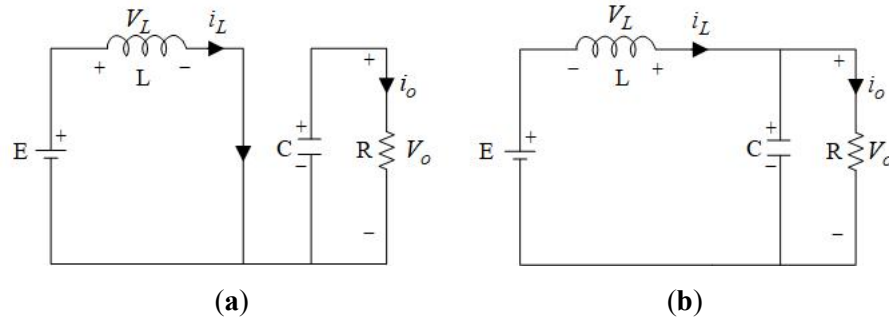


Figure 2.6: Boost converter operating principle: (a) when switch S is conducting; (b) when switch S is disconnecting.

When the inductance current is continuous, the transformation waveform and voltage waveform are shown in Figure 2.6 (b), the average output voltage V_o and the power supply voltage E have the following relationship:

$$V_o = \frac{E}{1 - D}, \quad (2.6)$$

where $D = t_{on}/T$, which is conduction ratio. Since $D \leq 1$, the average output voltage V_o is smaller than the supply voltage E .

3. Perturb and observe method for MPPT control module

Because photovoltaic cells' output characteristics fluctuate when ambient temperature and illumination intensity change. Under different environmental conditions, photovoltaic cells have different maximum power output values, therefore, in actual photovoltaic power generation system operation, real-time adjustment of the solar photovoltaic cell operating point, always allowing it to work near the maximum power point, known as maximum power point tracking (MPPT) [44].

MPPT is essentially a dynamic self-optimization process. It is accomplished by detecting the current output power, comparing it to the power recorded in the previous moment, selecting the control direction to track the maximum power, and repeating the detection, comparison, and adjustment procedure. The control block diagram for tracking maximum output power control is presented in Figure 2.7 [45].

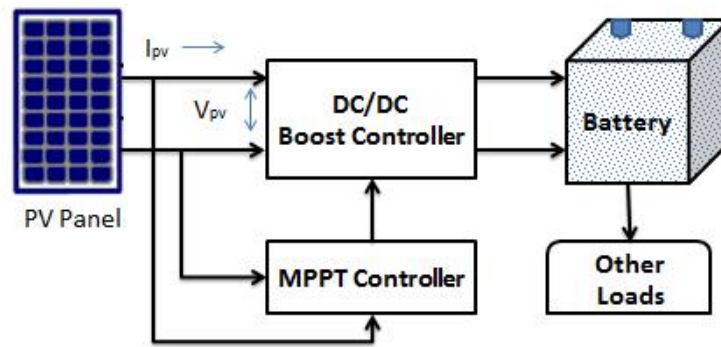


Figure 2.7: MPPT control for PV module [45].

A prevalent MPPT control mechanism is the perturb and observe method (P&O). In this way, the PV module's operating voltage is perturbed by a small increment, and the corresponding change in power P is observed. The operational point has shifted near to the MPP if P is positive. As a result, additional voltage disturbances in the same direction will cause the operating point to shift toward MPP. The operating point has diverged from MPP, and the direction of the disturbance must be reversed to return to MPP if P is negative. The P&O approach is depicted in Figure 2.8 as a flow chart, where k denotes the number of detections, $k \geq 1$, and $V(k)$ and $I(k)$ represent the voltage and current [45].

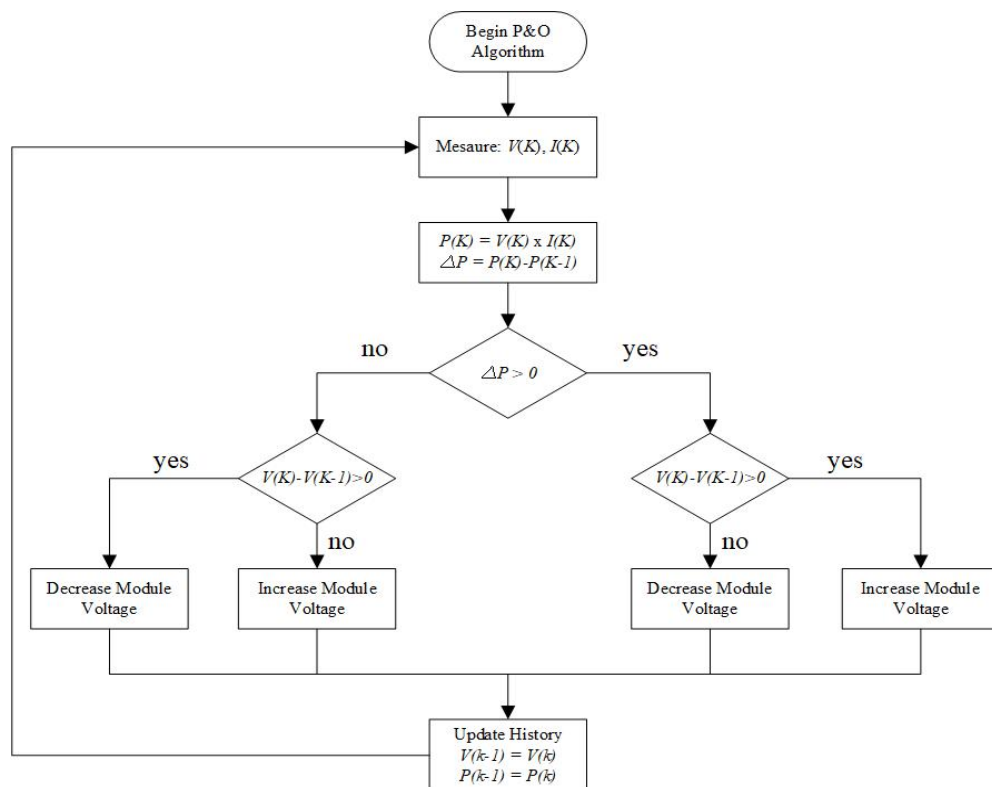


Figure 2.8: The flow chart of perturb and observation method [45].

Perturb and observe method (P&O) is used in the MPPT of photovoltaic power generation system in this project. Photovoltaic cells are powered to the source and then boosted by DC/DC Boost circuit to meet load demands. By adjusting the duty cycle of the switch (IGBT) in the Boost circuit to control the signal, the output power of the photovoltaic cell is close to the maximum power. As shown in Figure 2.9, the voltage and current output by photovoltaic cells are obtained through the MPPT module to obtain the reference voltage.

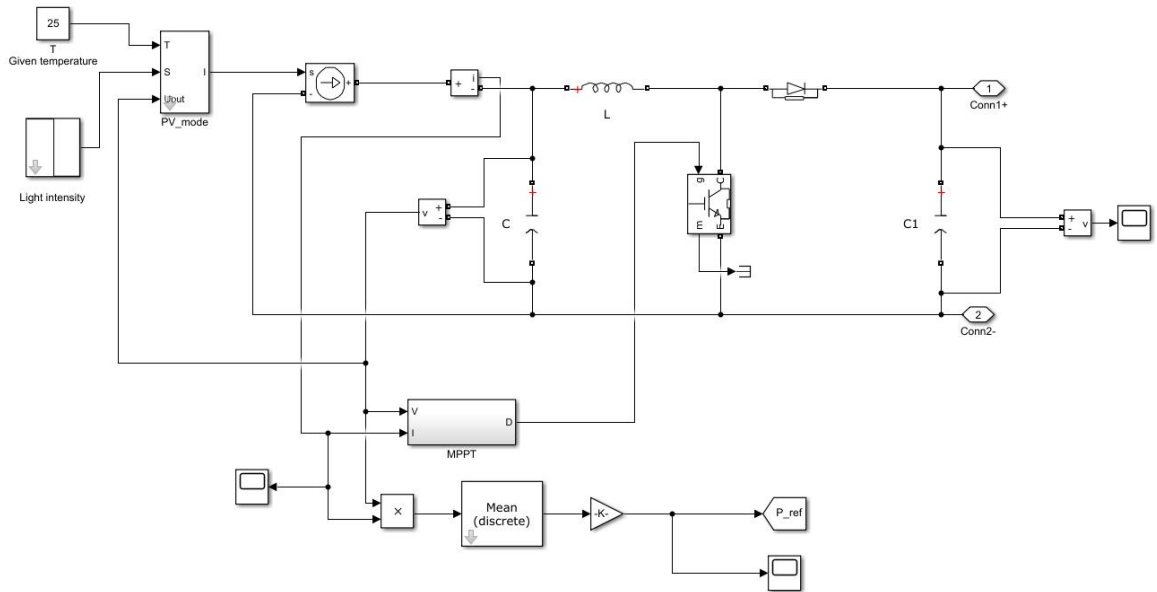


Figure 2.9: Perturb and observation method MPPT control Simulink model.

4. PV inverter control strategy

The inverter structure of PV modeled in Simulink is shown in Figure 2.10. Constant power (PQ) control is used for the inverter. The modulation mode of inverter adopts pulse width modulation (PWM). The inverter control adopts a double closed-loop control strategy for grid-connected control. The outer loop is a voltage loop, which is mainly aimed at controlling the input voltage of the inverter to maintain stability; the inner loop is a current loop, whose main goal is to control the output current of the inverter to be in the same frequency and phase as the grid voltage.

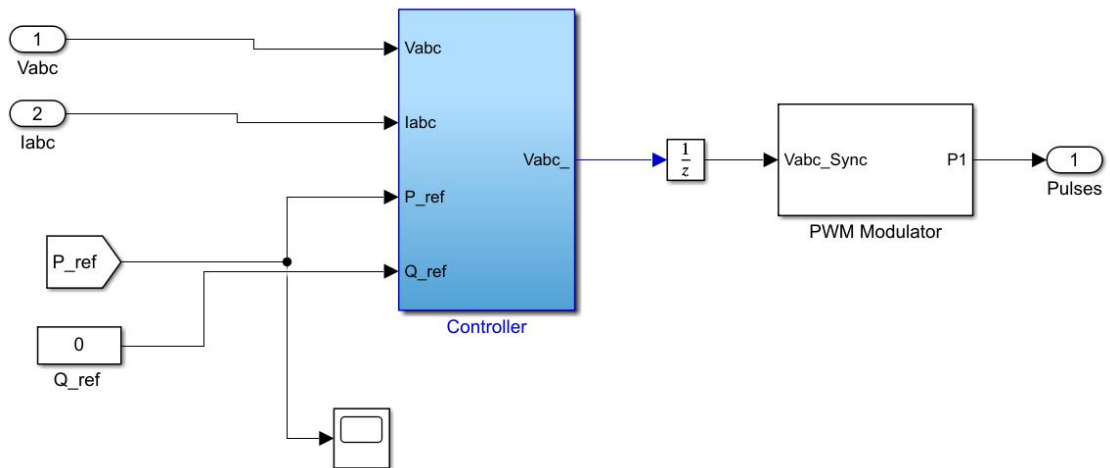


Figure 2.10: The inverter structure Simulink model of PV.

(1) Outer loop control

The outer loop control mode is constant power (PQ) control. The characteristic of this control strategy is that when the frequency and voltage rating of the AC network connected to the inverter change within the allowable range, the active and reactive power output of the distributed power supply remain unchanged. Constant power control is particularly suitable for distributed power sources such as photovoltaic power generation and wind power generation with intermittency and large power fluctuation [46].

The inverter control module is given in Figure 2.11. The three-phase voltage and current on the grid side are converted into v_d , v_q , i_d and i_q after dq transformation. After the PQ computation block, the average active power P and the average reactive power Q at the grid side can be obtained. The difference between the grid side active power P and reactive power Q compared with the reference active power P_{ref} and the reference reactive power Q_{ref} is passed into the PI controller. After tracking and processing by the PI controller, the output signals are the reference current signals i_{dref} and i_{qref} of the inner loop control. Then, the reference current signals are sent into the inner loop controller to complete the active and reactive power control.

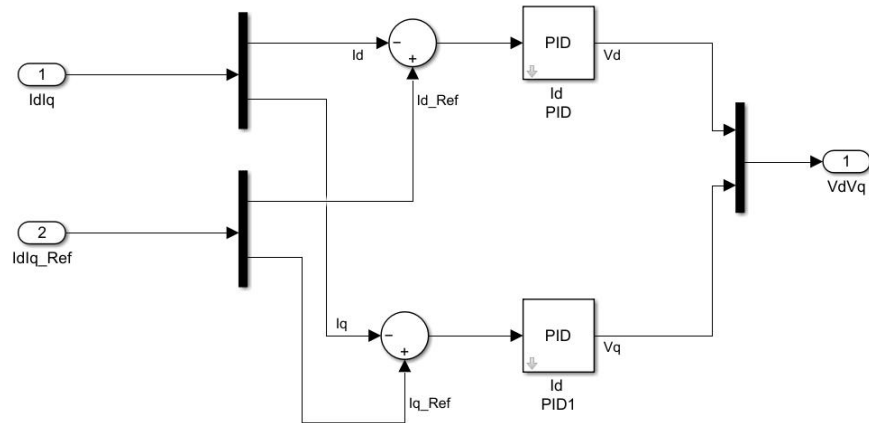


Figure 2.12: The current regulator module.

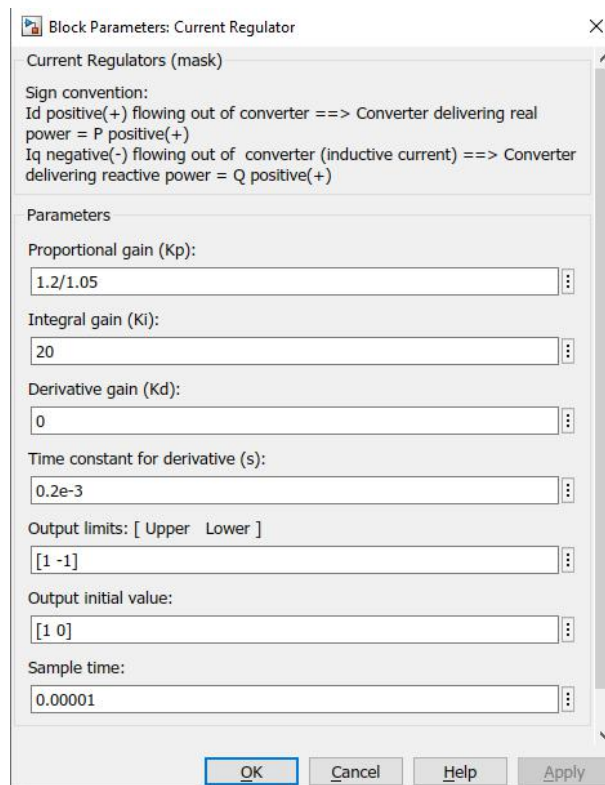


Figure 2.13: The current regulator module parameters for PV.

5. PV grid-connected model

Figure 2.14 shows the Simulink grid-connected model of the photovoltaic power generation system. The grid-connected photovoltaic model designed in this project mainly includes photovoltaic cells, photovoltaic MPPT control, a DC-DC Boost circuit, and DC/AC inverter. In this photovoltaic grid-connected model, the photovoltaic array is first controlled by MPPT, and after passing through the Boost circuit, the DC/AC inverter

inverts the output DC into AC, so as to be connected to the large grid. In the inverter, a three-level IGBT bridge with PWM control is used to model the inverter. The harmonics generated by the IGBT bridge are filtered using the 0.8 mH and 30 μ F three phase LC filter. The inverter is connected to the power grid with a 60V/138kV 400kVA, 60Hz three-phase transformer.

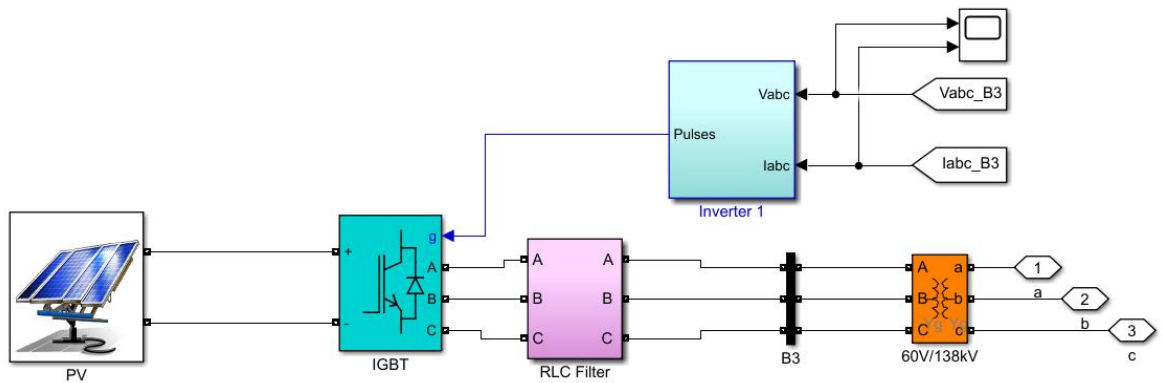


Figure 2.14: The grid-connected simulation model of photovoltaic power generation system.

Given the solar radiation during 0-0.5s and 1-1.5s 850 MW/m^2 , 1000 MW/m^2 during 0.5-1s, the active power output of the PV module is shown in Figure 2.15.

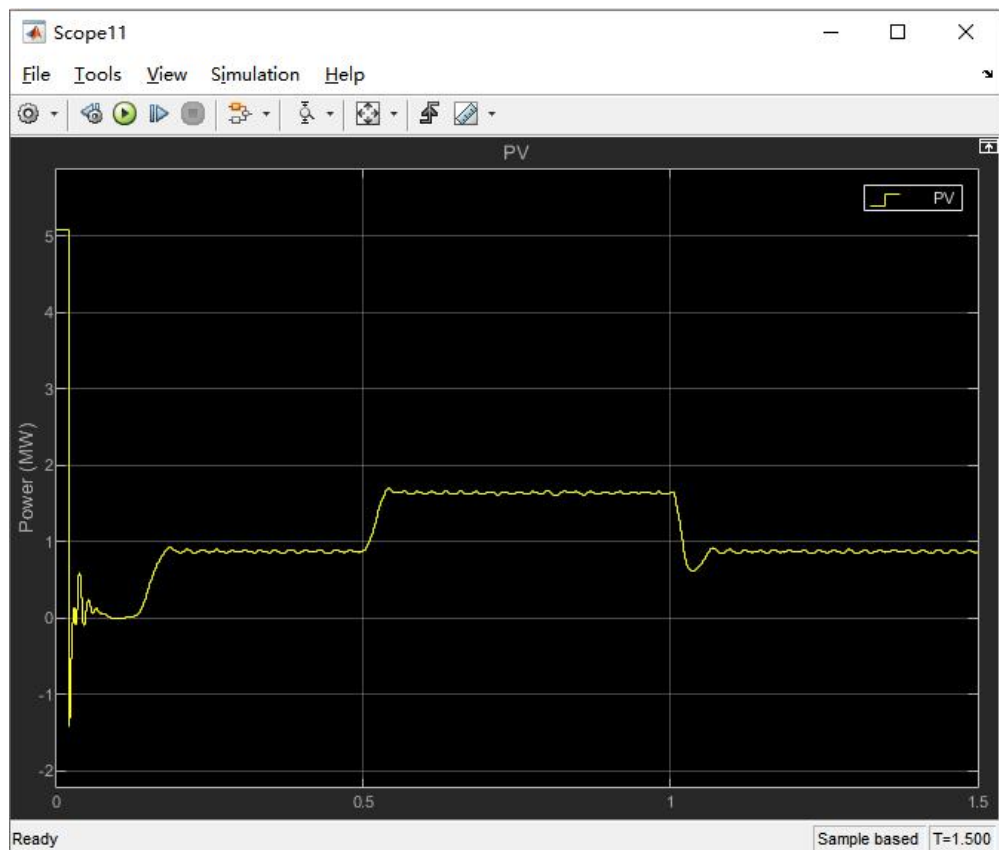


Figure 2.15: PV active power generation.

2.3.2 Wind power generation system modeling

The low-speed PMSG (permanent magnet synchronous generator) is employed in the permanent magnet direct drive wind power system because of its simple structure, excellent reliability, and low mechanical loss [48]. As a result, a permanent magnet direct drive wind turbine model is chosen. Figure 2.16 depicts the framework of a wind power generation system, which includes a PMSG, AC/DC rectifier, and DC/AC inverter, as well as the control module and grid [49].

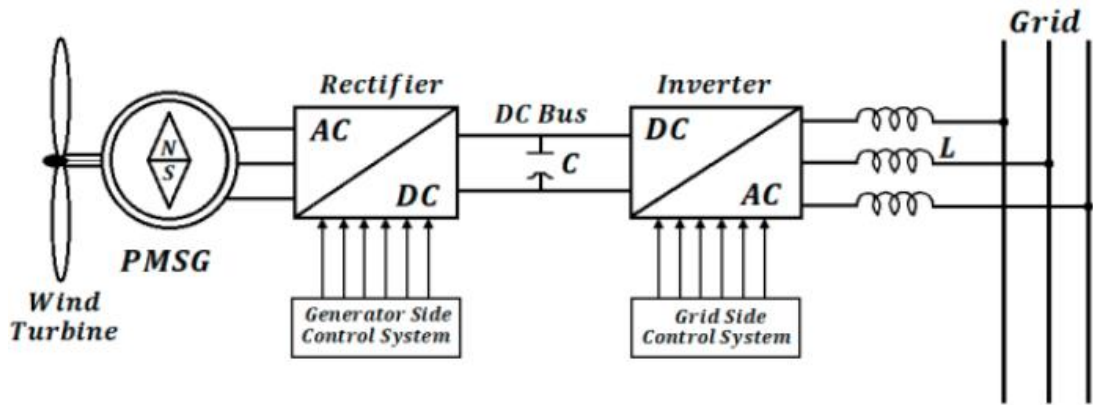


Figure 2.16: The structure of wind power generation system [49].

1. Wind power generator modeling

The amount of wind energy that can be used in a given amount of time is known as wind energy utilization power. The wind energy utilization coefficient C_p is calculated by dividing the power absorbed by fans by the kinetic energy of the airflow moving through the fan to obtain the wind energy utilization ratio. C_p takes into account wind speed, fan rotational speed, and blade pitch angle [48]. The active power P_s that the wind wheel actually obtains, according to Betz's law, is [50]:

$$P_s = 0.5\rho\pi R^2V_w^3C_p(\beta, \lambda), \quad (2.7)$$

where ρ denotes air density, β represents the blade pitch angle, R is the radius of the wind wheel, and λ is the tip speed ratio.

The wind wheel's aerodynamic torque is:

$$T_r = 0.5\rho\pi R^3V_w^2C_T(\beta, \lambda), \quad (2.8)$$

C_T signifies the aerodynamic torque coefficient, and the following is the link between the wind energy utilization coefficient C_p :

$$C_p(\beta, \lambda) = \lambda C_T(\beta, \lambda), \quad (2.9)$$

The negative value of rotor torque signal was sent into the permanent magnet synchronous motor module in MATLAB/Simscape to obtain the PMSG model [48].

2. Wind inverter control strategy

The inverter structure of the wind module modeled in Simulink is shown in Figure 2.17. The modulation mode of the inverter adopts pulse width modulation (PWM). The inverter also adopts double closed-loop control, which is DC voltage outer loop and current inner loop control. Figure 2.18 gives the controller module details.

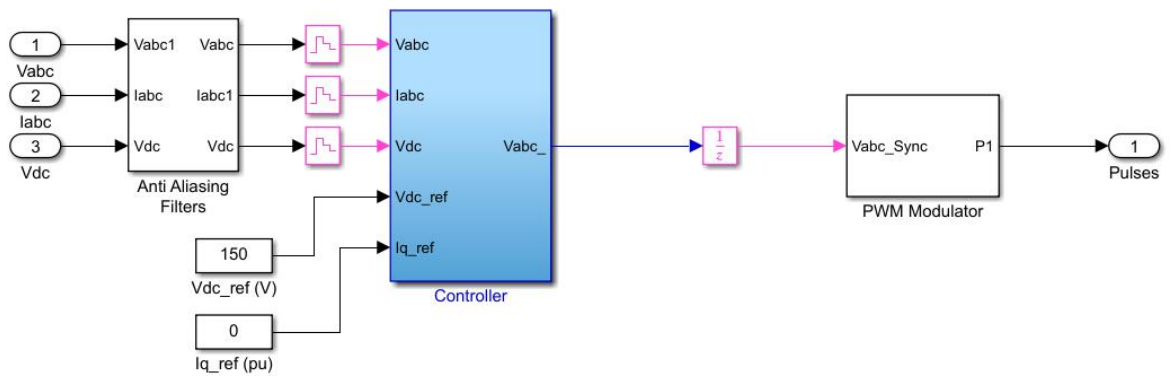


Figure 2.17: The inverter structure of wind module.

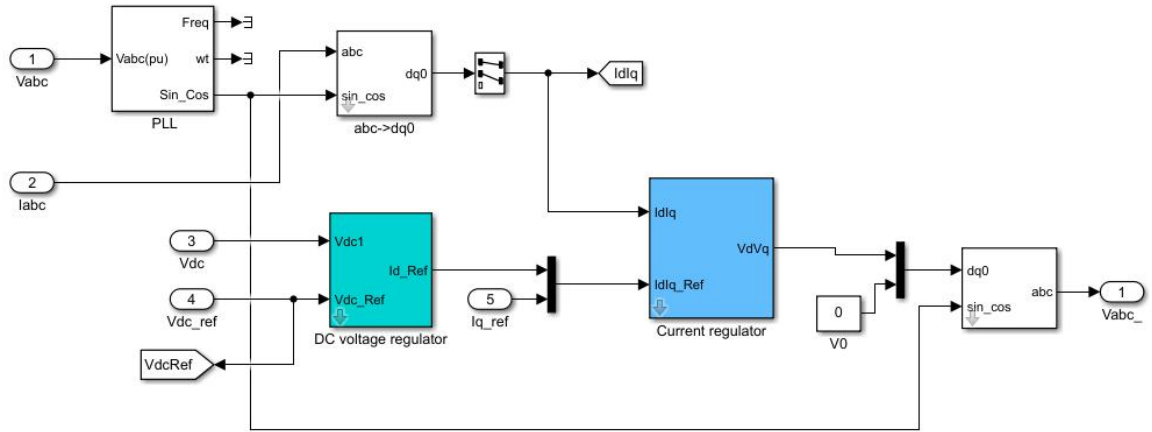


Figure 2.18: The controller module for wind.

In the DC voltage outer loop, v_{dc1} is the DC output voltage, v_{dc_ref} is the output voltage reference value. The DC voltage regulator module is given in Figure 2.19. The current regulator principle and structure are the same as in Figure 2.12. When the output voltage v_{dc1} is less than the reference voltage v_{dc_ref} , the deviation is positive, and the output of the PI regulator in the DC voltage regulator block increases continuously. After limiting the amplitude of the limiter, it is used as the command value of the current flowing through the current regulator. Assuming that the current flowing through the current regulator is unchanged, the deviation is positive and the output of the PI regulator current regulator block is also increasing. After limiting the amplitude and comparing it with the triangle carrier, the PWM pulse with an increasing conduction ratio is obtained. The conduction ratio of the IGBT of the insulated gate bipolar transistor increases continuously, and the current flowing through the boost reactor also increases rapidly, resulting in the dynamic deviation of the inner loop to zero [51]. Therefore, the conduction ratio is only affected by the output voltage loop. When the conduction ratio increases, the output voltage also increases. As a result, the deviation of the output voltage loop becomes smaller and smaller until it reaches zero. The outputs of the last two PI regulators are dynamic fixed values, and the system enters a stable working state.

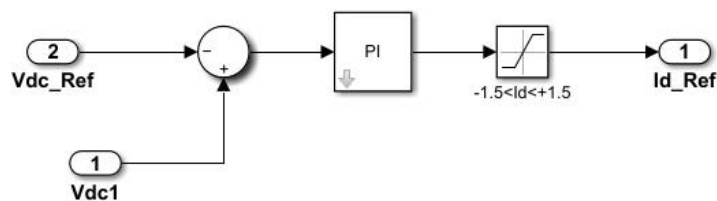


Figure 2.19: The DC voltage regulator module.

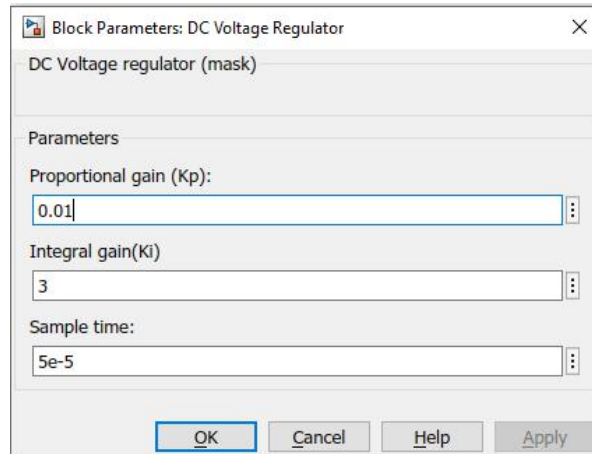


Figure 2.20: The DC voltage regulator parameters.

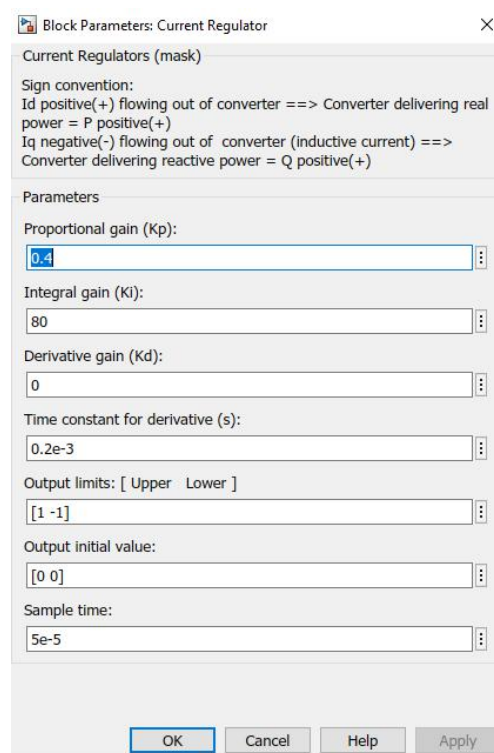


Figure 2.21: The current regulator parameters.

The parameter setting for DC voltage regulator and current regulator are given in Figure 2.20 and Figure 2.21, respectively.

3. Wind grid-connected model

The grid-connected wind generation model designed in this project mainly includes PMSG, MPPT module, AC/DC rectifier, and DC/AC inverter. The perturb and observe method is also adopted for the MPPT block to track and control the maximum power of wind power. In this wind generation grid-connected model, the PMSG is first controlled by MPPT, and

after passing through the AC/DC rectifier, the DC/AC inverter inverts the output DC into AC, so as to be connected to the large grid. In the inverter, a three-level IGBT bridge with PWM control is used to simulate the converter. The harmonics generated by the IGBT bridge are filtered using the 0.8 mH and 30 μ F three phase LC filter. The inverter is connected to the power grid with a 60V/138kV 400kVA, 60Hz three-phase transformer. Figure 2.22 depicts a Simulink simulation model of a wind power generation system.

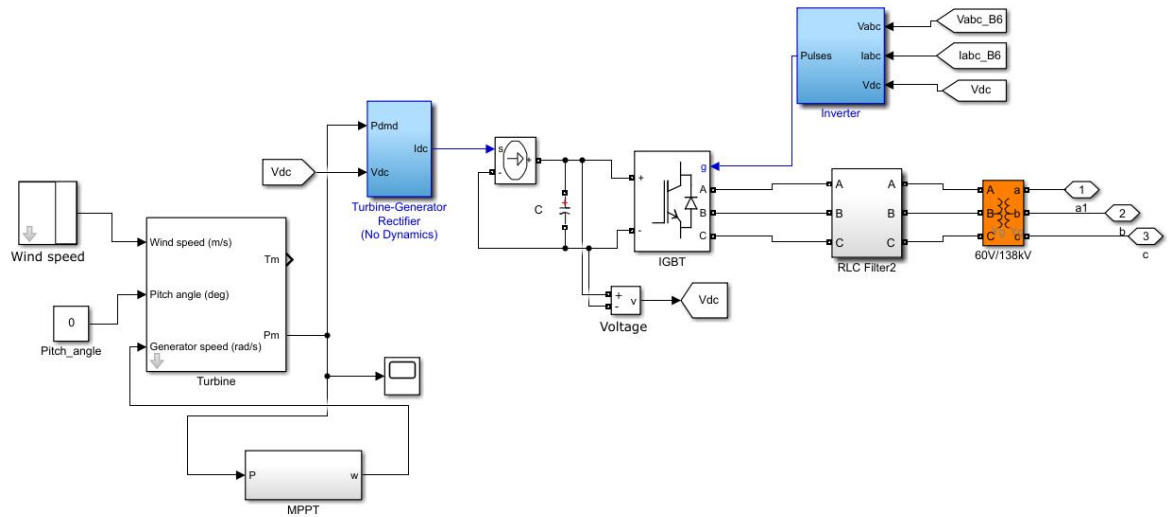


Figure 2.22: The grid-connected simulation model of wind power generation system.

Given the wind speed 0-0.5s and 0.8-1.5s 10.2 m/s, 8m/s during 0.5-1s, the active power output of the wind module is shown in Figure 2.23.

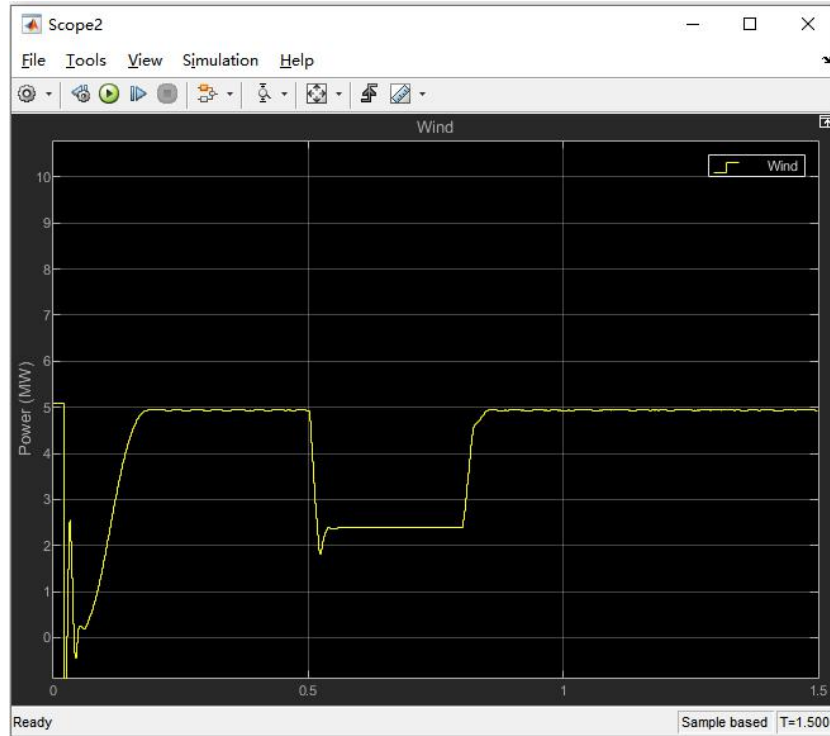


Figure 2.23: Wind active power generation.

2.3.3 Battery storage system modeling

1. DC/DC battery storage system

A bidirectional DC/DC buck-boost converter has been used to build a battery storage system. The topology diagram of a typical bidirectional interleaved buck-boost converter is presented in Figure 2.24 as below [52]:

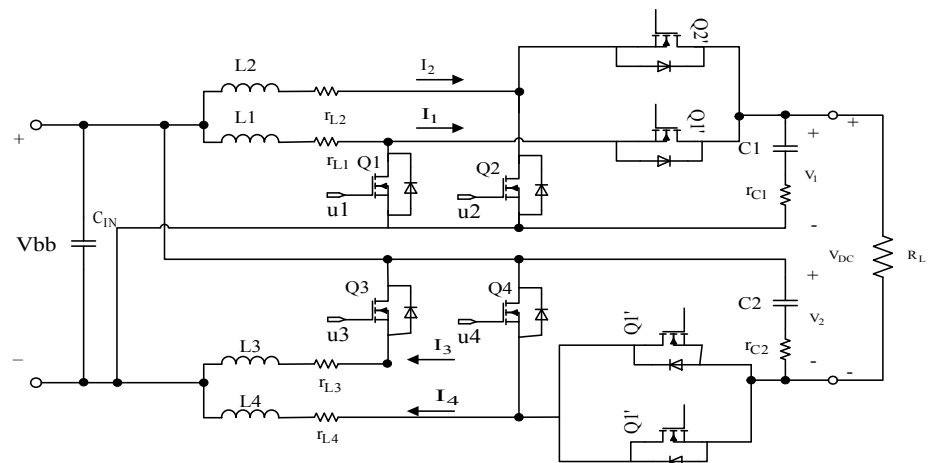


Figure 2.24: Bidirectional interleaved buck-boost converter [52].

There are two positive interleaved units and two negative interleaved units in this topology.

Besides, the voltage gain is supported by two coupled capacitors. The size of the inductors and capacitors is considerably decreased because the power is split among the four units. Therefore, the circuit is capable of working in both directions (buck and boost). Figure 2.25 shows the simulation model of the DC/DC battery storage system.

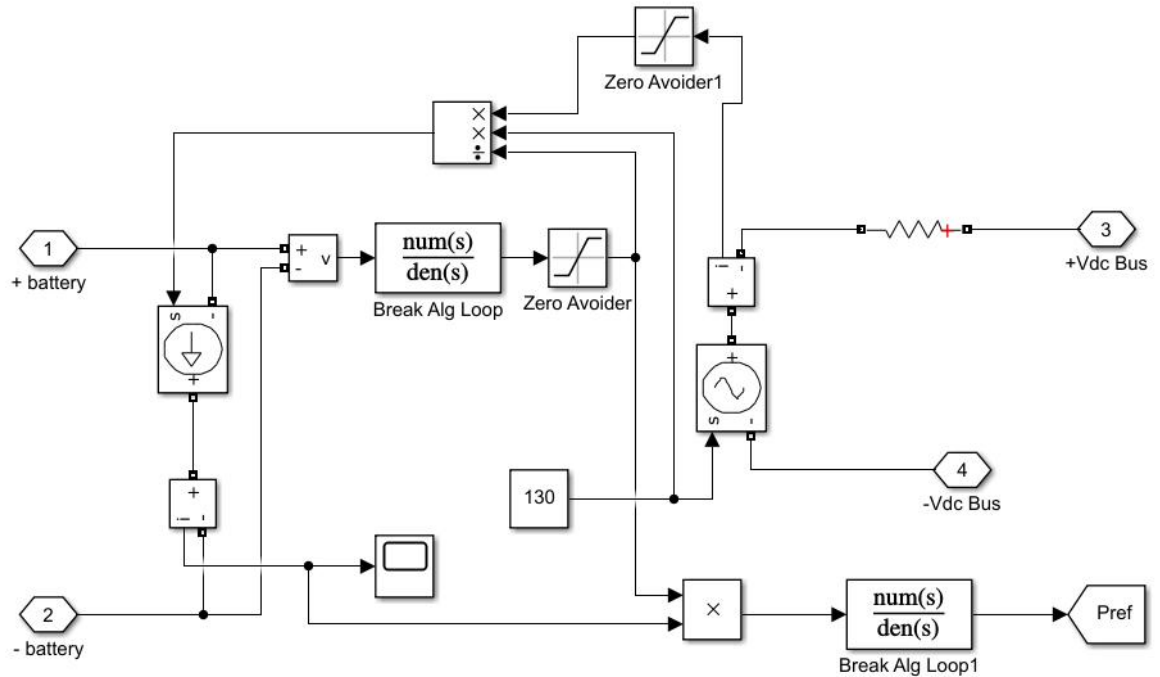


Figure 2.25: Simulation model of DC/DC battery storage system.

2. Battery Inverter control strategy

VF control mode is required for independent operation of the micro-grid, a bidirectional charge and discharge battery is analyzed in this project, in case of system failure, the battery can supply power to the island and operate in an independent mode. Therefore, the battery inverter has adopted the VF control strategy. Figure 2.26 gives the inverter block for the battery. The VF control inner structure is given in Figure 2.27.

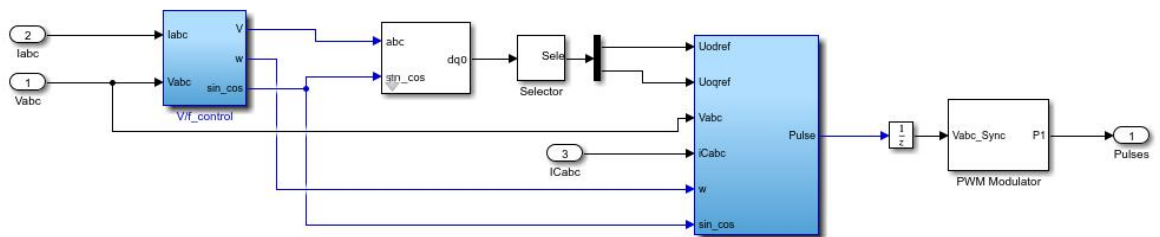


Figure 2.26: The inverter block for battery.

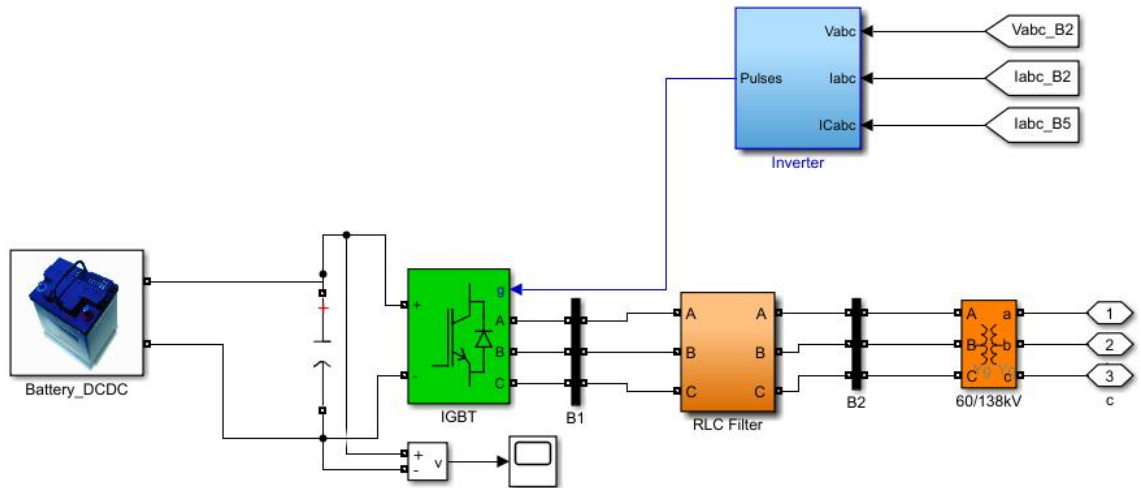


Figure 2.28: The grid-connected simulation model of DC/DC battery storage system.

2.3.4 Gas turbine modeling

Due to the long life span and high availability of industrial heavy duty gas turbine (HDGT) compared with other types of gas turbines, this project adopts this type of gas turbine for simulation. Figure 2.29 depicts a picture of a standard HDGT and its primary components. The three essential components of HDGTs are multi-stage axial flow compressors, can-annular combustors, and axial flow turbines. The air from the atmosphere comes into the compressor, where it is compressed; the compressed air is then directed into the combustion chamber, where it reacts with the injected fuel and burns to generate high-temperature gas, which is then directed into the gas turbine. The turbine wheel rotates with the compressor wheel, considerably increasing the useful power of the heated high-temperature gas, thus there is excess work as the gas turbine's output mechanical work while it drives the compressor. An operator is required to rotate the gas turbine when it is started from a standstill [53].

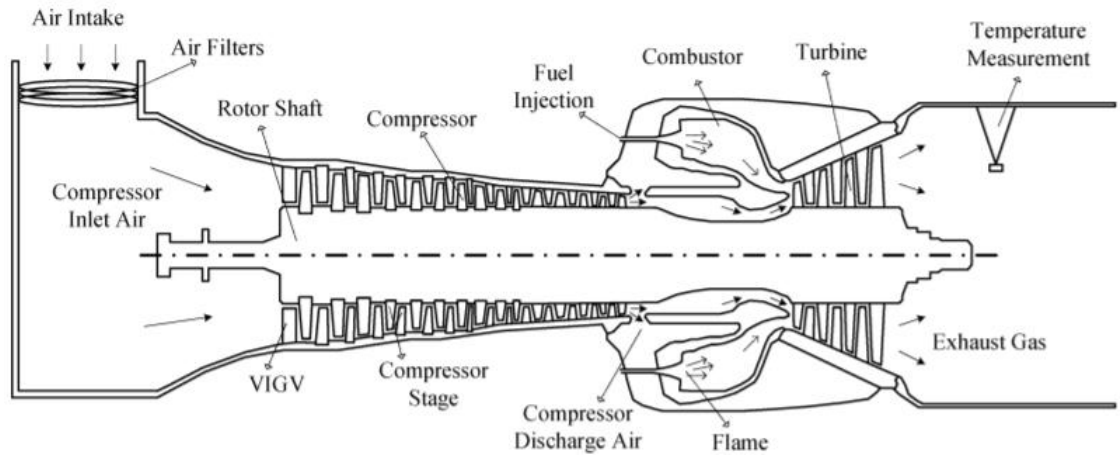


Figure 2.29: Schematic diagram of a typical HDGT and its major components [53].

In the gas turbine, the Brayton cycle is used. In a temperature-entropy framework, Figure 2.30 depicts a basic Brayton cycle. Under ambient conditions, the air is removed from point 1 and compressed to point 2 in an irreversible process by a compressor. The combustion chamber will be heated to point 3 by the heat input, at which point the combustion products and air expelled from the compressor will flow into the turbine and expand to point 4 by the combustion products and air discharged from the compressor. The air filter and combustion chamber pressure losses are ignored in the figure, processes 2-3 and 4-1 are assumed to be isobars [53].

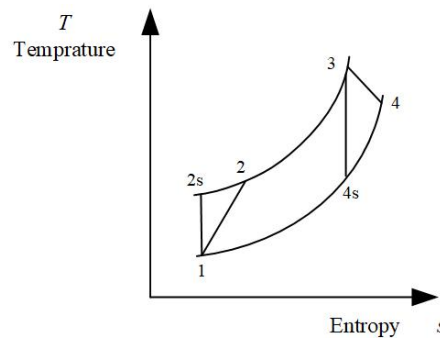


Figure 2.30: The Brayton cycle [53].

The processes inside compressors and turbines are irreversible and non-isentropic, but the process is assumed to be isentropic. Using these ideal processes, the irreversible adiabatic efficiencies of compressors and turbines are defined as follows [54]:

$$\eta_c = \frac{h_{2s} - h_1}{h_2 - h_1} = \frac{T_{2s} - T_1}{T_2 - T_1}, \quad (2.10)$$

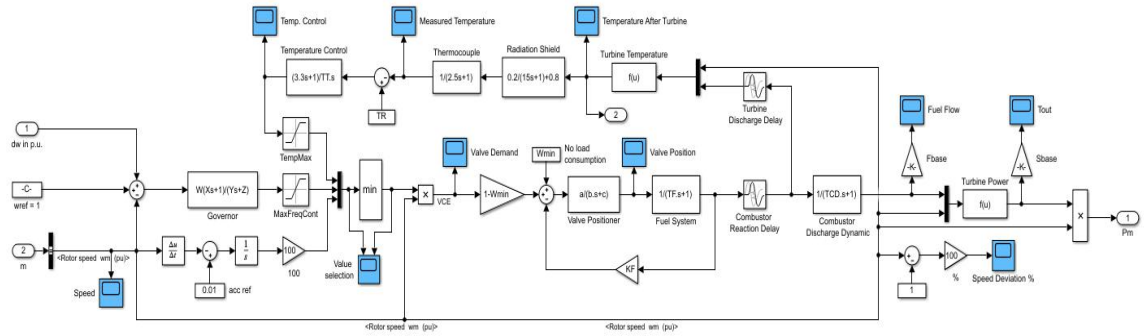


Figure 2.32: Simulation model of Rowen's model for HDGT.

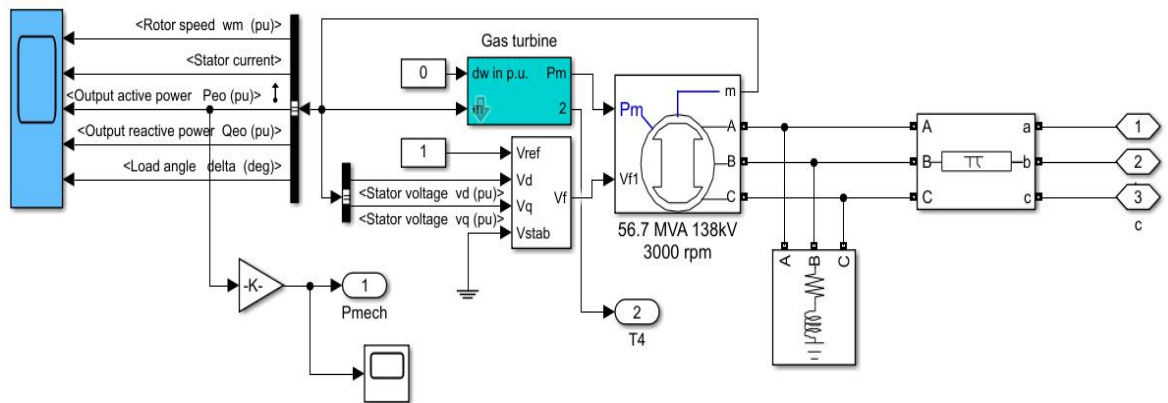


Figure 2.33: Simulink model of the whole gas turbine system.

2.3.5 Ground source heat pump modeling

In this project, the heat pump model has adopted the mathematical model in order to design the expected outputs for MES to connect all the coupling components and different energy networks. The heat pump unit, the underground pipe heat exchange section, and the users are the three basic components of a GSHP (ground source heat pump) system. The compressor, condenser, expansion valve, and evaporator comprise a basic heat pump unit. The heat exchange part of the underground buried pipe is composed of the underground buried pipe and a U-tube heat exchanger. The air conditioning terminal part is mainly a fan coil. Figure 2.34 depicts the system structure diagram as follows [57]:

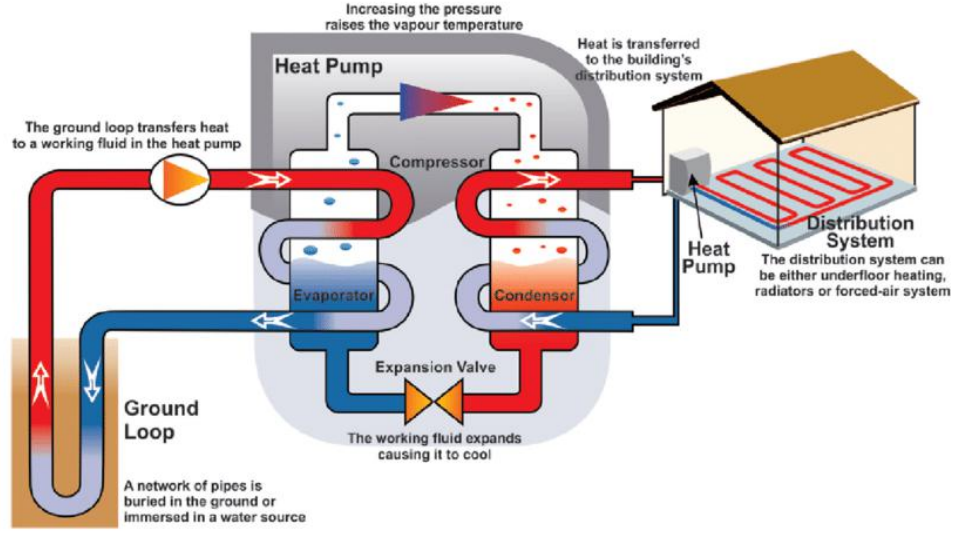


Figure 2.34: Schematic diagram of GSHP [57].

1. Mathematical model of buried tube heat exchanger

Because the heat transfer parameters of the underground heat exchanger are unstable, different modeling methods exist. This project adopts the classic heat transfer model of the infinite cylindrical source theory [58]. The relationship between the environmental soil temperature at the remote point and the temperature of the buried pipe is:

$$t_g - t_b = \frac{q}{K_s L} G(F_0, P), \quad (2.12)$$

where t_g is the environmental soil temperature at the remote point in $^{\circ}\text{C}$, t_b is the buried pipe temperature in $^{\circ}\text{C}$, q is heat exchange amount in W (when the heat exchanger absorbs heat, the value is positive, negative when it releases). K_s is the soil thermal conductivity in $W/(m \cdot K)$, L is the depth of buried pipe in m , G is green function, F_0 is Fourier number, P is the ratio of the distance between a location and the center of an underground pipe to its radius.

$$F_0 = 4\alpha t/d^2, \quad (2.13)$$

where α is the soil thermal diffusivity in m^2/s , t is the time in s , d is the drilling diameter in m .

The G function for calculating the heat transfer of a cylinder embedded in an infinite

medium, the fitting formula between G and F_0 under the typical radius ratio given by Ingersoll:

$$P = 1, G = 10^A, \quad (2.14)$$

$$A = -0.89129 + 0.36081 \times \lg(F_0) - 0.05508 \times \lg^2(F_0) + 3.5961 \times 10^{-3} \times \lg^3(F_0) \quad (2.15)$$

The heat transfer process between the circulating water and the soil in the heat exchanger can be regarded as a simple temperature difference heat transfer process, and the equation is:

$$G_c c_{p,w} (t_{cw1} - t_{cw2}) = K_d F_d \frac{t_{cw1} - t_{cw2}}{\ln \frac{t_{cw2} - t_b}{t_{cw1} - t_b}}, \quad (2.16)$$

where K_d is the soil heat transfer coefficient in $kw/m^2/K$, F_d is the soil heat transfer area in m^2 , G_c is the mass flow of chilled water in the evaporator in kg/s , $c_{p,w}$ represents the specific heat capacity of water at constant pressure, equals to $4.1868 kJ/(kg \cdot K)$.

The heat exchanger model built in Simulink is shown below:

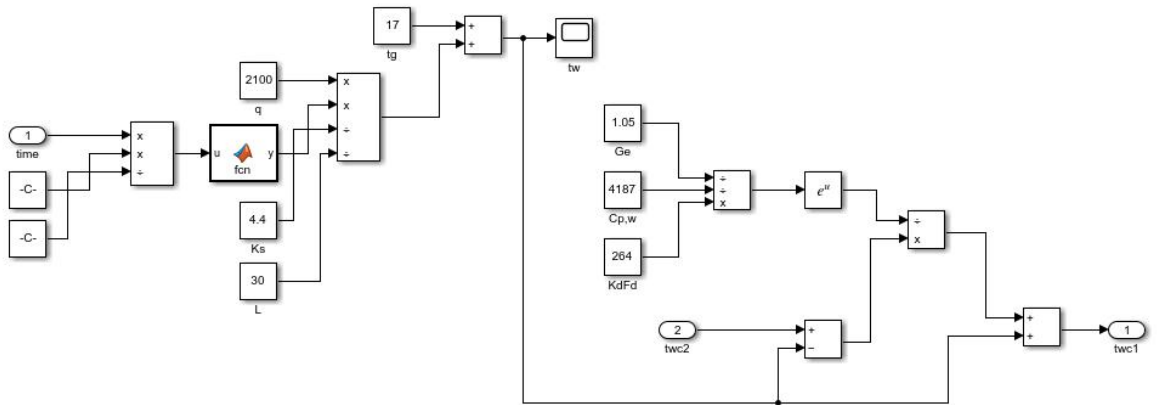


Figure 2.35: Heat exchanger simulation block.

2. Mathematical model of evaporator

The evaporator is a crucial heat exchange component of the heat pump unit, and it exchanges heat with the heat pump's working fluid. The following assumptions are adopted

to simplify the evaporator model [59]:

- (1). The average dryness of the refrigerant in the evaporator is taken as 0.7;
- (2). The refrigerant flows through the evaporator is equal to the refrigerant flow through the compressor;
- (3). Ignore the pressure drop and heat loss during the evaporation process in the evaporator.

The following Equation 2.17-2.42 for heat pump modeling are all taken from [59]. According to the energy conservation, the equation for the frozen waterside in the evaporator can be established as follows [59]:

$$\frac{1}{2}m_1c_{p,w}\frac{dt_{ew1}-dt_{ew2}}{d\tau}=G_e c_{p,w}(t_{ew1}-t_{ew2})-Q_e, \quad (2.17)$$

where τ is the time variable, Q_e is the cooling capacity in kW, m_1 is the quality of chilled water in the evaporator in kg. The chilled water flow through the evaporator is measured in kg/s by G_e . t_{ew1} , t_{ew2} are the temperature of the chilled water at the input and outlet of the evaporator in °C.

The refrigerant flows into the evaporator in a gas-liquid two-phase flow condition, absorbs heat during operation, evaporates to generate hot steam, and flows out of the evaporator into the compressor for the refrigerant side. The refrigerant internal energy change in this process can be assumed to be the same as the change in the enthalpy value. The energy conservation equation for this process is:

$$m_e \frac{dh_e}{d\tau} = Q_e - G_r(h_1 - h_4), \quad (2.18)$$

where m_e is the refrigerant quality in the evaporator in kg, G_r is the refrigerant flow through the evaporator in kg/s, h_e , h_1 , h_4 represents the average specific enthalpy of the refrigerant in the evaporator, evaporator outlet enthalpy, inlet enthalpy in kJ/kg.

The refrigerant's average specific enthalpy in the evaporator can be calculated as below:

$$m_e dh_e = x_e h_{ev} + (1 - x_e)h_{el}, \quad (2.19)$$

where h_{ev} and h_{el} represents saturated vapor enthalpy and liquid enthalpy of refrigerant in the evaporator in kJ/kg.

The relationship between the saturated vapor enthalpy value and saturated liquid enthalpy value of refrigerant R22 and temperature is:

$$h_{ev} = 338.02893 + 0.24532t, \quad (2.20)$$

$$h_{el} = -137.26 + 1.23463t. \quad (2.21)$$

The average specific enthalpy h_e can then be formulated as below:

$$\frac{dh_e}{d\tau} = \frac{dh_e}{dt_e} \frac{dt_e}{d\tau} = \left[x_e \frac{dh_{ev}}{dt_e} + (1 - x_e) \frac{dh_{el}}{dt_e} \right] \frac{dt_e}{d\tau}. \quad (2.22)$$

Then,

$$\frac{dh_e}{d\tau} = (1.23463 - 0.98931x_e) \frac{dt_e}{d\tau}, \quad (2.23)$$

Substitute $x_e = 0.7$ into the above equation, then,

$$\frac{dh_e}{d\tau} = 0.542113 \frac{dt_e}{d\tau}, \quad (2.24)$$

In the evaporation process, the refrigerant pressure is unchanged, there is a corresponding relationship between evaporation temperature and evaporation pressure, and the linear fitting formula is as follows:

$$p_e = \exp[21.3 - 2025.5/(t_e + 248.94)], \quad (2.25)$$

where t_e is the evaporation temperature of the evaporator in °C, p_e is the evaporation pressure in Pa.

The superheated steam at the outlet of the evaporator can be regarded as an ideal gas, and the outlet steam temperature t_1 is:

$$\frac{dt_1}{d\tau} = \frac{1}{c_{p,x}} \frac{dh_e}{d\tau} = \frac{0.24542}{c_{p,x}} \frac{dt_e}{d\tau}, \quad (2.26)$$

where $c_{p,x}$ denotes specific heat capacity of refrigerant at constant pressure in kJ/kg/K.

Then, the superheated steam specific capacity v_1 is:

$$v_1 = f(t_e, t_1). \quad (2.27)$$

Heat transfer between refrigerant and chilled water in evaporator (evaporator heat transfer) is:

$$Q_e = K_e F_e \left(\frac{t_{ew1} + t_{ew2}}{2} - t_e \right), \quad (2.28)$$

where K_e is the heat transfer coefficient of evaporator in kW/m²/K. F_e is the heat transfer area of evaporator in m².

The evaporator model built in Simulink is shown below:

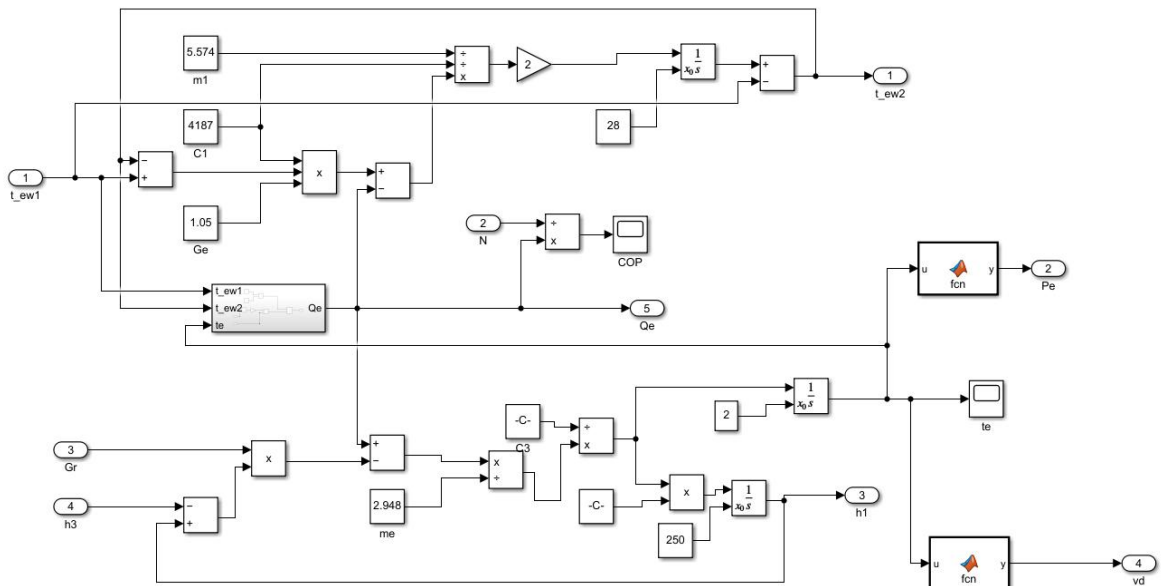


Figure 2.36: Evaporator simulation block.

3. Mathematical model of condenser

The high-temperature and high-pressure gas compressed by the compressor will enter the

compressor, and then be cooled and liquefied. The liquefaction process releases heat to the heat-releasing surface of the condenser, and the refrigerant is cooled down into saturated gas and high-pressure liquid in turn. For the condensation process, the following assumptions are assumed to simplify the model:

- (1). The average dryness of the refrigerant in the condenser is taken as 0.5;
- (2). The refrigerant flows through the condenser is equal to the refrigerant flow through the compressor;
- (3). Ignore the pressure drop and heat loss during the condensation process.

According to the conservation of energy, the equation for the cooling water side of the condenser can be established as:

$$\frac{1}{2}m_2c_{p,w}\frac{dt_{cw1} + dt_{cw2}}{d\tau} = Q_c - G_c c_{p,w}(t_{cw1} - t_{cw2}), \quad (2.29)$$

where τ is the time variable, Q_c is the heating capacity in kW, m_2 is the quality of cooling water in the condenser in kg. G_c is the cooling water flow in condenser in kg/s. t_{cw1} , t_{cw2} are the condenser input and output cooling water temperature in °C.

The refrigerant flows into the condenser in a gaseous condition during operation for the refrigerant side of the condenser, releases heat in the condenser, liquefies into a two-phase state, and flows out of the condenser. The change in refrigerant internal energy in this process can be considered equal to the change in refrigerant enthalpy value. This process' energy equation is as follows:

$$m_c \frac{dh_c}{d\tau} = G_r(h_2 - h_3) - Q_c, \quad (2.30)$$

where m_c is the refrigerant quality in the condenser in kg, G_r is the refrigerant flow through the condenser in kg/s, h_c , h_2 , h_3 represents the average specific enthalpy of refrigerant in condenser, enthalpy of condenser outlet, enthalpy of condenser inlet in kJ/kg.

In a condenser, the average specific enthalpy of refrigerant can be calculated as:

$$h_c = x_c h_{cv} + (1 - x_c) h_{cl}, \quad (2.31)$$

where h_{cv} and h_{cl} represents saturated vapor enthalpy and liquid enthalpy of refrigerant in the condenser in kJ/kg.

Similar to evaporator, we have:

$$\frac{dh_c}{d\tau} = \frac{dh_c}{dt_c} \frac{dt_c}{d\tau} = \left[x_c \frac{dh_{cv}}{dt_c} + (1 - x_c) \frac{dh_{cl}}{dt_c} \right] \frac{dt_c}{d\tau}. \quad (2.32)$$

Then,

$$\frac{dh_c}{d\tau} = (1.23463 - 0.98931 x_c) \frac{dt_c}{d\tau}. \quad (2.33)$$

Substitute $x_c = 0.5$ into the above equation, then,

$$\frac{dh_c}{d\tau} = 0.739975 \frac{dt_c}{d\tau}, \quad (2.34)$$

In the condensation process, the refrigerant pressure remains unchanged, there is a corresponding relationship between condensation temperature and condensation pressure, and the linear fitting formula is as follows:

$$p_c = \exp[21.3 - 2025.5/(t_c + 248.94)], \quad (2.35)$$

where t_c is the condensation temperature of the condenser in °C, p_c is the condensation pressure in Pa.

In the condenser, the heat transfer between the refrigerant and the cooling water is as follows:

$$Q_c = K_c F_c \left(\frac{t_{cw1} + t_{cw2}}{2} - t_c \right), \quad (2.36)$$

where K_c denotes the condenser's heat transfer coefficient in kW/m²/K. F_c represents the condenser's heat transfer area in m².

The condenser model built in Simulink is shown below:

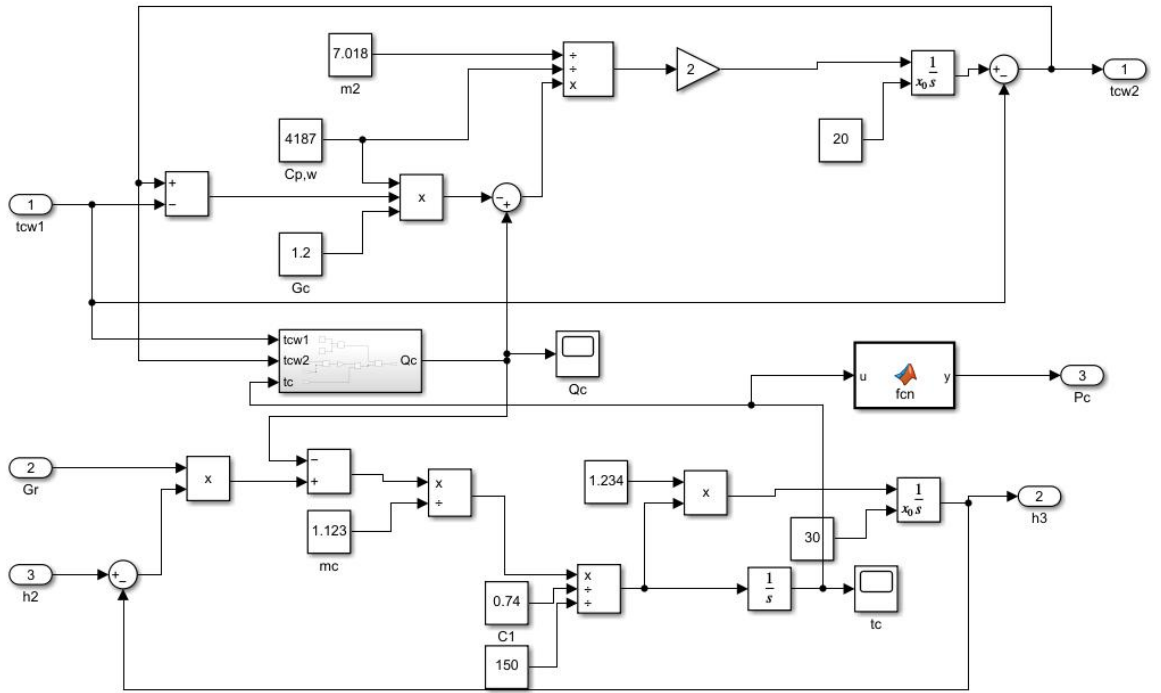


Figure 2.37: Condenser simulation block.

4. Mathematical model of compressor

In compressor modeling, the efficiency method is a relatively simple and general method. This method can simplify the complicated heat transfer and flow process of the compressor into a series of efficiency formulas to calculate the efficiency of the compressor, such as volume efficiency and friction efficiency. The component is selected as a single screw compressor, ignoring the heat loss of the cylinder wall, the following expression can be obtained.

Let $\varepsilon = p_c/p_e$, p_c is the refrigerant pressure in the condenser in Pa. According to the physical properties of R22 refrigerant, the correlation formula can be fitted as follows:

$$\eta_v = 0.0039\varepsilon^2 - 0.058\varepsilon + 0.9662, \quad (2.37)$$

$$\eta_e = 0.0065\varepsilon^3 - 0.0901\varepsilon^2 + 0.384\varepsilon + 0.321, \quad (2.38)$$

where η_v is the compressor volumetric efficiency, η_e is the compressor power consumption.

Mass flow of refrigerant through the compressor is:

$$G_r = \frac{V_h \eta_v}{3600 v_1}. \quad (2.39)$$

The compressor shaft power is:

$$N_t = \frac{n}{1-n} \eta_v V_s p_e \left[1 - \left(\frac{p_c}{p_e} \right)^{\frac{n-1}{n}} \right]. \quad (2.40)$$

The actual shaft power of compressor is:

$$N = \frac{N_t}{\eta_e}. \quad (2.41)$$

The refrigerant enthalpy value at compressor outlet is:

$$h_2 = h_1 + \frac{N}{G_r}, \quad (2.42)$$

where V_h is the output capacity of the compressor per hour, m^3/h . V_s is the air displacement per second of the compressor, m^3/s . N is the actual shaft power of the compressor in kW. n is the compression process multivariate index, which equals to 1.18.

The compressor model built in Simulink is shown below:

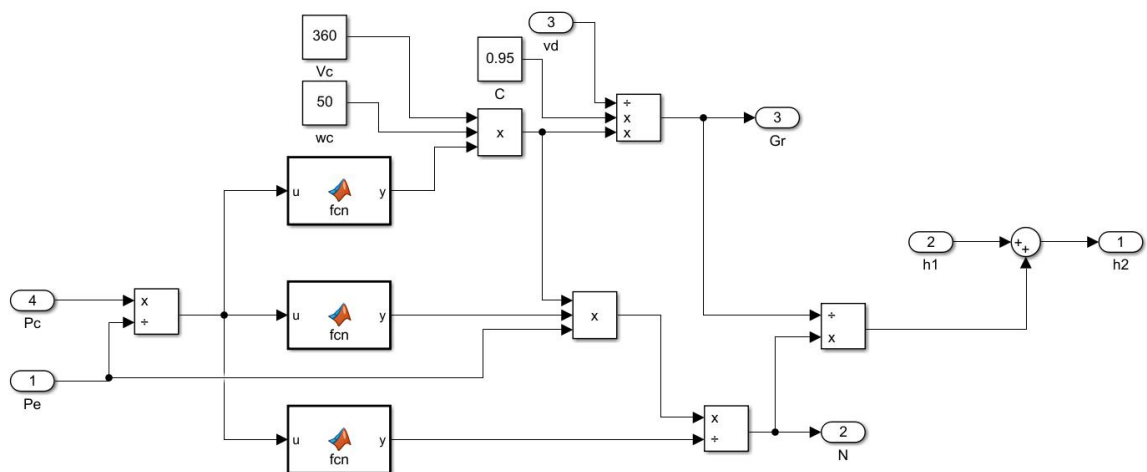


Figure 2.38: Compressor simulation block.

A typical ground source heat pump contains the compressor, condenser, heat exchange system, and evaporator. The simulation model of the ground source heat pump system can

be established in Simulink according to the relationship described in Equations 2.12-2.42 [59]. Figure 2.39 gives the simulation model of the ground source heat pump system.

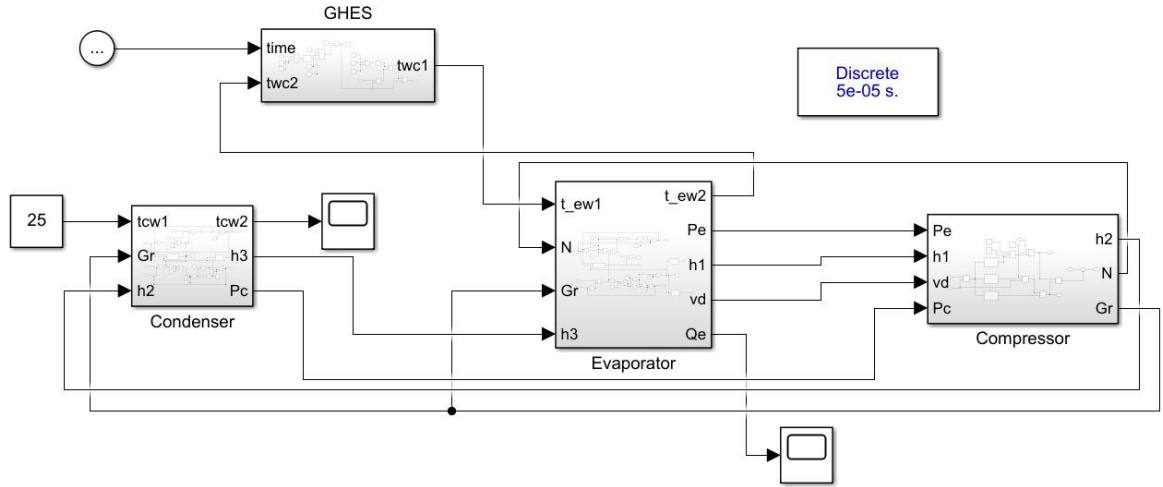


Figure 2.39: The simulation model of ground source heat pump.

2.3.6 CHP unit modeling

Power generation, heat generation, and gas consumption are the three main part of the CHP unit. The amount of natural gas consumed by CHP during the time interval t is [60]:

$$G_{CHP}^t = \frac{P_{CHP}^t}{\eta_{CHP} LHV_{ng}}, \quad (2.43)$$

where LHV_{ng} is the heating value of natural gas, η_{CHP} is the CHP unit efficiency, G_{CHP}^t is the natural gas consumption, and P_{CHP}^t is the electric power generation of CHP unit during time period t .

Therefore, the heat generated by CHP throughout time t can be calculated using the formula below:

$$H_{CHP}^t = \frac{P_{CHP}^t}{\eta_{CHP}} COP_{CHP}, \quad (2.44)$$

where COP_{CHP} is the coefficient of the performance parameter of the CHP unit, and H_{CHP}^t is the heat power generation of CHP unit during time period t .

2.3.7 GB modeling

During the time period t , the total amount of natural gas consumed by GB is below [60]:

$$G_{GB}^t = \frac{H_{GB}^t}{\eta_{GB} LHV_{ng}}, \quad (2.45)$$

where η_{GB} is the GB unit efficiency, G_{GB}^t is the natural gas consumption, and H_{GB}^t is the heat output of the GB unit during time period t .

2.3.8 P2G device modeling

During interval t , the total amount natural gas produced by P2G is [60]:

$$G_{P2G}^t = \frac{P_{P2G}^t \eta_{P2G}}{LHV_{ng}}, \quad (2.46)$$

where η_{P2G} is the P2G unit efficiency, G_{P2G}^t is the natural gas generation, P_{P2G}^t is the electric power consumption of P2G unit during time period t .

2.3.9 Energy storage devices modeling

1. ES devices

The ES device can realize the bi-directional energy flow and can also be used as a backup source when MES fails to supply power to customers. The charging and discharging power of ES can be modeled using the following equations [61]:

$$P_t^{charging} = \begin{cases} P_{t, max}^{charging}, & (P_{grid} - P_L) \geq P_{t, max}^{charging} \\ P_{grid} - P_L, & P_{t, max}^{charging} \geq (P_{grid} - P_L) \geq 0 \end{cases} \quad (2.47)$$

$$P_t^{discharging} = \begin{cases} -P_{t, max}^{discharging}, & -P_{t, max}^{discharging} \geq (P_{grid} - P_L) \\ P_{grid} - P_L, & 0 \geq (P_{grid} - P_L) \geq -P_{t, max}^{discharging} \end{cases} \quad (2.48)$$

where $P_t^{charging}$ and $P_t^{discharging}$ represents the quantity of charging and discharging power of the stored energy at hour t respectively. $P_{t, max}^{charging}$ and $P_{t, max}^{discharging}$ are the limits of the charging and discharging power of the stored energy. P_{grid} is the grid power

supply to the power system. P_L is the load power.

2. HS devices

Equation 2.49 describes the mathematical model of the heat storage device. The heat balance equation is given in Equation 2.50. The flow-in energy, flow-out heat energy, and HS capacity are subjected to the limitation in Equations 2.51, 2.52, and 2.53 respectively [61]:

$$H_{hs}^{i,t+1} = H_{hs}^{i,t} + H_{hs,in}^{i,t} - H_{hs,out}^{i,t}, \quad \forall i \in \Omega_{hs}, t \in \Gamma, \quad (2.49)$$

$$\sum H_{hs,in}^{i,t} = \sum H_{hs,out}^{i,t}, \quad (2.50)$$

$$0 \leq H_{hs,in}^{i,t} \leq \lambda_{i,t} \times H_{hs,in}^{i,max}, \quad \lambda_{i,t} \in \{0, 1\}, \quad (2.51)$$

$$0 \leq H_{hs,out}^{i,t} \leq (1 - \lambda_{i,t}) \times H_{hs,out}^{i,max}, \quad \lambda_{i,t} \in \{0, 1\}, \quad (2.52)$$

$$0 \leq H_{hs}^{i,t} \leq H_{hs}^{i,max}, \quad (2.53)$$

where $H_{hs}^{i,t}$ is the heat energy of heat storage device i at hour t , and $H_{hs}^{i,max}$ is the capacity of heat storage device i . $H_{hs,in}^{i,t}$ and $H_{hs,out}^{i,t}$ are the heat charging power and heat discharging power, $H_{hs,in}^{i,max}$ and $H_{hs,out}^{i,max}$ are the maximum flow-in heat energy and flow-out heat energy. Ω_{hs} is the set of heat storage devices. Γ is the 24 hour time set. $\lambda_{i,t}$ is the binary variable, $\lambda_{i,t} = 1$ represents the charging state, while $\lambda_{i,t} = 0$ represents the discharging state.

3. GS devices

The GS modeling functions are the same as HS, which can be presented in the following equations [62]:

$$G_{gs}^{y,t} = G_{gs}^{y,t-1} + G_{gs,in}^{y,t} - G_{gs,out}^{y,t}, \quad (2.54)$$

$$\sum G_{gs,in}^{y,t} = \sum G_{gs,out}^{y,t}, \quad (2.55)$$

$$0 \leq G_{gs, in}^{y,t} \leq G_{gs, in}^{y,max}, 0 \leq G_{gs, out}^{y,t} \leq G_{gs, out}^{y,max} \quad (2.56)$$

$$0 \leq G_{gs}^{y,t} \leq G_{gs}^{y,max}, \quad (2.57)$$

where $G_{gs}^{y,t}$ represents the gas volume of gas storage device y at hour t . $G_{gs}^{y,max}$ represents the capacity of gas storage device y . $G_{gs, in}^{y,t}$ and $G_{gs, out}^{y,t}$ are the input and output gas volume of gas storage device y at hour t . $G_{gs, in}^{y,max}$ and $G_{gs, out}^{y,max}$ are the upper limit of input and output gas volume, respectively.

2.3.10 V2G modeling

1. The principle of V2G

The V2G system contains three main parts, which are EV charging stations, power converters, and controllers of the power grid. Figure 2.40 gives the configuration of a V2G system [13]. A PWM DC/DC voltage source converter is used in each electric vehicle charging regulator. The three-phase grid voltage is converted to a DC voltage via a three-phase three-level rectifier/inverter. Electric vehicles are connected to the DC bus in parallel using an EV charger. To perform the charge and discharge operation of EV batteries, the DC/DC power converter at the EV-side controller is used to charge and discharge the EV [13].

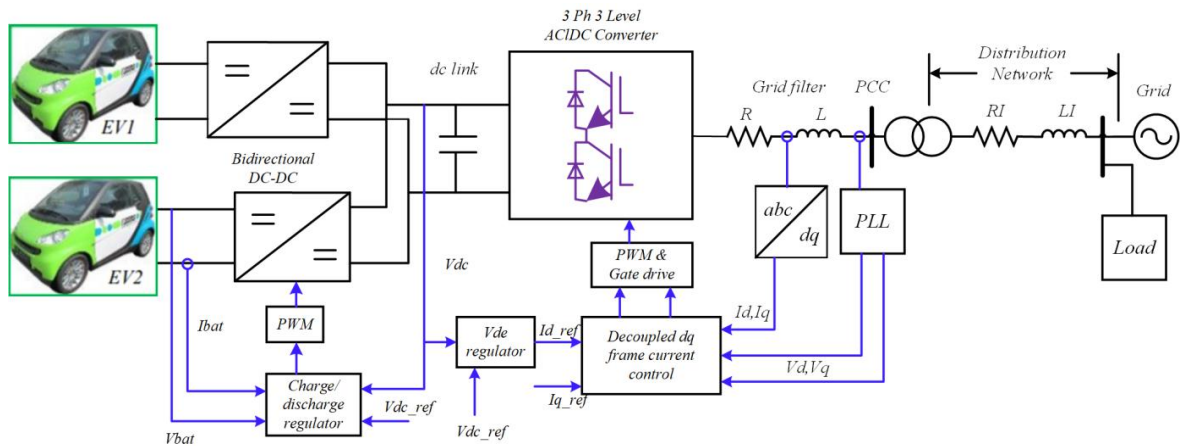


Figure 2.40: Configuration of V2G system [13].

2. V2G control strategy

The V2G charge-discharge machine's primary role is to achieve two-way electric energy

conversion between the power grid and the EV battery. At the same time, V2G charge-discharge machine must also have the power grid side current control, power factor correction, and battery reasonable charge and discharge functions, but also should have resistance to voltage disturbance, parameter changes, load changes can be adjusted in time and other dynamic adjustment ability. According to the working principle of V2G charge/discharge above, the front bi-directional AC/DC converter and the rear bi-directional DC/DC converter of the V2G charge-discharge machine are relatively independent, and they have different goals to achieve, which can be controlled separately.

(1). Control strategy of bi-directional AC/DC converter

When charging, the double closed-loop control system of the outer voltage loop and inner current loop is utilized, and when discharging, the current closed-loop control system is used. The current inner loop mainly completes the current input and output control of the AC/DC converter, such as the unit factor sine current setting. The voltage outer loop's major job is to sustain DC side voltage stability when charging by regulating the DC side voltage. To make the control system design process easier, a PI control scheme in a dq rotating coordinate system is adopted for the current loop and PI control for the voltage outer loop. Then the voltage signals are sent to the SVPWM block to complete the whole control process. The AC/DC block is shown in Figure 2.41. The control model for AC/DC converter is shown in Figure 2.42.

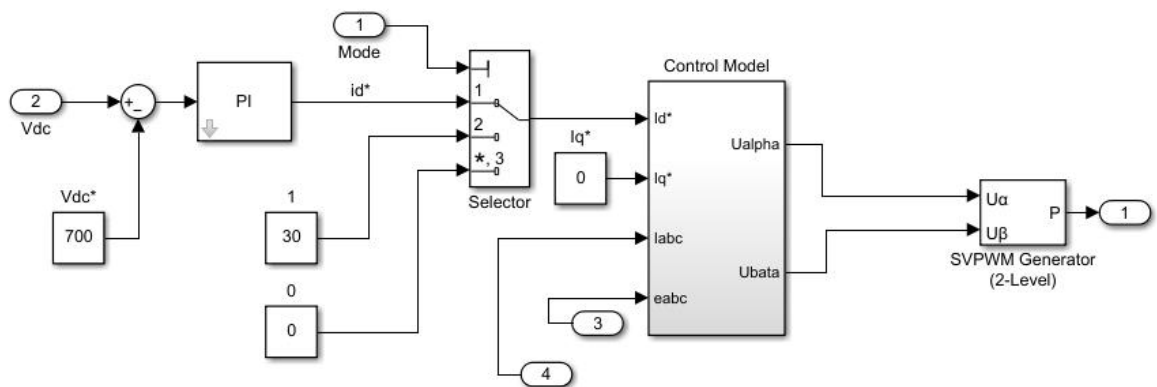


Figure 2.41: V2G AC/DC simulation block.

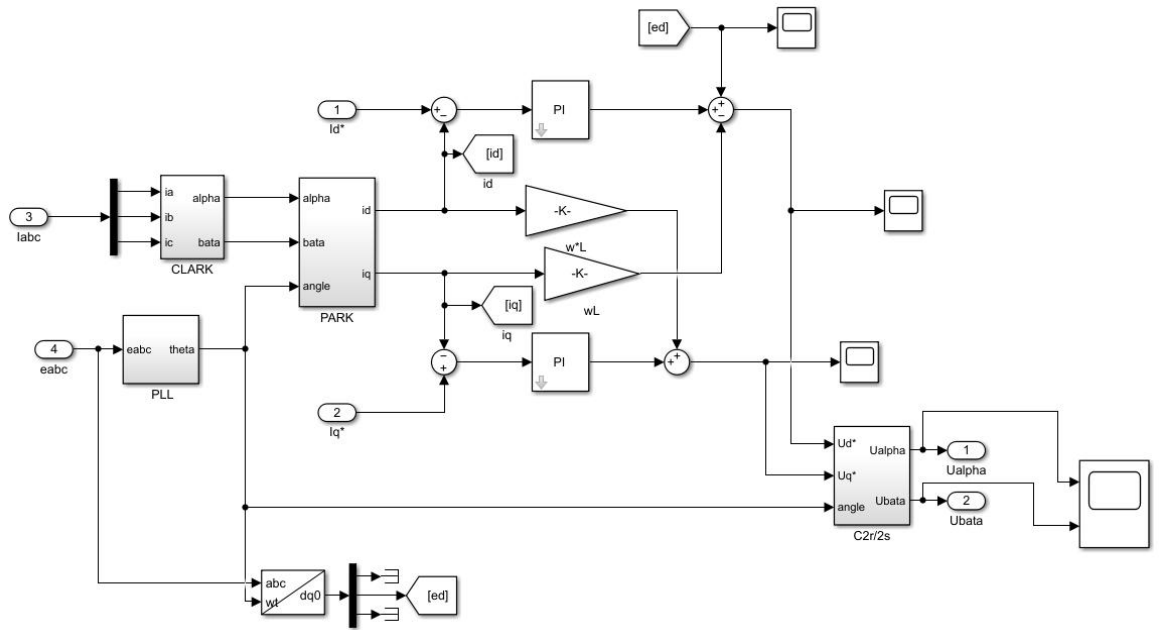


Figure 2.42: The control model for AC/DC converter in V2G.

(2). Control strategy of bi-directional DC/DC converter

The basic function of a bidirectional DC/DC converter is to realize the energy conversion between the DC side energy storage unit and the EV battery. The bidirectional DC/DC converter designed in this paper adopts different control strategies in charge and discharge mode due to their different functions. Figure 2.43 gives the DC/DC simulation block.

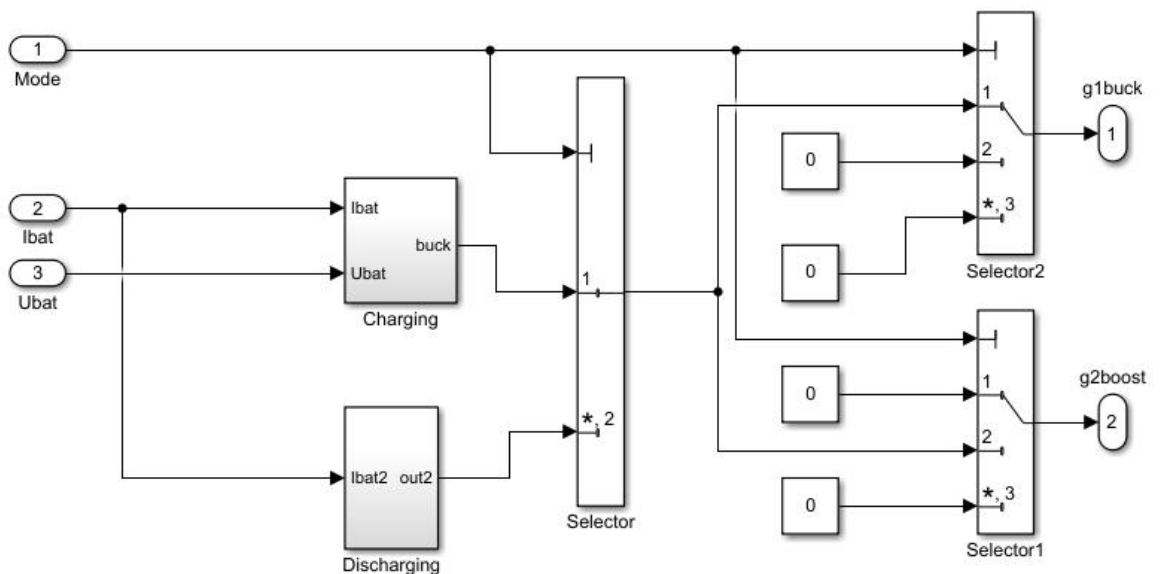


Figure 2.43: The DC/DC block for V2G.

control strategy. Figure 2.45 gives the discharging block simulation model.

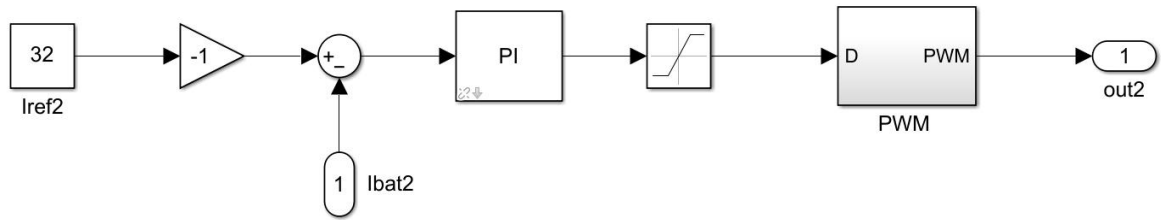


Figure 2.45: The discharging block for V2G.

After comparing the DC side current with the reference current, the control signal is obtained through the PI regulator. After PWM modulation, the on-off state of the power switch can be controlled to achieve constant current discharge.

(2). Space vector pulse width modulation (SVPWM)

After obtaining the instruction voltage signal needed to realize the function of the V2G charge/discharge machine through dq rotating coordinate transformation, the requisite voltage must be generated using a PWM converter to meet the goal of managing the input and output current. The modulation algorithm is to make PWM converter output according to the command signal, the commonly used modulation algorithm is hysteresis modulation, fixed switching frequency modulation, and space vector pulse width modulation (SVPWM).

The SVPWM algorithm is a quasi-circular rotation coordinate that uses a space voltage vector to bring the PWM converter's output closer to a sine wave and has good control performance. Compared with hysteresis modulation and SPWM modulation, space vector pulse width modulation (SVPWM) can achieve better control performance even at smaller switching frequencies. Because of the superiority of the SVPWM modulation algorithm, this project mainly studies and analyzes the space vector modulation algorithm. Through the above research and analysis of the overall control scheme of the V2G bidirectional AC/DC converter of the charge-discharge machine, Figure 2.46 depicts the overall control block diagram of a PWM converter that employs the SVPWM algorithm [64].

(2). EVs all behave in the same way daily throughout the year.

The following functions describe the available energy model of EV [27]:

$$F_z(z) = \int_{-\infty}^{\infty} \sum_{j=1}^m \frac{\rho^{(N-j)}}{(N-j)!} e^{-\rho} \frac{1}{j\sqrt{2\pi}\sigma} e^{-\frac{(\frac{\mu}{j}-\omega)^2}{2\sigma^2}}, \quad (2.58)$$

$$\rho = \frac{\delta}{\mu}, \quad (2.59)$$

where N represents the total number of EVs in a certain area. j denotes the number of EVs that are connected to the charging stations. σ is the standard deviation. The rate of electric vehicles entering the system is denoted as δ , whereas the rate of electric vehicles exiting the system is specified as μ . The available power in the EVs is ω .

This project considers 150 electric vehicles arrive and depart at a steady pace throughout the day and night, and the available electric power of the EVs can be calculated by dividing the electric energy over a time interval of h (in hours), where the available electric energy $F_z^{-1}(0.05)$ of the electric vehicles is supplied to the grid with a 95% probability.

$$power = \frac{F_z^{-1}(0.05)}{h}. \quad (2.60)$$

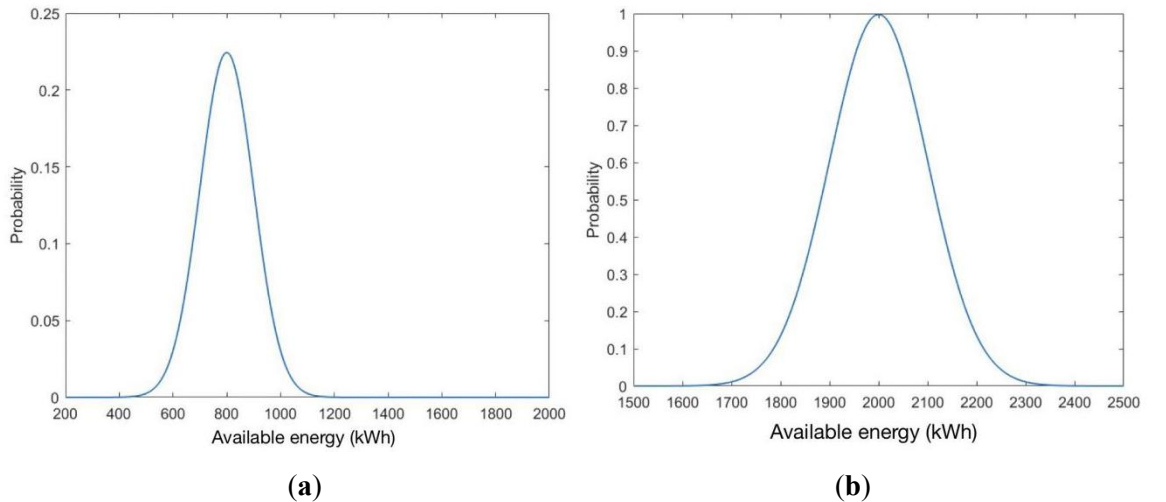


Figure 2.48: Probability density function for the available energy in 150 EVs (a) between 7 - 8 p.m.; (b) between 5-6 a.m. [27].

Since most vehicles leave after charging at 5 and 6 a.m., they come back to charge at 7 and

8 p.m. Figure 2.48 depicts the probability density distribution of available energy for 150 EVs between 7 and 8 p.m. and 5 and 6 a.m. Therefore, the available energy with various numbers of EVs throughout a day can be approximately characterized as the piecewise function depicted in Figure 2.49 [27].

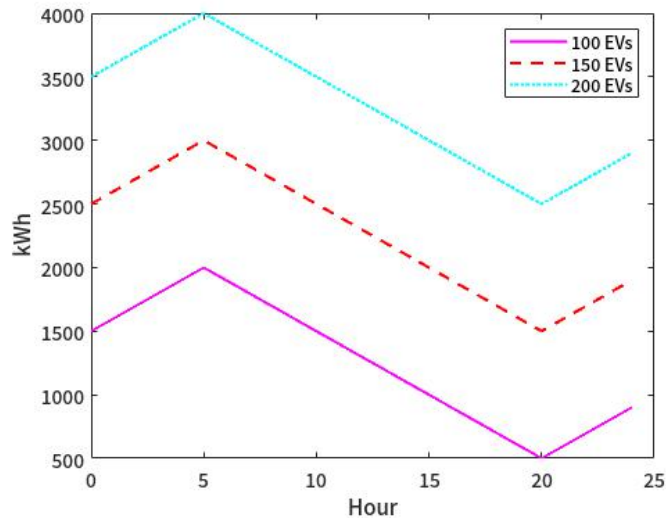


Figure 2.49: Configuration of V2G system [27].

2.4 Energy networks modeling

For the MES simulation design in Simulink, this project mainly considers the IEEE 24 bus system [69], the 13-node heat network [4], and the 9-node gas network [71]. The second MES is mainly used as a comparison object in the subsequent reliability optimization problem, which contains an IEEE 39 bus system [84], a 32-node heat network [85], and a 9-node gas network [86]. The second MES has been implemented in MATLAB using power-based models.

2.4.1 Power system modeling

1. Power transmission system

The IEEE 24 bus system is selected as the transmission model for assessing the reliability of the power system in MES 1. This 24 bus system has been shown in Figure 2.50. The transmission network consists of 24 busbars connected by 38 lines and 5 transformers. The transmission lines are at two voltage levels, 138 kV and 230 kV. The 230 kV system is the upper part of figure 1, with 230/138 kV transformer substations at buses 11, 12, and 24.

This power transmission system consists of ten generators which have been modeled as synchronous machines in simulation. The system has voltage corrective devices at the bus 14-synchronous condenser and bus 6-reactor. These devices increase the ability of the test system to maintain rated voltage, especially in some occasional situations.

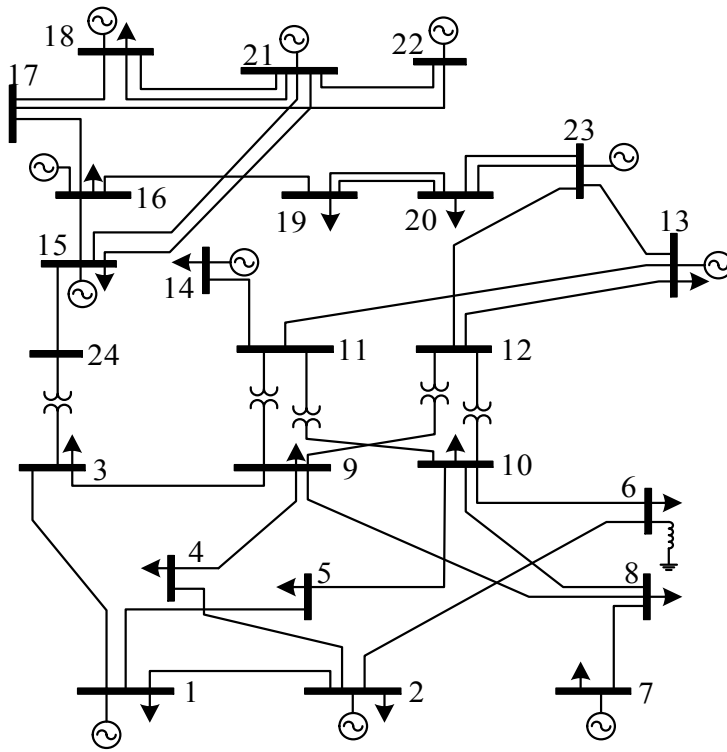


Figure 2.50: IEEE 24 Bus system [69].

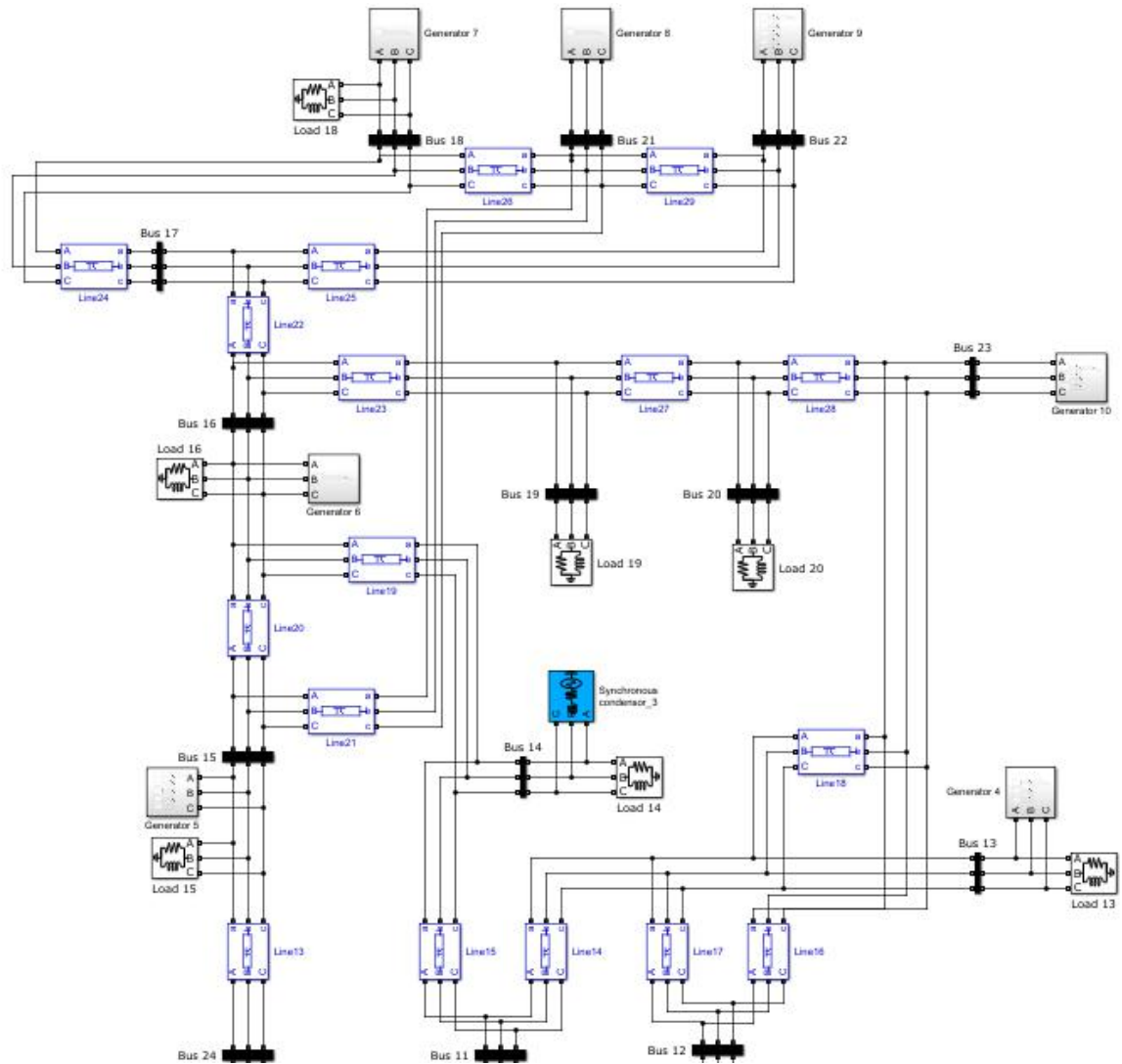


Figure 2.51: The upper part simulation model of IEEE 24 Bus system.

The upper part of the high voltage area 230 kV built in Simulink is shown in Figure 2.51. The lower part of the low voltage area 138 kV built in Simulink is shown in Figure 2.52. In addition to generators in the power grid, the WT, GT, battery, PV, and power distribution system have been added to the existing generators shown in Figure 2.49, which have been deployed on buses 1, 2, 4, 7, and 8 in IEEE 24 power system, have been considered in the MES design for delivering supplemental energy to the key load demands. The following chapters use simpler power-based models. The dynamic model for MES can provide the power result for the subsequent MCS reliability assessment. The bus 5 power has been used as the link to connect IEEE 24 bus power system with the gas network.

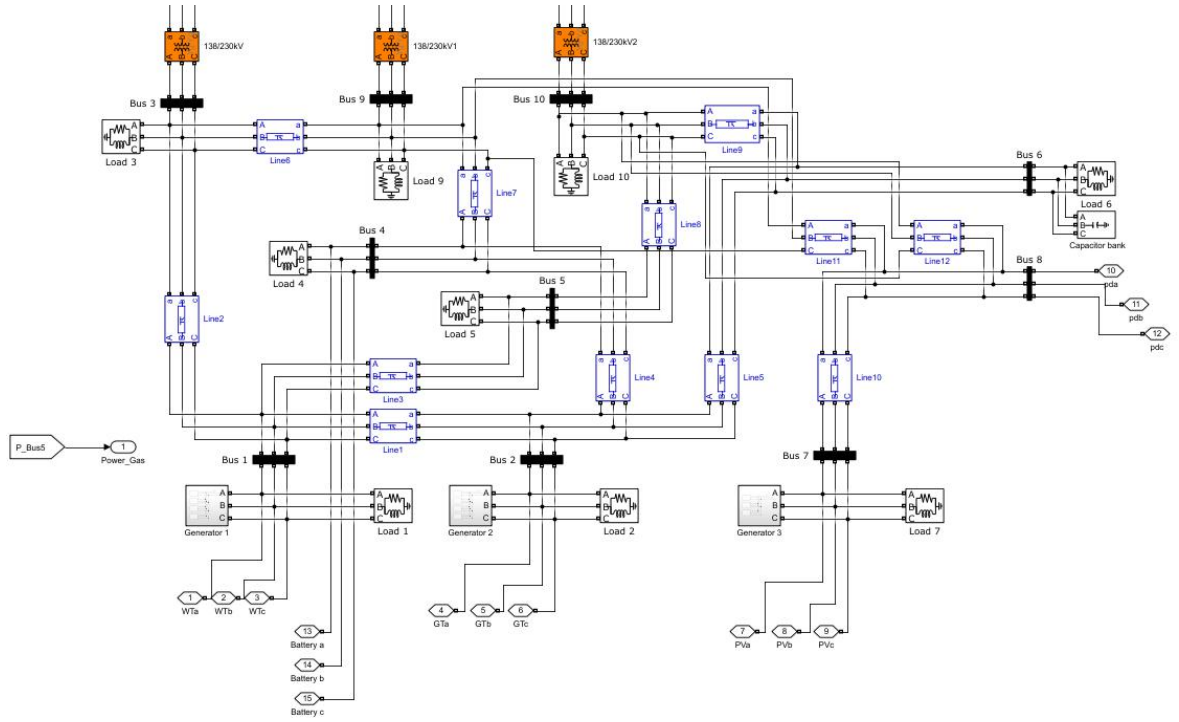


Figure 2.52: The lower part simulation model of IEEE 24 Bus system.

2. Power distribution system

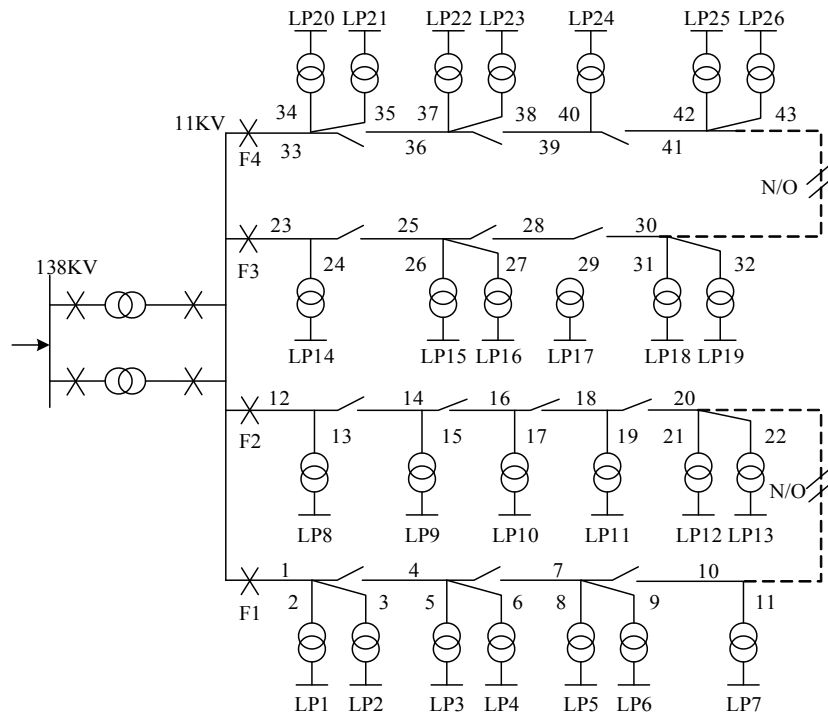


Figure 2.53: The schematic diagram of RBTS Bus 5 system [16].

The RBTS is a 6 bus test system with five load buses (bus2-bus6) from which bus 5 is

selected as the power distribution model for analysis purposes. The circuit diagram of bus 5 in RBTS is shown in Figure 2.53. The peak load of the distribution system at bus 5 is 20 MW. The system has three voltage levels, 138 kV, 11 kV, and 0.415 kV. The distribution network of bus 5 is a typical urban-type network, consisting of residential buildings, government institutions, office buildings, and commercial customers. The bus 5 distribution system model as shown below consists of 4 feeders with 26 load points and 2 tie switches that are normally open switches and 17 sectional switches. The feeders operate as radial feeders but are connected as a mesh through normally open switches. Figure 2.54 gives the simulation model of the power distribution system. The tie switch is the normally open switch. When the system is in normal operation, the tie switch is in the off state. When the system fails, for example, load 3 on feeder 1 fails, the sectional switches on both sides of load 3 are disconnected, and tie switch 1 is closed to continue to supply power to loads 5, 6, and 7.

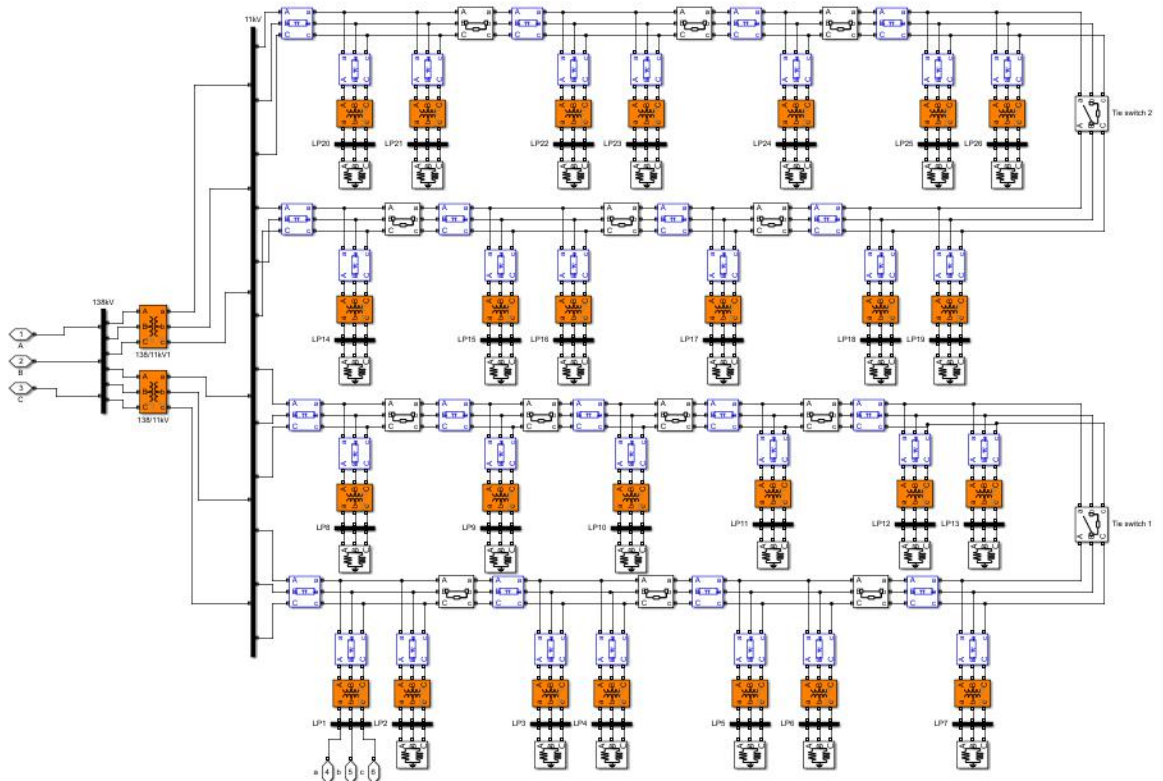


Figure 2.54: The simulation model of RBTS Bus 5 system.

2.4.2 Heating system modeling

The heating system of each load point in the heat network can use the following model

depicted in Figure 2.55 [63]. The input port is hot water from heat pump condenser side. The output port is the pumped water and can be connected to the next heat load.

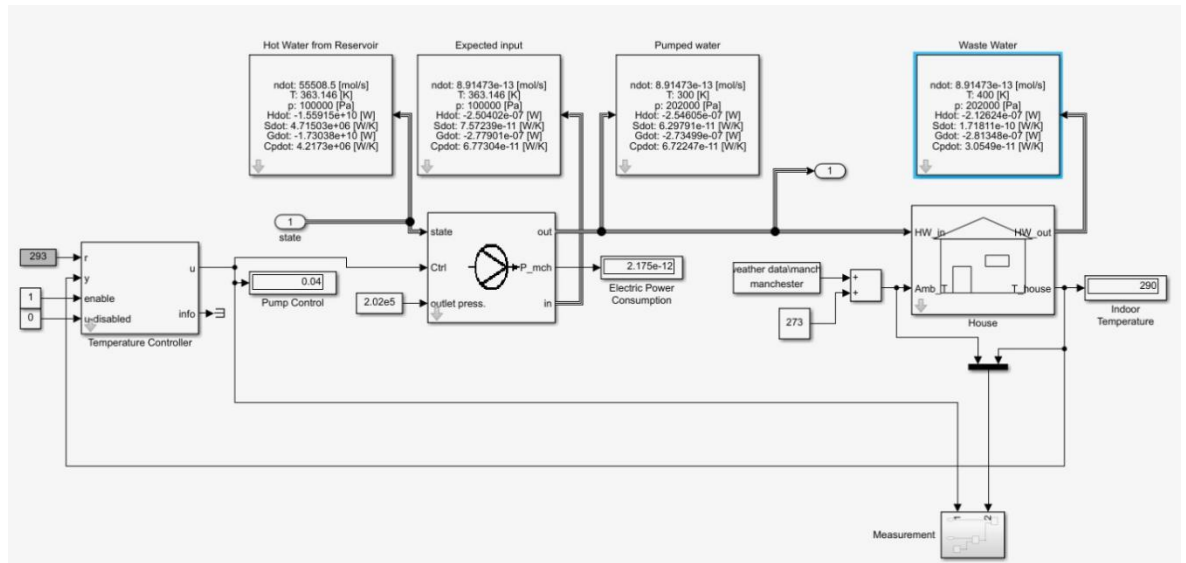


Figure 2.55: The heating system of each load [63].

The 13-node heat network [4] for MES 1 consists of 13 loads connected by 12 lines. Each heat pipe length is 200m. The simulation model of the heat network is given in Figure 2.56. The input port 1 is the condenser output water from heat pump module.

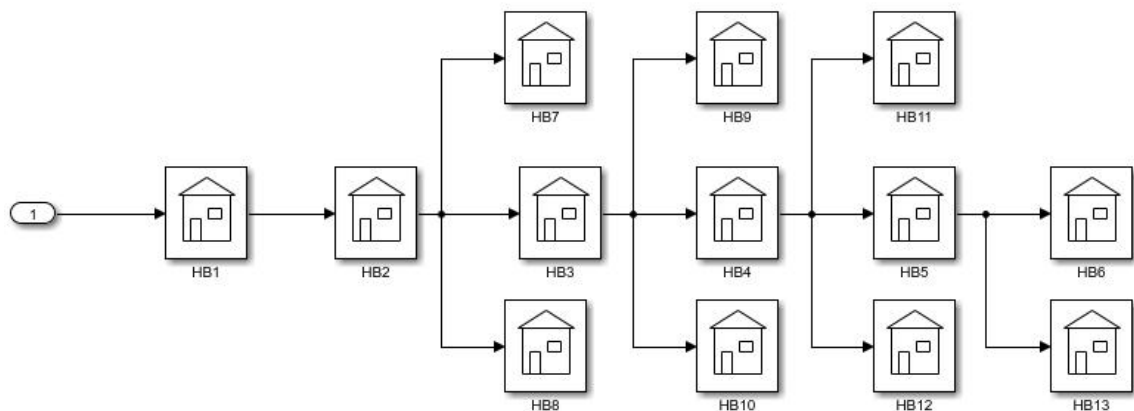


Figure 2.56: The 13 node heat network simulation model.

2.4.3 Gas network modeling

The 9-node gas network [71] for MES 1 consists of 5 loads connected by 9 pipelines. The

pipelines can be modeled using the following formula [71]:

$$\frac{P_{in} - P_{out}}{L} = 1.27 \times 10^{10} f \frac{Q_0^2}{d^5} \rho_0 \frac{T}{T_0}. \quad (2.61)$$

Where, P_{in} is the inlet pressure of natural gas pipeline (kPa). P_{out} is the outlet pressure of natural gas pipeline (kPa). L is the pipe length (km). f is the friction factor, which is 0.025. Q_0 is the volume flow rate of natural gas under standard conditions (m^3/s). ρ_0 is the density of natural gas under standard conditions (kg/m^3). T is the gas temperature (K). T_0 is the temperature (K) of natural gas in standard state.

The gas pipeline can be modeled in Simulink as follows:

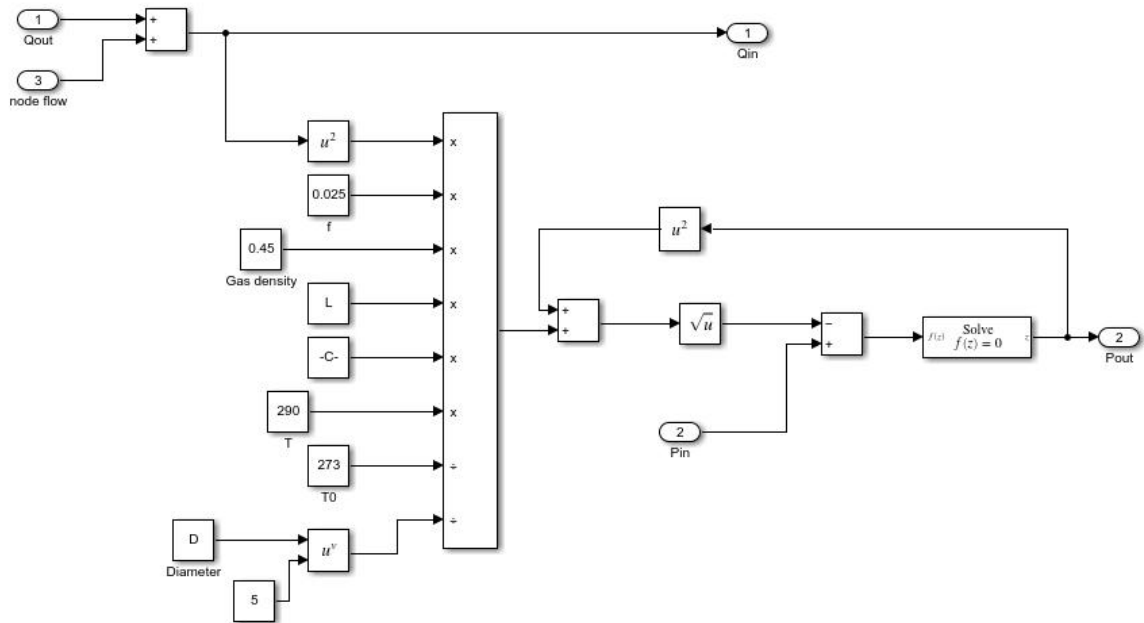


Figure 2.57: The gas pipeline simulation model.

Then, the 9 node gas network simulation model is shown in Figure 2.58. The compressor module is from the Thermolib block, which can provide the gas node flow data to the pipeline. Each pipeline has two outputs, which are gas pipe pressure and gas pipe flow. The input port 1 is IEEE 24 bus system bus 5 power. The input port 2 is CH4 gas fuel from Thermolib block. The output ports 1-9 stand for each gas pipe pressure. The output ports 10-18 stand for each gas pipe flow. The output ports have been connected to the gas load module to present all the gas load results shown in Figure 2.59.

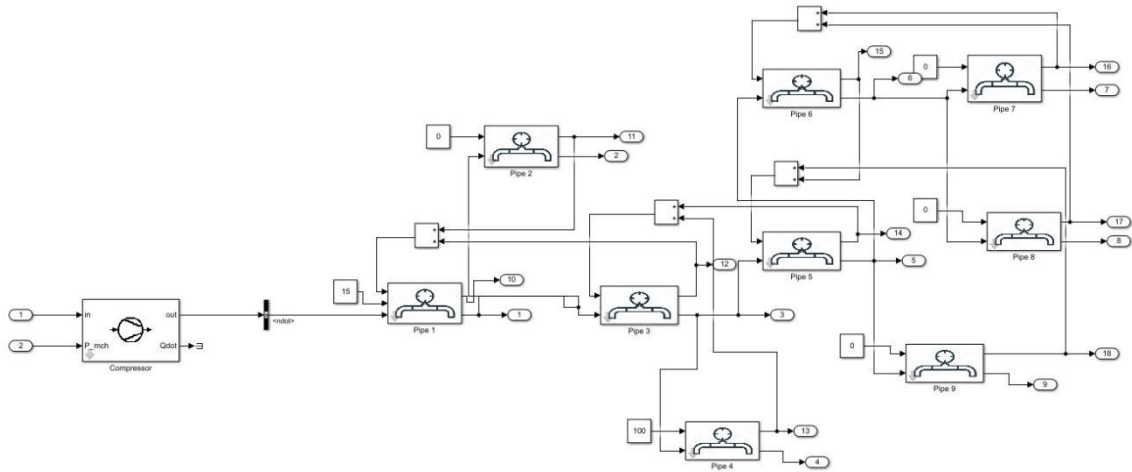


Figure 2.58: The 9 node gas network simulation model.

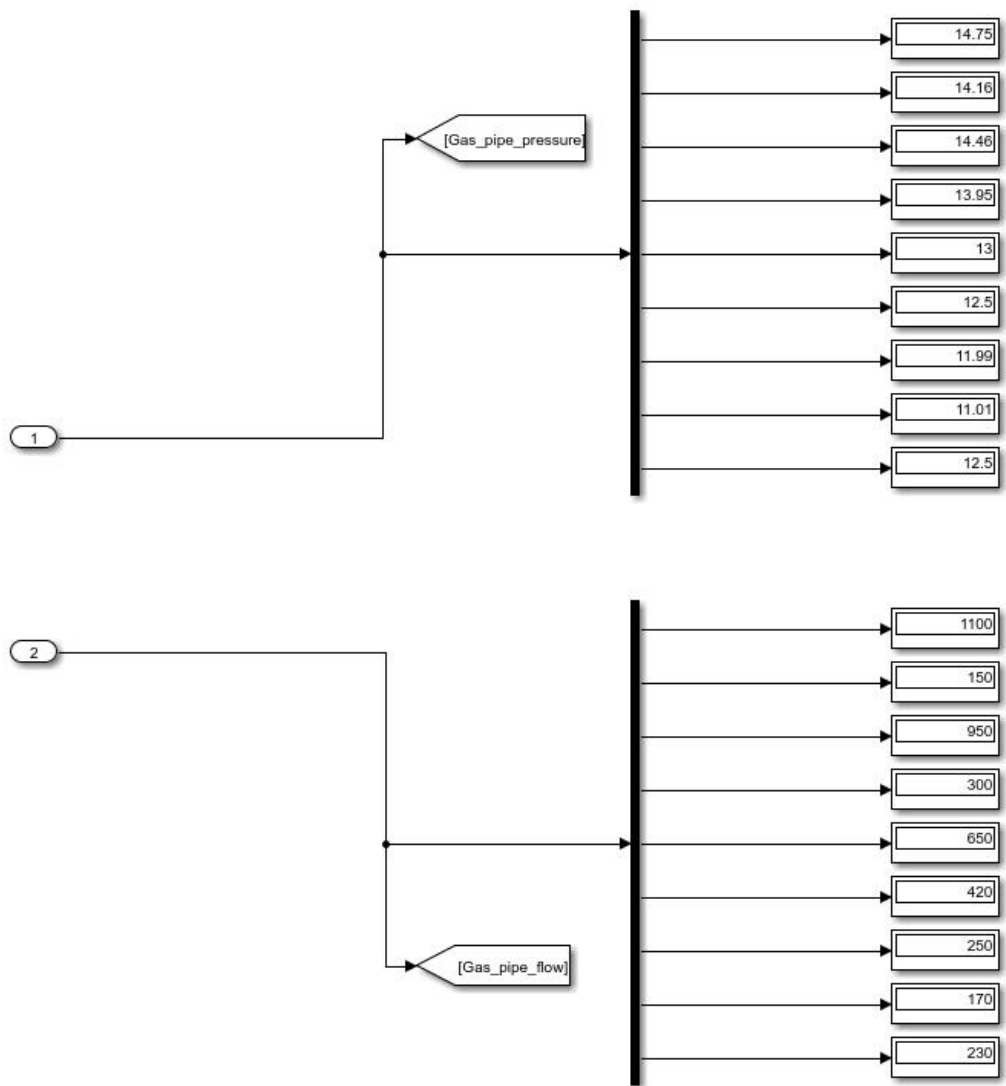


Figure 2.59: The gas load block.

2.5 Summary

This chapter mainly introduces the modeling part of MES components in Simulink. The simulation model of MES is given in Figure 2.60, which is built in 2020b MATLAB/Simulink. The transmission network has chosen IEEE 24 bus system [69], and the distribution network has selected the RBTS bus 5 system [70]. A 13-node heat network [4] and 9-node gas system [71] are chosen for the heat and gas system. The power GUI is discrete, and the sample time is 1e-6s. The wind, GT, battery, PV, and power distribution system are connected to bus 1, 2, 4, 7, 8 in IEEE 24 bus system, respectively. The V2G system has been connected to load point 1 in RBTS bus 5 power distribution system. The heat pump module has been connected with gas turbine output mechanical power. The heat pump high temperature side output have been used to provide heat for residents. The gas system has been connected with bus 5 power in IEEE 24 bus power system. The gas load block shows the 9 gas pipe pressures and gas pipe flows, respectively. The detailed dynamic models introduced above are valuable for understanding the behaviour of each component, and might be aggregated for system dynamic studies. The MCS optimization in chapter 4 needs simpler power-based models that will be covered in chapter 2.

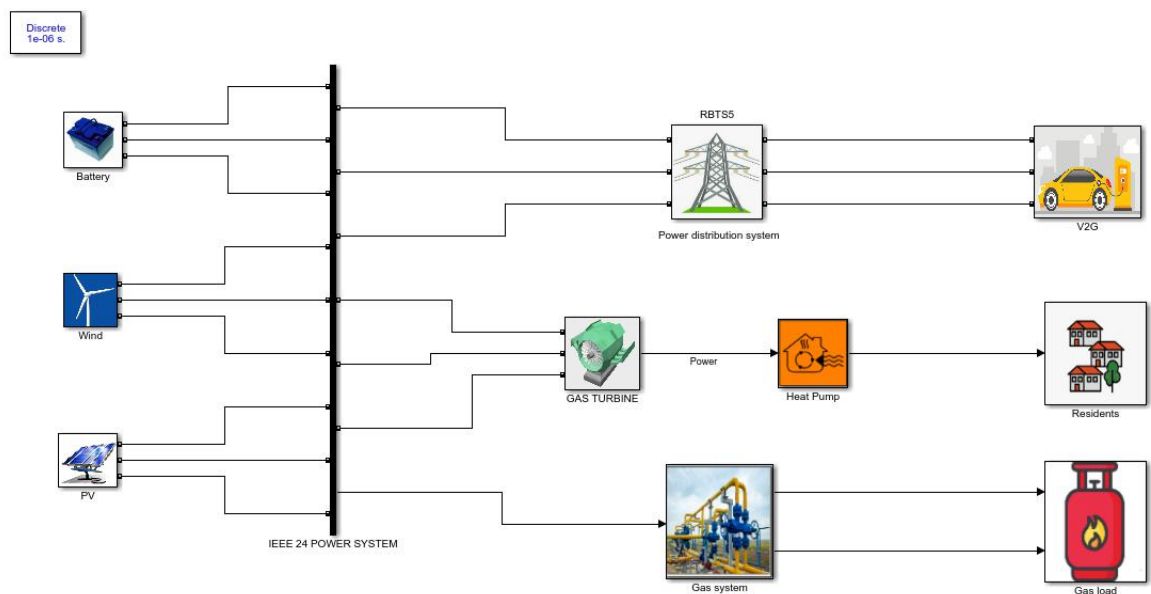


Figure 2.60: The Simulink model of the MES.

Chapter 3

Uncertainty modeling

3.1 Introduction

This chapter mainly introduces uncertainty modeling which includes the stochastic modeling of renewable energy generation and the BP neural network for load forecasting. The power generated by wind and PV often varies with the weather [65]. Therefore, considering the weather uncertainty in PV and wind model is quite essential to improve the overall MES reliability. Stochastic modeling for PV and wind renewable energy is adopted in this project. Moreover, time-varying load forecasting by the error back propagation (BP) [66] neural network is also considered to simulate a realistic operating MES. Compared to the most feed-forward neural network, the BP neural network can achieve training accuracy faster by modifying the weights continuously through the back propagation of errors [67].

3.2 Stochastic modeling of renewable energy generation

3.2.1 Wind power generation

The output of a wind turbine is determined by wind speed, which is represented using the Weibull distribution in this project. The Weibull probability density function is described by the equation below [65]:

$$f(V) = \frac{k}{c} \left(\frac{V}{c}\right)^{k-1} \exp \left[- \left(\frac{V}{c}\right)^k \right], \quad (3.1)$$

where the shape and scale parameters are represented by k and c respectively, and V represents wind speed.

The output power $P_w(t)$ can be calculated based on the sampling wind speed in Equation 3.1. Figure 3.1 shows the variation curve of WT output power.

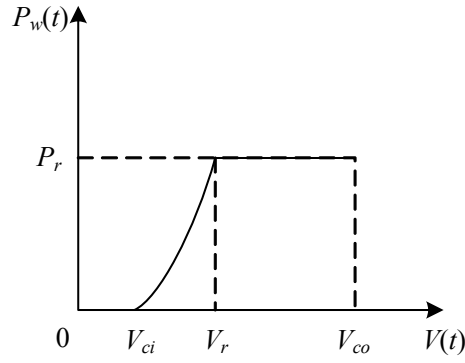


Figure 3.1: Variation curve of wind farm output power with wind speed [65].

The following formula can be used to determine a wind turbine's output power [65]:

$$P_w(t) = \begin{cases} 0 & (V \leq V_{ci} \text{ or } V \geq V_{co}) \\ P_r \frac{V - V_{ci}}{V_r - V_{ci}} & (V_{ci} \leq V \leq V_r), \\ P_r & (V_r \leq V \leq V_{co}) \end{cases} \quad (3.2)$$

where P_r denotes the wind turbine's rated power output, V_{ci} , V_r , and V_{co} denote the cut-in wind speed, rated wind speed, and cut-out wind speed, respectively.

3.2.2 Solar power generation

The Beta distribution is adopted to sample the uncertain solar radiation as follows [65]:

$$f(r) = \frac{\Gamma(\alpha + \beta)}{\Gamma(\alpha) + \Gamma(\beta)} \cdot \left(\frac{r}{r_{max}}\right)^{\alpha-1} \cdot \left(1 - \frac{r}{r_{max}}\right)^{\beta-1}, \quad (3.3)$$

where Γ denotes the gamma function, α and β are the shape parameters of the Beta distribution, and r_{max} and r are the maximal and actual solar radiation value, respectively.

The formulas for α and β are given in [65]. Based on the Beta distribution of solar energy, the output PV power P of the single PV module with a base power 100 MVA can be decided as follows:

$$P = \frac{f(r)r_{max}A\eta}{baseMVA}, \quad (3.4)$$

where A is the area of a single solar panel, η is the rated conversion efficiency of the PV unit.

The Matlab code for wind and PV distribution sample and power generation is shown below:

```

times=24; % daily sample
baseMVA = 100;
% Beta distribution for PV generation
Ppv_samp=zeros(1,times);
% Shape parameters of the Beta distribution
a_pv=0.6869;
b_pv=2.1320;
% Related parameters of pv generation
S_pv=100; % Area
n=0.14; % PV rated conversion efficiency
rmax=700; % maximal solar radiation rmax (MW/m2)
% PV active power output sample
pv_samp(1,:)=betarnd(a_pv,b_pv,1,times);
Ppv_samp(1,:)=pv_samp(1,:)*rmax*S_pv*n/baseMVA;

% shape and scale parameters of Weibull distribution
k_wt=1.5;
c_wt=5;
% Weibull distribution for wind generation
wt_samp =wblrnd(c_wt,k_wt,1,times);
% Related parameters of wind generation
Pr=1000; % Wind turbine's rated power output
vci=3; % cut-in wind speed
vr=13; % rated wind speed
vco=25; % cut-out wind speed

%wind power sample
for i=1:times
    if wt_samp(i)<vci
        Pwt_samp(i)=0;
    end
    if wt_samp(i)>vci&&wt_samp(i)<vr
        Pwt_samp(i)=(wt_samp(i)-vci)/(vr-vci)*Pr;
        if Pwt_samp(i)>Pr
            Pwt_samp(i)=Pr;
        end
    end
    if wt_samp(i)>vr&&wt_samp(i)<vco
        Pwt_samp(i)=Pr;
    end
    if wt_samp(i)>vco
        Pwt_samp(i)=0;
    end
end
End

for i=1:times
Pwt_samp(i)= Pwt_samp(i)/baseMVA ;
End

```

3.3 Time-varying load forecasting

It will be challenging to accurately portray the system reliability level using a single load

level (such as peak load or average load) for system reliability assessment. Therefore, it is of great significance to model and forecast the time-varying load for reliability evaluation of the whole MES. In recent years, artificial intelligence methods have become increasingly popular. Among them, the artificial neural network such as the error back propagation (BP) network [68] has been adopted to implement power generation forecasting or load forecasting. Compared to the most feed-forward neural networks, the BP neural network can achieve training accuracy faster by modifying the weights continuously through the back propagation of errors [67]. Neurons in the same layer do not have any connections, and the whole network can have one or more hidden layers, which can realize complex mapping relations. Due to its simple calculation, strong nonlinear mapping, and good generalization, it is adopted in this project to do load forecasting for the MES. The steps in the BP neural network training procedure are as follows [68]:

1. establish the network structure, initialize the network layer numbers, which include input layer i , hidden layer j , and output layer k , and input the number of neurons and activation function;
2. set the initial values of neural network connection weights w_{ij} , w_{jk} and neuron threshold θ_j , as well as the error minimum E , learning rate η , the largest training time n , while initializing the sample data;
3. the network is built using the input sample and the hidden layer output's actual output. To set the input and output, we pick up the test sample's input and output after selecting the sample. The neural network sequence was realized by MATLAB, and then the prediction accuracy was improved by adjusting the training times, learning rate, and the output layer of the hidden layer, and the test results were validated by test samples. We will get the result if it is reasonable, and continue to adjust in the meantime; Hidden node output:

$$o_j = f \left(\sum_i w_{ij} x_i - \theta_j \right). \quad (3.5)$$

Output node output:

$$y_k = f \left(\sum_j w_{jk} - \theta_k \right). \quad (3.6)$$

4. calculate total error's actual output and expected output:

$$E = \sqrt{\sum_{u=1}^N e_u^2 / N}, \quad (3.7)$$

where N stands for the sample number; e_u stands for the error between the actual output and expected output; u stands for the sample number. We can either discontinue the training or go to Step 5 if the error satisfied the requirements.

5. adjust the network connection weight of each neuron weight repeatedly, and repeat Step 3 to 5 to make E reach the error range.

3.4 Time varying load and cost model

The following equation describes the time-varying load [40]:

$$P_{Load}^t = L_y \times P_w \times P_d \times P_h^t, \quad (3.8)$$

where L_y denotes as annual peak load, P_w denotes the ratio of weekly load to annual peak, P_d denotes the ratio of daily load to weekly peak, P_h^t denotes the ratio of hourly load to daily peak.

In real situations, electricity costs rise with peak demand, and power outage loss costs vary as well [41]. Moreover, the cost of different type of user outage varies based on the load level and duration of the interruption. As a result, in the MES reliability assessment, taking into account a time-varying cost model (TVCM) for seven client sectors is critical [40].

The following formula calculates the time-varying cost weight factors W^t :

$$W^t = \frac{\text{Actual interruption cost at hour } t}{\text{Average interruption cost}}. \quad (3.9)$$

Equation 3.10 calculates the time-varying cost TVC^t at hour t by multiplying the appropriate weighting factor W^t with the average interruption cost (AIC) [40]:

$$TVC^t = W^t \times AIC. \quad (3.10)$$

3.5 Summary

This chapter mainly introduces the uncertainty modeling of renewable generations, which include the wind power generation and solar power generation. The artificial neural network such as the error back propagation (BP) network [68] has been adopted to realize the load forecasting due to its simple calculation, strong nonlinear mapping, and good generalization. The time-varying cost model is also given for calculating the subsequent optimization problem objective function.

Chapter 4

Reliability evaluation of multi-energy system with storage devices

4.1 Introduction

This chapter will introduce the reliability indices used in MES reliability evaluation, which include load-point indices and system-level indices. The reliability assessment approach will also be given in this chapter. Finally, the implementation of sequential Monte Carlo simulation on MES reliability evaluation with storage devices will be presented, taking into account weather uncertainties and time-varying load.

4.2 Reliability indices for MES

The reliability performance of a multi-energy system is typically evaluated using two index groups: load-point reliability indices and system-level reliability indices.

4.2.1 Load-point reliability indices

The average failure rate (λ , times/year), average outage time (U , hours/year), and average repair time (r , hours/time) are the three primary load-point reliability indices in MES. The formulas of these three indices are shown in the following equations [18].

1. Average failure rate λ_p

$$\lambda_p = \frac{f_p}{T_{up}^p}, \quad (4.1)$$

where the number of outages affecting load point p is represented by f_p . T_{up}^p is the operating time of load point p .

2. Average outage time U_p

$$U_p = \frac{T_{dn}^p}{f_p}, \quad (4.2)$$

where T_{dn}^p represents the load point p failure time.

3. Average repair time r_p

$$r_p = \frac{U_p}{\lambda_p}, \quad (4.3)$$

4.2.2 System-level reliability indices

The system-level reliability indices can be calculated using the load-point reliability indices. In this project, some of the frequently used indices were calculated to evaluate multi-energy system reliability.

1. System average interruption frequency index (SAIFI)

The SAIFI is calculated by dividing the total number of interrupted customers by the total number of customers serviced throughout the course of a year or working period [72].

$$SAIFI = \frac{\sum_{i=1}^n \lambda_i N_i}{\sum_{i=1}^n N_i}, \quad (4.4)$$

where λ_i denotes the average failure rate of load point i . The number of customers at load point i is N_i . n denotes the total number of buses.

2. System average interruption duration index (SAIDI)

The SAIDI is calculated by dividing the total outage time by the total number of customers serviced over the course of a year for each customer connected to the system.

$$SAIDI = \frac{\sum_{i=1}^n U_i N_i}{\sum_{i=1}^n N_i}, \quad (4.5)$$

where U_i is the average outage time of load point i .

3. Customer average interruption duration index (CAIDI)

The CAIDI stands for the average total duration of each failure per customer, which equals

to the total outage time divided by the total number of interruptions. It also equals to SAIDI divided by SAIFI.

$$CAIDI = \frac{\sum_{i=1}^n U_i N_i}{\sum_{i=1}^n \lambda_i N_i} = \frac{SAIDI}{SAIFI}, \quad (4.6)$$

4. Average service availability index (ASAI)

The ASAI is calculated by dividing total customer hours by total demand hours over total demand hours in a year.

$$ASAI = 1 - \frac{\sum_{i=1}^n U_i N_i}{8760 \times \sum_{i=1}^n N_i} = \frac{8760 - SAIDI}{SAIDI}, \quad (4.7)$$

5. Expected energy not supplied (EENS)

EENS represents the energy loss for all customers during the failures in one year.

$$EENS = \sum_{i=1}^n U_i L_i. \quad (4.8)$$

4.3 Monte Carlo simulation for reliability assessment

Reliability evaluation is among the most essential ways of assessing the stability of a multi-energy system. There are mainly two commonly used reliability evaluation methods, the analytical method and the simulation method [73]. The analytical method mainly uses mathematical methods to solve specific problems, but usually focuses on the average value of the index, and does not even consider future performance analysis [73]. The Monte Carlo simulation method is a probabilistic based method, which obtains the estimated value of the result by sampling random variables with different distributions, and is often used for risk assessment and uncertainty modeling [33]. It is particularly well suited to some problems that are difficult or impossible to address using analytical approaches due to a large number of random variables. Non-sequential Monte Carlo and sequential Monte Carlo are the two sorts of Monte Carlo simulations. In contrast to the non-sequential approach, the sequential Monte Carlo simulation models system states in chronological order. In this project, the sequential Monte Carlo simulation is chosen reliability evaluation and optimization due do the complex structure and time-varying feature of MES [34].

4.3.1 Sequential Monte Carlo simulation

With the change in the system components' status, the sequential Monte Carlo Simulation method replicates them in chronological order. A random number generator is used to create an artificial history for each component, generating a uniform random number $[0,1]$ for each component in order to give it a sequence of operating-repairing cycles [76]. To simulate the test system, the well-known two-state Markov model presented in Figure 4.1 was employed. The operating condition of the components is represented by the up-state, while the failure state is represented by the down-state. TTF (time to failure) is a term used to describe the up-state, while TTR (time to repair) is used to describe the down-state. The formulas of TTF and TTR are shown below:

$$TTF = -\frac{1}{\lambda} \ln \delta_1, \quad (4.9)$$

$$TTR = -r \ln \delta_2, \quad (4.10)$$

where λ and r represent the component's failure rate and repair time. δ_1 and δ_2 are the random numbers in $[0,1]$.

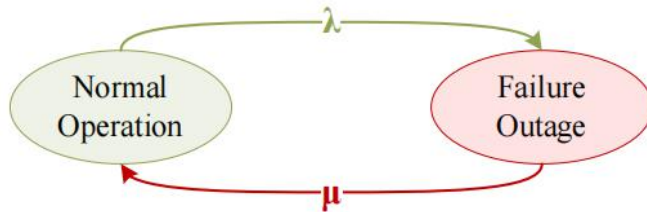


Figure 4.1: The two-state Markov model [4].

TTF and TTR are both random. The failure process, which occurs from up to down, is caused by an unanticipated occurrence that causes the component to fail. Monte Carlo Simulation creates a simulated sequence of component operation and fault history by sampling the up and down states of each component in the feeder at random. This enables general implications about the system's behavior and, in particular, the identification of components that are prone to downtime. The concepts of TTR and TTF for components are depicted in Figure 4.2.

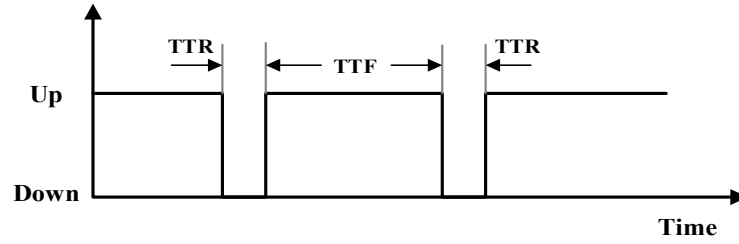


Figure 4.2: The operating and failure time of a component [76].

4.4 Reliability evaluation of MES with storage devices under weather uncertainties

The operation time and failure outage time of all components can be decided using the Markov two-state model in order to assess multi-energy system reliability. The application of sequential Monte Carlo simulation in the assessment of multi-energy system reliability with different energy storage devices considering time-varying cost models and load uncertainties can be presented in the Figure 4.3 flow chart, the following are the specific steps:

1. set the simulation period and input each component's failure rate and repair time, as well as the number of customers in the three energy networks.
2. obtain the load prediction curves using BP neural network. Due to weather uncertainty, Weibull and Beta distribution have been used to sample the daily time-varying wind speed and solar radiation. According to the Equation 3.2 and 3.4, the output power of wind and PV can be calculated. Then, run the power flow to obtain the daily time-series power curve. Finally, the time-series power curve can be used as input for BP neural network to forecast the annual load power curve.
3. for each component in the system, produce a random number and use Equation 4.9 to calculate TTF values.
4. compare the TTF values of all elements to determine the failure event j with the lowest TTF and the position.
5. for the element with the lowest TTF, produce two random numbers and convert them to times to repair (TTR_j) and times to switch (TTS_j).

6. according to the component failure, check the fault component belonging to which energy system.
7. check whether the fault occurs during the day (7 am to 19 pm). If the PV module fails at night, do not accumulate its failure time. If it fails in the daytime, accumulate its failure time.
8. according to the power path, check ① whether the failed event j affect the load point, if yes, accumulate the number of failures, uptime and downtime of the load point; otherwise only accumulate system uptime; ② whether the fault component connected bus install storage device, if yes, check whether the failure load can be provided by an energy storage device via time-series load prediction curves; if yes, the downtime is only the automatic switch's trip time.
9. calculate the duration of failure for load point i [40].

$$r_{ij} = k \times TTS_j + (1 - k) \times TTR_j, \quad (4.11)$$

where k is a control constant; $k=1$ denotes a load point whose service can be restored by switching action, $k=0$ represents failure cannot be repaired.

10. using time-varying load equation 4.12, estimate the load profile for load point i throughout the failure period, and calculate the average load L_{aij} using the following equation [40]:

$$L_{aij} = \frac{\sum_{t=ts}^{t=te} L_{ri}(t)}{te - ts + 1}, \quad (4.12)$$

11. calculate the per unit interruption cost pc_{ij} for load point i using the r_{ij} and the load point customer damage function $f(r_{ij})$ [40].

$$pc_{ij} = f(r_{ij}), \quad (4.13)$$

12. using the time-varying weight factor, calculate the adjusted per-unit interruption cost c_{ij} [40]:

$$c_{ij} = \frac{\sum_{t=t_s}^{t=t_e} W_i^t}{t_e - t_s + 1} \times p c_{ij}, \quad (4.14)$$

13. calculate the energy not supplied ENS_{ij} and the load point i interruption cost $COST_{ij}$ due to the failure event j [40].

$$ENS_{ij} = L_{aij} r_{ij}, \quad (4.15)$$

$$COST_{ij} = c_{ij} L_{aij}, \quad (4.16)$$

14. return to step 3 if the simulation time is less than the simulation year; otherwise, proceed to step 15.

15. calculate λ , r and U .

16. calculate $SAIDI$, $SAIFI$, $CAIDI$, $ASAI$ system-level reliability indices based on load-point reliability indices.

17. calculate the total ENS_i and the interruption cost $COST_i$ of the load point i [40].

$$ENS_i = \sum_{j=1}^{N_s} L_{aij} r_{ij}, \quad (4.17)$$

$$COST_i = \sum_{j=1}^{N_s} c_{ij} L_{aij}, \quad (4.18)$$

where N_s denotes the total number of failure events that occurred during the simulation time. The following equations can be used to determine the expected energy not supply $EENS_i$ and the expected interruption cost $ECOST_i$ [40]:

$$EENS_i = \frac{ENS_i}{TST}, \quad (4.19)$$

$$ECOST_i = \frac{COST_i}{TST}, \quad (4.20)$$

where TST stands for the total specified simulation period in years.

18. calculate the system $EENS$ and $ECOST$.

$$EENS = \sum_{i=1}^n EENS_i, \quad (4.21)$$

$$ECOST = \sum_{i=1}^n ECOST_i. \quad (4.22)$$

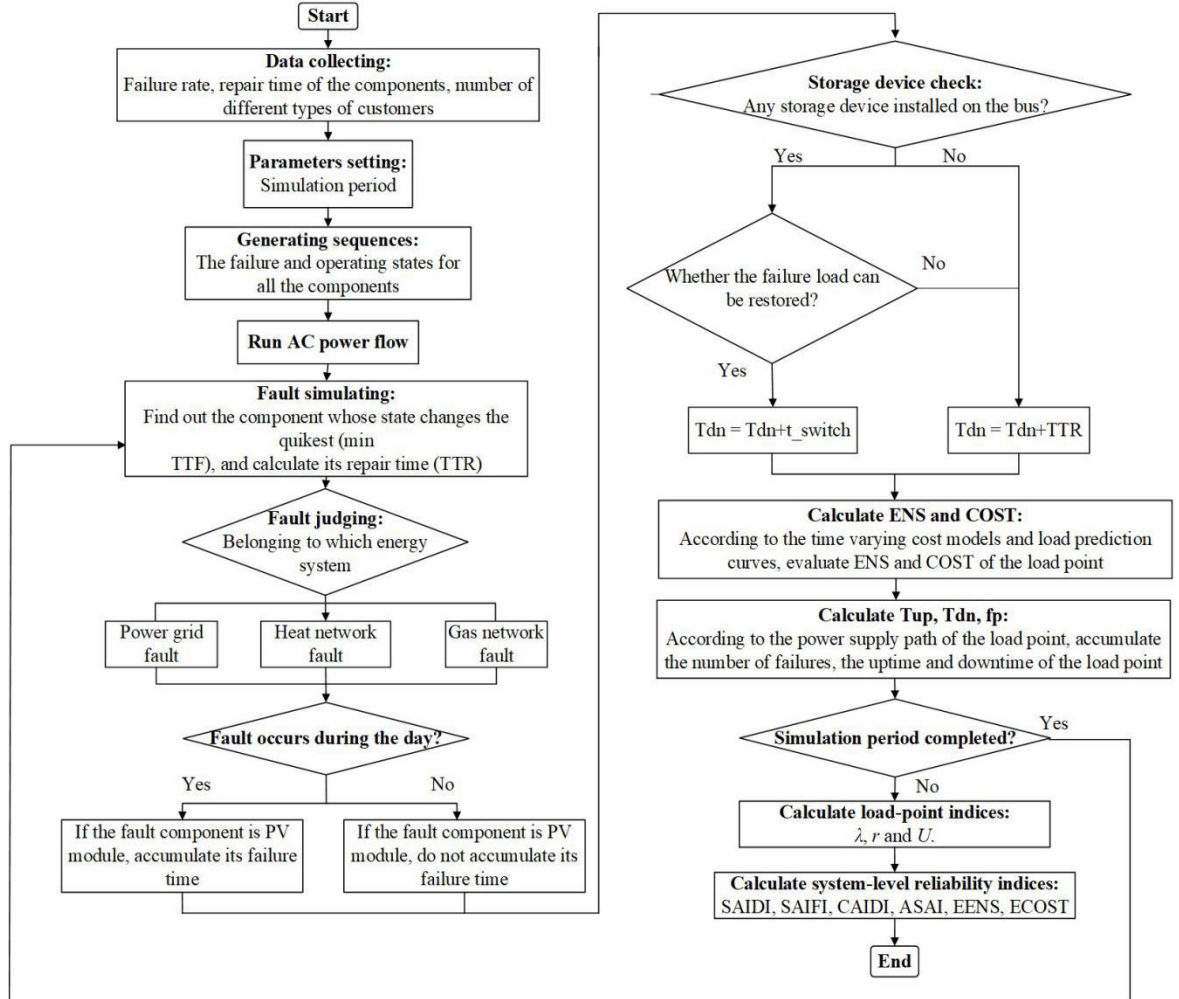


Figure 4.3: The MCS process with storage device under weather uncertainties.

4.5 Summary

The load-point and system-level reliability indices are summarized in this chapter as indications for MES reliability assessment. Monte Carlo simulation is adopted as the MES reliability assessment method. Finally, the application of sequential Monte Carlo simulation in the assessment of multi-energy system reliability with different energy storage devices considering time-varying cost models and weather uncertainties is given. The reliability assessment Matlab code can be found in Appendix A.1.

Chapter 5

Reliability optimization of multi-energy system with storage devices

5.1 Introduction

The reliability optimization problem is presented as a multi-objective problem with the major objectives of determining the ideal storage device position number in MES at the lowest possible cost and the highest reliability under weather uncertainty. Meta-heuristics are adopted to solve the formulated problem. In this study, three widely used multi-objective algorithms are chosen such as NSGA-II, MOPSO, and SPEA2.

5.2 Reliability optimization problem formulation

The multi-objective optimization problem consists of two objective functions based on two performance indicators, i.e. a reliability indicator and an economic indicator. SAIDI reliability index is adopted as the reliability indicator to reflect MES reliability performance. The cost indicator includes both system interruption costs and investment costs. The decision variable is the position of the energy storage device.

5.2.1 Reliability indicator

The following equation describes the calculation of SAIDI [72].

$$SAIDI = \sum_{sy=1}^{SY} \left(\sum_{i=1}^n \frac{U_i N_i}{N_i} \right) / SY, \quad (5.1)$$

where U_i denotes the average annual unavailability of load point i , N_i is the number of customers at load point i , n is the total number of buses, and SY is the total simulation years.

The average outage time U_i determined using the following formula:

$$U_i = \frac{T_{dn}^i}{f_i}, \quad (5.2)$$

where the number of outages affecting load point i is represented by f_i . T_{dn}^i represents the load point i failure time.

The installation of an energy storage device at a load point would directly affect the outage time. If the decision variable (the location of the storage device) is not zero, this means that there is a storage device installed. According to the time series load forecasting curves, if an energy storage device can supply the failure load during a failure event, the number of failures f_i won't be added up, and the system's downtime will just be the automatic switch's trip time. As a result, the relationship between the decision variables and the SAIDI objective function is established.

5.2.2 Economic indicator

The economic indicator of the multi-objective functions is the cost functions, which include the cost of system interruption and the cost of storage device investment. The following equation describes the interruption cost which caused by EENS due to system failure:

$$C_{interrupt} = \sum_{sy=1}^{SY} \left(\sum_{i=1}^n C_{loss}^{i,t} \times EENS_{i,t} \right) / SY, \quad (5.3)$$

where $C_{loss}^{i,t}$ is the outage cost during failure time t at load i , and $EENS_{i,t}$ is expected energy not supplied during failure time t at load i .

The C_{loss} and $EENS$ can be represented as [72]:

$$C_{loss}^{i,t} = \frac{\sum_{t=ts}^{t=te} W_i^t}{te - ts + 1} \times f(r_{ij}), \quad (5.4)$$

$$EENS_{i,t} = L_{aij} r_{ij}, \quad (5.5)$$

$$L_{aij} = \frac{\sum_{t=ts}^{t=te} L_{ri}^t}{te - ts + 1}, \quad (5.6)$$

$$r_{ij} = k \times TTS_j + (1 - k) \times TTR_j, \quad (5.7)$$

where L_{aij} is the average load during failure event j at load point i , L_{ri}^t represents the load demand in the load profile. ts and te represents failure start and end hour, respectively, and t denotes the time step. r_{ij} is defined as the failure duration, TTS_j and TTR_j represent time to switch and time to failure affected by failure event j , respectively. $f(r_{ij})$ is the load point customer damage function. W_i^t denotes the cost weight factor for hour t .

Because storage devices are the only ones we place and utilize to improve and optimise the system's reliability, the investment cost is merely the storage device cost. The investment cost function is given below:

$$C_{investment} = N \times C_{install_i}, \quad (5.8)$$

where N is the total number of the storage devices installed, and $C_{install_i}$ represents the installation cost co-efficient for the storage device i .

5.2.3 Objective function

To discover the best energy storage configuration schemes, the optimization problem is formulated as a non-linear problem. The decision variable is the position of the energy storage device. The following are the two objective functions:

- Objective 1: Minimize the reliability index SAIDI.

The first objective function is as follows:

$$obj_1 = \min(SAIDI). \quad (5.9)$$

- Objective 2: Minimize the total cost.

The second objective function is as follows:

$$obj_2 = \min(Cost) = \min(C_{interrupt} + C_{investment}) \quad (5.10)$$

$$= \min(C_{loss} \times EENS + N \times C_{install_i}).$$

5.2.4 Constraints

(1) Energy balance constraints

The energy balance constraints for the three energy networks are provided in Equations 5.11, 5.12, and 5.13, respectively:

$$P_{gen}^t + P_{GT}^t + P_{CHP}^t + P_{PV}^t + P_{WT}^t + P_{discharging}^t = P_{Load}^t + P_{EV}^t + P_{charging}^t + P_{P2G}^t \quad (5.11)$$

$$H_{GB}^t + H_{CHP}^t + H_{hs, out}^t = H_{Load}^t + H_{hs, in}^t \quad (5.12)$$

$$G_{P2G}^t + G_{gs, out}^t = G_{Load}^t + G_{gs, in}^t + G_{GB}^t + G_{CHP}^t \quad (5.13)$$

(2) Energy storage devices constraints

ES (Equations 5.14-5.15), HS (Equations 5.16-5.17), and GS (Equations 5.18) have charging and discharging powers that are limited by their minimum and maximum values. Equations 5.19-5.20 describe the energy balance relationship between flow-in and flow-out energy in HS and GS. Equations 5.21, 5.22, 5.23 describe the energy limit at hour t of ES, HS and GS:

$$0 \leq P_{charging}^t \leq P_{charging}^{max} \quad (5.14)$$

$$0 \leq P_{discharging}^t \leq P_{discharging}^{max} \quad (5.15)$$

$$0 \leq H_{hs, in}^{i,t} \leq \lambda_{i,t} \times H_{hs, in}^{i,max}, \lambda_{i,t} \in \{0, 1\}, \quad (5.16)$$

$$0 \leq H_{hs, out}^{i,t} \leq (1 - \lambda_{i,t}) \times H_{hs, out}^{i,max}, \lambda_{i,t} \in \{0, 1\}, \quad (5.17)$$

$$0 \leq G_{gs, in}^{y,t} \leq G_{gs, in}^{y,max}, 0 \leq G_{gs, out}^{y,t} \leq G_{gs, out}^{y,max} \quad (5.18)$$

$$\sum H_{hs, in}^{i,t} = \sum H_{hs, out}^{i,t} \quad (5.19)$$

$$\sum G_{gs, in}^{y,t} = \sum G_{gs, out}^{y,t} \quad (5.20)$$

$$0 \leq E_p^t \leq E_p^{max}, \quad (5.21)$$

$$0 \leq H_{hs}^{i,t} \leq H_{hs}^{i,max}, \quad (5.22)$$

$$0 \leq G_{gs}^{y,t} \leq G_{gs}^{y,max}, \quad (5.23)$$

where E_p^t represents the electricity of ES at hour t , and E_p^{max} is the capacity of ES.

(3) PV and wind turbine constraints

The PV and wind turbine power cannot exceed the capacity, which are given in Equations 5.24-5.25, respectively:

$$0 \leq P_{PV}^t \leq P_{PV}^{max}, \quad (5.24)$$

$$P_{WT}^{min} \leq P_{WT}^t \leq P_{WT}^{max}. \quad (5.25)$$

5.2.5 Normalization of objective functions

Different evaluation indicators typically have different dimensions and dimensional units, affecting data analysis outcomes. Normalization is necessary to tackle the problem of objective function comparability by eliminating the dimensional impact between objective functions. All indices are in the same order of magnitude when the original data is normalized, allowing for thorough comparison and analysis.

In order to find the maximum and minimum values of each objective function, single optimization for each objective function (Equations 5.9 and 5.10) is needed. For example, using the single objective optimization algorithm PSO or GA to obtain the maximum and minimum fitness value. The single optimization process would provide one optimal value, in contrast to multi-objective optimization, which has several sets of optimal values along the Pareto front. After then, each objective function will be bound by 0-1 after normalization [77] in the following equation:

$$0 \leq \frac{obj_1 - \min obj_1}{\max obj_1 - \min obj_1} \leq 1, \quad (5.26)$$

$$0 \leq \frac{obj_2 - \min obj_2}{\max obj_2 - \min obj_2} \leq 1. \quad (5.27)$$

5.2.6 Problem formulation

Thus, the multi-objective reliability optimization problem can be expressed as:

$$\min[SAIDI, C_{interrupt} + C_{investment}]. \quad (5.28)$$

Subject to: Equations 5.11-5.25.

5.3 Multi-objective optimization algorithms

In general, deterministic methods (also known as analytical methods) and probability-based approaches are the two types of optimization algorithms. The analytical approaches in which the solution strategy is guided by well-defined principles and does not include any random elements. The probability-based approach, whose evolution is based on random decisions during the evolution process. In this project, the optimization problem is tremendously complex and non-convex, with a large number of variables and strongly coupled subsystems. Moreover, the objective functions are calculated through MCS by random sampling from the random variables. The weather uncertainty modeling also considered, which uses the Weibull distribution to model uncertain winds and Beta distribution to model uncertain PV. Therefore, the meta-heuristic methods are a viable choice as these methods can guarantee to reach the global optimum through population-based search.

NSGA-II, MOPSO, and SPEA2 appear to be the most frequently utilized Pareto-based MOEA (multi-objective evolutionary algorithm). The main principle of NSGA-II [35] is the fast non-dominated sorting, which can rank all the particles and preserve the elite solution. The principle of SPEA2 [36] is similar to that of NSGA2. It also adopts non-dominated sorting but adds clustering analysis to prune the non-inferior solution set. MOPSO [37] calculates the fitness values to obtain the optimal solution by constantly updating the particle's velocity and position. The principle and process are relatively simple compared to NSGA-II and SPEA2. Due to their different characteristics, the three algorithms are adopted in this project to demonstrate and compare the effectiveness of the generated outcomes.

5.3.1 NSGA-II

NSGA-II is an enhanced version of NSGA [35], which was firstly introduced by Deb, Pratap, Agarwal, and Meyarivan. The improved NSGA-II method successfully addressed the obvious criticisms such as high computational complexity of non-dominated sorting,

lack of elitism, and the necessity to manually set the sharing parameter [78], which is currently one of the most prevalent MOEAs (multi-objective evolution algorithms).

Non-dominated sorting, elite preserving operator, crowding distance, and selection operator are the four main principles of NSGA-II [79].

a. Non-dominated sorting

The principle of Pareto dominance is used in the non-dominated sorting. Non-dominant sorting assigns the first rank to the non-dominant member of the original population and then removes it from the population. After that, this process continues to sort the residual individuals of the population in a non-dominant way. The non-dominated individuals in the residual population are allocated the second rank and placed on the second front. This procedure will continue until all members of the population have been assigned to different fronts based on their ranks [79]. (see Figure 5.1 (a))

b. Elite preserving operator

The elite-preserving technique maintains elite solutions in a population by passing them down through the generations until a new solution emerges.

c. Crowding distance

The crowding distance can measure the number of solutions surrounding a particular solution [79]. By comparing two different crowded distance solutions, it is concluded that the solution with a larger crowded distance exists in the less crowded region. The crowding distance for the i^{th} solution is the average length of one side of the cube, which can be calculated using the formula below:

$$cd(i) = \sum_{j=1}^k \frac{f_j^{i+1} - f_j^{i-1}}{f_j^{max} - f_j^{min}}, \quad (5.29)$$

where k is the number of objective functions, i is the number of individuals, f_j^i is the objective function value, the maximum and minimum values of the j^{th} objective function among all people are represented by f_j^{max} and f_j^{min} , respectively. Figure 5.1 (b) shows the mechanism of crowding distance.

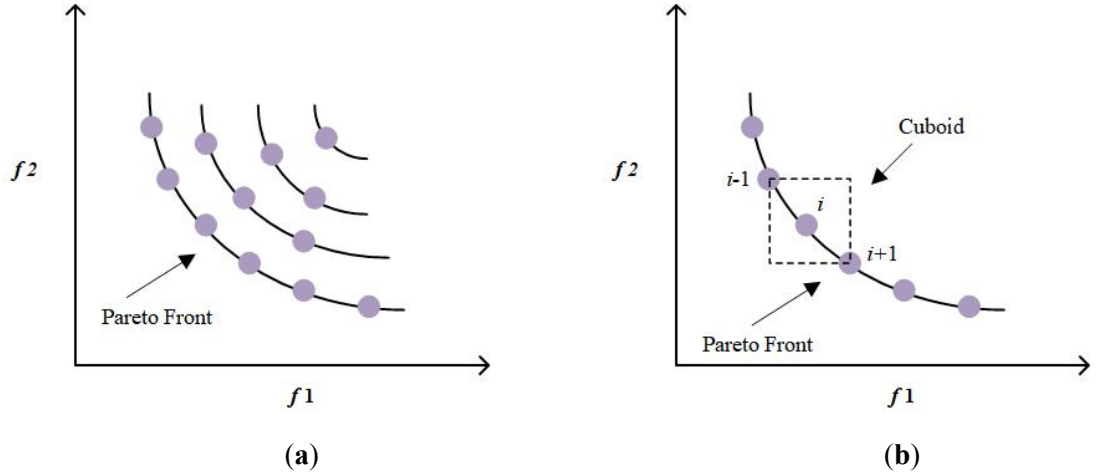


Figure 5.1: (a) Non-dominated sorting procedure; (b) Crowding distance calculation [79].

d. Selection operator

The population for the following generation is chosen using a crowded tournament selection operator. The population members' rank and crowding distances are used to make the decision. The following principles should be considered during the choosing process:

- (1) if two populations have members of differing ranks, the population with the better rank is chosen as the next generation;
- (2) when two population members are of equal rank, the one with the greatest crowding distance is chosen to be the next generation.

The process of the NSGA-II algorithm for reliability optimization is shown below [80].

Step 1: Set NSGA-II parameters: population size (N_{pop}) = 50, archive size ($N_{archive}$) = 50, mutation rate (u) = 0.02, crossover parameter (γ) = 0.7, maximum number of iterations ($MaxIt$) = 200.

Step 2: Set the search variables' dimensions: lower and upper bound of decision variables: (1) the number of electricity storage devices should be in the interval [0, 24] for MES 1 and [0, 39] for MES 2; (2) the number of heat storage devices should be in the interval [0, 13] for MES 1 and [0, 32] for MES 2; (3) the number of gas storage devices should be in the interval [0, 9] for MES 1 and [0, 20] for MES 2.

Step 3: **Non-dominated sorting:** sorting procedure based on non-dominance criteria.

Step 4: **Crowding distance calculation:** when the sorting process is complete, the crowding distance value is allocated forward. Individuals are selected from the population depending on their rank and the crowding distance.

Step 5: **Selection:** individuals are selected based on a binary tournament selection method with a crowded-comparison operator.

Step 6: **Recombination and selection:** individuals from the next generation are selected from the descendant population and the current generation population. After each front fills a new generation, the simulation is stopped when the population size exceeds the existing population size.

Based on the principle of NSGA-II, the reliability optimization code using NSGA-II algorithm can be found in Appendix A.2.

5.3.2 SPEA2

SPEA2 was developed by Professor Eckart et al. [81], which is based on the theoretical support of SPEA. There are four primary characteristics of SPEA2: (1) the external stores the non-dominated solution in a consistently updating population, (2) the quantity of external non-dominated individuals that dominate an individual's fitness is utilized to measure their fitness, (3) the Pareto dominance relationship is adopted to preserve population variety, and (4) the non-dominated set is minimized while its attributes are preserved by using clustering technique [81].

Assume the number of population P is N , and the number of archive set Q is M . The algorithm execution process is as follows:

Step 1: **Initialize:** produces the initial population P as well as an empty external non-dominated P' .

Step 2: **Copy and remove:** remove the member of P' that has been covered in P , and dominating members of P should be copied to P' .

Step 3: **Clustering:** P' should be pruned using clustering if the number of non-dominated

solutions stored externally exceeds a defined maximum N' .

Step 4: **Calculate:** calculate each individual's fitness value both in P and P'.

Step 5: **Select:** select individuals from P+ P'.

Step 6: **Apply:** apply problem-specific crossover and mutation operators.

Step 7: Stop when reached the maximum number of generations; otherwise, proceed to step 2.

Based on the principle of SPEA2, the reliability optimization code using SPEA2 algorithm can be found in Appendix A.3.

5.3.3 MOPSO

MOPSO was first developed by Professor Coello et al in 2004 [37]. It can find out the local and global optimal solutions from the external repository set and guide the particle to address the multi-objective optimization problems by evolving the population of the optimal solutions.

Suppose that in a D-dimensional search space, the following Equations 5.29 and 5.30 give the position and velocity vector of each particle:

$$x_i(t) = [x_{i,1}(t), x_{i,2}(t), \dots, x_{i,D}(t)], \quad (5.30)$$

$$v_i(t) = [v_{i,1}(t), v_{i,2}(t), \dots, v_{i,D}(t)], \quad (5.31)$$

where $x_{i,D}(t)$ and $v_{i,D}(t)$ are the position and velocity of the particle i in the D-dimensional space in the t^{th} iteration, respectively.

Equations 5.31 and 5.32 give the history and global optimal solution:

$$pbest_i(t) = [p_{i,1}(t), p_{i,2}(t), \dots, p_{i,D}(t)], \quad (5.32)$$

$$gbest(t) = [g_1(t), g_2(t), \dots, g_D(t)], \quad (5.33)$$

In the $(t + 1)^{th}$ iteration, the vector of the i^{th} particle is shown as follows:

$$v_i(t+1) = \omega(t) \cdot v_i(t) + c_1 \cdot rand_1 \cdot (pbest_i(t) - x_i(t)) + c_2 \cdot rand_2 \cdot (gbest(t) - x_i(t)), \quad (5.34)$$

$$x_i(t+1) = x_i(t) + v_i(t+1), \quad (5.35)$$

where w is the weighting factor, c_1 and c_2 are the acceleration factors, $rand_1$ and $rand_2$ are the random numbers in the interval $[0,1]$.

MOPSO was obtained by adding Pareto domination and the external repository in PSO. The newly added set of external repositories in MOPSO can store the optimal solutions obtained during iterations and select the global optimal position from the external repository for the current iterations. The algorithm execution process is as follows:

Step 1: input the parameters of MOPSO, the number of iterations, the number of population (POP) and the number of external repository (REP);

Step 2: initialize $x_i(0)$, $v_i(0)$;

Step 3: evaluate each particle in POP , store non-dominated particles in the repository (REP);

Step 4: set the initial position as $pbest_i(0)$, select $gbest(0)$ from the repository;

Step 5: update each particle's velocity and position;

$$v_i(t+1) = \omega(t) \cdot v_i(t) + c_1 \cdot rand_1 \cdot (pbest_i(t) - x_i(t)) + c_2 \cdot rand_2 \cdot (gbest(t) - x_i(t)), \quad (5.36)$$

$$x_i(t+1) = x_i(t) + v_i(t+1), \quad (5.37)$$

Step 6: keep the particles in the search space to prevent them from crossing the boundary.

If the decision variable exceeds its bounds, we do two things: first, we take the value of its associated border, and second, we multiply its velocity by -1 to search in the opposite direction.

Step 7: evaluate each particle in POP while updating the contents of the REP . This upgrade involves adding all of the currently uncontrolled sites to the repository. During the process, any dominating locations from the repository are removed. Because the repository's capacity is restricted, we use a secondary criterion for retention when it

fills up.

Step 8: update the particle's position if it is better than the position stored in its memory:

$$pbest(i) = POP(i), \quad (5.38)$$

Step 9: return to step 5 if the current iteration is less than the maximum iterations.

Otherwise, save the results as the simulation's outcomes and end.

Based on the principle of MOPSO, the reliability optimization code using MOPSO algorithm can be found in Appendix A.4.

5.4 Reliability optimization process

The common feature of these three algorithms is non-dominated ordering. Assuming that any two solutions of S1 and S2, S1 are superior to S2 all the time, S1 is said to dominate S2. If the solution of S1 is not dominated by any other solutions, S1 is said to be the non-dominated solution, also known as the Pareto solution [82]. When the algorithm is executed a certain number of times, we need to consider the stop criterion, this project uses the adaptive stop criterion (also known as the stagnation criterion). The algorithm terminates once the objective function converges to the optimal value and does not change after a certain number of iterations [83].

Figure 5.2 depicts the optimization process for all three techniques, with the following optimization steps:

Step 1: initialize all the variables.

Step 2: Monte Carlo simulation is used to examine the objective functions, and the non-dominated solutions are saved in the repository.

Step 3: update the non-dominated solution.

Step 4: terminate if the adaptive stop criterion has been satisfied; otherwise, go to step 2.

Step 5: obtain the optimal solutions.

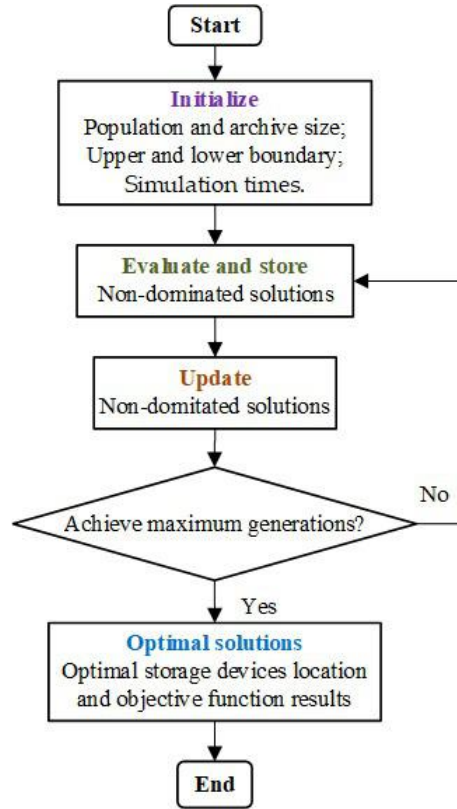


Figure 5.2: The reliability optimization flow chart.

5.5 Summary

This chapter primarily introduces the reliability optimization problem formulation, which is a multi-objective problem aimed at selecting the optimal placement of the storage device in the power grid, heat network, and gas network at the lowest possible cost and highest reliability under weather uncertainty. Meta-heuristics such as NSGA-II, MOPSO, and SPEA2 are adopted to address the optimization problem and make a contrast of the reliability optimization results. Case studies are carried out to demonstrate the feasibility of the suggested technique on two different MES layouts with increasing complexity in the following Chapter 6.

Chapter 6

Case studies for reliability evaluation and optimization in MES

6.1 Introduction

Case studies are developed to exemplify the technique's applicability. Multi-objective algorithms such as NSGA-II, MOPSO, and SPEA2 are employed to solve the outlined reliability optimization problem mentioned in Chapter 5. Two different MES layouts with increasing complexity are used. The first MES contains an IEEE 24 bus system [69], a 13-node heat network [4], and a 9-node gas network [71]. The second MES contains an IEEE 39 bus system [84], a 32-node heat network [85], and a 9-node gas network [86]. The first MES includes stochastic WT and PV elements, however, the second MES has conventional components, and is used to test the optimization algorithms. The sensitivity analysis is also introduced to reflect the change degree and trend of system reliability caused by the small change in component parameters.

6.2 Simulation parameters

Case studies are performed with MATLAB 2020b on a PC with an Intel® Core™ i5-7200 2.5 GHz CPU and 8 GB RAM. To receive reliable outcomes, the simulation time for the MCS reliability evaluation is set to 20 years with a one-hour time step and 100 MCS runs per iteration. Tables 6.1 and 6.2 show the parameters for the Weibull and Beta distributions in wind and PV uncertainty modeling, respectively [65].

Table 6.1. Weibull distribution parameters.

Weibull distribution parameters	k	c (m/s)	V_{ci} (m/s)	V_r (m/s)	V_{co} (m/s)	P_r (MW)
Value	1.5	5	3	13	25	1000

Table 6.2. Beta distribution parameters.

Beta distribution parameters	α	β	A (m ²)	r_{max} (MW/m ²)	η	baseMVA
Value	0.6869	2.132	100	700	0.14	100

Figure 6.1 depicts the probability distributions for wind speed and solar radiation.

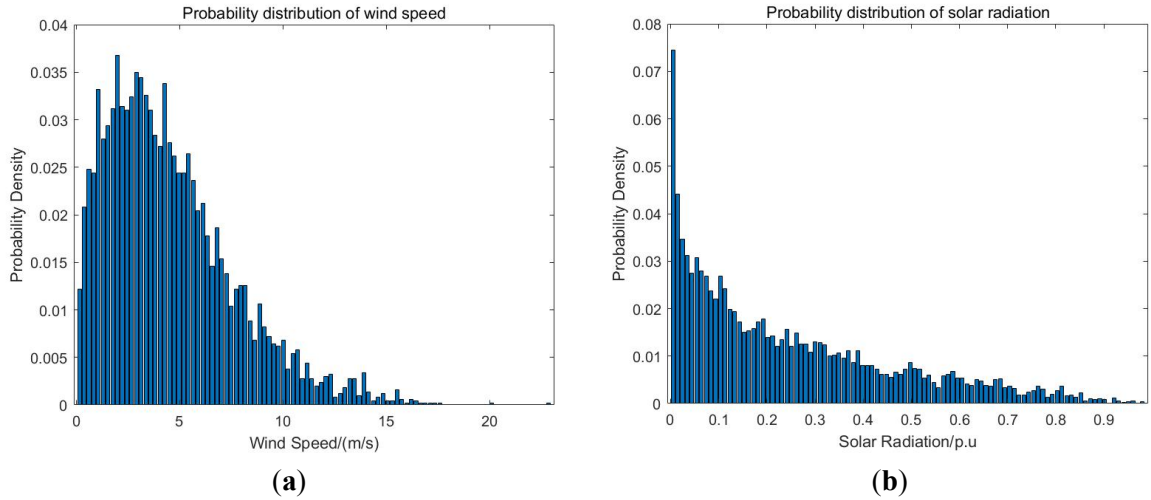


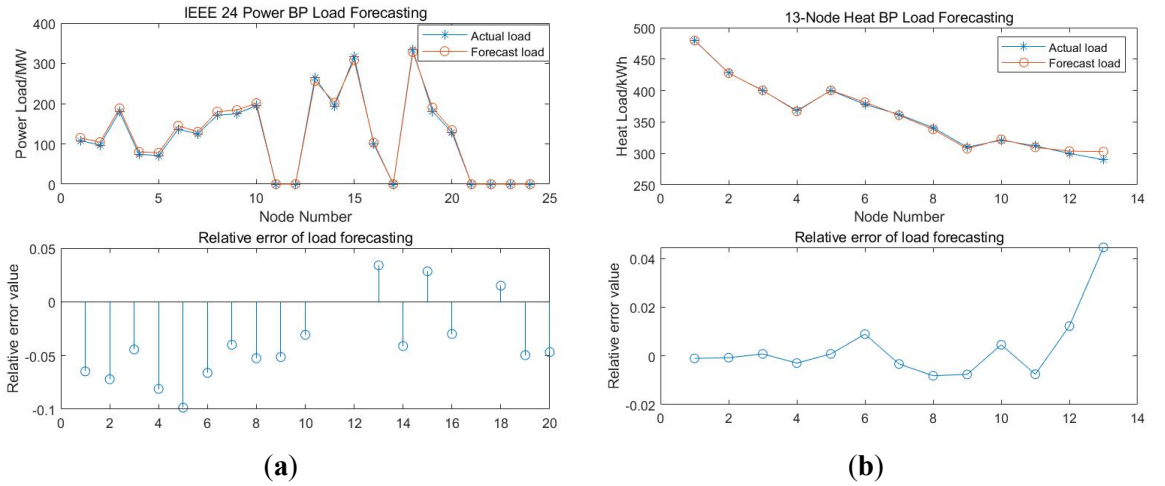
Figure 6.1: (a) Weibull distribution of wind speed; (b) Beta distribution of solar radiation.

BP neural network parameter setting are given in Table 6.3 [87].

Table 6.3: BP neural network parameters.

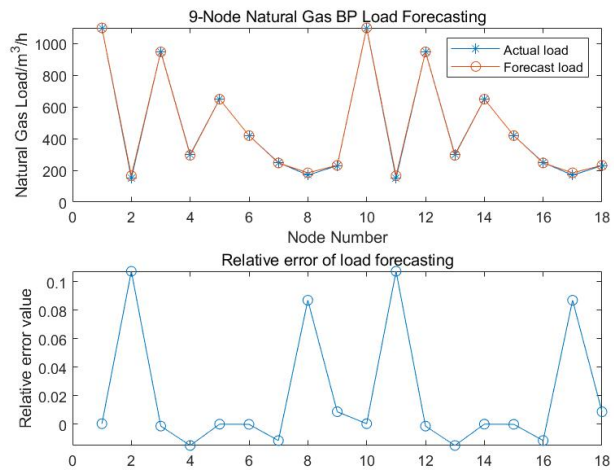
BP neural network	Parameters setting
Number of network layers	Input layer: 1; Hidden layer: 1; Output layer: 1
Number of neurons in each layer	Input layer: 4; Hidden layer: 9; Output layer: 1
Maximum number of iterations	5000
Training target error	0.1=10%
Initial value of training learning rate	0.1=10%

The daily load forecast results for the IEEE 24 power bus system, 13-node heat system, and 9-node natural gas system in MES 1 are presented in the following Figure 6.2. The daily load forecast results for the IEEE 39 power bus system, 32-node heat system, and 20-node natural gas system in MES 2 are given in the following Figure 6.3. The training results reveal that all loads have a relative error of less than 0.2, indicating that the training aim was fulfilled. In the IEEE 24 power system, the maximum absolute error is 0.1, 0.04 in the 13-node heat network, and 0.11 in the 9-node natural gas network. In the IEEE 39 power system, the highest absolute error is 0.01; in the 32-node heat network, it is 0.004; and in the 20-node natural gas network, it is 0.13. The daily load forecast result shown in the following figures is a sample of the annual load curves. The MCS reliability evaluation is set to 20 years with a one-hour time step and 100 MCS runs per iteration.



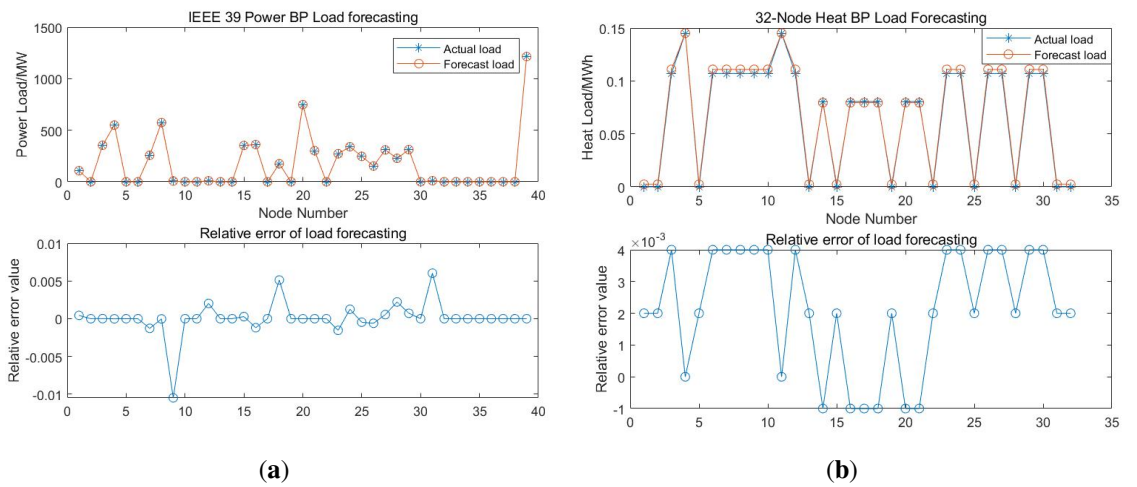
(a)

(b)



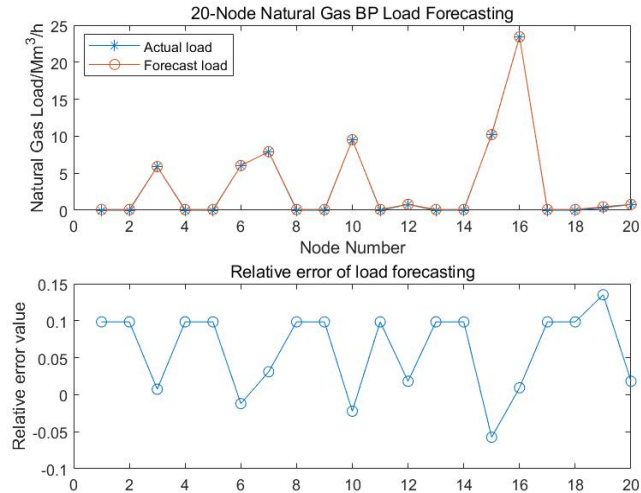
(c)

Figure 6.2: BP neural network training performance for MES 1: (a) 24-node power load forecasting; (b) 13-node heat load forecasting; (c) 9-node gas load forecasting.



(a)

(b)



(c)

Figure 6.3: BP neural network training performance for MES 2: (a) 39-node power load forecasting; (b) 32-node heat load forecasting; (c) 20-node gas load forecasting.

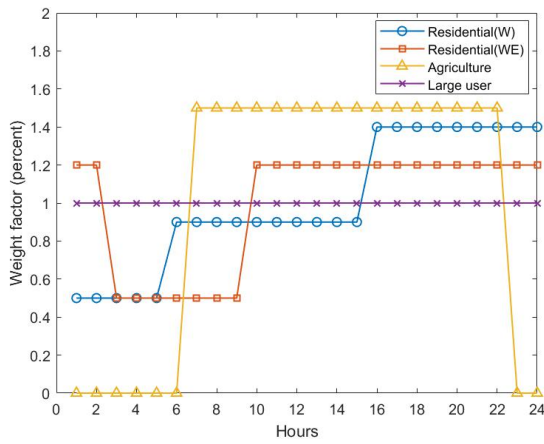
Parameter Settings for reliability assessment of multi-energy systems using Monte Carlo simulation can be found in [4]. Table 6.4 also provides the reliability failure rate and repair time reliability data of all the components [4]. Table 6.5 provides the interruption cost model data for seven types of customers [40]. Figure 6.4 gives the time-varying cost weight factors for seven types of customers on both weekdays (W) and weekends (WE). Table 6.6 indicates the installation costs for various types of storage devices. Table 6.7 provides the capabilities of PV, WT, and GT.

Table 6.4: The failure rate and repair time of the components in MES [4].

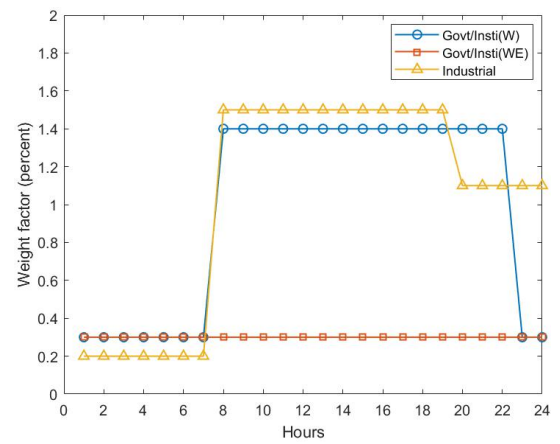
Component	Failure rate (occ./yr)	Repair time (h)
PV	0.400	20
Wind turbine	0.400	20
Gas turbine	0.120	75
Transformer	0.020	768
Power to gas unit	0.030	200
Combined heat and power unit	0.030	200
Heat pump	0.065	50
Gas boiler	0.025	300
Electricity storage device	0.050	50
Natural gas storage device	0.050	50
Heat storage device	0.050	50
Transmission line (per km)	0.065	5
Natural gas pipeline (per km)	0.065	8
Heat pipeline (per km)	0.065	10

Table 6.5: Sector interruption cost (\$/kW) [40].

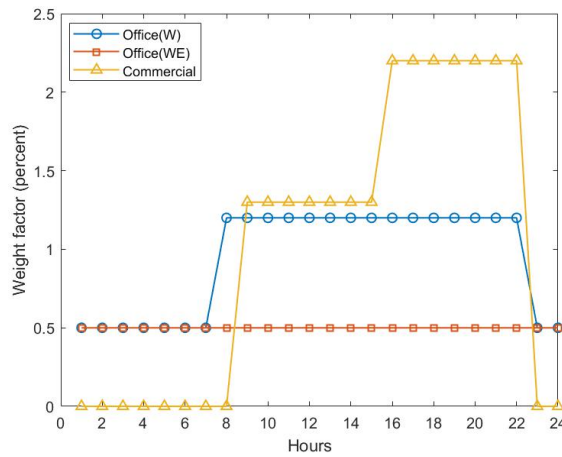
User sector	Interruption duration (min) & cost (\$/kW)				
	1 min	20 min	60 min	240 min	480 min
Large user	1.005	1.508	2.225	3.968	8.240
Industrial	1.625	3.868	9.085	25.16	55.81
Commercial	0.381	2.969	8.552	31.32	83.01
Agriculture	0.060	0.343	0.649	2.064	4.120
Residential	0.001	0.093	0.482	4.914	15.69
Govt.&Inst.	0.044	0.369	1.492	6.558	26.04
Office	4.778	9.878	21.06	68.83	119.2



(a)



(b)



(c)

Figure 6.4: Time-varying cost weight factors: (a) For residential, agriculture and large user customers; (b) For Govt/Inst and industrial customers; (c) For office and Commercial customers [40].

Table 6.6: The installation cost coefficient and capacity for storage devices.

Component	$C_{install_i}$	Capacity for MES 1	Capacity for MES 2
ES	187 \$/MWh	300 MWh	600 MWh
HS	6.05 \$/MWh	0.5 MWh	0.5 MWh
GS	3.665 \$/MMBtu	500 m^3	10 Mm^3

Table 6.7: The capacity of PV, WT, and GT.

Component	Capacity (MW)
PV	100
WT	500
GT	120

The first MES contains an IEEE 24 bus system [69], a 13-node heat network [4], and a 9-node gas network [71]. The IEEE 24 bus system consists of 24 busbars connected by 38 lines and 5 transformers. The transmission lines are at two voltage levels, 138 kV and 230 kV, with 230/138 kV transformer substations at buses 11, 12, and 24. The line length and forced outage rate data are given in Table 6.8 [69]. This IEEE 24 bus system consists of ten generators. The generating unit location and its reliability data are given in Table 6.9 and 6.10, respectively [69]. The power system has 17 load points with seven different customer types. There are seven customer types, which represent by “1-Industrial”, “2-Agriculture”, “3-Large user”, “4-Commercial”, “5-Government”, “6-Office”, “7-Residential”. The load power and customer data are shown in Table 6.11 [69].

Table 6.8: IEEE 24 bus system transmission line length and forced outage rate [69].

From Bus	To Bus	Length miles	Outage rate (1/yr)	Outage duration (h)
1	2	3	0.24	16
1	3	55	0.51	10
1	5	22	0.33	10
2	6	33	0.48	10
3	9	50	0.38	10
3	24	31	0.02	768
2	4	0	0.39	10
4	9	27	0.36	10
5	10	23	0.34	10
6	10	16	0.33	35
7	8	16	0.30	10
8	9	43	0.44	10
8	10	43	0.44	10
9	11	0	0.02	768
9	12	0	0.02	768
10	11	0	0.02	768
10	12	0	0.02	768
11	13	33	0.40	11
11	14	29	0.39	11
12	13	33	0.40	11

Table 6.8 (continue): IEEE 24 bus system transmission line length and forced outage rate [69].

From Bus	To Bus	Length miles	Outage rate (1/yr)	Outage duration (h)
12	23	67	0.52	11
13	23	60	0.49	11
14	16	27	0.38	11
15	16	12	0.33	11
15	21	34	0.41	11
15	21	34	0.41	11
15	24	36	0.41	11
16	17	18	0.35	11
16	19	16	0.34	11
17	18	10	0.32	11
17	22	73	0.54	11
18	21	18	0.35	11
18	21	18	0.35	11
19	20	27.5	0.38	11
19	20	27.5	0.38	11
20	23	15	0.34	11
20	23	15	0.34	11
21	22	47	0.45	11

Table 6.9: IEEE 24 bus system generator locations [69].

Bus	Unit 1 MW	Unit 2 MW	Unit 3 MW	Unit 4 MW	Unit 5 MW	Unit 6 MW
1	20	20	76	76		
2	20	20	76	76		
7	100	100	100			
13	197	197	197			
15	12	12	12	12	12	155
16	155					
18	400					
21	400					
22	50	50	50	50	50	50
23	155	155	350			

Table 6.10: IEEE 24 bus system generating unit reliability data [69].

Unit size MW	Number of units	Forced outage rate (1/yr)	MTTF (h)	MTTR (h)	Scheduled maintenance (wks/year)
12	5	0.02	2940	60	2
20	4	0.10	450	50	2
50	6	0.01	1980	20	2
76	4	0.02	1960	40	3
100	3	0.04	1200	50	3
155	4	0.04	960	40	4
197	3	0.05	950	50	4
350	1	0.08	1150	100	5
400	2	0.12	1100	150	6

Table 6.11: IEEE 24 bus system load and customer data [69].

Load points	Average load level (MW)	Customer Type	Number of customers
1	108	3	67
2	97	1	134
3	180	2	200
4	74	4	68
5	71	5	57
6	136	6	114
7	125	1	150
8	171	7	218
9	175	2	197
10	195	1	210
13	265	7	337
14	194	7	216
15	317	6	335
16	100	6	158
18	333	3	189
19	181	7	278
20	128	7	189

The 13-node heat network [4] for MES 1 consists of 13 loads connected by 12 lines. Each heat pipe length is 200m. The load and customer data is given in Table 6.12 [4].

Table 6.12: 13-node heat network load and customer data [4].

Load points	Average load level (MW)	Customer Type	Number of customers
1	4.82	1	118
2	4.99	3	78
3	4.31	4	219
4	2.98	5	98
5	4.64	6	176
6	4.31	7	248
7	3.02	2	75
8	3.21	6	132
9	2.98	7	112
10	3.47	4	129
11	3.19	7	56
12	2.98	7	42
13	2.98	7	45

The 9-node gas network [71] for MES 1 consists of 5 loads connected by 9 lines. The gas pipeline length data is given in Table 6.13 [4]. Table 6.14 gives the load and customer data for 9-node gas network [4].

Table 6.13: 9-node gas network pipe length [71].

Line No.	Pipe length (m)
1	100
2	50
3	150
4	80
5	200
6	150
7	100
8	80
9	120

Table 6.14: 9-node gas network load and customer data [71].

Load points	Average load level (m^3/h)	Customer Type	Number of customers
2	150	2	45
4	200	4	35
7	250	7	32
8	170	7	17
9	230	7	26

The second MES contains an IEEE 39 bus system [84], a 32-node heat network [85], and a 9-node gas network [86]. The IEEE 39 bus system consists of 21 load points connected by 46 lines and 12 transformers. There are mainly two transformer types, which are 345kV/22kV and 345kV/230kV. The line length data is given in Table 6.15 [84]. Table 6.16 gives the load and customer data for the 32-node heat network [84]. This system has 10 generators, and the data is shown in Table 6.17. The second MES is acting as three separate conventional networks.

Table 6.15: IEEE 39 bus system line data [84].

From Bus	To Bus	Line length (m)
1	2	43.4838
1	39	26.4500
2	3	15.9758
2	25	9.0988
2	30	0
3	4	22.5354
3	18	14.0714
4	5	13.5424
4	14	13.6482
5	6	2.7508
5	8	11.8496
6	7	9.7336
6	11	8.6756
6	31	0

Table 6.15 (continue): IEEE 39 bus system line data [84].

From Bus	To Bus	Line length (m)
7	8	4.8668
8	9	38.4054
9	39	26.45
10	11	4.5494
10	13	4.5494
10	32	0
12	11	0
12	13	0
13	14	10.6858
14	15	22.9586
15	16	9.9452
16	17	9.4162
16	19	20.6310
16	21	14.2830
16	24	6.2422
17	18	8.6756
17	27	18.3034
19	20	0
19	33	0
20	34	0
21	22	14.812
22	23	10.1568
22	35	0
23	24	37.03
23	36	0
25	26	34.1734
25	37	0
26	27	15.5526
26	28	50.1492
26	29	66.125
28	29	15.9758
29	38	0

Table 6.16: IEEE 39 bus system load and customer data [84].

Load points	Average load level (MW)	Customer type	Number of customers
1	97.6	7	200
3	322	7	322
4	500	4	500
7	233.8	5	200
8	522	6	500
9	6.5	7	132
12	8.53	3	23
15	320	4	320
16	329	6	330
18	158	3	160
20	680	2	680
21	274	6	270
23	247.5	7	240
24	308.6	7	300

Table 6.16 (continue): IEEE 39 bus system load and customer data [84].

Load points	Average load level (MW)	Customer type	Number of customers
25	224	7	220
26	139	7	140
27	281	7	280
28	206	7	200
29	283.5	7	280
31	9.2	1	60
39	1104	1	1000

Table 6.17: IEEE 39 bus system generator data [84].

Bus	P_G MW	Q_G Mvar	Q_{max} Mvar	Q_{min} Mvar
30	250	161.762	400	140
31	677.871	221.574	300	-100
32	650	206.965	300	150
33	632	108.293	250	0
34	508	166.688	167	0
35	650	210.661	300	-100
36	560	100.165	240	0
37	540	-1.36945	250	0
38	830	21.7327	300	-150
39	1000	78.4674	300	-100

The 32-node heat network [85] for MES 2 consists of 21 loads connected by 32 pipelines. The pipe length data is given in Table 6.18 [85]. The load and customer data is given in Table 6.19 [85].

Table 6.18: 32-node heat network pipe length [85].

Pipe No.	From node	To node	Length (m)
1	1	2	257.6
2	2	3	97.5
3	2	4	51
4	2	5	59.5
5	5	6	271.3
6	5	7	235.4
7	7	8	177.3
8	7	9	102.8
9	7	10	247.7
10	5	11	160.8
11	11	12	129.1
12	11	13	186.1
13	13	14	136.2
14	14	15	41.8
15	15	16	116.8
16	15	17	136.4
17	14	18	136.4

Table 6.18 (continue): 32-node heat network pipe length [85].

Pipe No.	From node	To node	Length (m)
18	14	19	44.9
19	19	20	136.4
20	19	21	134.1
21	19	22	41.7
22	22	23	161.1
23	22	24	134.2
24	22	25	52.1
25	25	26	136
26	25	27	123.3
27	25	28	61.8
28	28	29	95.2
29	28	30	105.1
30	31	28	70.6
31	31	7	261.8
32	32	11	201.3

Table 6.19: 32-node heat network load and customer data [85].

Load points	Average load level (MW)	Customer type	Number of customers
3	0.107	1	110
4	0.145	3	150
6	0.107	4	110
7	0.107	5	110
8	0.107	6	110
9	0.107	3	110
10	0.107	1	110
11	0.145	6	150
12	0.107	7	110
14	0.0805	7	80
16	0.0805	7	80
17	0.0805	7	80
18	0.0805	7	80
20	0.0805	7	80
21	0.0805	7	80
23	0.107	2	110
24	0.107	4	110
26	0.107	6	110
27	0.107	7	110
29	0.107	3	110
30	0.107	7	110

The 20-node Belgian natural gas system [86] for MES 2 consists of 9 loads connected by 20 pipelines. The gas pipeline length data is given in Table 6.20 [86]. Table 6.21 gives the load and customer data for 9-node gas network [86].

Table 6.20: 20-node Belgian natural gas system pipe length [86].

Pipe No.	From node	To node	Length (m)
1	1	2	4
2	1	2	4
3	2	3	6
4	2	3	6
5	3	4	26
6	5	6	43
7	6	7	29
8	7	4	19
9	4	14	55
10	8	9	5
11	8	9	5
12	9	10	20
13	9	10	20
14	10	11	25
15	10	11	25
16	11	12	42
17	12	13	40
18	13	14	5
19	14	15	10
20	15	16	25
21	11	17	10.5
22	17	18	26
23	18	19	98
24	19	20	6

Table 6.21: 20-node Belgian natural gas system load and customer data [86].

Load points	Average load level (MW)	Customer type	Number of customers
3	5.88	1	60
6	6.05	5	61
7	7.88	3	80
10	9.55	4	100
12	0.775	7	80
15	10.27	2	105
16	23.42	6	240
19	0.33	7	30
20	0.775	7	80

Different parameter settings will result in different optimization results, therefore, appropriate parameter settings are required to ensure the reliability of the optimal solution. All three optimization algorithms have the same parameters such as population size, maximum generations, and repository size. The distinction is that MOPSO obtains the next generation by updating the particle velocity and position through the acceleration factor, whereas NSGA-II and SPEA2 use the crossover rate and mutation rate to drive the non-dominated solution to get the next generation. The parameters were tested through trials in

order to select the most plausible options. The population size, generation number, and mutation rate all begin at low values, while the crossover rate begins to decline. The number of generations and the size of the population can affect the execution time. MOPSO requires a large population size since it takes longer to execute than the other two methods. Table 6.22 presents the NSGA-II, MOPSO, and SPEA2 parameters [88].

Table 6.22: Multi-objective optimization algorithms parameters [88].

MOPSO	NSGA-II	SPEA2
Population size = 100	Population size = 50	Population size = 50
Generations = 200	Generations = 200	Generations = 200
Repository size = 100	Archive size = 50	Archive size = 50
$c_1 = 1.8$	Crossover rate = 0.7	Crossover rate = 0.7
$c_2 = 2$	Mutation rate = 0.01	Mutation rate = 0.01
$w = 0.7$		
$\omega_{damp} = 0.9$		

6.3 Case study 1 for reliability optimization under weather uncertainties

Figure 6.5 presents a schematic diagram of the first multi-energy system. MES 1 is comprised of an IEEE 24 bus system [69], a 13-node heat network [4], and a 9-node natural gas network [71]. In addition to generators in the power grid, the WT, GT, CHP, P2G, PV, and V2G systems, which have been deployed on buses 1, 2, 4, 5, 7, and 8 in IEEE 24 power system, have been considered in the MES design for delivering supplemental energy to the key load demands. The GB serves as the coupling element between the heat network and the gas network by being connected to bus 1 of the heat network and bus 1 of the gas network. CHP, P2G, GB, and V2G coupling components can enable multi-energy flows and increase energy efficiency in the MES.

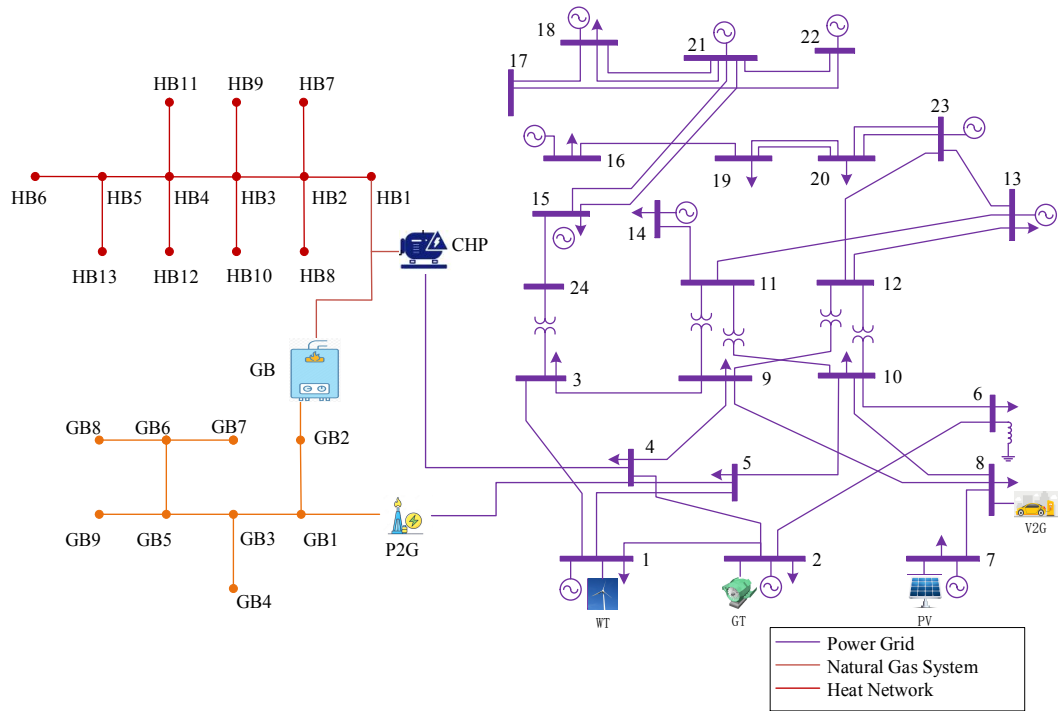


Figure 6.5: The schematic diagram of the first multi-energy system.

The convergence characteristics of two objectives SAIDI and cost are depicted in Figure 6.6. Before the maximum iterations, all three algorithms converge to their minimum value, and the adaptive stop criterion is satisfied. There is no early stopping (the optimization stops early even though the objective function continues to provide significant improvements) or late stopping (the optimization stops when there is no significant improvement for many of the last generations) [83] occurs. The convergence of the algorithm is thus proved.

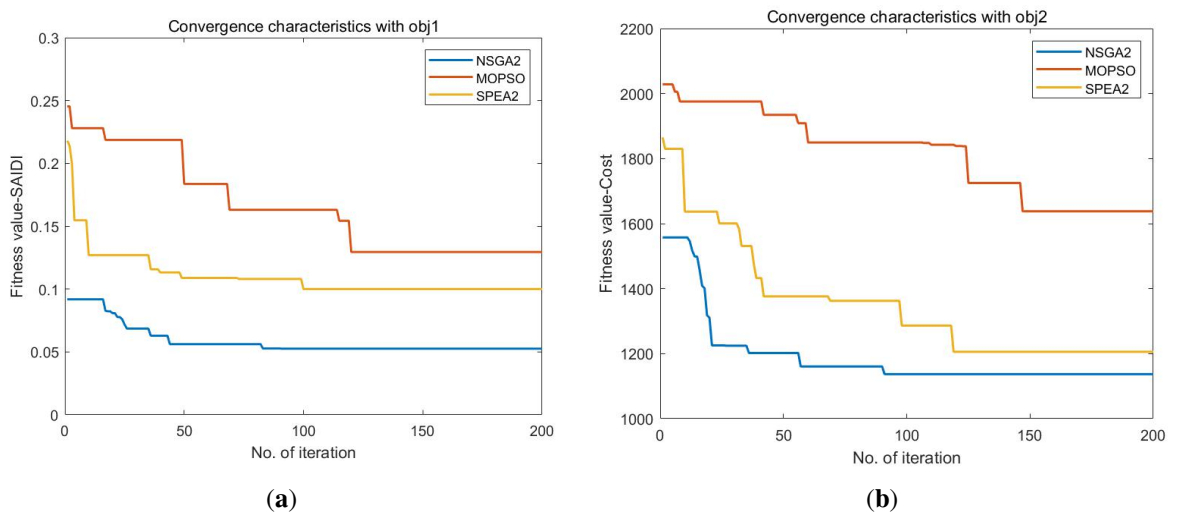


Figure 6.6: Convergence curve of: (a) SAIDI (h/Ca); (b) Cost (k\$).

Figure 6.7 shows the Pareto fronts obtained by solving the reliability optimization problem stated in Equations 5.9 and 5.10 using the three multi-objective optimization techniques discussed in Chapter 4. The two objective functions are represented by horizontal and vertical coordinates. The NSGA-II method leads to greater optimal values for the objective functions than the other two methods, resulting in a high-quality solution. Moreover, NSGA-II is the first to converge, followed by SPEA2.

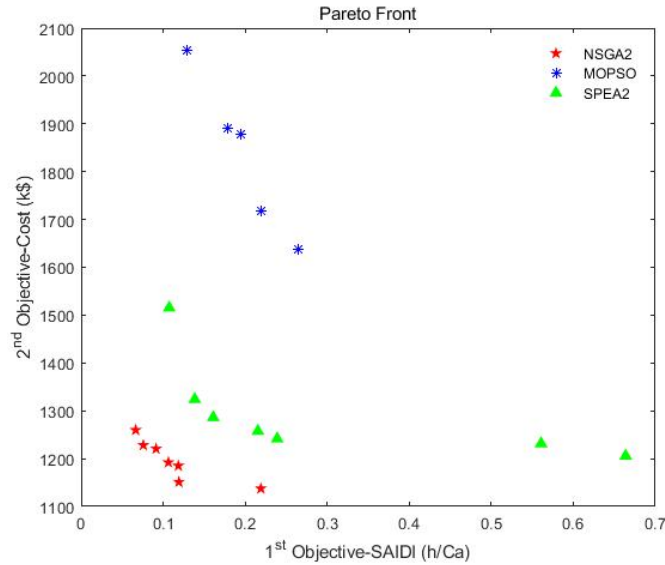


Figure 6.7: Pareto Front results of three multi-objective algorithms for MES 1.

Tables 6.23, 6.24, and 6.25 summarize the optimal results attained by three different algorithms. All three tables are arranged from high to low in terms of cost. The optimal solution of the Pareto Front is a set that contains more than one optimal solution. Therefore, customers can choose their ideal case based on the offered tables. However, it is worth mentioning that less interruption duration requires a higher cost. NSGA-II costs only 1.2598e3 k\$ and achieves the lowest SAIDI value of 0.0665, given in the no.1 case of NSGA-II, whereas MOPSO costs 2.0529e3 k\$ and achieves the lowest SAIDI value of 0.1295, and SPEA2 costs 1.5154e3 k\$ and achieves the lowest SAIDI value of 0.1074. It is obvious to see that SPEA2 excelled MOPSO but underperformed NSGA-II based on the three tables. However, it should be noted that higher reliability does not imply more storage devices; the MES reliability would be related to both storage device placements and system interruption costs; the third set of data in the NSGA-II results has 27 storage devices, whereas the fourth set of data has 30 storage devices. The execution times of these three techniques are compared in Table 6.26. NSGA-II and SPEA2 are obviously faster than MOPSO.

Table 6.23: NSGA-II optimization result for MES 1.

NSGA-II	Storage device optimal location			Obj_1 —SAIDI (h/Ca)	Obj_2 —Cost (k\$)
	Power grid	Heat network	Gas network		
1	Bus 1, 2, 3, 4, 6, 8, 9, 10, 13, 14, 15, 16, 18, 19, 20, 22	Bus 1, 2, 3, 4, 5, 6, 10	Bus 1, 2, 4, 5, 6, 8	0.0665	1.2598e3
2	Bus 1, 2, 3, 4, 6, 7, 8, 9, 10, 13, 14, 15, 16, 18, 19, 20, 22	Bus 1, 2, 5, 7, 10, 11	Bus 1, 4, 5, 7, 8	0.0758	1.2282e3
3	Bus 1, 2, 3, 4, 6, 8, 9, 10, 13, 14, 15, 16, 18, 19, 20, 22	Bus 2, 3, 5, 6, 10	Bus 1, 2, 4, 5, 7, 8	0.0913	1.2207e3
4	Bus 1, 2, 3, 4, 6, 8, 9, 10, 13, 14, 15, 16, 18, 19, 20, 22	Bus 1, 2, 3, 4, 5, 6, 7, 10, 11	Bus 1, 4, 5, 8, 9	0.1064	1.1922e3
5	Bus 1, 2, 3, 4, 6, 8, 9, 10, 13, 14, 15, 16, 18, 19, 20, 22	Bus 1, 2, 3, 5, 7, 9, 10	Bus 1, 4, 5, 7, 8	0.1185	1.1851e3
6	Bus 1, 2, 3, 4, 6, 8, 9, 10, 13, 14, 15, 16, 18, 19, 20, 22	Bus 1, 2, 3, 4, 5, 6, 10	Bus 2, 4, 5, 8	0.1191	1.1511e3
7	Bus 2, 3, 4, 6, 8, 9, 10, 13, 14, 15, 16, 18, 19, 20, 22	Bus 1, 2, 5, 6, 7, 10, 11	Bus 2, 4, 5, 8	0.2191	1.1376e3

Table 6.24: MOPSO optimization result for MES 1.

MOPSO	Storage device optimal location			Obj_1 —SAIDI (h/Ca)	Obj_2 —Cost (k\$)
	Power grid	Heat network	Gas network		
1	Bus 1, 2, 3, 4, 5, 6, 8, 9, 10, 12, 13, 14, 15, 18	Bus 1, 2, 3, 4, 5, 6, 7	Bus 2, 4, 7, 8	0.1295	2.0529e3
2	Bus 1, 2, 3, 4, 8, 9, 10, 11, 13, 15, 16, 17, 18, 19, 20	Bus 2, 5, 6, 7, 9	Bus 1, 2, 4, 5, 6	0.1792	1.8907e3
3	Bus 1, 2, 3, 6, 8, 9, 10, 13, 14, 15, 16, 18, 20, 22, 23, 24	Bus 1, 2, 3, 6, 7, 10, 11, 12	Bus 2, 3, 5, 6, 7, 8, 9	0.1948	1.8781e3
4	Bus 1, 2, 3, 4, 5, 6, 8, 10, 13, 14, 15, 16, 17, 18, 19, 20, 22	Bus 2, 5, 7, 8, 10, 11, 12	Bus 3, 5, 6, 7, 8	0.2196	1.7172e3
5	Bus 1, 2, 3, 4, 6, 7, 8, 9, 13, 14, 15, 16, 18, 19, 20	Bus 1, 2, 4, 5, 6, 7	Bus 1, 2, 4, 6, 7	0.2654	1.6380e3

Table 6.25: SPEA2 optimization result for MES 1.

SPEA2	Storage device optimal location			Obj_1 —SAIDI (h/Ca)	Obj_2 —Cost (k\$)
	Power grid	Heat network	Gas network		
1	Bus 1, 2, 3, 4, 5, 6, 9, 10, 12, 13, 14, 15, 16, 19, 20	Bus 1, 2, 3, 5, 6, 10, 11	Bus 1, 3, 5, 6, 7	0.1074	1.5154e3
2	Bus 1, 2, 3, 4, 6, 8, 9, 10, 13, 14, 15, 16, 19, 20	Bus 1, 3, 4, 6, 10, 11	Bus 1, 3, 5, 6, 7	0.1385	1.3242e3
3	Bus 1, 2, 3, 4, 6, 8, 9, 10, 13, 14, 15, 16, 19, 20	Bus 1, 3, 5, 6, 10, 11	Bus 1, 3, 5, 6, 7	0.1611	1.2863e3
4	Bus 2, 3, 4, 6, 8, 9, 10, 13, 14, 15, 16, 19, 20	Bus 1, 3, 4, 6, 10, 11	Bus 1, 3, 5, 6, 7	0.2155	1.2576e3
5	Bus 2, 3, 4, 6, 8, 9, 10, 13, 14, 15, 16, 19, 20	Bus 1, 2, 3, 6, 10, 11	Bus 1, 3, 5, 6, 7	0.2391	1.2416e3
6	Bus 1, 3, 4, 6, 8, 9, 10, 13, 14, 15, 16, 19, 20	Bus 2, 3, 6, 10, 11	Bus 1, 3, 5, 6, 7	0.5608	1.2315e3
7	Bus 1, 3, 4, 6, 8, 9, 10, 13, 14, 15, 16, 19, 20	Bus 1, 2, 3, 4, 6, 10, 11	Bus 3, 5, 6, 7	0.6639	1.2058e3

Table 6.26: Comparison of execution times for MES 1.

Optimization algorithms	Executing time (min)
NSGA-II	139.52
MOPSO	582.28
SPEA2	133.12

It is apparent that increased investment in the storage device improves MES 1 reliability, resulting in decreased interruption costs. The reliability indicators of the MES before and after optimization in MES 1 are compared in Table 6.27. There are more components as energy storage devices are added, resulting in a modest increase in the system average interruption frequency SAIFI. From 1.4945 h/Ca to 0.1404 h/Ca, the system average interruption duration (SAIDI) declined by 90.78%. From 7.548 h/Ca to 0.5431 h/Ca, the customer average interruption duration (CAIDI) dropped by 92.80%. ASAI has a high level of average system availability, and the optimization of ASAI is relatively minimal. Despite the modest increase in ASAI, the system outage duration was greatly decreased.

Table 6.27: Comparison of reliability indices before and after optimization for MES 1.

Reliability indices	Before optimization	After optimization
SAIFI (1/Ca)	0.1980	0.2585
SAIDI (h/Ca)	1.4945	0.1404
CAIDI (h/Ca)	7.5480	0.5431
ASAI	0.9998	0.9999

6.4 Case study 2 for reliability optimization under weather uncertainties

Figure 6.8 depicts the MES 2 schematic diagram which contains an IEEE 39 bus system [84], a 32-node heat grid [85], and a 20-node Belgian natural gas network [86]. PV, WT, GT, CHP, V2G, and P2G systems, have been considered in the MES design for delivering supplemental energy to the critical load demands, and have been placed on buses 1, 3, 20, 23, 26, and 29 accordingly. The GB serves as the coupling element between the heat network and the gas network by being connected to bus 1 of the heat network and bus 1 of the gas network.

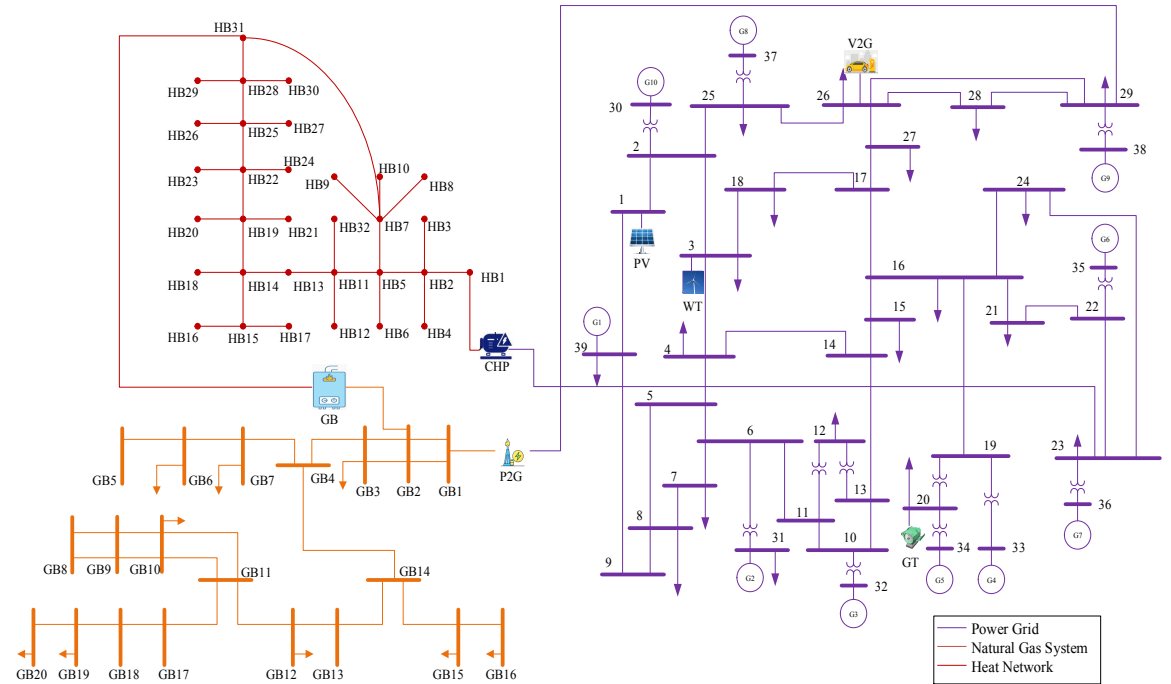


Figure 6.8: The schematic diagram of the second multi-energy system.

The convergence characteristics of the two objectives are shown in Figure 6.9. Before the maximum number of iterations is achieved, all three algorithms converge to their minimum value, and the adaptive stop criteria is achieved; no early stopping or late stopping [83] happens. The convergence of the algorithm is thus proved again in MES 2.

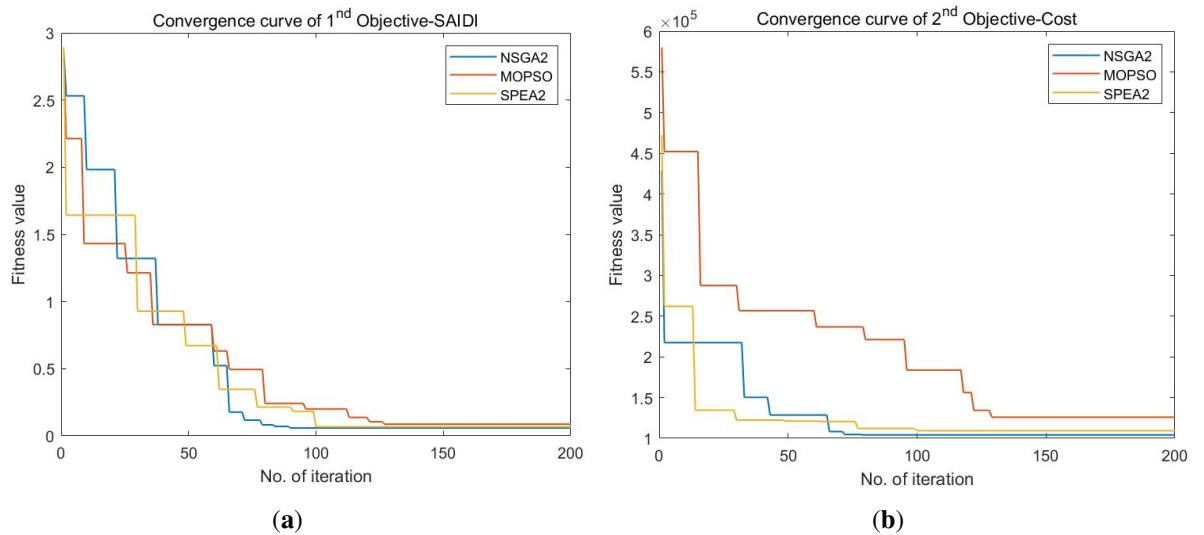


Figure 6.9: Convergence curve of: (a) SAIDI (h/Ca); (b) Cost (k\$).

Figure 6.10 shows the Pareto fronts obtained by solving the reliability optimization problem stated in Equations 5.9 and 5.10 using the three multi-objective optimization techniques exemplified in Chapter 4. In comparison to the other two methods, the NSGA-

II method still generates superior optimal values for the objective functions.

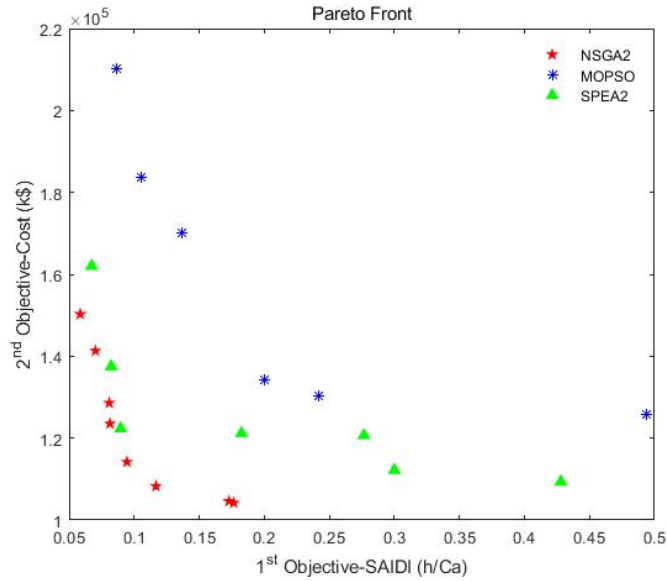


Figure 6.10: Pareto Front results of three multi-objective algorithms for MES 2.

Tables 6.28, 6.29, and 6.30 summarize the optimal results attained by three different algorithms. All three tables are arranged from high to low in terms of cost. NSGA-II costs only 1.5028e5 k\$ and achieves the SAIDI value of 0.0585, given in the no.1 case for NSGA-II, whereas MOPSO costs 2.1029e5 k\$ and achieves the lowest SAIDI value of 0.0867, and SPEA2 costs 1.6200e5 k\$ and achieves the lowest SAIDI value of 0.0673. It is obvious to see that SPEA2 excelled MOPSO but underperformed NSGA-II based on the three tables. However, it should be noted again that higher reliability does not imply more storage devices; the second set of data has 41 storage devices, while the fourth set of data has 49 storage devices in the NSGA-II optimization result. The execution times of these three techniques are compared in Table 6.31. NSGA-II and SPEA2 are still faster than MOPSO.

Table 6.28: NSGA-II optimization result for MES 2.

NSGA-II	Storage device optimal location			Obj_1 —SAIDI (h/Ca)	Obj_2 —Cost (k\$)
	Power grid	Heat network	Gas network		
1	Bus 1, 3, 6, 7, 12, 13, 15, 18, 19, 20, 21, 22, 25, 28, 29, 30, 31, 32, 35, 37, 39	Bus 1, 2, 4, 5, 14, 15	Bus 1, 2, 3, 5, 6, 7, 9, 10, 12, 13	0.0585	1.5028e5
2	Bus 1, 3, 4, 6, 7, 12, 13, 16, 18, 19, 20, 21, 22, 25, 28, 29, 30, 31, 32, 35, 37, 39	Bus 1, 2, 4, 9, 12, 15	Bus 2, 3, 5, 6, 7, 9, 10, 11, 12, 13, 15, 16, 19	0.0702	1.4132e5

Table 6.28 (continue): NSGA-II optimization result for MES 2.

NSGA-II	Storage device optimal location			Obj_1 —SAIDI (h/Ca)	Obj_2 —Cost (k\$)
	Power grid	Heat network	Gas network		
3	Bus 1, 3, 4, 6, 7, 12, 13, 16, 18, 20, 21, 22, 25, 28, 29, 30, 31, 32, 35, 37, 39	Bus 1, 3, 8, 14, 21	Bus 2, 3, 5, 6, 7, 9, 10, 11, 12, 13, 15, 16, 19	0.0808	1.2859e5
4	Bus 1, 2, 3, 4, 5, 6, 7, 12, 13, 16, 18, 19, 20, 21, 22, 24, 25, 28, 29, 30, 31, 32, 35, 37, 39	Bus 3, 11, 12, 13, 14, 17, 18, 21, 22, 23, 24	Bus 2, 3, 5, 6, 7, 9, 10, 11, 12, 13, 15, 16, 19	0.0814	1.2354e5
5	Bus 1, 3, 4, 5, 6, 7, 12, 13, 18, 19, 20, 21, 22, 25, 28, 29, 30, 31, 32, 35, 37, 39	Bus 2, 3, 4, 5, 6, 10, 11, 20	Bus 2, 3, 5, 6, 7, 9, 10, 11, 12, 13, 15, 16, 19	0.0944	1.1417e5
6	Bus 1, 2, 3, 4, 5, 6, 7, 12, 13, 14, 16, 18, 20, 21, 22, 25, 28, 29, 30, 31, 32, 34, 37, 39	Bus 2, 3, 4, 5, 6, 10, 11, 20	Bus 2, 3, 5, 6, 7, 9, 10, 11, 12, 13, 16, 19	0.1167	1.0826e5
7	Bus 1, 2, 4, 6, 7, 12, 13, 16, 18, 19, 20, 21, 22, 25, 28, 29, 30, 31, 32, 34, 37, 39	Bus 4	Bus 2, 3, 5, 6, 7, 9, 10, 11, 12, 13, 15, 16, 19	0.1728	1.0461e5
8	Bus 1, 4, 5, 6, 7, 11, 12, 13, 16, 18, 19, 20, 22, 25, 28, 29, 30, 31, 32, 35, 37, 39	Bus 5	Bus 2, 3, 5, 6, 7, 9, 10, 11, 12, 13, 15, 16, 19	0.1765	1.0419e5

Table 6.29: MOPSO optimization result for MES 2.

MOPSO	Storage device optimal location			Obj_1 —SAIDI (h/Ca)	Obj_2 —Cost (k\$)
	Power grid	Heat network	Gas network		
1	Bus 1, 4, 5, 7, 11, 12, 14, 16, 17, 18, 19, 20, 23, 24, 25, 29, 30, 31, 34, 35, 37, 38	Bus 2, 5, 7, 8, 9, 10, 12, 16, 17, 18, 20, 22, 23, 24, 25, 27, 28, 30, 31	Bus 1, 2, 3, 4, 5, 6, 7, 8, 9, 10, 11, 12, 14, 15, 18, 19	0.0867	2.1029e5
2	Bus 2, 3, 4, 7, 8, 11, 16, 17, 18, 22, 23, 24, 25, 26, 27, 28, 31, 38, 39	Bus 1, 2, 3, 4, 6, 7, 10, 12, 13, 14, 15, 16, 20, 21, 22, 23, 24, 26, 31	Bus 2, 3, 4, 5, 6, 7, 9, 10, 11, 12, 14	0.1054	1.8381e5
3	Bus 1, 3, 5, 6, 8, 10, 11, 13, 14, 15, 16, 17, 19, 20, 21, 22, 26, 27, 28, 30, 31, 33, 36, 39	Bus 1, 2, 3, 4, 6, 8, 10, 11, 13, 14, 15, 16, 18, 20, 22, 23, 24, 25, 26, 27, 29, 30, 32	Bus 1, 2, 4, 6, 7, 8, 10, 12, 13, 16, 18	0.1371	1.7001e5
4	Bus 1, 2, 3, 4, 5, 6, 9, 16, 17, 19, 20, 22, 27, 28, 29, 30, 35, 36	Bus 2, 3, 4, 5, 7, 9, 12, 13, 15, 16, 17, 18, 20, 23, 25, 26	Bus 1, 2, 3, 4, 5, 6, 7, 10, 11, 12, 13, 15	0.1999	1.3435e5
5	Bus 3, 4, 5, 7, 8, 9, 14, 19, 22, 30, 31	Bus 1, 2, 3, 4, 7, 8, 9, 12, 14, 19, 20, 29	Bus 3, 4, 6, 7, 9, 10, 15	0.2417	1.3032e5
6	Bus 1, 2, 4, 8, 10, 11, 12, 13, 14, 16, 17, 19, 26, 27, 28, 35	Bus 3, 4, 5, 6, 8, 9, 11, 13, 14, 16, 17, 18, 23, 24, 25, 29	Bus 2, 3, 4, 6, 7, 8, 10, 11, 12, 15, 19	0.4941	1.2588e5

Table 6.30: SPEA2 optimization result for MES 2.

SPEA2	Storage device optimal location			Obj_1 —SAIDI (h/Ca)	Obj_2 —Cost (k\$)
	Power grid	Heat network	Gas network		
1	Bus 1, 3, 4, 5, 6, 8, 9, 11, 14, 16, 17, 19, 22, 24, 28, 29, 31, 34	Bus 1, 2, 3, 5, 6, 7, 9, 10, 11, 12, 14, 15, 16, 20, 21, 23, 25, 26	Bus 1, 2, 3, 4, 5, 6, 7, 8, 10, 11, 12, 14, 15, 19	0.0673	1.6200e5
2	Bus 2, 3, 4, 5, 6, 8, 9, 11, 14, 16, 17, 19, 22, 24, 28, 29, 31, 34	Bus 1, 2, 3, 5, 6, 7, 9, 10, 11, 13, 14, 15, 16, 20, 21, 23, 25, 26	Bus 1, 3, 4, 5, 6, 7, 8, 10, 11, 12, 14, 15, 19	0.0823	1.3749e5
3	Bus 2, 3, 4, 5, 6, 8, 9, 10, 11, 14, 17, 19, 25, 28, 30, 36, 38	Bus 1, 2, 3, 4, 5, 7, 8, 12, 13, 14, 15, 16, 18, 20, 29	Bus 1, 3, 4, 5, 6, 7, 9, 10, 12, 14, 15, 16	0.0895	1.2237e5
4	Bus 1, 3, 6, 7, 9, 10, 12, 14, 17, 18, 23, 24, 28, 32	Bus 1, 2, 3, 5, 6, 10, 12, 15, 18, 21, 22, 24	Bus 1, 3, 4, 5, 6, 7, 10, 11, 12, 18, 19	0.1825	1.2120e5
5	Bus 1, 2, 3, 4, 5, 7, 9, 10, 11, 13, 15, 18, 22, 29, 30	Bus 1, 2, 3, 4, 6, 7, 10, 16, 17, 20, 26, 28	Bus 2, 3, 4, 5, 6, 7, 10, 13, 14, 18	0.2766	1.2066e5
6	Bus 1, 2, 4, 5, 6, 7, 8, 9, 10, 14, 16, 17, 21, 25, 32, 33, 37, 39	Bus 2, 3, 4, 5, 7, 8, 9, 13, 17, 22, 29	Bus 3, 6, 7, 8, 9, 10, 11, 12, 15, 17, 24, 30	0.3000	1.1218e5
7	Bus 1, 3, 4, 7, 8, 9, 10, 11, 12, 14, 18, 19, 24, 26, 28, 30, 33, 36, 39	Bus 1, 4, 6, 8, 9, 11, 13, 15, 16, 18, 21, 23, 26, 27	Bus 1, 3, 4, 5, 6, 7, 8, 10, 11, 12, 18, 20	0.4280	1.0934e5

Table 6.31: Comparison of execution times for MES 2.

Optimization algorithms	Executing time (min)
NSGA-II	288.67
MOPSO	876.92
SPEA2	283.34

The reliability indicators of the MES before and after optimization in MES 2 are compared in Table 6.32. There are more components as energy storage devices are added, resulting in a modest increase in the system average interruption frequency SAIFI. From 1.4805 h/Ca to 0.1936 h/Ca, the system average interruption duration (SAIDI) declined by 86.92%. From 6.9256 h/Ca to 0.7802 h/Ca, the customer average interruption duration (CAIDI) dropped by 88.73%. ASAI has a high level of average system availability, and the optimization of ASAI is relatively minimal. Despite the modest increase in ASAI, the system outage duration was greatly decreased.

Table 6.32: Comparison of reliability indices before and after optimization for MES 2.

Reliability indices	Before optimization	After optimization
SAIFI (1/Ca)	0.2138	0.2481
SAIDI (h/Ca)	1.4805	0.1936
CAIDI (h/Ca)	6.9256	0.7802
ASAI	0.9998	0.9999

6.5 Sensitivity analysis

When assessing a system's reliability, it is helpful to identify how the findings change when component characteristics change. Knowing the sensitivity of different factors to system reliability can provide engineers with some ideas on how to enhance system reliability. As a result, sensitivity analysis of system reliability assessment is critical for many reasons. First of all, sensitivity analysis can be used to reflect the impact of reliability parameters on evaluation outcomes. Engineers' concerns about their parameters can be decreased if some parameters are not sensitive to the findings of reliability evaluation. Secondly, the results of the sensitivity analysis can be used to calibrate the system and historical reliability data effectively. Last but not least, sensitivity analysis can be used to determine whether or not specific reliability parameters will have a substantial influence on the system. The sensitivity index reflects the change degree and trend of system reliability caused by the small change in component parameters. The following formula is used to calculate the sensitivity of the system reliability index to variations in a reliability parameter [89]:

$$S_{index} = \frac{\frac{\Delta Index}{Index}}{\frac{\Delta Parameter}{Parameter}}, \quad (6.1)$$

where $\Delta Index$ represents the variation of reliability indices; $\Delta Parameter$ represents the variation of reliability parameters.

The following two scenarios are considered when analyzing the sensitivity of reliability evaluation results to parameter variation:

Scenario 1: the failure rate of the three most significant components (line, transformer, and coupling components such as CHP, P2G, and GB) is reduced by 10% separately. The sensitive analysis results for MES 1 and MES 2 are given in Table 6.33 and Table 6.34, respectively. The reliability indices are more sensitive to the failure rate of the lines according to the results both in MES 1 and 2. In other words, using additional lines is recommended to improve multi-energy system reliability.

Table 6.33: Sensitivity analysis result of MES 1 to failure rate in scenario 1.

Sensitivity Components	λ_{line}	λ_T	λ_C
S_{SAIFI}	5.69%	1.17%	0.958%
S_{SAIDI}	13.26%	2.95%	4.03%
S_{CAIDI}	8.02%	1.8%	3.11%
S_{ASAI}	0.01%	0%	0%

Table 6.34: Sensitivity analysis result of MES 2 to failure rate in scenario 1.

Sensitivity Components	λ_{line}	λ_T	λ_C
S_{SAIFI}	7.4%	2.23%	3.8%
S_{SAIDI}	7.21%	4.15%	4.7%
S_{CAIDI}	1.93%	0.8%	3.87%
S_{ASAI}	0.01%	0.01%	0.01%

Scenario 2: the repair time of the line, transformer, and coupling components is reduced by 10%. The sensitive analysis results for MES 1 and MES 2 are given in Table 6.35 and Table 6.36, respectively. The reliability indices are still more sensitive to the overhead lines in MES 1. However, with more elements added to MES 2, system reliability indices are more sensitive to transformers and coupling components as shown in Table 5.20.

Table 6.35: Sensitive analysis result of MES 1 to repair time in scenario 2.

Sensitivity Components	r_{line}	r_T	r_C
S_{SAIFI}	1.81%	1.28%	0.88%
S_{SAIDI}	12.32%	1.24%	1.13%
S_{CAIDI}	10.7%	2.3%	0.88%
S_{ASAI}	0.01%	0%	0%

Table 6.36: Sensitive analysis result of MES 2 to repair time in scenario 2.

Sensitivity Components	r_{line}	r_T	r_C
S_{SAIFI}	0.31%	1%	2.98%
S_{SAIDI}	7.96%	10.8%	9.84%
S_{CAIDI}	5.09%	9.86%	9.53%
S_{ASAI}	0.01%	0.01%	0.01%

From Tables 6.33 to 6.36, we can obtain:

- (1) The reduction of the failure rate mainly affects system average interruption frequency (SAIFI).
- (2) Compare to the SAIFI index, the SAIDI and CAIDI index are more sensitive to the variation of parameters both in MES 1 and 2.
- (3) Compare to failure rate reduction, repair time reduction could drastically decrease SAIDI and CAIDI, among all the cases in MES 2.
- (4) However, when it comes to the large-scale multi-energy system (MES 2) as it contains more complex network structures and more lines, line failure rate reduction and transformer and coupling component repair time reduction have a higher influence on the entire MES 2 reliability.
- (5) As for the average system availability, ASAI in this example has reached a high level, the sensitivity of each component's reliability parameter to ASAI is quite small.

6.6 Summary

In this chapter, case studies with increasing complexity are implemented on two different MES layouts to test the validity of the suggested technique in dealing with the defined reliability optimization problem illustrated in Chapter 5. The reliability optimization problem is designed to find the optimal location of storage devices in the power system, heat network, and gas network at the lowest possible cost and highest reliability under weather uncertainty. The widely utilized multi-objective algorithms NSGA-II, MOPSO, and SPEA2 are employed to solve the given reliability optimization problem in a

comparative analysis. Moreover, the sensitive analysis is also introduced in this chapter to reflect the change degree and trend of system reliability caused by the small change in component parameters. As the sensitivity analysis was conducted in two MESs, the results show that the sensitivity factor would be different due to the size and scale of the MES.

Chapter 7

Multi-energy system resilience to extreme weather

7.1 Introduction

The study on energy resilience is receiving more attention as people become increasingly conscious of the hazards posed by extreme events which include catastrophic natural disasters or man-made attacks on energy infrastructure. Severe weather events, such as HILP (high-impact, low-probability) events, can have a substantial impact on MES operational resilience [90]. Therefore, MES must not only be reliable in the face of recognized and severe attacks, but it must also be resilient to HILP [91]. In this chapter resilient modeling and evaluation of the MES and resilience enhancement strategies are given to see their impact of the MES resilience on different wind speeds.

7.2 Multi-energy system resilience definition

The multi-phase performance response curve in Figure 7.1 is used to exemplify the MESs' resilience level, i.e. their capability to withstand, accept, and recuperate from unexpected events [93].

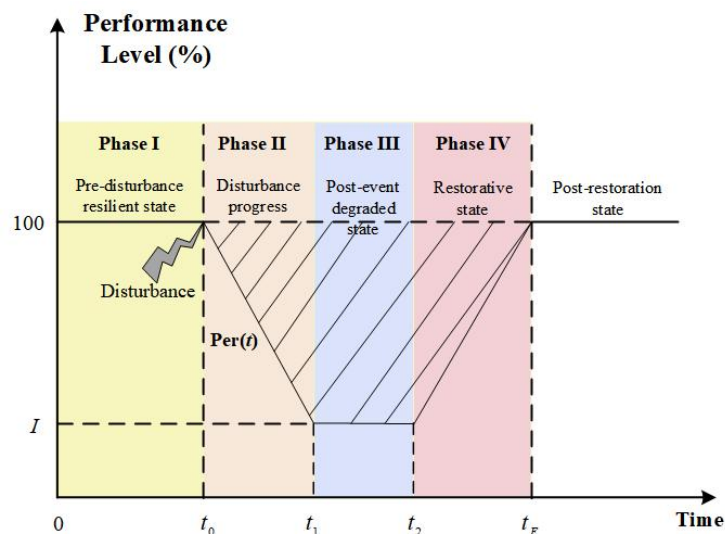


Figure 7.1: The multiphase robust performance response curve of MESs [93].

Figure 7.1 shows the multi-phase performance response curve of MESs which can be divided into four phases [94]:

1. *Phase I*, pre-disturbance phase ($t \in [0, t_0]$) describes the hazard avoidance of MES between regular operation to random failure. Before the disturbance events occur at t_0 , the MESs original performance level $Per(t)$ is 100%.
2. *Phase II*, disturbance progress phase ($t \in [t_0, t_1]$) indicates MESs' ability to absorb and withstand the effects of original faults. To ensure that MESs run reliably, the system operator will redistribute all available resources (for example, generation units, gas sources, and energy loads) during this period. When the time changes from t_0 to t_1 , the level of performance of MESs $Per(t)$ can drop from 100% to I .
3. *Phase III*, post-event degraded phase ($t \in [t_1, t_2]$) reflects the amount of time it will take to prepare a catastrophe restoration strategy. The performance level $Per(t)$ remains in the post-disruption degraded condition I for a period of time before being restored at time t_2 throughout this phase.
4. *Phase IV*, restoration phase ($t \in [t_1, t_2]$) depicts the MESs recovery process, in which repair teams have been assigned to implement catastrophe recovery plans. With the restoration of damaged components, the performance level $Per(t)$ of MESs will recuperate from I to 100%.

This section investigates the resilience of MESs. Firstly, resilient modeling of the multi-energy system under extreme weather will be presented, which includes line fragile modeling, substation fragile modeling, and components availability modeling; Then, sequential Monte Carlo simulation has been adopted to assess multi-energy system resilience under the effect of time-varying and space-varying of extreme weather using the fragile models and multi-temporal AC optimal power flow; Moreover, a combination of operational and infrastructure reliability indicators that have been introduced by EENS (Expected Energy Not Supplied, MWh/year) and LOLF (Loss of Load Frequency, occs/year) are used to reflect the resilience degradation owing to rising intensities of extreme events [91]; Finally, the assessment of various resilience strengthening measures, including redundancy, robustness, responsiveness are considered to compare the effectiveness of the resilient measures.

7.3 Resilience modeling of MESs under extreme weather

To examine the impact of windstorms on the resilience of MESs, the fragile modeling of several components in MESs has been established.

1. Line fragile modeling

The overhead line fragility curve, which connects the failure probability of a transmission line to wind speed, is presented in Figure 7.2 to represent the fragility of overhead lines to wind speed [93]. The line fragile modeling can be expressed as below:

$$P_L(w) = \begin{cases} \overline{P}_L, & \text{if } w < w_{critical} \\ P_{L_hw}(w), & \text{if } w_{critical} \leq w < w_{collapse}, \\ 1, & \text{if } w \geq w_{collapse} \end{cases} \quad (7.1)$$

where $P_L(w)$ means the line failure probability as a function of wind speed w ; \overline{P}_L denotes the line failure probability in good weather, which is set to 1×10^{-2} . The failure probability of the lines is related to high wind speeds between $w_{critical}$ and $w_{collapse}$, which are set to 30 and 60 m/s, respectively [91].

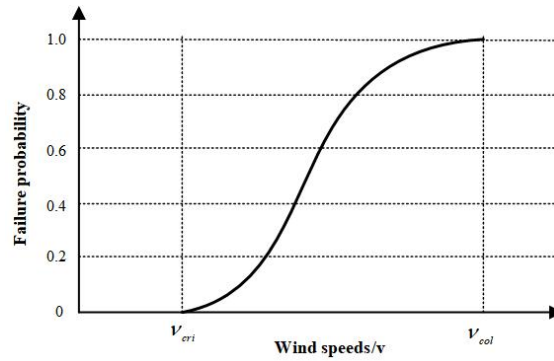


Figure 7.2: Overhead line fragile curve [93].

The underground pipes such as buried cables, heat pipes and gas pipes are more resilient to windstorms than overhead lines. This project assumes the underground pipes failure probability have no relationship with wind speed, which can be expressed as below [93]:

$$P_{ij}^{pipes}(w) = P_{ij}^{pipes, 0}, \quad (7.2)$$

Where $P_{ij}^{pipes, 0}$ represents the failure probability of underground pipes under normal condition.

2. Electrical substation fragile modeling

The following function can be used to simulate substation i failure probability at the given wind speed [95]:

$$P_i^{subs}(w) = \phi\left(\frac{\ln(w) - \mu}{\sigma}\right), \quad (7.3)$$

where μ and σ represents the logarithmic mean and standard deviation, respectively. The parameters are determined by the substation's structural characteristics and architecture. The values of μ and σ in the fragility functions for the suburban substation, for example, are 5.419 and 0.419, respectively. The authors in [93] provides the estimation findings of and for a variety of substation layouts (open, suburban, light urban, and so on).

3. Components' availability modeling

The operation states of different components are introduced in the availability function. Using state sampling techniques, the operation state a_{ij}^t of overhead line ij at time t could be obtained according to the present failure probability $P_{ij}^{line}(w)$ and past operation states a_{ij}^{t-1} [96].

$$a_{ij}^t = \begin{cases} a_{ij}^{t-1} \cdot 1, & \text{if } P_{ij}^{line}(w) \leq r \\ a_{ij}^{t-1} \cdot 0, & \text{if } P_{ij}^{line}(w) > r \end{cases} \quad (7.4)$$

where r is a random number between 0 and 1. a_{ij}^t can be either 0 or 1, where 1 represents normal state, while 0 represents failure state.

7.4 Multi-temporal and multi-regional resilience assessment of MESs using sequential MCS

The procedure of resilience assessment of MESs can be divided into the following steps:

- (1) initialize all the parameters of MESs and determine the initial operation states of all components.
- (2) obtain the failure probability of all components according to real-time wind speeds using the fragile functions. The transmission network is separated into three zones

with homogeneous weather conditions to account for the regional weather impact in distinct transmission locations.

- (3) determine the initial failure component using TTF (time to failure) [40]:

$$TTF = -\frac{1}{\lambda} \ln \delta_1, \quad (7.5)$$

where λ refers to the component's failure probability; δ_1 is the random numbers between 0 and 1.

- (4) generate its TTR (time to repair). Due to increased overall damage at higher wind speeds can also affect TTR , a TTR that grows in proportion to the damage level is applied. Here, three damage level have considered which include low, moderate and severe. For each damage level, TTR_{normal} is multiplied by a uniformly distributed random factor within a specified range, which is expressed in the following function [91]:

$$TTR = \begin{cases} TTR_{normal}, & w_{max} \leq 20 \text{ m/s} \\ k_1 \times TTR_{normal}, & 20 \text{ m/s} < w_{max} \leq 40 \text{ m/s}, \\ k_2 \times TTR_{normal}, & 40 \text{ m/s} < w_{max} \leq 60 \text{ m/s} \end{cases} \quad (7.6)$$

where $k_1 \sim U(2,4)$ and $k_2 \sim U(5,7)$, k_1 and k_2 are random numbers within these specified ranges. It should be noticed that for the low damage level, no multiplication factor is utilized. For more severe damaged level, it might take up two weeks to restore the failure component under this situation.

- (5) according to the component failure, check the fault component belongs to which energy system.
- (6) run AC optimal power flow and record system information.
- (7) judge whether the fault occurs during the day (7 am to 19 pm). If PV module fails at night, do not accumulate its failure time. If it fails in the daytime, accumulate its failure time.
- (8) according to the power path, judge whether the failed event j affect the load point, if yes, accumulate the number of failures, uptime and downtime of the load point;

otherwise only accumulate system uptime;

- (9) for the load point i determine the failure duration r_{ij} [40].

$$r_{ij} = k \times TTS_j + (1 - k) \times TTR_j, \quad (7.7)$$

where k denotes a control constant; $k = 1$ for the load point whose operation could be recovered by switching action, and $k = 0$ for the load point whose service cannot be restored by switching action.

- (10) using time-sequential AC power flow statistics, during the failure interval, establish the probable load profile for load point i , and determine the average load L_{aij} by Equation 6.7 [40]:

$$L_{aij} = \frac{\sum_{t=t_s}^{t=t_e} L_{ri}(t)}{t_e - t_s + 1}, \quad (7.8)$$

- (11) if the simulation time is less than the simulation year, go back to step 3; otherwise, proceed to step 12.
- (12) calculate resilient indices. Reliability indices LOLF and EENS are used to reflect the resilience degradation caused by the extreme event.

$$LOLF = \frac{\sum_{i=1}^n \lambda_i N_i}{\sum_{i=1}^n N_i}, \quad (7.9)$$

$$EENS = \sum_{i=1}^n EENS_i = \sum_{i=1}^n \frac{ENS_i}{TST} = \sum_{i=1}^n \frac{\sum_{j=1}^{N_s} L_{aij} r_{ij}}{TST}. \quad (7.10)$$

7.5 Resilience enhancement analysis and adaptation strategies

There are numerous resilience enhancement methods that can be used for adaptation, in this project three approaches for improving the MES resilience are introduced below [91]:

- (1) redundancy, by paralleling the addition of identical transmission lines to the existing ones. By replacing the defective line with a spare line, the load point down time would just be the switch trip time;

- (2) robustness, by shifting the fragility curves to the right to improve the components' endurance to high wind speeds (e.g. the base case and robust case of wind fragile curves in Figure 7.3). In other words, the failure probability would decrease compared to the original curve under the same wind speed in the fragile modeling;
- (3) responsiveness, in which the weather event is supposed to have no effect on TTR , i.e., no multiplication factor is employed to increase TTR_{normal} for high wind speeds, $k_1 = k_2 = 0$ in the TTR function [91]. Under this case, system failure time would be dramatically reduced, resulting in a significant improvement in MES reliability.

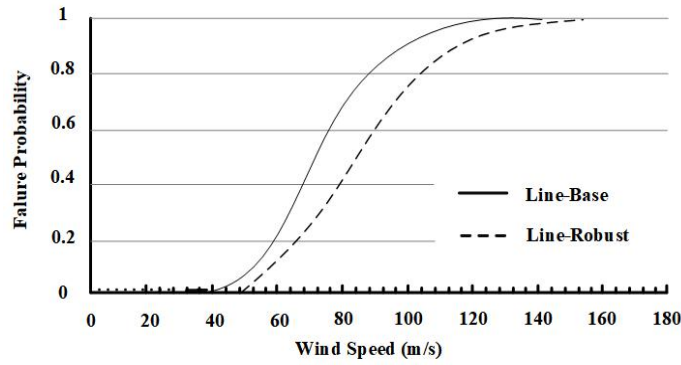


Figure 7.3: Wind fragile curves of transmission lines (base and robust case studies) [91].

Among the three resilience enhancement strategies, the network's infrastructural resilience is boosted by strategies (1) and (2), while its operational resilience and response to weather events is improved by strategy (3) [91].

An evaluation indicator is necessary to offer improvement information to the overall network resilience to evaluate the influence of resilience enhancement measures. In this project, load curtailment index is adopted to evaluate MES resilience. The expected energy load curtailment indices [97] for electrical network, heat network, and gas network are expressed in the following equations, respectively.

$$EELC_i = \sum_{st=1}^{ST} \left(\frac{\Delta P_{iL}^{b \cdot \Delta t}}{D_{iL}^0} \right) / ST, \quad (7.11)$$

$$EHLC_i = \sum_{st=1}^{ST} \left(\frac{\Delta H_{iL}^{b \cdot \Delta t}}{D_{iH}^0} \right) / ST, \quad (7.12)$$

$$EGLC_i = \sum_{st=1}^{ST} \left(\frac{\Delta G_{iL}^{b \cdot \Delta t}}{D_{iG}^0} \right) / ST, \quad (7.13)$$

where $\Delta P_{iL}^{b \cdot \Delta t}$, $\Delta H_{iL}^{b \cdot \Delta t}$, and $\Delta G_{iL}^{b \cdot \Delta t}$ represents the power, heat and gas load curtailments respectively. D_{iL}^0 , D_{iH}^0 , and D_{iG}^0 represents the initial electric, heat and gas load at node i . Δt is the time interval, which is considered to be 1 hour. ST represents the total simulation times of MCS.

Then, the transmission lines' load curtailment indices are sorted to identify which lines are the most critical, and adaption solutions are compared to the ranking findings.

7.6 Resilience study of MES 1

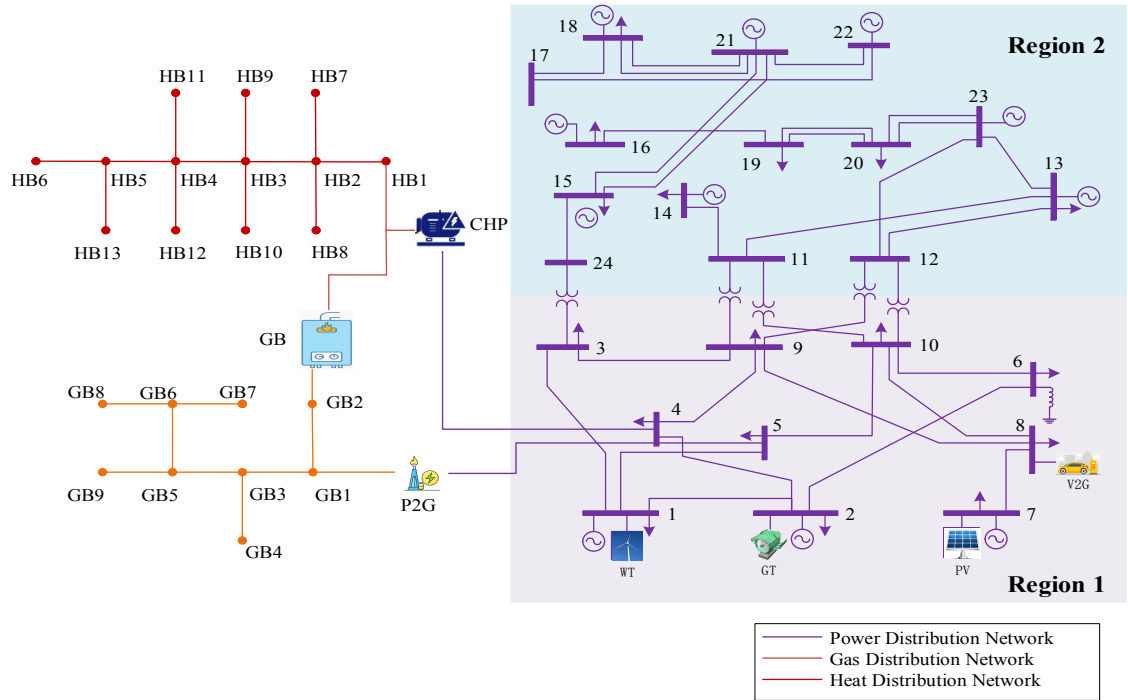


Figure 7.4: Weather regions of test MES.

The test system is MES 1 which includes an IEEE 24 bus system, a 13-node heat network, and a 9-node gas network. the power grid is divided into 2 weather regions as shown in Figure 7.4 to simulate the wind event's spatial and regional consequences, as previously described [91]. The division of the weather regions is based on the low voltage area (Region 1) and high voltage area (Region 2) of the IEEE 24 bus system. Figure 7.5 depicts the probability density function of regional wind profiles with $w_{max} = 40$ m/s. Hourly regional wind profiles with $w_{max} = 40$ m/s are shown in Figure 7.6 [91].

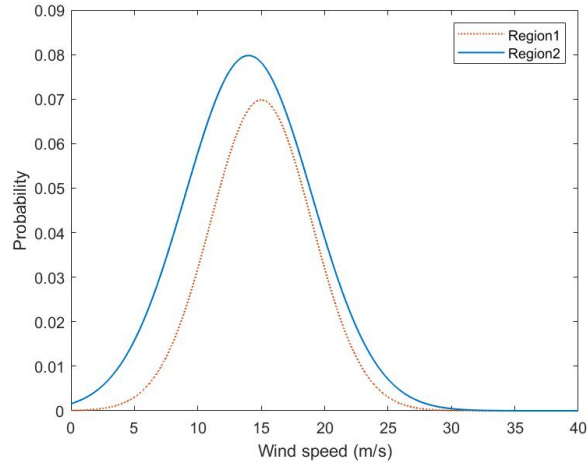


Figure 7.5: Probability density function of regional wind profiles with $w_{max} = 40$ m/s [91].

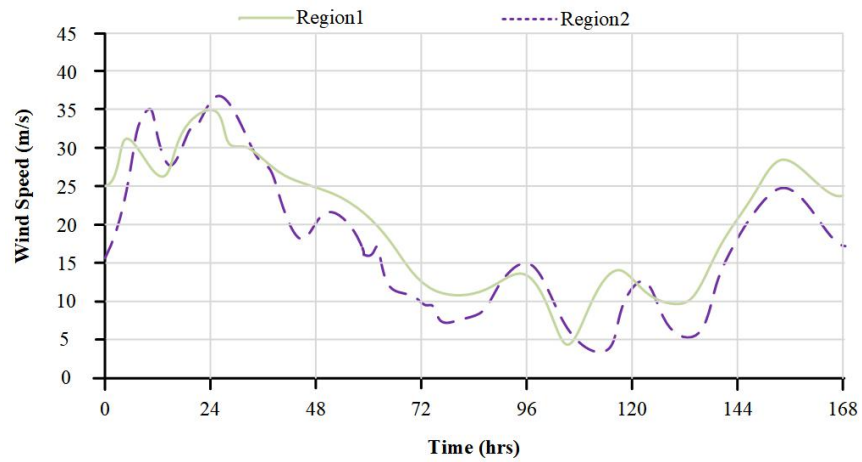


Figure 7.6: Hourly wind profiles with $w_{max} = 40$ m/s [91].

For the basic case study, Figure 7.7 displays the results of resilient indices LOLF and EENS with increasing w_{max} , from which the test network is highly operationally robust at wind speeds below 30 m/s when LOLF and EENS are near to zero. Moreover, the test system's operational resilience allows it to effectively tolerate a limited amount of transmission interruptions, preventing failure spread. After that, for wind speeds greater than 30 m/s, a substantial, nonlinear increase in LOLF and EENS is observed. Windstorms with speeds over 30 m/s can also have a significant impact, albeit they are uncommon (as indicated by the LOLF). Therefore, this section mainly aids in determining the wind speed threshold where the network will be less resilient.

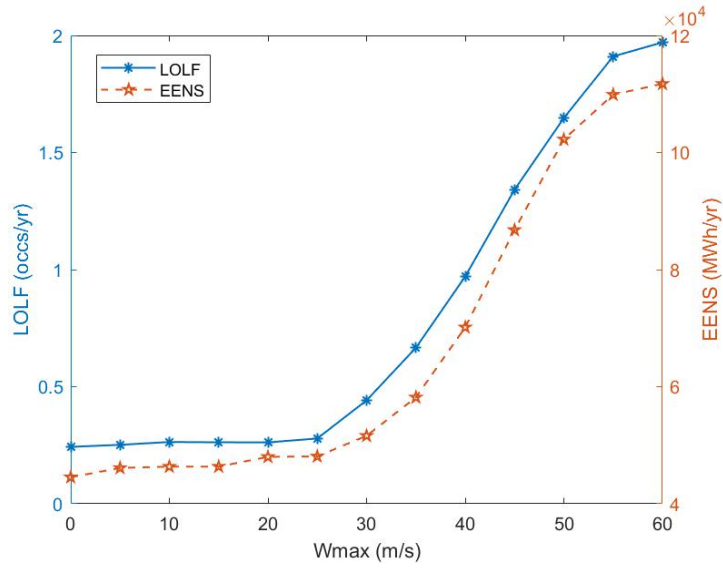
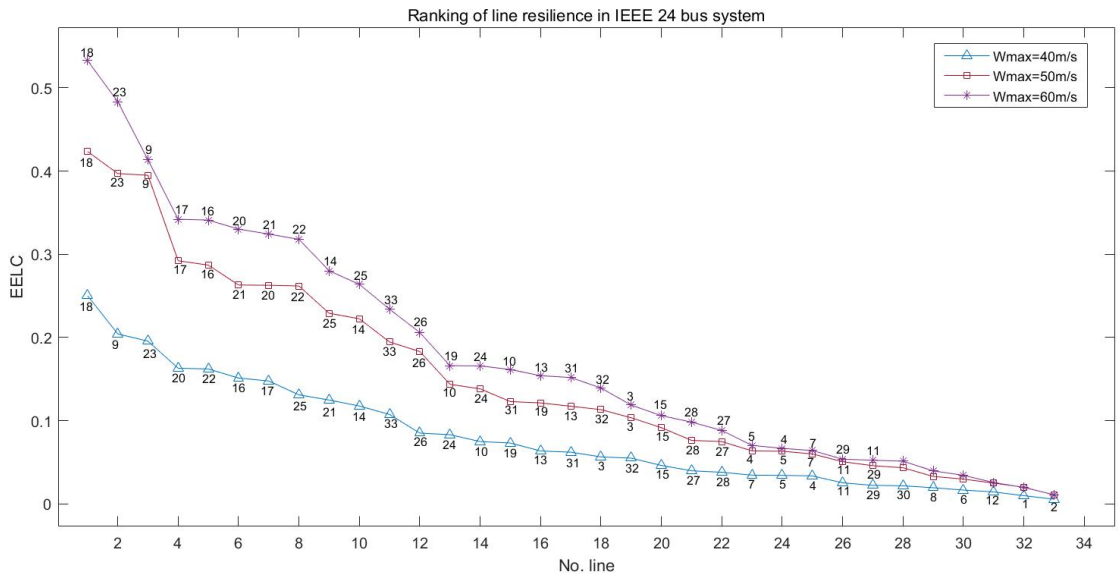
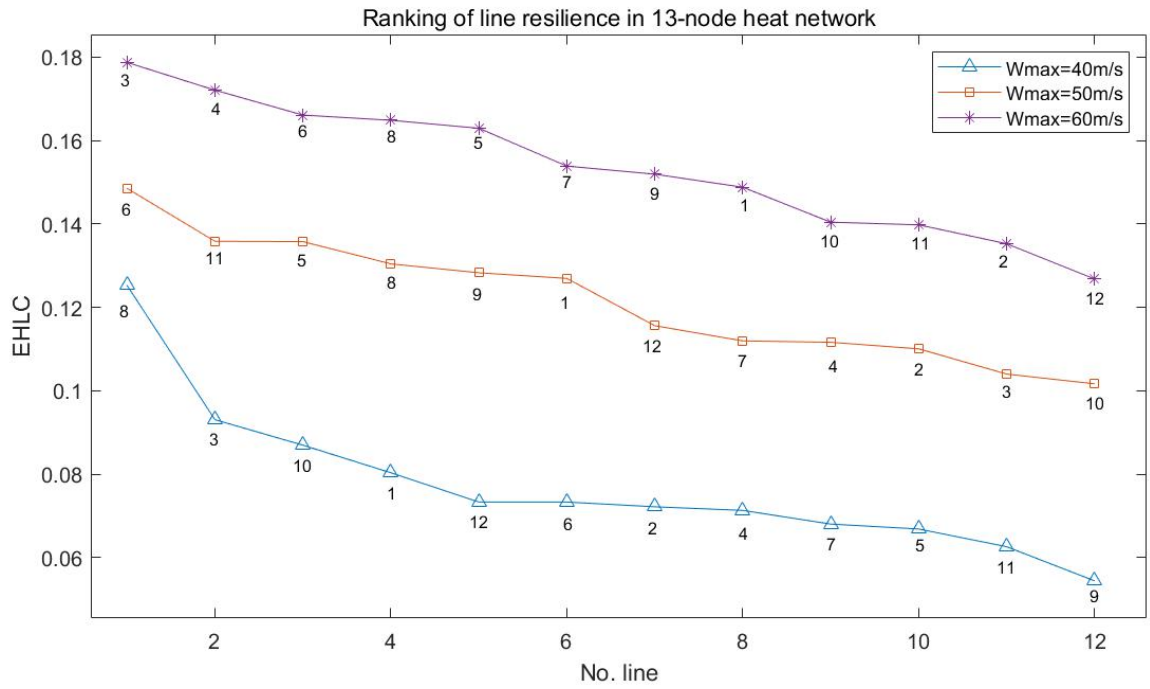


Figure 7.7: Impact of increasing maximum wind speed on LOLF and EENS.

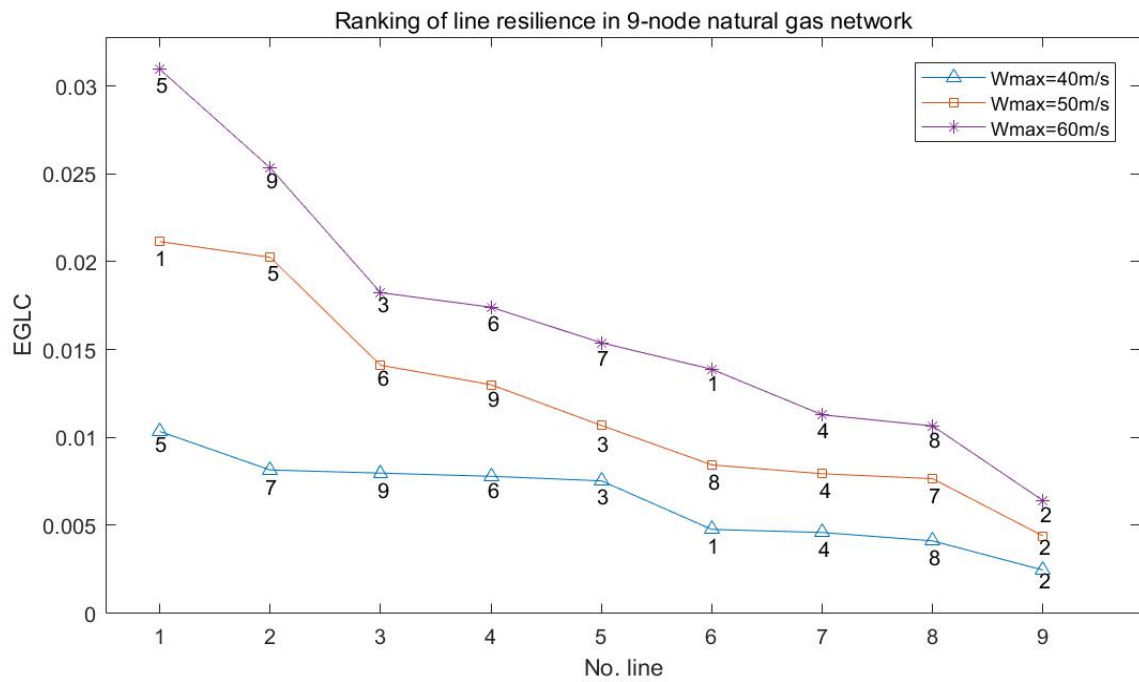
The ranking results of load curtailment indices EELC, EHLC, and EGLC are presented in Figure 7.8. The load curtailments indices (i.e., the percentage of load curtailments (EENS) during the entire simulation time) are represented on the vertical axis, while the lines ranking (i.e., 1 to 33, the number of lines in the power system) is shown on the horizontal axis.



(a)



(b)



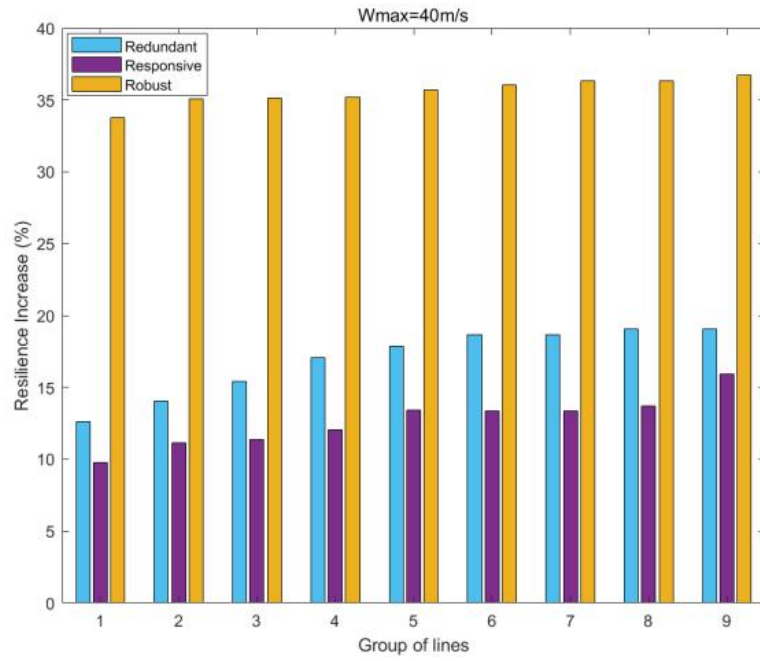
(c)

Figure 7.8: Ranking results of: (a) EELC; (b) EHLC; (c) EGLC.

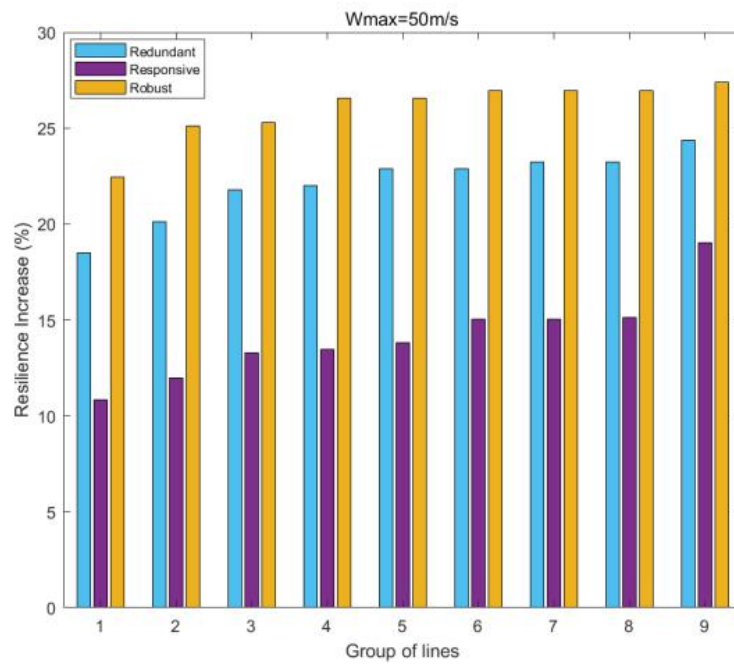
As a result of the varied reductions in EENS, the lines' criticality varies with different maximum wind speeds. For example, line 18 is the most important for all wind levels in the IEEE 24 power system shown in Figure 7.8 (a), however, circuit 23's criticality is ranked second for $w_{max} = 50$ and 60 m/s, but third for $w_{max} = 40$ m/s. Lines 3, 6, and 8

are among the most critical in the 13-node heat network (see Figure 7.8 (b)) since their ranking results are all near the top of the rankings. As for the 9-node gas network presented in Figure 7.8 (c), line 5 shows the most significant as its ranking result is 1, 2, 1 under the maximum wind speed 40 m/s, 50m/s, and 60 m/s, respectively. These findings are crucial since they inform possible investment decisions on certain lines based upon resilience objectives. It can also be noted that the lines feeding the largest demand node are among the most crucial.

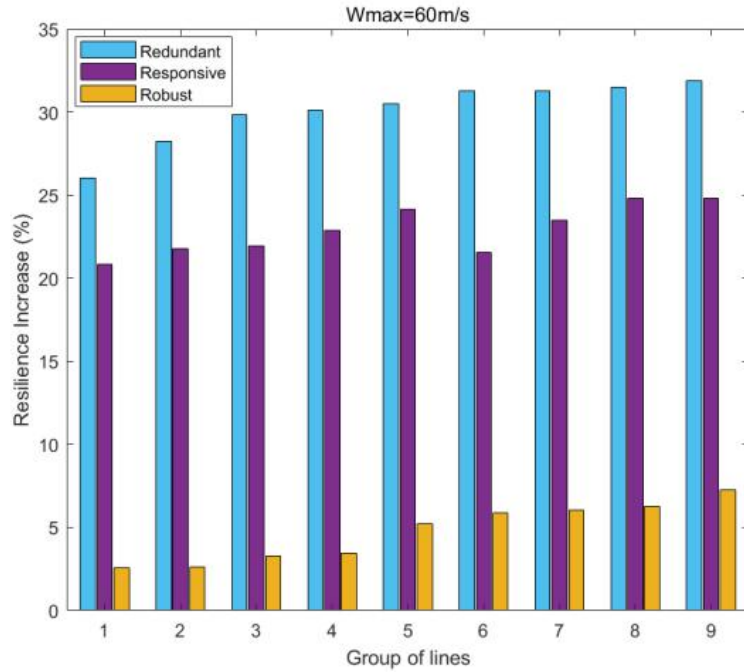
Adaptation choices for "redundancy," "robustness," and "responsiveness" are included in the resilience enhancement case studies. The results of the load curtailment index ranking are used to apply these case studies to transmission lines depending on their contribution to system resilience. For the "redundant" case, a second transmission line, identical to the first, is added; for the "robustness" scenario, the transmission lines to withstand high wind speeds is improved; and for the "responsiveness" case, TTR_{normal} is used to determine how long it takes to repair a transmission corridor. Rather than deploying these resilience enhancement solutions to a single transmission line, they are aggregated into resilience enhancement groups based on their load curtailment indices ranking results, with each group consisting of 6 lines (3 lines in power system, 2 lines in heat network, and 1 line in natural gas network). For example, the first group will consist of each wind level's first six most essential circuits. (i.e., line 18, 9, 23 in the power system, line 8, 3 in the heat network, and line 5 in the natural gas system when $w_{max} = 40$ m/s), the first 12 important circuits will be included in the second group.



(a)



(b)



(c)

Figure 7.9: The impact of resilience enhancement at different wind speeds: (a) $w_{max} = 40$ m/s; (b) $w_{max} = 50$ m/s; (c) $w_{max} = 60$ m/s.

Figure 7.9 depicts the percentage improvement in resilience achieved by using resilience adaption methods, as measured by the reduction in EENS. The horizontal axis of Figure 7.9 represents the resilience enhancement groups, the first group has 6 lines while the second group has 12 lines, and so on. When the first six crucial lines are improved, the decrease in EENS in the case studies indicates that MES resilience has presented a significant increase, which can be found in Figure 7.9 (a), the robust case has improved system resilience 33% when $w_{max} = 40$ m/s. As the resilience of further line groups is strengthened, the overall resilience is increased even more, but the process is smoother, which is expected because as their EELC, EHLC, and EGLC indices decrease, their influence on the resiliency of MES decreases. Moreover, with the increase in wind speed, the advantage of robust strategy diminishes, as the data shows the resilient enhancement has declined from 36% in $w_{max} = 40$ m/s to 7% in $w_{max} = 60$ m/s in group 9, while the redundant case shows better performance than the responsive case but they all render an upwards trend. When making comparisons of the resilient strategies' performance, the third robust strategy can improve multi-energy system resilience the most when the maximum wind speed is less than 50 m/s, whereas the impact of the redundant case is

greater than that of the responsive case, and they perform better when the maximum wind speed is 60 m/s than the robust case. It is also worth mentioning that the priority of resilience-enhancing activities may vary depending on wind speed [98].

7.7 Summary

This chapter investigates the resilience of MESs. Considering the hazards posed by extreme events that would attack the energy infrastructure, the MES not only needs to be reliable but also resilient to HILP events. Therefore, resilient modeling and evaluation of MES are given in the last chapter, the resilience enhancement strategies have been taken into account as well. The simulation results have concluded that the priority of resilience strengthening actions may vary depending on the wind speed profile.

Chapter 8

Conclusions and future work

The project presents a methodology for reliability assessment in two different multi-energy systems with storage devices while accounting for weather uncertainty through sequential Monte Carlo simulation. Moreover, reliability optimization is formulated as a non-linear problem to determine the optimal energy storage configuration schemes for improving MES reliability using NSGA-II, MOPSO, and SPEA2. The effectiveness of the proposed methodology has been demonstrated on the different MES layouts with increasing complexity. The suggested approach has also been subjected to a sensitivity analysis on the two MESs in order to reflect the degree and trend of system reliability caused by the small change in component failure rate and repair time reliability parameters. Moreover, considering the hazards posed by extreme wind events that would damage the energy infrastructure, the resilient modeling and evaluation of MES are also given.

8.1 Achievements and contributions

According to the aims and objectives proposed at the beginning of this thesis, the following achievements and contributions can be drawn from the case studies of this project.

- (1) Compared with most studies focusing on single-energy system or single-objective optimization, this project models three energy systems including electricity, heat and gas, and takes into account the uncertain factors of solar and wind, and adopts the sequential Monte Carlo simulation to assess MES reliability. Then, the reliability of MES was optimized using three different meta-heuristic optimization algorithms.
- (2) Among the two case studies for reliability optimization, NSGA-II outperforms two other optimization methods MOPSO and SPEA2, by maintaining a wider range of solutions and achieving a better non-dominated front. The best of the three approaches investigated here is NSGA-II, which can converge near to the true Pareto optimal front and converge the fastest. However, it is worth mentioning that less interruption duration requires higher cost. Therefore, customers can choose their ideal case based

on the offered tables.

- (3) The sensitivity analysis results show that the failure rate mainly affects system average interruption frequency (SAIFI). Moreover, compared to the SAIFI index, the SAIDI and CAIDI index are more sensitive to the variation of parameters both in MES 1 and 2. Reducing the failure rate and repair time of the overhead line could drastically improve MES 1 reliability, however, when it comes to the larger scale multi-energy system (MES 2) as it contains more complex network structures and more lines, overhead line failure rate reduction and transformer and coupling component repair time reduction all have a higher influence on the entire MES 2 reliability. Finally, ASAI in the experimental tests has reached a high level, and the sensitivity of each component's reliability parameter to ASAI is quite small.
- (4) When considering the performance of the resilient enhancement strategies, it can be concluded that the priority of resilience strengthening actions may vary depending on the wind speed and is also based on the real situation to determine the most reasonable strategy for improving MES operational resilience. Expand and quantify.

8.2 Future expansions

Although this study has delivered a general scope of reliability optimization for MES, more related work needs to be explored in future work. The following are some potential research expansions for MES:

- a) **Robust optimization of MES considering load uncertainty.** Besides the uncertainty in the wind and solar power generation, there are many other uncertainties in MES such as different energy system load uncertainties. Considering all the load-varying characteristics is important to MES economy operation. Moreover, apart from the reliability optimization, the robust optimization for MES under load uncertainty can reduce the economic risk of the optimal allocation scheme and strengthen the stability of the system's economic benefit.
- b) **Electric vehicles participation in the demand response of MES as active loads.** Due to the nature of two-way charging and discharging of electric vehicles, they can be used as a typical active load to reasonably guide and control their charging and

discharging behavior by means of demand response. Electric vehicles can also participate in peak regulation and frequency modulation of the system to assist in the safe and stable operation of MES.

- c) **Vulnerability analysis of MES.** The MES vulnerability is its inability to tolerate a bad circumstance, control its effects, and stabilize after the scenario has occurred [103]. In addition to different energy storage system configuration schemes that can optimize system reliability, the vulnerability analysis of MES can also provide an idea of which components in MES have the greatest effect on the reliability, thus maximizing the improvement of MES reliability.
- d) **Hybrid energy flow calculation method for MES.** The MES which mainly adopts renewable energy generation uses the coupling mechanism between multiple energy sources to realize multi-energy complementarity, promote the consumption of renewable energy, and improve the energy utilization efficiency of the system. Therefore, further research into a hybrid energy flow calculation model for MES is essential to explore where the power flow can help improve both the reliability and resilience of the system.

References

- [1] S. Vaclav, “Energy Transitions: Global and National Perspectives. & BP Statistical Review of World Energy,” 2017.
- [2] Anon, “Integration of CCHP with Renewable Energy,” *Handbook of Energy Systems in Green Buildings.*, 2018.
- [3] M. Pierluigi, “Multi-energy systems: An overview of concepts and evaluation models,” *Energy.*, 2014.
- [4] Z. Meng, et al. “Reliability evaluation of electricity-gas-heat multi-energy consumption based on user experience,” *International Journal of Electrical Power & Energy Systems.*, vol. 130, pp. 106926, 2021.
- [5] A. Mbayer, and W. JC. Melis, “Modelling of a CHP system with electrical and thermal storage,” *2015 50th International Universities Power Engineering Conference (UPEC).*, pp. 1–5, 2015.
- [6] P. Giorgio, and S. Rainieri, “Modeling of a thermal energy storage system coupled with combined heat and power generation for the heating requirements of a University Campus,” *Applied Thermal Engineering.*, vol. 30, no. 10, pp. 1255-1261, 2010.
- [7] C. Zhan, et al. “The Modeling and Simulation of the CCHP System,” *2018 2nd IEEE Conference on Energy Internet and Energy System Integration (EI2).*, pp. 1-5, 2018.
- [8] C. Zheng, X. Zhai, J.Wu, and G.Yang, “Modeling of CCHP system and analysis of thermal storage strategy by using TRNSYS software,” *CIESC Journal.*, 2015.
- [9] B. Marco, and G. Fambri, “Optimising energy flows and synergies between energy networks,” *Energy.*, vol. 173, pp. 400-412, 2019.
- [10] F. Eike, S. Göttlich, and O. Kolb, “Modeling and simulation of gas networks coupled to power grids,” *Journal of Engineering Mathematics.*, vol. 119, no.1, pp. 217-239, 2019.
- [11] H. Mohammad, et al, “Optimal operation of integrated electrical and natural gas

- networks with a focus on distributed energy hub systems,” *Sustainability.*, vol. 12, no. 20, pp. 8320, 2020.
- [12]R. Mauricio, et al, “Modeling and testing of a bidirectional smart charger for distribution system EV integration,” *IEEE Transactions on Smart Grid.*, vol. 9, no. 1, pp. 152-162, 2016.
- [13]S. Khairy, and H. A. Gabbar, “Electric vehicle to power grid integration using three-phase three-level AC/DC converter and PI-fuzzy controller,” *Energies.*, vol. 9, no. 7, pp. 532, 2016.
- [14]S. Nazmus, et al, “Modelling and simulation of natural gas generator and EV charging station: a step to microgrid technology,” *Int. J. Renew. Energy Res.*, vol. 7, no. 1, pp. 399-410, 2017.
- [15]J. D. Kueck, *Measurement practices for reliability and power quality.*, Oak Ridge National Lab.(ORNL), Oak Ridge, TN (United States), 2005.
- [16]B. Roy, and S. Jonnavithula, “A test system for teaching overall power system reliability assessment,” *IEEE transactions on Power Systems.*, vol. 11, no. 4, pp. 1670-1676, 1996.
- [17]H, Jun, et al, “Reliability modeling and evaluation of urban multi-energy systems: A review of the state of the art and future challenges,” *IEEE Access.*, vol. 8, pp. 98887-98909, 2020.
- [18]Z. Shenxi, et al, “Reliability evaluation of electricity-heat integrated energy system with heat pump,” *CSEE Journal of Power and Energy Systems.*, vol. 4, no. 4, pp. 425-433, 2018.
- [19]J. J. Wang, et al, “Reliability and availability analysis of redundant BCHP (building cooling, heating and power) system,” *Energy.*, vol. 61, pp. 531-540, 2013.
- [20]J. Yu, et al, “Reliability evaluation of integrated electrical and natural-gas system with power-to-gas,” *Proceedings of the CSEE.*, vol. 38, no. 3, pp.708-715, 2018.
- [21]H. Jia, et al, “Review of reliability analysis for integrated energy systems with

- integration of cyber physical systems,” *Power System Technology.*, vol. 43, no. 1, pp. 1-11, 2019.
- [22] G. Li, et al, “Reliability evaluation of integrated energy systems based on smart agent communication,” *Applied Energy.*, vol. 167, pp.397-406, 2016.
- [23] G. M. Zamani, and R. Ghaffarpour, “Reliability evaluation of multi-carrier energy system with different level of demands under various weather situation,” *Energy.*, vol. 196, pp. 117091, 2020.
- [24] H. Liu, et al, “Impact assessment of operation strategy of multiple energy storage system on reliability of integrated energy microgrid,” *Power system automation.*, vol. 43, no.10, pp. 36-45, 2019.
- [25] S. Wang. et al, “Operational Reliability Evaluation of Distributed Multi-energy Systems Considering Optimal Control of Energy Storages,” *2021 IEEE/IAS Industrial and Commercial Power System Asia (I&CPS Asia).*, 2021.
- [26] S. Ge, et al, “Reliability evaluation of multi-energy microgrids: Energy storage devices effects analysis,” *Energy Procedia.*, vol. 158, pp. 4453-4458, 2019.
- [27] A. Mustafa, M. Khater, and M. AlMuhaini, “Impact of vehicle-to-grid technology on the reliability of distribution systems,” *2017 9th IEEE-GCC Conference and Exhibition (GCCCE).*, pp. 1–6, 2017.
- [28] A. Bakkiyaraj, and N. Kumarappan, “Optimal reliability planning for a composite electric power system based on Monte Carlo simulation using particle swarm optimization,” *International Journal of Electrical Power & Energy Systems.*, vol. 47, pp. 109-116, 2013.
- [29] M. Zhang, et al, “Optimal design and operation of regional multi-energy systems with high renewable penetration considering reliability constraints,” *IEEE Access.*, vol. 8 , pp. 205307-205315, 2020.
- [30] B. Shima, H. Ibrahim, and A. Elbaset, “Multi-objective optimization of grid-connected PV-wind hybrid system considering reliability, cost, and environmental aspects,” *Sustainable Cities and Society.*, vol. 60, pp. 102178, 2020.

- [31] L. Peruzzi, et al. “The reliability of technological systems with high energy efficiency in residential buildings,” *Energy and Buildings.*, vol. 68, pp. 19-24, 2014.
- [32] A. Michèle, *On predictive control for coordination in multi-carrier energy systems.*, Diss. ETH Zurich, 2011.
- [33] R. Samik, “Introduction to monte carlo simulation,” *2008 Winter simulation conference.*, IEEE, 2008.
- [34] R. Billinton, and W. Li, “A system state transition sampling method for composite system reliability evaluation,” *IEEE Transactions on Power Systems.*, vol. 8, no. 3, pp. 761-770, 1993.
- [35] K. Deb, et al, “A fast elitist non-dominated sorting genetic algorithm for multi-objective optimization: NSGA-II,” *International conference on parallel problem solving from nature.* Springer., Berlin, Heidelberg, pp. 849–858, 2000.
- [36] X. Liu, and D. Zhang, “An Improved SPEA2 algorithm with local search for multi-objective investment decision-making,” *Applied Sciences.*, vol. 9, no. 8, pp. 1675, 2019.
- [37] C. A. C. Coello, G. T. Pulido, and M. Salazar Lechuga, “Handling multiple objectives with particle swarm optimization,” *IEEE Transactions on evolutionary computation.*, vol. 8, no. 3, pp. 256-279, 2004.
- [38] Y. Z. Wang, et al, “Research on resilience of power systems under natural disasters—A review,” *IEEE Transactions on Power Systems.*, vol. 31, no. 2, pp. 1604-1613, 2015.
- [39] N. Bhusal, et al, “Power system resilience: Current practices, challenges, and future directions,” *IEEE Access.*, vol. 8, pp. 18064-18086, 2022.
- [40] P. Wang, and R. Billinton, “Time sequential distribution system reliability worth analysis considering time varying load and cost models,” *IEEE Transactions on Power Delivery.*, vol. 14, no. 3, pp. 1046-1051, 1999.
- [41] O. Dzobo, and K. O. Awodele, “Probabilistic Power System Reliability Assessment: Distributed Renewable Energy Sources,” *Novel Advancements in Electrical Power*

Planning and Performance., IGI Global, pp. 94-117, 2020.

- [42] M. Rosa-Clot, and T. Giuseppe Marco, *Submerged and floating photovoltaic systems: modelling, design and case studies.*, academic press, 2017.
- [43] P. Karamanakos, T. Geyer, and S. Manias, "Direct voltage control of DC–DC boost converters using enumeration-based model predictive control," *IEEE transactions on power electronics.*, vol.29, no. 2, pp. 968-978, 2013.
- [44] A. L. Kumar, S. Albert Alexander, and M. Rajendran, *Power Electronic Converters for Solar Photovoltaic Systems.*, Academic Press, 2020.
- [45] U. U. Khan, et al, "Design and implementation of a low-cost MPPT controller for solar PV system," *2016 International Conference on Open Source Systems & Technologies (ICOSST).*, IEEE, pp. 156-163, 2016.
- [46] H. Zhang, et al, "Three-phase grid-connected photovoltaic system with SVPWM current controller," *2009 IEEE 6th International Power Electronics and Motion Control Conference.* IEEE, 2009.
- [47] R. Kadri, et al, "Design of a single-phase grid-connected photovoltaic system based on deadbeat current control with LCL filter," *Proceedings of 14th International Power Electronics and Motion Control Conference EPE-PEMC 2010.*, pp. T3-147, 2010.
- [48] Y. Zhu, et al, "A novel maximum power point tracking control for permanent magnet direct drive wind energy conversion systems," *Energies.*, vol. 5, no. 5, pp. 1398-1412, 2012.
- [49] ULUTAŞ, Alper, and D. U. R. U. Tarık, "Variable-Speed Direct-Drive Permanent Magnet Synchronous Generator Wind Turbine Modeling and Simulation," *Kocaeli Journal of Science and Engineering.*, vol. 2, no. 1, pp. 21-27, 2019.
- [50] Q. Li, et al, "Modeling and Control of Wind/PV/Battery Micro-grid Based on Matlab/Simulink," *4th International Conference on Information Technology and Management Innovation.*, Atlantis Press, 2015.
- [51] T. X. Ma, M. Z. Song, and Y. M. Li, "Study on synchronization technology and its

- relative problems of wind power generation system,” *Jilin Electric Power.*, vol. 8, no. 218, pp. 46-49, 2006.
- [52] A. Alsaleem, *A bidirectional converter for battery based energy system for residential applications.*, Colorado School of Mines, 2015.
- [53] M. Tavakoli, B. Vahidi, and W. Gawlik, “An educational guide to extract the parameters of heavy duty gas turbines model in dynamic studies based on operational data,” *IEEE Transactions on power systems.*, vol. 24, no. 3, pp. 1366-1374, 2009.
- [54] F. P. De Mello, and D. J. Ahner, “Dynamic models for combined cycle plants in power system studies,” *IEEE Transactions on Power Systems (Institute of Electrical and Electronics Engineers); (United States).*, vol. 9, no. 2, pp. 3, 1994.
- [55] W. I. Rowen, “Simplified mathematical representations of heavy-duty gas turbines,” pp. 865-869, 1983.
- [56] *Simplified Synchronous Machine*. [online] Available at: <<https://uk.mathworks.com/help/physmod/sps/powersys/ref/simplifiedsynchronousmachine.html>> [Accessed 20 August 2022].
- [57] M. Climo, et al, “The rise and rise of geothermal heat pumps in New Zealand. IPENZ,” 2014.
- [58] G. O. Fare, and P. Basu, *An Annular Cylinder Source Model for Heat Transfer through Energy Piles.*, no. 13-4949, 2013.
- [59] J. E. Bose, “Design/data manual for closed-loop ground-coupled heat pump systems,” *ASHRAE.*, 1985.
- [60] Y. Li, et al, “An improved two-stage robust optimization model for CCHP-P2G microgrid system considering multi-energy operation under wind power outputs uncertainties,” *Energy.*, vol. 223, pp. 120048, 2021.
- [61] N. Shi, and Y. Luo, “Energy storage system sizing based on a reliability assessment of power systems integrated with wind power,” *Sustainability.*, vol. 9, no. 3, pp. 395, 2017.

- [62] O. Ogunmodede, et al, "Optimizing design and dispatch of a renewable energy system," *Applied Energy.*, vol. 287, pp. 116527, 2021.
- [63] Thermolib.de. 2022. [online] Available at: <<https://www.thermolib.de/media/thermolib/downloads/Thermolib-UserManual.pdf>> [Accessed 23 August 2022].
- [64] B. Fan, et al, "Coordinate strategy of dual-pulse-width-modulation converter based on direct power control with load power feed-forward," *Measurement and Control.*, vol. 53.5-6, pp. 859-869, 2020.
- [65] V. K. Prajapati, and V. Mahajan, "Reliability assessment and congestion management of power system with energy storage system and uncertain renewable resources," *Energy.*, vol. 215, pp. 119134, 2021.
- [66] G. L. Wu, G. X. Zu, and J. Zheng, "A method for forecasting alpine area load based on artificial neural network model," *Journal of Physics: Conference Series.*, vol. 1994. no. 1, 2021.
- [67] C. E. Borges, Y. K. Playa, and I. Fernandez, "Evaluating combined load forecasting in large power systems and smart grids," *IEEE Transactions on Industrial Informatics.*, vol. 9, no. 3, pp. 1570-1577, 2012.
- [68] D. Niu, et al, "Research on short-term power load time series forecasting model based on BP neural network," *2010 2nd International Conference on Advanced Computer Control.*, vol. 4. IEEE, 2010.
- [69] Subcommittee, Probability Methods, "IEEE reliability test system," *IEEE Transactions on power apparatus and systems.*, vol. 6, pp. 2047-2054, 1979.
- [70] R. Billinton, and S. Jonnavithula, "A test system for teaching overall power system reliability assessment," *IEEE transactions on Power Systems.*, vol. 11, no. 4, pp. 1670-1676, 1996.
- [71] F. X. Chu, and D. Yu, "Matlab Simulink library for steady flow simulation of gas pipeline networks," *Journal of Civil Aviation University of China.*, vol. 32, no. 4, pp. 43, 2014.

- [72] M. R. Tur, "Reliability assessment of distribution power system when considering energy storage configuration technique," *IEEE Access.*, vol. 8, pp. 77962-77971, 2020.
- [73] A. S. N. Huda, and R. Živanović, "Distribution system reliability assessment using sequential multilevel Monte Carlo method," *2016 IEEE Innovative Smart Grid Technologies-Asia (ISGT-Asia).*, pp. 867-872, 2016.
- [74] H. Lei, and C. Singh, "Non-sequential Monte Carlo simulation for cyber-induced dependent failures in composite power system reliability evaluation," *IEEE Transactions on Power Systems.*, vol. 32, no. 2, pp. 1064-1072, 2016.
- [75] N. Roslan, N. M. Fauzi, and M. M. Ridzuan, "Sequential and Nonsequential Monte Carlo in Assessing Reliability Performance of Distribution Network," *2020 Emerging Technology in Computing, Communication and Electronics (ETCCE).*, pp. 1-6, 2020.
- [76] T. M. Aljohani, and Mohammed J. Beshir, "Matlab code to assess the reliability of the smart power distribution system using monte carlo simulation," *Journal of Power and Energy Engineering.*, vol. 5, no. 8, pp. 30-44, 2017.
- [77] O. Grodzevich, and O. Romanko, "Normalization and other topics in multi-objective optimization," 2006.
- [78] K. Deb, et al, "A fast and elitist multiobjective genetic algorithm: NSGA-II," *IEEE transactions on evolutionary computation.*, vol. 6, no. 2, pp. 182-197, 2002.
- [79] S. Verma, M. Pant, and V. Snasel, "A Comprehensive Review on NSGA-II for Multi-Objective Combinatorial Optimization Problems," *IEEE Access.*, vol. 9, pp. 57757-57791, 2021.
- [80] Y. Yusoff, M. S. Ngadiman, and A. M. Zain, "Overview of NSGA-II for optimizing machining process parameters," *Procedia Engineering.*, vol. 15, pp. 3978-3983, 2011.
- [81] E. Zitzler, and L. Thiele, "Multiobjective evolutionary algorithms: a comparative case study and the strength Pareto approach," *IEEE transactions on Evolutionary Computation.*, vol. 3, no. 4, pp. 257-271, 1999.
- [82] Y. Tian, et al, "Effectiveness and efficiency of non-dominated sorting for evolutionary

- multi-and many-objective optimization,” *Complex & Intelligent Systems.*, vol. 3, no. 4, pp. 247-263, 2017.
- [83] C. Gianfranco, and A. Mazza, “Metaheuristic Optimization of Power and Energy Systems: Underlying Principles and Main Issues of the ‘Rush to Heuristics’,” *Energies.*, vol. 13, no. 19, pp.5097, 2020.
- [84] “Real Time Power System Simulation I RTDS Technologies,” [Online]. Available: <http://www.rtds.com/indexindex.html>.
- [85] X. Liu, et al, “Combined analysis of electricity and heat networks,” *Applied Energy.*, vol. 162, pp. 1238-1250, 2016.
- [86] H. Zhang, et al, “Power system resilience assessment considering of integrated natural gas system,” *IET International Conference on Resilience of Transmission and Distribution Networks (RTDN 2017).*, PP.1-7, 2017.
- [87] C. E. Borges, Y. K. Peña, and I. Fernandez, “Evaluating combined load forecasting in large power systems and smart grids,” *IEEE Transactions on Industrial Informatics.*, vol. 9, no. 3, pp. 1570-1577, 2012.
- [88] A. Jain, S. Lalwani, and M. Lalwani, “A comparative analysis of MOPSO, NSGA-II, SPEA2 and PESA2 for multi-objective optimal power flow,” *2018 2nd International Conference on Power, Energy and Environment: Towards Smart Technology (ICEPE).*, pp.1-6, 2018.
- [89] A. R. Alesaadi, M. Nafar, and A. H. Gheisari, “Sensitivity Analysis in Power Systems Reliability Evaluation,” *International Journal of Electrical and Computer Engineering.*, vol. 4, no. 10, pp. 1520-1522, 2010.
- [90] IPCC Climate Change, “The physical science basis,” *Contribution of working group I to the fifth assessment report of the intergovernmental panel on climate change.*, pp. 159-254, 2013.
- [91] M. Panteli, et al, “Power system resilience to extreme weather: fragility modeling, probabilistic impact assessment, and adaptation measures,” *IEEE Transactions on Power Systems.*, vol. 32, no. 5, pp. 3747-3757, 2016.

- [92] J. L. Carlson, et al. *Resilience: Theory and Application.*, no. ANL/DIS-12-1. Argonne National Lab.(ANL), Argonne, IL (United States), 2012.
- [93] M. Bao, et al, “Modeling and evaluating nodal resilience of multi-energy systems under windstorms,” *Applied Energy.*, vol. 270, pp. 115136, 2020.
- [94] J. Lu, et al, “Resilience assessment and its enhancement in tackling adverse impact of ice disasters for power transmission systems,” *Energies.*, vol. 11, no. 9, pp. 2272, 2018.
- [95] A. F. Mensah, *Resilience assessment of electric grids and distributed wind generation under hurricane hazards.*, Diss. 2015.
- [96] A. Mehrtash, P. Wang, and L. Goel, “Reliability evaluation of power systems considering restructuring and renewable generators,” *IEEE Transactions on Power Systems.*, vol. 27, no. 1, pp. 243-250, 2011.
- [97] M. Panteli, et al, “Metrics and quantification of operational and infrastructure resilience in power systems,” *IEEE Transactions on Power Systems.*, vol. 32, no. 6, pp. 4732-4742, 2017.
- [98] A. J. Casson, E. Luna, and E. Rodriguez-Villegas, “Performance metrics for the accurate characterisation of interictal spike detection algorithms,” *Journal of neuroscience methods.*, vol. 177, no. 2, pp. 479-487, 2009.
- [99] A. Shabanpour-Haghighi, and A. R. Seifi, “An integrated steady-state operation assessment of electrical, natural gas, and district heating networks,” *IEEE Transactions on Power Systems.*, vol. 31, no. 5, pp.3636-3647, 2015.
- [100] S. Mostapha Kalami Heris, “Non-dominated Sorting Genetic Algorithm II (NSGA-II),” (<https://www.mathworks.com/matlabcentral/fileexchange/52869-non-dominated-sorting-genetic-algorithm-ii-nsga-ii>), MATLAB Central File Exchange, Yarpiz, 2022.
- [101] Mostapha Kalami Heris, “Strength Pareto Evolutionary Algorithm 2 (SPEA2) in MATLAB,” (URL: <https://yarpiz.com/74/ypea122-spea2>), Yarpiz, 2015.
- [102] Mostapha Kalami Heris, “Multi-Objective PSO in MATLAB,” (URL: <https://yarpiz.com/59/ypea121-mopso>), Yarpiz, 2015.

- [103] W. Huang, et al, "Reliability and vulnerability assessment of multi-energy systems: An energy hub based method," IEEE Transactions on Power Systems., vol. 36, no. 5 , pp.3948-3959, 2021.

Appendix A

A.1 MES reliability assessment code

```
function z=MyCost(x)

x(1,:)=round(x(1,:));

year=1000;

load result24.mat;

Type1=[3,1,2,4,5,6,1,7,2,1,1,1,7,7,6,6,1,3,7,7,1,1,1,1];

load interrupt_fee.mat;

load Weight_factor.mat;

%The average load of each load point(MW)
lp_trans_power=[107.077213779364,60.2532767656026,181.754095190489,96.3818871666775,109.326683
348597,134.907214700247,124.429801941293,171.529395364880,175.285122604786,198.029532091456,0,
0,267.895258404406,197.274480497000,314.126650426578,101.128510551377,0,329.722379012546,181.3
68993770735,125.771939887093,0,0,0,0];
%Number of users at each load point
load lp_trans_users.mat;

lambda_transmission_transformer=0.02;
lambda_WT=0.4;
lambda_PV=0.4;
lambda_BS=0.05;
lambda_GT=0.12;
lambda_CHP=0.03;
lambda_P2G=0.03;
lambda_V2G=0.05;
load lambda_transmission_line.mat;
load lambda_DG.mat;
r_transmission_transformer=768;
r_WT=20;
r_PV=20;
r_BS=50;
r_GT=75*0.9;
r_CHP=200*0.9;
r_P2G=200*0.9;
r_V2G=50;
t_switch=0.02;
load r_transmission_line.mat;
load r_DG.mat;

numbus=24;
lp_number_failures=zeros(1,numbus);           %Initialize
Tdni=zeros(1,numbus);
Tupi=zeros(1,numbus);
ENStvl=zeros(1,numbus);
COSTtvl=zeros(1,numbus);

lp_outage_rate=zeros(numbus,1);
```

```

lp_outage_duration=zeros(numbus,1);
lp_outage_time=zeros(numbus,1);

%Initializes the failure rate and repair time of each component
for i=1:38 %1:33
    outage_rate(i)=lambda_transmission_line(i);
    outage_time(i)=r_transmission_line(i);
end

outage_rate(7)=lambda_transmission_transformer;
outage_rate(14)=lambda_transmission_transformer;
outage_rate(15)=lambda_transmission_transformer;
outage_rate(16)=lambda_transmission_transformer;
outage_rate(17)=lambda_transmission_transformer;
outage_time(7)=r_transmission_transformer;
outage_time(14)=r_transmission_transformer;
outage_time(15)=r_transmission_transformer;
outage_time(16)=r_transmission_transformer;
outage_time(17)=r_transmission_transformer;

for i=39:39
    outage_rate(i)=lambda_WT;
    outage_time(i)=r_WT;
end
for i=40:40
    outage_rate(i)=lambda_PV;
    outage_time(i)=r_PV;
end
for i=41:41
    outage_rate(i)=lambda_V2G;
    outage_time(i)=r_V2G;
end
for i=42:42
    outage_rate(i)=lambda_GT;
    outage_time(i)=r_GT;
end
for i=43:43
    outage_rate(i)=lambda_CHP;
    outage_time(i)=r_CHP;
end
for i=44:44
    outage_rate(i)=lambda_P2G;
    outage_time(i)=r_P2G;
end
for i=45:76
    outage_rate(i)=lambda_DG(i-44);
    outage_time(i)=r_DG(i-44);
end
for i=77:100
    outage_rate(i)=lambda_BS;
    outage_time(i)=r_BS;
end

load eff_24.mat;

s=1;

```

```

%% Sequential MCS
while s<=1
Time=0;
T=0;
while (Time<=year)

E1=rand(1,100);

for i=1:100
TTF_trans(i)=-1/outage_rate(i)*log(E1(i));
end

%Determine the minimum TTF and its fault element number k
[TTF_trans_min,k1]=min(TTF_trans);    % unit (year)

TTR_trans=-outage_time(k1)*log(rand(1)); % unit (h)

numbus=1;
while (numbus>=1)&&(numbus<=24)
Time=Time+TTF_trans_min+TTR_trans/8760;
tian=fix(Time/24);
if tian==0
    tian=1;
elseif tian>=8
    tian=rem(tian,7);
end
shi=round(rem(Time*8760,24));
if shi==0;
    shi=24;
end
shi1=round(shi+t_switch);

shi2=round(shi+TTR_trans);
shi2_shang=fix(shi2/24);
shi2_yu=rem(shi2,24);

if eff_24(k1,numbus)==0
    lp_number_failures(1,numbus)=lp_number_failures(1,numbus)+0;
    Tupi(1,numbus)=Tupi(1,numbus)+TTF_trans_min+TTR_trans/8760;    %unit (year)
    Tdni(1,numbus)=Tdni(1,numbus)+0;
    ENStvl(1,numbus)=ENStvl(1,numbus)+0;
    COSTtvl(1,numbus)=COSTtvl(1,numbus);
elseif (k1<=38)
    gonglv=result24(shi).branch(k1,14);
    if (gonglv<=0)&&(numbus==result24(shi).branch(k1,1))
        lp_number_failures(1,numbus)=lp_number_failures(1,numbus)+1;
        Tupi(1,numbus)=Tupi(1,numbus)+TTF_trans_min;    %unit (year)
        Tdni(1,numbus)=Tdni(1,numbus)+t_switch;
        L=0;
        L=L+result24(shi).bus(numbus,3);
        ENStvl(1,numbus)=ENStvl(1,numbus)+t_switch*L/(t_switch+1);
        if tian<=5

COSTtvl(1,numbus)=COSTtvl(1,numbus)+L/(t_switch+1)*interrupt_fee(Type1(numbus),t_switch/0.01+1)*
Weight_factor(Type1(numbus),shi)/(t_switch+1);
        else

COSTtvl(1,numbus)=COSTtvl(1,numbus)+L/(t_switch+1)*interrupt_fee(Type1(numbus),t_switch/0.01+1)*

```

```

Weight_factor(Type1(umbus)+7,shi)/(t_switch+1);
    end

elseif ((any(umbus==x(1:24))==1)&&(abs(gonglv)<=300))
    lp_number_failures(1,umbus)=lp_number_failures(1,umbus)+1;
    Tupi(1,umbus)=Tupi(1,umbus)+TTF_trans_min;           %unit (year)
    Tdni(1,umbus)=Tdni(1,umbus)+t_switch;
    L=0;
    L=L+result24(shi).bus(umbus,3);
    ENStvl(1,umbus)=ENStvl(1,umbus)+t_switch*L/(t_switch+1);

    if tian<=5

COSTtvl(1,umbus)=COSTtvl(1,umbus)+L/(t_switch+1)*interrupt_fee(Type1(umbus),t_switch/0.01+1)*
Weight_factor(Type1(umbus),shi)/(t_switch+1);
        else

COSTtvl(1,umbus)=COSTtvl(1,umbus)+L/(t_switch+1)*interrupt_fee(Type1(umbus),t_switch/0.01+1)*
Weight_factor(Type1(umbus)+7,shi)/(t_switch+1);
        end

else
    lp_number_failures(1,umbus)=lp_number_failures(1,umbus)+1;
    Tupi(1,umbus)=Tupi(1,umbus)+TTF_trans_min;
    Tdni(1,umbus)=Tdni(1,umbus)+TTR_trans;
    L=0;
    W=0;
    Whe=0;
    gonghe=0;

    if shi2_shang==0
        for i=shi:shi2
            L=L+result24(i).bus(umbus,3);
        end
        if tian<=5
            for i=shi:shi2
                W=W+Weight_factor(Type1(umbus),i);
            end
        else
            for i=shi:shi2
                W=W+Weight_factor(Type1(umbus)+7,i);
            end
        end
    end
else
    for i=shi:24
        L=L+result24(i).bus(umbus,3);
    end
    for i=1:24
        gonghe=gonghe+result24(i).bus(umbus,3);
    end
    L=L+(shi2_shang-1)*gonghe;
    for i=1:shi2_yu
        L=L+result24(i).bus(umbus,3);
    end
end

if shi2_shang>=1

```

```

if tian<=5
    for i=shi:24
        W=W+Weight_factor(Type1(numbus),i);
    end
else
    for i=shi:24
        W=W+Weight_factor(Type1(numbus)+7,i);
    end
end
elseif shi2_shang>=2
    for i=tian+1:shi2_shang+tian+1
        if 1<=rem(i,5)<=5
            for j=1:24
                W=W+Weight_factor(Type1(numbus),j);
            end
        else
            for j=1:24
                W=W+Weight_factor(Type1(numbus)+7,j);
            end
        end
    end
end
if shi2_yu~=0
    for i=1:shi2_yu
        if shi2_shang+tian+2<=5
            W=W+Weight_factor(Type1(numbus),i);
        else
            W=W+Weight_factor(Type1(numbus)+7,i);
        end
    end
end
end
else
    if shi2_yu~=0
        for i=1:shi2_yu
            if shi2_shang+tian+2<=5
                W=W+Weight_factor(Type1(numbus),i);
            else
                W=W+Weight_factor(Type1(numbus)+7,i);
            end
        end
    end
end
end
ENStvl(1,numbus)=ENStvl(1,numbus)+round(TTR_trans)*L/(round(TTR_trans)+1);

```

```

COSTtvl(1,numbus)=COSTtvl(1,numbus)+L/(round(TTR_trans)+1)*interrupt_fee(Type1(numbus),round(T
TR_trans)/0.01+1)*W/(round(TTR_trans)+1);

```

```

end

```

```

elseif (k1==40)
    if 7<=shi<=19
        lp_number_failures(1,numbus)=lp_number_failures(1,numbus)+1;
        Tupi(1,numbus)=Tupi(1,numbus)+TTF_trans_min;
        Tdni(1,numbus)=Tdni(1,numbus)+TTR_trans;
        L=0;
    W=0;
    Whe=0;
    gonghe=0;

```

```

if shi2_shang==0
    for i=shi:shi2
        L=L+result24(i).bus(numbus,3);
    end
    if tian<=5
        for i=shi:shi2
            W=W+Weight_factor(Type1(numbus),i);
        end
    else
        for i=shi:shi2
            W=W+Weight_factor(Type1(numbus)+7,i);
        end
    end
else
    for i=shi:24
        L=L+result24(i).bus(numbus,3);
    end
    for i=1:24
        gonghe=gonghe+result24(i).bus(numbus,3);
    end
    L=L+(shi2_shang-1)*gonghe;
    for i=1:shi2_yu
        L=L+result24(i).bus(numbus,3);
    end
end

if shi2_shang>=1
    if tian<=5
        for i=shi:24
            W=W+Weight_factor(Type1(numbus),i);
        end
    else
        for i=shi:24
            W=W+Weight_factor(Type1(numbus)+7,i);
        end
    end
elseif shi2_shang>=2
    for i=tian+1:shi2_shang+tian+1
        if 1<=rem(i,5)<=5
            for j=1:24
                W=W+Weight_factor(Type1(numbus),j);
            end
        else
            for j=1:24
                W=W+Weight_factor(Type1(numbus)+7,j);
            end
        end
    end
    if shi2_yu~=0
        for i=1:shi2_yu
            if shi2_shang+tian+2<=5
                W=W+Weight_factor(Type1(numbus),i);
            else
                W=W+Weight_factor(Type1(numbus)+7,i);
            end
        end
    end
else
    if shi2_yu~=0

```

```

    for i=1:shi2_yu
        if shi2_shang+tian+2<=5
            W=W+Weight_factor(Type1(umbus),i);
        else
            W=W+Weight_factor(Type1(umbus)+7,i);
        end
    end
end
end
ENStvl(1,umbus)=ENStvl(1,umbus)+round(TTR_trans)*L/(round(TTR_trans)+1);

COSTtvl(1,umbus)=COSTtvl(1,umbus)+L/(round(TTR_trans)+1)*interrupt_fee(Type1(umbus),round(T
TR_trans)/0.01+1)*W/(round(TTR_trans)+1);

else
    lp_number_failures(1,umbus)=lp_number_failures(1,umbus)+0;
    Tupi(1,umbus)=Tupi(1,umbus)+TTF_trans_min+TTR_trans/8760;
    Tdni(1,umbus)=Tdni(1,umbus)+0;
    ENStvl(1,umbus)=ENStvl(1,umbus)+0;
    COSTtvl(1,umbus)=COSTtvl(1,umbus);
end

elseif (77<=k1<=100)
    if (any(umbus==x(1:24))==1)
        lp_number_failures(1,umbus)=lp_number_failures(1,umbus)+1;
        Tupi(1,umbus)=Tupi(1,umbus)+TTF_trans_min;
        Tdni(1,umbus)=Tdni(1,umbus)+t_switch;
        L=0;
        L=L+result24(shi).bus(umbus,3);
        ENStvl(1,umbus)=ENStvl(1,umbus)+t_switch*L/(t_switch+1);
        if tian<=5

COSTtvl(1,umbus)=COSTtvl(1,umbus)+L/(t_switch+1)*interrupt_fee(Type1(umbus),t_switch/0.01+1)*
Weight_factor(Type1(umbus),shi)/(t_switch+1);
        else

COSTtvl(1,umbus)=COSTtvl(1,umbus)+L/(t_switch+1)*interrupt_fee(Type1(umbus)+7,shi)/(t_switch+1)*
Weight_factor(Type1(umbus)+7,shi)/(t_switch+1);
        end

    else
        lp_number_failures(1,umbus)=lp_number_failures(1,umbus)+0;
        Tupi(1,umbus)=Tupi(1,umbus)+TTF_trans_min+TTR_trans/8760;
        Tdni(1,umbus)=Tdni(1,umbus);
        ENStvl(1,umbus)=ENStvl(1,umbus)+0;
        COSTtvl(1,umbus)=COSTtvl(1,umbus);
    end
end
elseif (46<=k1<=76)

    powgen=result(shi).gen(k1-91,2);

    if (any(umbus==x(1:24))==1)&&(powgen<=300)
        lp_number_failures(1,umbus)=lp_number_failures(1,umbus)+1;
        Tupi(1,umbus)=Tupi(1,umbus)+TTF_trans_min;
        Tdni(1,umbus)=Tdni(1,umbus)+t_switch;
        L=0;
        L=L+result24(shi).bus(umbus,3);
        ENStvl(1,umbus)=ENStvl(1,umbus)+t_switch*L/(t_switch+1);
        if tian<=5

```



```

COSTtv1(1,numbus)=COSTtv1(1,numbus)+L/(t_switch+1)*interrupt_fee(Type1(numbus),t_switch/0.01+1)*
Weight_factor(Type1(numbus),shi)/(t_switch+1);
else

COSTtv1(1,numbus)=COSTtv1(1,numbus)+L/(t_switch+1)*interrupt_fee(Type1(numbus),t_switch/0.01+1)*
Weight_factor(Type1(numbus)+7,shi)/(t_switch+1);
end

else
lp_number_failures(1,numbus)=lp_number_failures(1,numbus)+1;
Tupi(1,numbus)=Tupi(1,numbus)+TTF_trans_min;
Tdni(1,numbus)=Tdni(1,numbus)+TTR_trans;
L=0;
W=0;
Whe=0;
gonghe=0;

if shi2_shang==0
for i=shi:shi2
L=L+result24(i).bus(numbus,3);
end
if tian<=5
for i=shi:shi2
W=W+Weight_factor(Type1(numbus),i);
end
else
for i=shi:shi2
W=W+Weight_factor(Type1(numbus)+7,i);
end
end
else
for i=shi:24
L=L+result24(i).bus(numbus,3);
end
for i=1:24
gonghe=gonghe+result24(i).bus(numbus,3);
end
L=L+(shi2_shang-1)*gonghe;
for i=1:shi2_yu
L=L+result24(i).bus(numbus,3);
end
end

if shi2_shang>=1
if tian<=5
for i=shi:24
W=W+Weight_factor(Type1(numbus),i);
end
else
for i=shi:24
W=W+Weight_factor(Type1(numbus)+7,i);
end
end
elseif shi2_shang>=2
for i=tian+1:shi2_shang+tian+1
if 1<=rem(i,5)<=5
for j=1:24
W=W+Weight_factor(Type1(numbus),j);

```

```

        end
    else
        for j=1:24
            W=W+Weight_factor(Type1(umbus)+7,j);
        end
    end
end
if shi2_yu~=0
for i=1:shi2_yu
    if shi2_shang+tian+2<=5
        W=W+Weight_factor(Type1(umbus),i);
    else
        W=W+Weight_factor(Type1(umbus)+7,i);
    end
end
end
else
    if shi2_yu~=0
    for i=1:shi2_yu
        if shi2_shang+tian+2<=5
            W=W+Weight_factor(Type1(umbus),i);
        else
            W=W+Weight_factor(Type1(umbus)+7,i);
        end
    end
end
end
ENStvl(1,umbus)=ENStvl(1,umbus)+round(TTR_trans)*L/(round(TTR_trans)+1);

```

$COSTvl(1,umbus)=COSTvl(1,umbus)+L/(round(TTR_trans)+1)*interrupt_fee(Type1(umbus),round(TTR_trans)/0.01+1)*W/(round(TTR_trans)+1);$

```

    end
else
    lp_number_failures(1,umbus)=lp_number_failures(1,umbus)+1;
    Tupi(1,umbus)=Tupi(1,umbus)+TTF_trans_min;
    Tdni(1,umbus)=Tdni(1,umbus)+TTR_trans;
    L=0;
    W=0;
    Whe=0;
    gonghe=0;

    if shi2_shang==0
        for i=shi:shi2
            L=L+result24(i).bus(umbus,3);
        end
        if tian<=5
            for i=shi:shi2
                W=W+Weight_factor(Type1(umbus),i);
            end
        else
            for i=shi:shi2
                W=W+Weight_factor(Type1(umbus)+7,i);
            end
        end
    end
else
    for i=shi:24
        L=L+result24(i).bus(umbus,3);
    end
end

```

```

for i=1:24
    gonghe=gonghe+result24(i).bus(numbus,3);
end
L=L+(shi2_shang-1)*gonghe;
for i=1:shi2_yu
    L=L+result24(i).bus(numbus,3);
end
end

if shi2_shang>=1
    if tian<=5
        for i=shi:24
            W=W+Weight_factor(Type1(numbus),i);
        end
    else
        for i=shi:24
            W=W+Weight_factor(Type1(numbus)+7,i);
        end
    end
elseif shi2_shang>=2
    for i=tian+1:shi2_shang+tian+1
        if 1<=rem(i,5)<=5
            for j=1:24
                W=W+Weight_factor(Type1(numbus),j);
            end
        else
            for j=1:24
                W=W+Weight_factor(Type1(numbus)+7,j);
            end
        end
    end
    if shi2_yu~=0
        for i=1:shi2_yu
            if shi2_shang+tian+2<=5
                W=W+Weight_factor(Type1(numbus),i);
            else
                W=W+Weight_factor(Type1(numbus)+7,i);
            end
        end
    end
else
    if shi2_yu~=0
        for i=1:shi2_yu
            if shi2_shang+tian+2<=5
                W=W+Weight_factor(Type1(numbus),i);
            else
                W=W+Weight_factor(Type1(numbus)+7,i);
            end
        end
    end
end
ENStvl(1,numbus)=ENStvl(1,numbus)+round(TTR_trans)*L/(round(TTR_trans)+1);

COSTvl(1,numbus)=COSTvl(1,numbus)+L/(round(TTR_trans)+1)*interrupt_fee(Type1(numbus),round(TTR_trans)/0.01+1)*W/(round(TTR_trans)+1);

end
numbus=numbus+1;
end

```

```

T=T+1;
end

%% Calculate each load point indices
numbus=24;
for i=1:numbus
    lp_outage_rate(i,s)=lp_number_failures(i)/Tupi(i);
    if lp_number_failures(i)== 0
        lp_outage_duration(i,s)=0;
    else
        lp_outage_duration(i,s)=Tdni(i)/lp_number_failures(i);
    end
    lp_outage_time(i,s)=lp_outage_rate(i)*lp_outage_duration(i);
end
s=s+1;
end

for i=1:numbus
    lp_outage_rate(1,i)=mean(lp_outage_rate(i,:));
    lp_outage_deration(1,i)=mean(lp_outage_duration(i,:));
    lp_outage_time(1,i)=mean(lp_outage_time(i,:));
end

%% Calculate system reliability indices
a1=0;
b1=0;
for i=1:numbus
    A(i)=lp_outage_rate(1,i)*lp_trans_users(i);
    a1=a1+A(i);
    b1=b1+lp_trans_users(i);
end
SAIFI_trans=a1/b1;

c1=0;
for i=1:numbus
    C(i)=lp_outage_time(1,i)*lp_trans_users(i);
    c1=c1+C(i);
end
SAIDI_trans=c1/b1;
CAIDI_trans=c1/a1;

ASAI_trans=(8760-SAIDI_trans)/8760;
ENS_trans=0;
for i=1:numbus
    F(i)=lp_outage_time(1,i)*lp_trans_power(i);
    ENS_trans=ENS_trans+F(i);
end

ECOST1=sum(COSTtvl)/year;

%%
heat_capacity=[481.575294686984,499.261131555399,430.623507139521,298.167501397124,464.1598406
30996,430.623507139521,302.434089912957,321.182148307327,298.248257028910,347.028233449281,31
8.695480144611,298.493763801679,298.493763801679]*10e-3; %MW
ld_ero=0.05;
for k=1:13

```



```

s=1;

Time=0;
T=0;
while (Time<=year)

E3=rand(1,27);

for i=1:27
TTF_heat(i)=-1/failure_rate_heat(i)*log(E3(i));
end

[TTF_heat_min,h]=min(TTF_heat);

TTR_heat=-repair_time_heat(h)*log(rand(1));

numload=1;
while (numload>=1)&&(numload<=13)
Time=Time+TTF_heat_min+TTR_heat/8760;
tian=fix(Time/24);
if tian==0
    tian=1;
elseif tian>=8
    tian=rem(tian,7);
end
shi=round(rem(Time*8760,24));
if shi==0;
    shi=24;
end
shi1=round(shi+t_hs_switch);

shi2=round(shi+TTR_heat);
shi2_shang=fix(shi2/24);
shi2_yu=rem(shi2,24);

    if heat(h,numload)==0
        lp_heat_number_faults(1,numload)=lp_heat_number_faults(1,numload)+0;
        Tu(1,numload)=Tu(1,numload)+TTF_heat_min+TTR_heat/8760;
        Td(1,numload)=Td(1,numload)+0;
        ENStvl(1,numload)=ENStvl(1,numload)+0;
        COSTtvl(1,numload)=COSTtvl(1,numload);
    else if (h<=14)
        if (any(numload==x(25:37))==1)
            lp_heat_number_faults(1,numload)=lp_heat_number_faults(1,numload)+1;
            Tu(1,numload)=Tu(1,numload)+TTF_heat_min;
            Td(1,numload)=Td(1,numload)+t_hs_switch;
            L=0;
            L=L+Hvl(numload,shi);
            ENStvl(1,numload)=ENStvl(1,numload)+t_hs_switch*L/(t_hs_switch+1);

            if tian<=5

COSTtvl(1,numload)=COSTtvl(1,numload)+L/(t_hs_switch+1)*interrupt_fee2*Weight_factor(Type2(numlo
ad),shi)/(t_hs_switch+1);
            else

COSTtvl(1,numload)=COSTtvl(1,numload)+L/(t_hs_switch+1)*interrupt_fee2*Weight_factor(Type2(numlo

```

```

ad)+7,shi)/(t_hs_switch+1);
    end

else
lp_heat_number_faults(1,numload)=lp_heat_number_faults(1,numload)+1;
Tu(1,numload)=Tu(1,numload)+TTF_heat_min;
Td(1,numload)=Td(1,numload)+TTR_heat;
L=0;
W=0;
Whe=0;
gonghe=0;
if shi2_shang==0
    for i=shi:shi2
        L=L+Hvl(numload,i);
    end
    if tian<=5
        for i=shi:shi2
            W=W+Weight_factor(Type2(numload),i);
        end
    else
        for i=shi:shi2
            W=W+Weight_factor(Type2(numload)+7,i);
        end
    end
else
    for i=shi:24
        L=L+Hvl(numload,i);
    end
    for i=1:24
        gonghe=gonghe+Hvl(numload,i);
    end
    L=L+(shi2_shang-1)*gonghe;
    for i=1:shi2_yu
        L=L+Hvl(numload,i);
    end
end

if shi2_shang>=1
    if tian<=5
        for i=shi:24
            W=W+Weight_factor(Type2(numload),i);
        end
    else
        for i=shi:24
            W=W+Weight_factor(Type2(numload)+7,i);
        end
    end
elseif shi2_shang>=2
    for i=tian+1:shi2_shang+tian+1
        if 1<=rem(i,5)<=5
            for j=1:24
                W=W+Weight_factor(Type2(numload),j);
            end
        else
            for j=1:24
                W=W+Weight_factor(Type2(numload)+7,j);
            end
        end
    end
end

```

```

end
if shi2_yu~=0
for i=1:shi2_yu
if shi2_shang+tian+2<=5
W=W+Weight_factor(Type2(numload),i);
else
W=W+Weight_factor(Type2(numload)+7,i);
end
end
end
else
if shi2_yu~=0
for i=1:shi2_yu
if shi2_shang+tian+2<=5
W=W+Weight_factor(Type2(numload),i);
else
W=W+Weight_factor(Type2(numload)+7,i);
end
end
end
end
ENStvl(1,numload)=ENStvl(1,numload)+round(TTR_heat)*L/(round(TTR_heat)+1);
COSTtvl(1,numload)=COSTtvl(1,numload)+L/(round(TTR_heat)+1)*interrupt_fee2*W/(round(TTR_heat)+1);

```

```

end
else if (h>=15)
if (any((numload)==x(25:37))==1)
lp_heat_number_faults(1,numload)=lp_heat_number_faults(1,numload)+1;
Tu(1,numload)=Tu(1,numload)+TTF_heat_min;
Td(1,numload)=Td(1,numload)+t_hs_switch;
L=0;
L=L+Hvl(numload,shi);
ENStvl(1,numload)=ENStvl(1,numload)+t_hs_switch*L/(t_hs_switch+1);

if tian<=5
COSTtvl(1,numload)=COSTtvl(1,numload)+L/(t_hs_switch+1)*interrupt_fee2*Weight_factor(Type2(numload),shi)/(t_hs_switch+1);
else

```

```

COSTtvl(1,numload)=COSTtvl(1,numload)+L/(t_hs_switch+1)*interrupt_fee2*Weight_factor(Type2(numload)+7,shi)/(t_hs_switch+1);
end

```

```

else
lp_heat_number_faults(1,numload)=lp_heat_number_faults(1,numload)+0;
Tu(1,numload)=Tu(1,numload)+TTF_heat_min+TTR_heat/8760;
Td(1,numload)=Td(1,numload);
ENStvl(1,numload)=ENStvl(1,numload)+0;
COSTtvl(1,numload)=COSTtvl(1,numload);
end
else
lp_heat_number_faults(1,numload)=lp_heat_number_faults(1,numload)+1;
Tu(1,numload)=Tu(1,numload)+TTF_heat_min;
Td(1,numload)=Td(1,numload)+TTR_heat;
L=0;

```



```

W=0;
Whe=0;
gonghe=0;
if shi2_shang==0
    for i=shi:shi2
        L=L+Hvl(numload,i);
    end
    if tian<=5
        for i=shi:shi2
            W=W+Weight_factor(Type2(numload),i);
        end
    else
        for i=shi:shi2
            W=W+Weight_factor(Type2(numload)+7,i);
        end
    end
end
else
    for i=shi:24
        L=L+Hvl(numload,i);
    end
    for i=1:24
        gonghe=gonghe+Hvl(numload,i);
    end
    L=L+(shi2_shang-1)*gonghe;
    for i=1:shi2_yu
        L=L+Hvl(numload,i);
    end
end
end

if shi2_shang>=1
    if tian<=5
        for i=shi:24
            W=W+Weight_factor(Type2(numload),i);
        end
    else
        for i=shi:24
            W=W+Weight_factor(Type2(numload)+7,i);
        end
    end
end
elseif shi2_shang>=2
    for i=tian+1:shi2_shang+tian+1
        if 1<=rem(i,5)<=5
            for j=1:24
                W=W+Weight_factor(Type2(numload),j);
            end
        else
            for j=1:24
                W=W+Weight_factor(Type2(numload)+7,j);
            end
        end
    end
end
if shi2_yu~=0
    for i=1:shi2_yu
        if shi2_shang+tian+2<=5
            W=W+Weight_factor(Type2(numload),i);
        else
            W=W+Weight_factor(Type2(numload)+7,i);
        end
    end
end
end

```

```

        end
    else
        if shi2_yu~=0
            for i=1:shi2_yu
                if shi2_shang+tian+2<=5
                    W=W+Weight_factor(Type2(numload),i);
                else
                    W=W+Weight_factor(Type2(numload)+7,i);
                end
            end
        end
    end
    ENStvl(1,numload)=ENStvl(1,numload)+round(TTR_heat)*L/(round(TTR_heat)+1);

    COSTtvl(1,numload)=COSTtvl(1,numload)+L/(round(TTR_heat)+1)*interrupt_fee2*W/(round(TTR_heat)+1);

    end
end
numload=numload+1;
end

T=T+1;
end

%% Calculate each load point indices
numload=13;
for i=1:numload
    lp_heat_failure_rate(i,s)=lp_heat_number_faults(i)/Tu(i);
    if lp_heat_number_faults(i)==0
        lp_heat_failure_duration(i,s)=0;
    else
        lp_heat_failure_duration(i,s)=Td(i)/lp_heat_number_faults(i);
    end
    lp_heat_failure_time(i,s)=lp_heat_failure_rate(i)*lp_heat_failure_duration(i);
end

for i=1:numload
    lp_heat_failure_rate(1,i)=mean(lp_heat_failure_rate(i,:));
    lp_heat_failure_duration(1,i)=mean(lp_heat_failure_duration(i,:));
    lp_heat_failure_time(1,i)=mean(lp_heat_failure_time(i,:));
end
%% Calculate system reliability indices
a3=0;
b3=0;
for i=1:numload
    A(i)=lp_heat_failure_rate(1,i)*users_heat(i);
    a3=a3+A(i);
    b3=b3+users_heat(i);
end
SAIFI_heat=a3/b3;

c3=0;
for i=1:numload
    C(i)=lp_heat_failure_time(1,i)*users_heat(i);
    c3=c3+C(i);

```

```

end
SAIDI_heat=c3/b3;
CAIDI_heat=c3/a3;

ASAI_heat=(8760-SAIDI_heat)/8760;

ENS_heat=0;
for i=1:numload
    F(i)=lp_heat_failure_time(1,i)*heat_capacity(i);
    ENS_heat=ENS_heat+F(i);
end

ECOST2=sum(COSTtvl)/year;

%%
lp_gas_demand=[1048.74146659868,167.614798999769,915.067797070137,368.776491804551,737.068172
187054,564.571063413647,335.859266623214,172.820483080334,287.788707060469];
load users_GN.mat;

ld_ero=0.05;
for k=1:9
    Gvl(k,:)=normrnd(lp_gas_demand(k),lp_gas_demand(k)*ld_ero,1,24);
end

Type3=[1,2,3,4,5,6,7,7,7];

interrupt_fee3=2/2.74;%/m^3

lambda_gas_pipeline=0.065;
lambda_p2g=0.03;
lambda_gs=0.05;
lambda_gb=0.025;

r_gas_pipeline=8;
r_p2g=200*0.9;
r_gs=50;
r_gb=300*0.9;
t_switch=0.5;

length_gas_pipeline = [100,50,150,80,200,150,100,80,120]*10e-3;

numgl=9;
lp_gas_number_faults=zeros(1,numgl);
Tdown=zeros(1,numgl);
Tup=zeros(1,numgl);
ENStvl=zeros(1,numgl);
COSTtvl=zeros(1,numgl);

lp_gas_failure_rate=zeros(numgl,1);
lp_gas_failure_duration=zeros(numgl,1);
lp_gas_failure_time=zeros(numgl,1);

for i=1:9
    failure_rate_gas(i)=lambda_gas_pipeline*length_gas_pipeline(i);
    repair_time_gas(i)=r_gas_pipeline*length_gas_pipeline(i)*0.9;
end

```

```

for i=10:10
    failure_rate_gas(i)=lambda_p2g;
    repair_time_gas(i)=r_p2g;
end
for i=11:11
    failure_rate_gas(i)=lambda_gb;
    repair_time_gas(i)=r_gb;
end
for i=12:20
    failure_rate_gas(i)=lambda_gs;
    repair_time_gas(i)=r_gs;
end

load gas_path.mat;
s=1;

while s<=1
    Time=0;
    T=0;
    while (Time<=year)

        E5=rand(1,20);

        for i=1:20
            TTF_gas(i)=-1/failure_rate_gas(i)*log(E5(i));
        end

        [TTF_gas_min,k5]=min(TTF_gas);

        TTR_gas=-repair_time_gas(k5)*log(rand(1));

        numgl=1;
        while (numgl>=1)&&(numgl<=9)
            Time=Time+TTF_gas_min+TTR_gas/8760;
            tian=fix(Time/24);
            if tian==0
                tian=1;
            elseif tian>=8
                tian=rem(tian,7);
            end
            shi=round(rem(Time*8760,24));
            if shi==0;
                shi=24;
            end
            shi1=round(shi+t_switch);

            shi2=round(shi+TTR_gas);
            shi2_shang=fix(shi2/24);
            shi2_yu=rem(shi2,24);

            if gas_path(k5,numgl)==0
                lp_gas_number_faults(1,numgl)=lp_gas_number_faults(1,numgl)+0;
                Tup(1,numgl)=Tup(1,numgl)+TTF_gas_min+TTR_gas/8760;
                Tdown(1,numgl)=Tdown(1,numgl)+0;
                ENStvl(1,numgl)=ENStvl(1,numgl)+0;
                COSTtvl(1,numgl)=COSTtvl(1,numgl);
            elseif (1<=k5<=9)

```

```

if (any(numgl==x(38:46))==1)&&(lp_gas_demand(numgl)<=500)
lp_gas_number_faults(1,numgl)=lp_gas_number_faults(1,numgl)+1;
Tup(1,numgl)=Tup(1,numgl)+TTF_gas_min;
Tdown(1,numgl)=Tdown(1,numgl)+t_switch;
L=0;
L=L+Gvl(numgl,shi);
ENStvl(1,numgl)=ENStvl(1,numgl)+t_switch*L/(t_switch+1);

    if tian<=5

COSTtvl(1,numgl)=COSTtvl(1,numgl)+L/(t_switch+1)*interrupt_fee3*Weight_factor(Type3(numgl),shi)/(t_switch+1);
    else

COSTtvl(1,numgl)=COSTtvl(1,numgl)+L/(t_switch+1)*interrupt_fee3*Weight_factor(Type3(numgl)+7,shi)/(t_switch+1);
    end

else
lp_gas_number_faults(1,numgl)=lp_gas_number_faults(1,numgl)+1;
Tup(1,numgl)=Tup(1,numgl)+TTF_gas_min;
Tdown(1,numgl)=Tdown(1,numgl)+TTR_gas;
L=0;
W=0;
Whe=0;
gonghe=0;
if shi2_shang==0
    for i=shi:shi2
        L=L+Gvl(numgl,i);
    end
    if tian<=5
        for i=shi:shi2
            W=W+Weight_factor(Type3(numgl),i);
        end
    else
        for i=shi:shi2
            W=W+Weight_factor(Type3(numgl)+7,i);
        end
    end
end
else
    for i=shi:24
        L=L+Gvl(numgl,i);
    end
    for i=1:24
        gonghe=gonghe+Gvl(numgl,i);
    end
    L=L+(shi2_shang-1)*gonghe;
    for i=1:shi2_yu
        L=L+Gvl(numgl,i);
    end
end
end

if shi2_shang>=1
    if tian<=5
        for i=shi:24
            W=W+Weight_factor(Type3(numgl),i);
        end
    else
        for i=shi:24

```

```

        W=W+Weight_factor(Type3(numgl)+7,i);
    end
end
elseif shi2_shang>=2
    for i=tian+1:shi2_shang+tian+1
        if 1<=rem(i,5)<=5
            for j=1:24
                W=W+Weight_factor(Type3(numgl),j);
            end
        else
            for j=1:24
                W=W+Weight_factor(Type3(numgl)+7,j);
            end
        end
    end
end
if shi2_yu~=0
    for i=1:shi2_yu
        if shi2_shang+tian+2<=5
            W=W+Weight_factor(Type3(numgl),i);
        else
            W=W+Weight_factor(Type3(numgl)+7,i);
        end
    end
end
else
    if shi2_yu~=0
        for i=1:shi2_yu
            if shi2_shang+tian+2<=5
                W=W+Weight_factor(Type3(numgl),i);
            else
                W=W+Weight_factor(Type3(numgl)+7,i);
            end
        end
    end
end
ENStvl(1,numgl)=ENStvl(1,numgl)+round(TTR_gas)*L/(round(TTR_gas)+1);

COSTtvl(1,numgl)=COSTtvl(1,numgl)+L/(round(TTR_gas)+1)*interrupt_fee3*W/(round(TTR_gas)+1);

end
elseif (k5>=11)
    if (any(numgl==x(38:46))==1)||(k5==11)
        lp_gas_number_faults(1,numgl)=lp_gas_number_faults(1,numgl)+1;
        Tup(1,numgl)=Tup(1,numgl)+TTF_gas_min;
        Tdown(1,numgl)=Tdown(1,numgl)+t_switch;
        L=0;
        L=L+Gvl(numgl,shi);
        ENStvl(1,numgl)=ENStvl(1,numgl)+t_switch*L/(t_switch+1);

        if tian<=5

COSTtvl(1,numgl)=COSTtvl(1,numgl)+L/(t_switch+1)*interrupt_fee3*Weight_factor(Type3(numgl),shi)/(t_switch+1);
        else

COSTtvl(1,numgl)=COSTtvl(1,numgl)+L/(t_switch+1)*interrupt_fee3*Weight_factor(Type3(numgl)+7,shi)/(t_switch+1);
        end
end

```

```

else
lp_gas_number_faults(1,numgl)=lp_gas_number_faults(1,numgl);
Tup(1,numgl)=Tup(1,numgl)+TTF_gas_min+TTR_gas/8760;
Tdown(1,numgl)=Tdown(1,numgl);
ENStvl(1,numgl)=ENStvl(1,numgl)+0;
COSTtvl(1,numgl)=COSTtvl(1,numgl);
end
else
lp_gas_number_faults(1,numgl)=lp_gas_number_faults(1,numgl)+1;
Tup(1,numgl)=Tup(1,numgl)+TTF_gas_min;
Tdown(1,numgl)=Tdown(1,numgl)+TTR_gas;
L=0;
W=0;
Whe=0;
gonghe=0;
if shi2_shang==0
for i=shi:shi2
L=L+Gvl(numgl,i);
end
if tian<=5
for i=shi:shi2
W=W+Weight_factor(Type3(numgl),i);
end
else
for i=shi:shi2
W=W+Weight_factor(Type3(numgl)+7,i);
end
end
else
for i=shi:24
L=L+Gvl(numgl,i);
end
for i=1:24
gonghe=gonghe+Gvl(numgl,i);
end
L=L+(shi2_shang-1)*gonghe;
for i=1:shi2_yu
L=L+Gvl(numgl,i);
end
end
end

if shi2_shang>=1
if tian<=5
for i=shi:24
W=W+Weight_factor(Type3(numgl),i);
end
else
for i=shi:24
W=W+Weight_factor(Type3(numgl)+7,i);
end
end
elseif shi2_shang>=2
for i=tian+1:shi2_shang+tian+1
if 1<=rem(i,5)<=5
for j=1:24
W=W+Weight_factor(Type3(numgl),j);
end
else
for j=1:24

```

```

        W=W+Weight_factor(Type3(numgl)+7,j);
    end
end
end
if shi2_yu~=0
for i=1:shi2_yu
    if shi2_shang+tian+2<=5
        W=W+Weight_factor(Type3(numgl),i);
    else
        W=W+Weight_factor(Type3(numgl)+7,i);
    end
end
end
else
if shi2_yu~=0
for i=1:shi2_yu
    if shi2_shang+tian+2<=5
        W=W+Weight_factor(Type3(numgl),i);
    else
        W=W+Weight_factor(Type3(numgl)+7,i);
    end
end
end
end
ENStvl(1,numgl)=ENStvl(1,numgl)+round(TTR_gas)*L/(round(TTR_gas)+1);

COSTtvl(1,numgl)=COSTtvl(1,numgl)+L/(round(TTR_gas)+1)*interrupt_fee3*W/(round(TTR_gas)+1);

    end
    numgl=numgl+1;
end

T=T+1;
end

numgl=9;
for i=1:numgl
    lp_gas_failure_rate(i,s)=lp_gas_number_faults(i)/Tup(i);
    if lp_gas_number_faults(i)==0
        lp_gas_failure_duration(i,s)=0;
    else
        lp_gas_failure_duration(i,s)=Tdown(i)/lp_gas_number_faults(i);
    end
    lp_gas_failure_time(i,s)=lp_gas_failure_rate(i)*lp_gas_failure_duration(i);
end
s=s+1;
end

for i=1:numgl
lp_gas_failure_rate(1,i)=mean(lp_gas_failure_rate(i,:));
lp_gas_failure_duration(1,i)=mean(lp_gas_failure_duration(i,:));
lp_gas_failure_time(1,i)=mean(lp_gas_failure_time(i,:));
end

a5=0;
b5=0;

```



```

for i=1:numgl
    A(i)=lp_gas_failure_rate(1,i)*users_GN(i);
    a5=a5+A(i);
    b5=b5+users_GN(i);
end
SAIFI_gas=a5/b5;

c5=0;
for i=1:numgl
    C(i)=lp_gas_failure_time(1,i)*users_GN(i);
    c5=c5+C(i);
end
SAIDI_gas=c5/b5;
CAIDI_gas=c5/a5;

ASAI_gas=(8760-SAIDI_gas)/8760;

ENS_gas=0;
for i=1:numgl
    F(i)=lp_gas_failure_time(1,i)*lp_gas_demand(i);
    ENS_gas=ENS_gas+F(i);
end

ECOST3=sum(COSTtv1)/year;

SAIFI=(a1+a3+a5)/(b1+b3+b5);
SAIDI=(c1+c3+c5)/(b1+b3+b5);
CAIDI=SAIDI/SAIFI;
ASAI=(8760-SAIDI)/8760;

cost=0;
geshu=0;
Cinstall=0;
for i=1:24
    if x(i)>=1
        geshu=geshu+1;
    else
        geshu=geshu;
    end
end

Cinstall=geshu*56.1;%187 per MWh*300*1e-3

geshu=0;
for i=1:13
    if x(i+24)>=1
        geshu=geshu+1;
    else
        geshu=geshu;
    end
end

Cinstall=Cinstall+geshu*5*1.21*0.5;

geshu=0;
for i=1:9
    if x(i+24+13)>=1
        geshu=geshu+1;
    end
end

```

```
else
    geshu=geshu;
end
end

Cinstall=Cinstall+geshu*3.665/28.26*500*1e-3;%MMBtu-m^3*500m^3

cost=ECOST1+ECOST2+ECOST3*1e-3+Cinstall;

z1=(SAIDI-0.05591)/(1.8622-0.05591);
z2=(cost-1492.13)/(9522.87-1492.13);
z=[z1,z2];
```

A.2 NSGA-II optimization code [100]

```
%% Problem Definition

CostFunction=@(x) MyCost(x); % Cost Function

nVar=46;

VarMin=0; % Lower Bound of Variables
VarMax=24; % Upper Bound of Variables

% Number of Objective Functions
nObj=2;

%% NSGA-II Parameters

MaxIt=200; % Maximum Number of Iterations

nPop=50; % Population Size

pCrossover=0.7; % Crossover Percentage
nCrossover=2*round(pCrossover*nPop/2); % Number of Parnets (Offsprings)

pMutation=0.4; % Mutation Percentage
nMutation=round(pMutation*nPop); % Number of Mutants

mu=0.02; % Mutation Rate

sigma=0.1*(VarMax-VarMin); % Mutation Step Size

%% Initialization

empty_individual.Position=[];
empty_individual.Cost=[];
empty_individual.Rank=[];
empty_individual.DominationSet=[];
empty_individual.DominatedCount=[];
empty_individual.CrowdingDistance=[];

pop= repmat(empty_individual,nPop,1);

for i=1:nPop

    pop(i).Position(1:24)=unifrnd(0,24,[1 24]);
    pop(i).Position(25:37)=unifrnd(0,13,[1 13]);
    pop(i).Position(38:46)=unifrnd(0,9,[1 9]);
    pop(i).Position=round(pop(i).Position);

end

for i=1:nPop
    [B, I] = unique(pop(i).Position(1:24), 'first');
    A=setdiff(1:24, I);
    for j=1:numel(A)
        pop(i).Position(A(j))=0;
    end
end
```

```

end

for i=1:nPop
    [B, I] = unique(pop(i).Position(25:37), 'first');
    A=setdiff(1:13, I);
    for j=1:numel(A)
        pop(i).Position(A(j)+24)=0;
    end
end

for i=1:nPop
    [B, I] = unique(pop(i).Position(38:46), 'first');
    A=setdiff(1:9, I);
    for j=1:numel(A)
        pop(i).Position(A(j)+37)=0;
    end
end

for i=1:nPop
    pop(i).Cost=CostFunction(pop(i).Position);
end

for i=1:nPop
    if isnan(pop(i).Cost)==1
        pop(i).Cost=CostFunction(pop(i).Position);
    end
end

% Non-Dominated Sorting
[pop, F]=NonDominatedSorting(pop);

% Calculate Crowding Distance
pop=CalcCrowdingDistance(pop,F);

% Sort Population
[pop, F]=SortPopulation(pop);

%% NSGA-II Main Loop

for it=1:MaxIt

    % Crossover
    popc= repmat(empty_individual,nCrossover/2,2);
    for k=1:nCrossover/2

        i1=randi([1 nPop]);
        p1=pop(i1);

        i2=randi([1 nPop]);
        p2=pop(i2);

        [popc(k,1).Position, popc(k,2).Position]=Crossover(p1.Position,p2.Position);
        popc(k,1).Position=round(popc(k,1).Position);
        popc(k,2).Position=round(popc(k,2).Position);
    end

end

```

```

for i=1:numel(popc)
    for j=1:nVar
        if (popc(i).Position(j)<VarMin)
            popc(i).Position(j)=VarMin;
        end
    end
end

hang=size(popc(:,1));
for i=1:hang
    [B, I] = unique(popc(i,1).Position(1:24), 'first');
    A=setdiff(1:24, I);
    for j=1:numel(A)
        popc(i,1).Position(A(j))=0;
    end

    [B, I] = unique(popc(i,1).Position(25:37), 'first');
    A=setdiff(1:13, I);
    for j=1:numel(A)
        popc(i,1).Position(A(j)+24)=0;
    end

    [B, I] = unique(popc(i,1).Position(38:46), 'first');
    A=setdiff(1:9, I);
    for j=1:numel(A)
        popc(i,1).Position(A(j)+37)=0;
    end

    [B, I] = unique(popc(i,2).Position(1:24), 'first');
    A=setdiff(1:24, I);
    for j=1:numel(A)
        popc(i,2).Position(A(j))=0;
    end

    [B, I] = unique(popc(i,2).Position(25:37), 'first');
    A=setdiff(1:13, I);
    for j=1:numel(A)
        popc(i,2).Position(A(j)+24)=0;
    end

    [B, I] = unique(popc(i,2).Position(38:46), 'first');
    A=setdiff(1:9, I);
    for j=1:numel(A)
        popc(i,2).Position(A(j)+37)=0;
    end

end

for k=1:nCrossover/2
    popc(k,1).Cost=CostFunction(popc(k,1).Position);
    popc(k,2).Cost=CostFunction(popc(k,2).Position);
end

```

```

for i=1:numel(popc)
if isnan(popc(i).Cost)==1
    popc(i).Cost=CostFunction(popc(i).Position);
end
end

popc=popc(:);

% Mutation
popm=repmat(empty_individual,nMutation,1);
for k=1:nMutation

    i=randi([1 nPop]);
    p=pop(i);

    popm(k).Position=Mutate(p.Position,mu,sigma);
    popm(k).Position=round(popm(k).Position);
end

for i=1:numel(popm)
    for j=1:nVar
        if (popm(i).Position(j)<VarMin)
            popm(i).Position(j)=VarMin;
        end
    end
end

hang=size(popm(:,1));
for i=1:hang
    [B, I] = unique(popm(i,1).Position(1:24), 'first');
    A=setdiff(1:24, I);
    for j=1:numel(A)
        popm(i,1).Position(A(j))=0;
    end

    [B, I] = unique(popm(i,1).Position(25:37), 'first');
    A=setdiff(1:13, I);
    for j=1:numel(A)
        popm(i,1).Position(A(j)+24)=0;
    end

    [B, I] = unique(popm(i,1).Position(38:46), 'first');
    A=setdiff(1:9, I);
    for j=1:numel(A)
        popm(i,1).Position(A(j)+37)=0;
    end

end

for k=1:nMutation
    popm(k).Cost=CostFunction(popm(k).Position);
end

for i=1:numel(popm)
if isnan(popm(i).Cost)==1
    popm(i).Cost=CostFunction(popm(i).Position);
end
end

```

```

end
    end

% Merge
pop=[pop
    popc
    popm];

for i=1:numel(pop)
    for j=1:nVar
        if (pop(i).Position(j)<VarMin)
            pop(i).Position(j)=VarMin;
        end
    end
end

for i=1:nPop
    if isnan(pop(i).Cost)==1
        pop(i).Cost=CostFunction(pop(i).Position);
    end
end

% Non-Dominated Sorting
[pop, F]=NonDominatedSorting(pop);

% Calculate Crowding Distance
pop=CalcCrowdingDistance(pop,F);

% Sort Population
pop=SortPopulation(pop);

% Truncate
pop=pop(1:nPop);

% Non-Dominated Sorting
[pop, F]=NonDominatedSorting(pop);

% Calculate Crowding Distance
pop=CalcCrowdingDistance(pop,F);

for i=1:numel(pop)
    for j=1:nVar
        if (pop(i).Position(j)<VarMin)
            pop(i).Position(j)=VarMin;
        end
    end
end

for i=1:numel(pop)
    if isnan(pop(i).Cost)==1
        pop(i).Cost=CostFunction(pop(i).Position);
    end
end

% Sort Population
[pop, F]=SortPopulation(pop);

```

```

    % Store F1
    F1=pop(F{1});

    for i=1:numel(F1)
    a(i)=F1(i).Cost(1);
    end

    for i=1:numel(F1)
    b(i)=F1(i).Cost(2);
    end

    nsga1_24(it)=min(a);
    nsga2_24(it)=min(b);

    if it>=2
        if nsga1_24(it)>=nsga1_24(it-1)
            nsga1_24(it)=nsga1_24(it-1);
        end
    end

    if it>=2
        if nsga2_24(it)>=nsga2_24(it-1)
            nsga2_24(it)=nsga2_24(it-1);
        end
    end

    % Show Iteration Information
    %disp(['Iteration ' num2str(it) ': Number of F1 Members = ' num2str(numel(F1))]);

    % Plot F1 Costs
    %figure(1);
    %PlotCosts(F1);
    % pause(0.01);

end

%% Results
toc
disp(['operation time: ',num2str(toc)]);
disp('optimal location')
F1.Position
costs=GetCosts(F1);
figure(1);
plot(costs(1,:),costs(2,:),'rx');
hold on;
xlabel('1^{st} Objective-SAIDI');
ylabel('2^{nd} Objective-Cost');

```


A.3 SPEA2 optimization code [101]

```
%% Problem Definition

CostFunction=@(x) MyCost(x);

nVar=46;          % Number of Decision Variables

VarMin=0;        % Decision Variables Lower Bound
VarMax=24;       % Decision Variables Upper Bound

%% SPEA2 Settings

MaxIt=200;       % Maximum Number of Iterations

nPop=50;         % Population Size

nArchive=50;     % Archive Size

K=round(sqrt(nPop+nArchive)); % KNN Parameter

pCrossover=0.7;
nCrossover=round(pCrossover*nPop/2)*2;

pMutation=1-pCrossover;
nMutation=nPop-nCrossover;

crossover_params.gamma=0.1;
crossover_params.VarMin=VarMin;
crossover_params.VarMax=VarMax;

mutation_params.h=0.2;
mutation_params.VarMin=VarMin;
mutation_params.VarMax=VarMax;

%% Initialization

empty_individual.Position=[];
empty_individual.Cost=[];
empty_individual.S=[];
empty_individual.R=[];
empty_individual.sigma=[];
empty_individual.sigmaK=[];
empty_individual.D=[];
empty_individual.F=[];

pop= repmat(empty_individual,nPop,1);
for i=1:nPop
    pop(i).Position(1:24)=unifrnd(0,24,[1 24]);
    pop(i).Position(25:37)=unifrnd(0,13,[1 13]);
    pop(i).Position(38:46)=unifrnd(0,9,[1 9]);
    pop(i).Position=round(pop(i).Position);
end

for i=1:nPop
```

```

    [B, I] = unique(pop(i).Position(1:24), 'first');
    A=setdiff(1:24, I);
    for j=1:numel(A)
        pop(i).Position(A(j))=0;
    end
end

for i=1:nPop
    [B, I] = unique(pop(i).Position(25:37), 'first');
    A=setdiff(1:13, I);
    for j=1:numel(A)
        pop(i).Position(A(j)+24)=0;
    end
end

for i=1:nPop
    [B, I] = unique(pop(i).Position(38:46), 'first');
    A=setdiff(1:9, I);
    for j=1:numel(A)
        pop(i).Position(A(j)+37)=0;
    end
end

for i=1:nPop
    pop(i).Cost=CostFunction(pop(i).Position);
end

    for i=1:numel(pop)
        if isnan(pop(i).Cost)==1
            pop(i).Cost=CostFunction(pop(i).Position);
        end
    end
end

```

```
archive=[];
```

```
%% Main Loop
```

```
for it=1:MaxIt
```

```
    Q=[pop
        archive];
```

```
    nQ=numel(Q);
```

```
    dom=false(nQ,nQ);
```

```
    for i=1:nQ
        Q(i).S=0;
    end
```

```
    for i=1:nQ
        for j=i+1:nQ
```

```
            if Dominates(Q(i),Q(j))
                Q(i).S=Q(i).S+1;
                dom(i,j)=true;
            end
```

```
        elseif Dominates(Q(j),Q(i))
```

```

        Q(j).S=Q(j).S+1;
        dom(j,i)=true;

    end

    end

end

S=[Q.S];
for i=1:nQ
    Q(i).R=sum(S(dom(:,i)));
end

Z=[Q.Cost]';
SIGMA=pdist2(Z,Z,'seuclidean');
SIGMA=sort(SIGMA);
for i=1:nQ
    Q(i).sigma=SIGMA(:,i);
    Q(i).sigmaK=Q(i).sigma(K);
    Q(i).D=1/(Q(i).sigmaK+2);
    Q(i).F=Q(i).R+Q(i).D;
end

nND=sum([Q.R]==0);
if nND<=nArchive
    F=[Q.F];
    [F, SO]=sort(F);
    Q=Q(SO);
    archive=Q(1:min(nArchive,nQ));

else
    SIGMA=SIGMA(:,[Q.R]==0);
    archive=Q([Q.R]==0);

    k=2;
    while numel(archive)>nArchive
        while min(SIGMA(k,:))==max(SIGMA(k,:)) && k<size(SIGMA,1)
            k=k+1;
        end

        [~, j]=min(SIGMA(k,:));

        archive(j)=[];
        SIGMA(:,j)=[];
    end

end

PF=archive([archive.R]==0); % Approximate Pareto Front

% Plot Pareto Front
%figure(1);
%PlotCosts(PF);
% pause(0.01);

% Display Iteration Information
% disp(['Iteration ' num2str(it) ': Number of PF members = ' num2str(numel(PF))]);

if it>=MaxIt

```

```

    break;
end

% Crossover
popc= repmat(empty_individual,nCrossover/2,2);
for c=1:nCrossover/2

    p1=BinaryTournamentSelection(archive,[archive.F]);
    p2=BinaryTournamentSelection(archive,[archive.F]);

    [popc(c,1).Position, popc(c,2).Position]=Crossover(p1.Position,p2.Position,crossover_params);
    popc(c,1).Position=round(popc(c,1).Position);
    popc(c,2).Position=round(popc(c,2).Position);
end

hang=size(popc(:,1));
for i=1:hang
    [B, I] = unique(popc(i,1).Position(1:24), 'first');
    A=setdiff(1:24, I);
    for j=1: numel(A)
        popc(i,1).Position(A(j))=0;
    end

    [B, I] = unique(popc(i,1).Position(25:37), 'first');
    A=setdiff(1:13, I);
    for j=1: numel(A)
        popc(i,1).Position(A(j)+24)=0;
    end

    [B, I] = unique(popc(i,1).Position(38:46), 'first');
    A=setdiff(1:9, I);
    for j=1: numel(A)
        popc(i,1).Position(A(j)+37)=0;
    end

    [B, I] = unique(popc(i,2).Position(1:24), 'first');
    A=setdiff(1:24, I);
    for j=1: numel(A)
        popc(i,2).Position(A(j))=0;
    end

    [B, I] = unique(popc(i,2).Position(25:37), 'first');
    A=setdiff(1:13, I);
    for j=1: numel(A)
        popc(i,2).Position(A(j)+24)=0;
    end

    [B, I] = unique(popc(i,2).Position(38:46), 'first');
    A=setdiff(1:9, I);
    for j=1: numel(A)
        popc(i,2).Position(A(j)+37)=0;
    end
end

```

```

end

    for c=1:nCrossover/2
    popc(c,1).Cost=CostFunction(popc(c,1).Position);
    popc(c,2).Cost=CostFunction(popc(c,2).Position);
    end

for i=1: numel(popc)
if isnan(popc(i).Cost)==1
    popc(i).Cost=CostFunction(popc(i).Position);
end
end
popc=popc(:);

% Mutation
popm= repmat(empty_individual,nMutation,1);
for m=1:nMutation

    p=BinaryTournamentSelection(archive,[archive.F]);

    popm(m).Position=Mutate(p.Position,mutation_params);
    popm(m).Position=round(popm(m).Position);

end

hang=size(popm(:,1));
for i=1:hang
    [B, I] = unique(popm(i,1).Position(1:24), 'first');
    A=setdiff(1:24, I);
    for j=1: numel(A)
        popm(i,1).Position(A(j))=0;
    end

    [B, I] = unique(popm(i,1).Position(25:37), 'first');
    A=setdiff(1:13, I);
    for j=1: numel(A)
        popm(i,1).Position(A(j)+24)=0;
    end

    [B, I] = unique(popm(i,1).Position(38:46), 'first');
    A=setdiff(1:9, I);
    for j=1: numel(A)
        popm(i,1).Position(A(j)+37)=0;
    end

end

end

for m=1:nMutation
    popm(m).Cost=CostFunction(popm(m).Position);
end

```

```

for i=1:numel(popm)
if isnan(popm(i).Cost)==1
    popm(i).Cost=CostFunction(popm(i).Position);
end
end

% Create New Population
pop=[popc
    popm];
for i=1:numel(pop)
if isnan(pop(i).Cost)==1
    pop(i).Cost=CostFunction(pop(i).Position);
end
end

    for i=1:numel(PF)
a(i)=PF(i).Cost(1);
end

for i=1:numel(PF)
b(i)=PF(i).Cost(2);
end

spea1_24(it)=min(a);
spea2_24(it)=min(b);

if it>=2
    if spea1_24(it)>=spea1_24(it-1)
        spea1_24(it)=spea1_24(it-1);
    end
end

if it>=2
    if spea2_24(it)>=spea2_24(it-1)
        spea2_24(it)=spea2_24(it-1);
    end
end

end

%% Results

figure(2);
PlotCosts(PF);
toc
disp(['operation time: ',num2str(toc)]);
disp('optimal location')
PF.Position

```

A.4 MOPSO optimization code [102]

```
CostFunction=@(x) MyCost(x);
nVar=46;
VarMin=0;
VarMax=24;

VelMax=(VarMax-VarMin)/10;

%% MOPSO
nPop=50; % Population Size

nRep=50; % Repository Size

MaxIt=200; % Maximum Number of Iterations

phi1=2.05;
phi2=2.05;
phi=phi1+phi2;
chi=2/(phi-2+sqrt(phi^2-4*phi));

w=chi; % Inertia Weight
wdamp=0.9; % Inertia Weight Damping Ratio
c1=chi*phi1; % Personal Learning Coefficient
c2=2; % Global Learning Coefficient

alpha=0.1; % Grid Inflation Parameter

nGrid=7; % Number of Grids per each Dimension

beta=4; % Leader Selection Pressure Parameter

gamma=2; % Extra (to be deleted) Repository Member Selection Pressure

%%

particle=CreateEmptyParticle(nPop);

for i=1:nPop
    particle(i).Velocity=0;
    particle(i).Position(1:24)=unifrnd(0,24,[1 24]);
    particle(i).Position(25:37)=unifrnd(0,13,[1 13]);
    particle(i).Position(38:46)=unifrnd(0,9,[1 9]);
    % Inicializa the position of variable
    particle(i).Position=round(particle(i).Position);
end
for i=1:nPop
    [B, I] = unique(particle(i).Position(1:24), 'first');
    A=setdiff(1:24, I);
    for j=1:numel(A)
        particle(i).Position(A(j))=0;
    end
end
for i=1:nPop
    [B, I] = unique(particle(i).Position(25:37), 'first');
    A=setdiff(1:13, I);
    for j=1:numel(A)
```

```

    particle(i).Position(A(j)+24)=0;
end
end
for i=1:nPop
    [B, I] = unique(particle(i).Position(38:46), 'first');
    A=setdiff(1:9, I);
    for j=1:numel(A)
        particle(i).Position(A(j)+37)=0;
    end
end

for i=1:nPop
    particle(i).Cost=CostFunction(particle(i).Position); % objective function
    particle(i).Best.Position=particle(i).Position;
    particle(i).Best.Cost=particle(i).Cost;
end
for i=1:nPop
    if isnan(particle(i).Cost(1))==1
        particle(i).Cost=CostFunction(particle(i).Position);
    end
end
particle=DetermineDomination(particle);

rep=GetNonDominatedParticles(particle);
for i=1:numel(rep)
    if isnan(rep(i).Cost(1))==1
        rep(i).Cost=CostFunction(rep(i).Position);
    end
end

rep_costs=GetCosts(rep);
G=CreateHypercubes(rep_costs,nGrid,alpha);

for i=1:numel(rep)
    [rep(i).GridIndex rep(i).GridSubIndex]=GetGridIndex(rep(i),G);
end

%% MOPSO main loop

for it=1:MaxIt
    for i=1:nPop
        rep_h=SelectLeader(rep,beta);

        particle(i).Velocity=w*particle(i).Velocity ...
            +c1*rand*(particle(i).Best.Position - particle(i).Position) ...
            +c2*rand*(rep_h.Position - particle(i).Position);

        particle(i).Velocity=min(max(particle(i).Velocity,-VelMax),+VelMax);

        particle(i).Position=particle(i).Position + particle(i).Velocity;

        flag1=(particle(i).Position(1:24)<0 | particle(i).Position(1:24)>24);
        flag2=(particle(i).Position(25:37)<0 | particle(i).Position(25:37)>13);
        flag3=(particle(i).Position(38:46)<0 | particle(i).Position(38:46)>9);
        flag=[flag1,flag2,flag3];
        particle(i).Velocity(flag)=-particle(i).Velocity(flag);
    end
end

```



```

particle(i).Position(1:24)=min(max(particle(i).Position(1:24),0),24);
particle(i).Position(25:37)=min(max(particle(i).Position(25:37),0),13);
particle(i).Position(38:46)=min(max(particle(i).Position(38:46),0),9);
particle(i).Position=round(particle(i).Position);
[B, I] = unique(particle(i).Position(1:24), 'first');
A=setdiff(1:24, I);
for j=1:numel(A)
    particle(i).Position(A(j))=0;
end

[B, I] = unique(particle(i).Position(25:37), 'first');
A=setdiff(1:13, I);
for j=1:numel(A)
    particle(i).Position(A(j)+24)=0;
end

[B, I] = unique(particle(i).Position(38:46), 'first');
A=setdiff(1:9, I);
for j=1:numel(A)
    particle(i).Position(A(j)+37)=0;
end

particle(i).Cost=CostFunction(particle(i).Position);

if Dominates(particle(i),particle(i).Best)
    particle(i).Best.Position=particle(i).Position;
    particle(i).Best.Cost=particle(i).Cost;

elseif ~Dominates(particle(i).Best,particle(i))
    if rand<0.5
        particle(i).Best.Position=particle(i).Position;
        particle(i).Best.Cost=particle(i).Cost;
    end
end

end

for i=1:nPop
    if isnan(particle(i).Cost(1))==1
        particle(i).Cost=CostFunction(particle(i).Position);
    end
end

particle=DetermineDomination(particle);
nd_particle=GetNonDominatedParticles(particle);

rep=[rep
    nd_particle];

rep=DetermineDomination(rep);
rep=GetNonDominatedParticles(rep);

for i=1:numel(rep)
    if isnan(rep(i).Cost(1))==1
        rep(i).Cost=CostFunction(rep(i).Position);
    end
end

for i=1:numel(rep)

```

```

    [rep(i).GridIndex rep(i).GridSubIndex]=GetGridIndex(rep(i),G);
end

if numel(rep)>nRep
    EXTRA=numel(rep)-nRep;
    rep=DeleteFromRep(rep,EXTRA,gamma);

    rep_costs=GetCosts(rep);
    G=CreateHypercubes(rep_costs,nGrid,alpha);

end
costs=GetCosts(particle);

for i=1:numel(rep)
a(i)=rep(i).Cost(1);
end

for i=1:numel(rep)
b(i)=rep(i).Cost(2);
end

mopso1(it)=min(a);
mopso2(it)=min(b);

if it>=2
    if mopso1(it)>=mopso1(it-1)
        mopso1(it)=mopso1(it-1);
    end
end

if it>=2
    if mopso2(it)>=mopso2(it-1)
        mopso2(it)=mopso2(it-1);
    end
end

%figure(1)
%plot(costs(1,:),costs(2:),'b. ');
%hold on;
%plot(rep_costs(1,:),rep_costs(2:),'rx');
%legend('Main Population','Repository');
%xlabel('1^{st} Objective-SAIDI');
%ylabel('2^{nd} Objective-Cost');
%pause(0.01);
%zlabel('3^{rd} Objective-CAIDI');

% disp(['Iteration ' num2str(it) ': Number of Repository Particles = ' num2str(numel(rep))]);

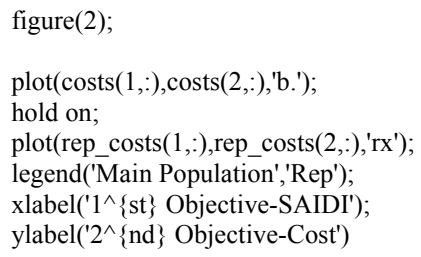
w=w*wdamp;
end

%% result
toc
disp(['operation time: ',num2str(toc)]);
costs=GetCosts(particle);
rep_costs=GetCosts(rep);
disp('optimal location')
rep.Position

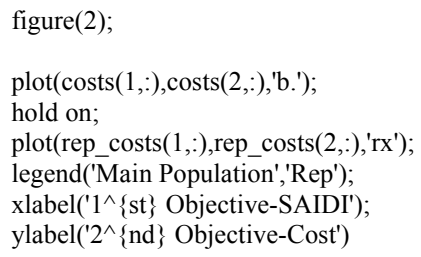
```

```
figure(2);

plot(costs(1,:),costs(2,:),'b.');
```



```
hold on;
plot(rep_costs(1,:),rep_costs(2,:),'rx');
```



```
legend('Main Population','Rep');
xlabel('1^{st} Objective-SAIDI');
ylabel('2^{nd} Objective-Cost')
```